A METHODOLOGY FOR THE DESIGN OF SPACEBORNE PENCIL-BEAM SCATTEROMETER SYSTEMS

by

Michael W. Spencer

A dissertation submitted to the faculty of

Brigham Young University

in partial fulfillment of the requirements for the degree of

Doctor of Philosophy

Department of Electrical and Computer Engineering

Brigham Young University

December 2001

BRIGHAM YOUNG UNIVERSITY

GRADUATE COMMITTEE APPROVAL

of a dissertation submitted by

Michael W. Spencer

This dissertation has been read by each member of the following graduate committee and by majority vote has been found to be satisfactory.

Date	David G. Long, Chair
Date	David V. Arnold
Date	Randal W. Beard
Date	Michael A. Jensen
Date	Richard H. Selfridge

BRIGHAM YOUNG UNIVERSITY

As chair of the candidate's graduate committee, I have read the dissertation of Michael W. Spencer in its final form and have found that (1) its format, citations, and bibliographical style are consistent and acceptable and fulfill university and department style requirements; (2) its illustrative materials including figures, tables, and charts are in place; and (3) the final manuscript is satisfactory to the graduate committee and is ready for submission to the university library.

Date

David G. Long
Chair, Graduate Committee

Accepted for the Department

A. Lee Swindlehurst
Graduate Coordinator

Accepted for the College

Douglas M. Chabries
Dean, College of Engineering and Technology

ABSTRACT

A METHODOLOGY FOR THE DESIGN OF SPACEBORNE PENCIL-BEAM SCATTEROMETER SYSTEMS

Michael W. Spencer

Electrical and Computer Engineering

Doctor of Philosophy

Spaceborne scatterometer instruments are important tools for the remote sensing of the Earth's environment. In addition to the primary goal of measuring ocean winds, data from scatterometers have proven useful in the study of a variety of land and cryosphere processes as well. Several satellites carrying scatterometers have flown in the last two decades. These previous systems have been "fan-beam" scatterometers, where multiple antennas placed in fixed positions are used. The fan-beam scatterometer approach, however, has disadvantages which limit its utility for future missions. An alternate approach, the conically-scanning "pencil-beam" scatterometer technique, alleviates many of the problems encountered with earlier systems and provides additional measurement capability. Due to these advantages, the pencil-beam approach has been selected by NASA as the basis for future scatterometer missions. Whereas the fan-beam approach is mature and well understood, there is a need for a fundamental study of the unique aspects of the pencil-beam technique.

In this dissertation, a comprehensive treatment of the design issues associated with pencil-beam scatterometers is presented. A new methodology is established for evaluating and optimizing the performance of conically-scanning radar systems. Employing this methodology, key results are developed and used in the design of the *SeaWinds* instrument – NASA's first pencil-beam scatterometer. Further, the theoretical framework presented in this study is used to propose new scatterometer techniques which will significantly improve the spatial resolution and measurement accuracy of future instruments.

ACKNOWLEDGMENTS

This work is dedicated to my wife, Miriam, and to my children, Emily, Jack, and Mary; whose patience and support made the completion of this dissertation possible. I will fondly remember the time our family spent in Utah.

I also acknowledge Dr. Wu-Yang Tsai of JPL and Dr. David G. Long of BYU, who encouraged and facilitated my pursuit of a mid-career doctorate.

Contents

List of Tables

List of Figures

Chapter 1

Introduction

1.1 Radar Remote Sensing of the Environment

Remote sensing of the environment from space is becoming an increasingly important tool for researchers studying this planet and its physical processes. Data from Earth-orbiting satellites contribute to such diverse fields as geology, oceanography, meteorology, climatology, archeology, agriculture, and urban planning. Researchers seek not only to understand natural geophysical processes, but also endeavor to assess man's impact on the environment. Critical issues confronting Earth scientists include the prediction of natural hazards (such as earthquakes and severe weather events), global warming, ozone depletion, and tropical forest reduction. The science of remote sensing involves the determination of geophysical parameters from electromagnetic radiation that is either reflected from or emitted by the Earth's surface. Sensing systems have been developed which operate from the radio to the ultraviolet region of the electromagnetic spectrum.

An important class of remote sensing devices employs radar [15, 95]. In radar remote sensing, the Earth is illuminated with a microwave frequency signal, and the resulting reflection from the surface is detected. The characteristics of the reflected signal are a function of the surface electromagnetic scattering properties, which are, in turn, related to various geophysical parameters of interest. In addition to the unique phenomenologies that a radar can observe, other advantages of active microwave remote sensing include the ability to make measurements at night and through cloud cover.

1.2 Scatterometer Measurements

An important class of radar instrument, and the focus of this dissertation, is the *scatterometer*. A scatterometer is a sensor specifically designed to precisely measure the normalized backscatter cross-section (σ^o) of the Earth's surface [15, 95]. In this section, an overview of scatterometer applications is presented. In order to motivate the problems addressed throughout this dissertation, key challenges confronting future scatterometer designers are also discussed.

1.2.1 Current Scatterometer Applications

The main purpose of scatterometers has been to determine ocean surface wind speed and direction. The wind *speed* can be determined by a microwave radar because higher winds produces a larger σ^o on the ocean surface. The wind *direction* can also be inferred because σ^o varies as a function of illumination azimuth angle – i.e., observed backscatter is larger when the radar is looking "up-wind" or "down-wind" as opposed to "cross-wind." Consequently, backscatter data from a radar which views a given point on the ocean from multiple azimuth directions can be used to determine the surface wind vector. Scatterometer wind data has contributed significantly to the scientific study of air/sea interaction, storms, and global climate phenomena such as El Nino [8, 42, 57]. Scatterometer winds are also being used operationally to improve the fidelity of numerical weather forecasts [2, 6].

In addition to ocean winds, scatterometer backscatter data is being applied to an expanding list of land and ice applications. Although the spatial resolution achieved is much lower than that of synthetic-aperture radar (SAR) systems, scatterometers have proven advantageous in these research areas because of (1) the frequent Earth coverage associated with the wide scatterometer swath, and (2) excellent radiometric calibration stability which enables the detection of subtle climate change signatures [81, 101]. Examples of new scatterometer applications include polar ice mapping and classification [28, 55], snow coverage and depth analysis [65, 100], soil freeze/freeze thaw tracking [76, 99], vegetation classification and change studies

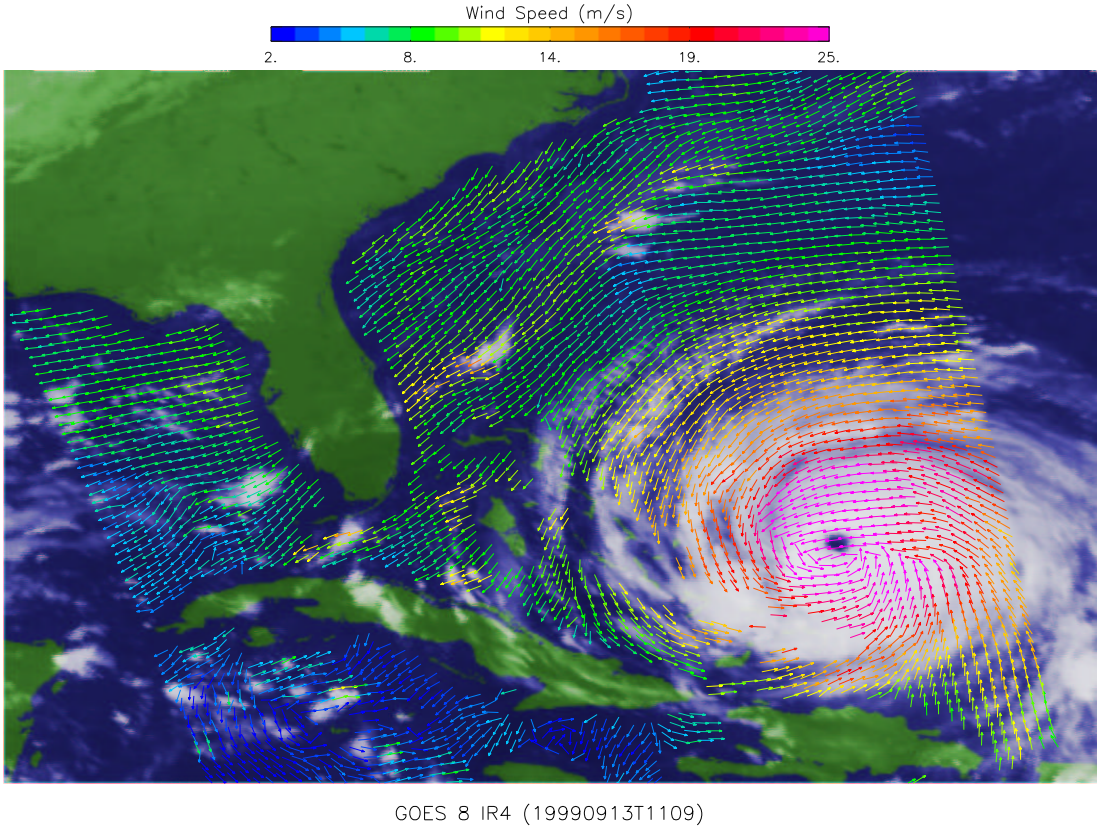

Figure 1.1: *SeaWinds* scatterometer wind field overlaid on cloud image of hurricane Floyd, September 1999.

[22, 50], flooding [66], and soil moisture retrieval [97]. Indeed, the scatterometer is becoming a true general purpose global climate sensing device.

1.2.2 Design Challenges for Future Scatterometers

As the scientific application of scatterometer data expands, so does the need for better scatterometer instrument designs. A key area of present interest is spatial resolution improvement. Current scatterometer systems have inherent spatial resolution on the order of 25 km, which is too coarse for many geophysical applications. An order of magnitude improvement in resolution is required to observe many phenomenologically significant mesoscale wind features associated with storms and in coastal waters [20, 70]. For land and ice applications, spatial resolution comparable

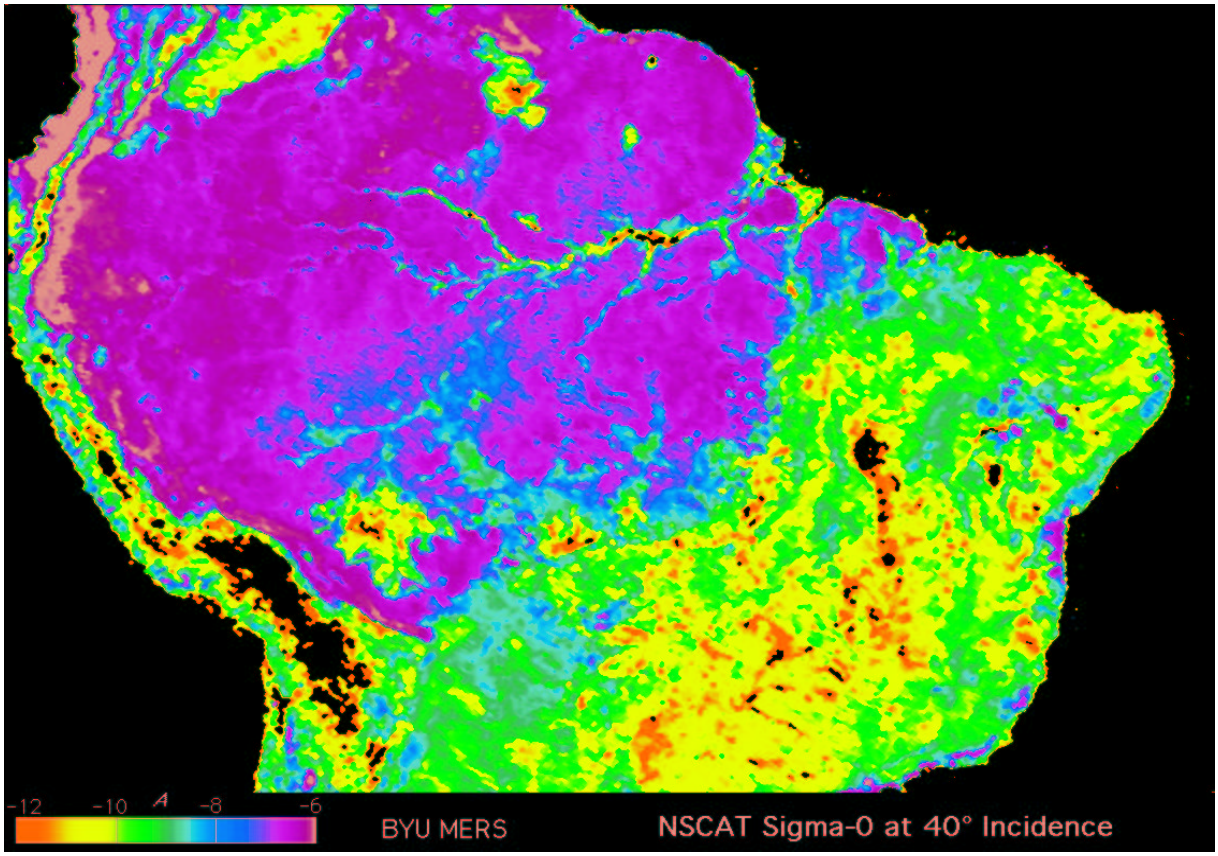

Figure 1.2: Backscatter image of the Amazon region of South America from NSCAT data.

to current visible/IR and SAR imaging sensors – on the order of 1 km – is desired to address such issues as flooding, ecosystem boundaries, snow cover, and sea ice extent [5, 76, 90].

In addition to spatial resolution, there is a desire to improve the quality of geophysical parameters derived from the scatterometer measurements. Because the accuracy of a given geophysical parameter (such as wind, soil moisture, etc.) is directly related to the accuracy with which the surface backscatter is measured, a key scatterometer design challenge is the reduction of backscatter measurement variance. The ability to detect different scattering phenomena can also be used to improve the quality of the ultimate geophysical product. Whereas current scatterometers measure only the co-polarized backscatter from the surface, it has been shown that

polarimetric measurements of both the co- and cross-polarized returns simultaneously can dramatically improve ocean surface wind retrievals [93, 104]. Naturally, along with these enhancements to scatterometer performance, future design concepts must be both technologically feasible and compatible with realizable spacecraft.

1.3 Scatterometer Design Approaches

To date, two fundamentally different strategies for scatterometer design have emerged: the "fan-beam" approach, employed by earlier instruments, and the "pencil-beam" approach, a relatively new technique which shows promise for many future applications. The features of these approaches are described in turn.

1.3.1 Fan-Beam Scatterometers

The first radar instrument to thoroughly demonstrate the feasibility of wind measurement from space was the Seasat-A Scatterometer System (SASS) which was flown aboard the Seasat mission in 1978 [24]. The SASS instrument employed a "fan-beam" antenna approach. With the fan-beam design, several fixed antennas are used to cast long, narrow illumination patterns at the multiple azimuth angles required for wind retrieval [see Fig. 1.3(a)]. The narrow width of the antenna beam pattern provides resolution in one dimension, and Doppler or range filtering is employed to provide resolution in the long dimension of the footprint. As shown in Fig. 1.3(a), each point on the ground is viewed from different azimuth angles (corresponding to the different antennas on either side of the spacecraft) as the satellite flies by.

The SASS mission demonstrated the validity of the scatterometer wind technique and the utility of the resulting wind data. Due to this success, other fan-beam systems have been developed and flown during the last decade. These have included the C-Band scatterometer aboard the European Remote Sensing Satellite series (ERS-1 and -2) and the Ku-Band NASA Scatterometer (NSCAT) which flew aboard the Japanese Advanced Earth Observation Satellite (ADEOS-I) [3, 64].

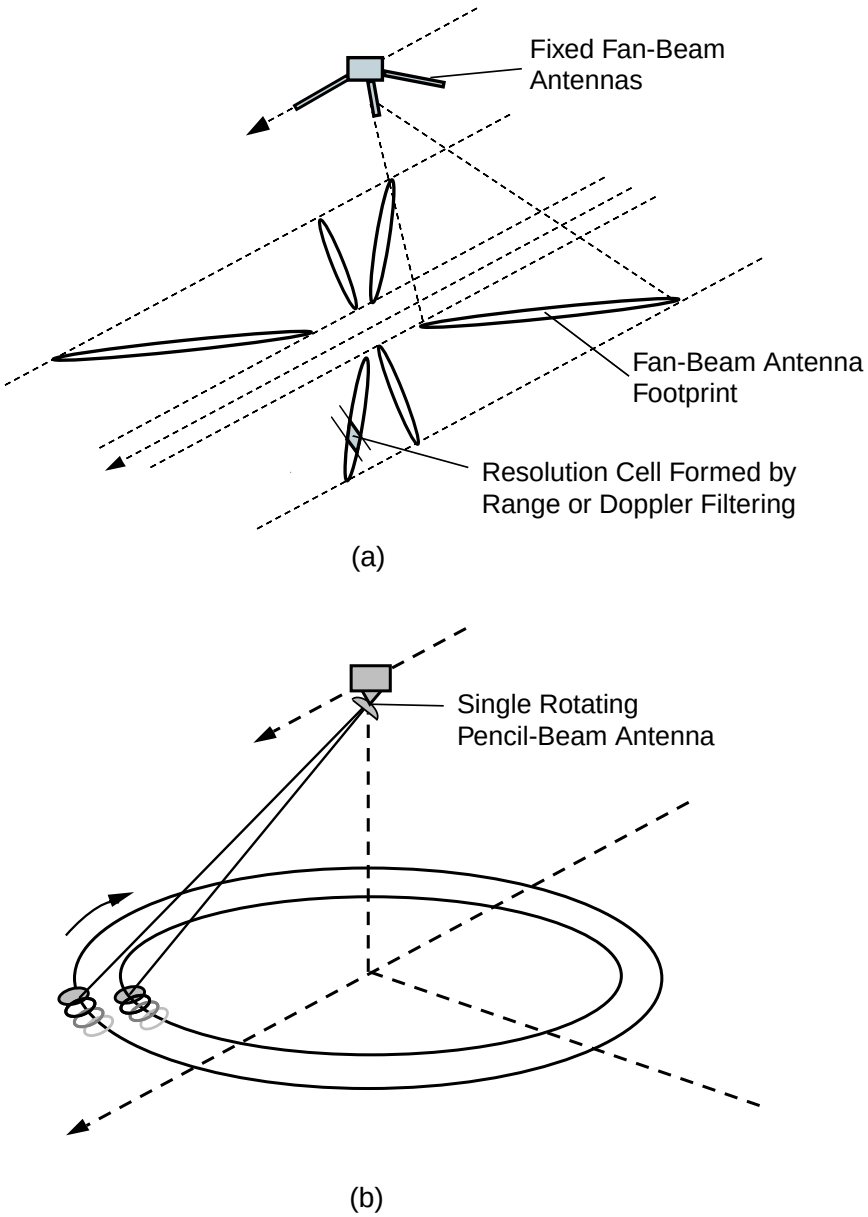

Figure 1.3: Conceptual diagram of scatterometer system options: a) Multiple antenna "fan-beam" wind scatterometer, b) Conically scanning "pencil-beam" scatterometer.

Although extremely successful, fan-beam systems suffer from several disadvantages that make them difficult to implement and limit the quality of data they collect [81]. The first disadvantage is the requirement for multiple antennas. These large (typically longer than three meters) antennas generally require complex deployment mechanisms, and wide, unobstructed fields-of-view. Consequently, these systems are difficult and expensive to accommodate aboard spacecraft. A second disadvantage is that the backscatter measurements obtained with fan-beam systems cover a wide range of surface incidence angles. Because scattering phenomenology – and ultimately the geophysical interpretation of the backscatter data – changes as a function of incidence angle, the retrieval of environmental parameters is thus made more difficult [21, 68]. For wind applications there is even a low incidence angle region near nadir where wind vectors can not be effectively be retrieved at all. This "nadir-gap" limits Earth coverage and causes discontinuities in the measurements of large scale features [21].

1.3.2 Pencil-Beam Scatterometers

An alternate scatterometer design, which alleviates many of the disadvantages encountered with the fan-beam technique, is the "pencil-beam" approach. In contrast to fan-beam systems, pencil-beam systems employ a single antenna which is conically scanned about the nadir axis to provide multiple azimuth measurements [see Fig 1.3(b)] [15, 21, 81]. Pencil-beam systems designed to measure ocean wind illuminate the surface with two beams slightly offset in angle: an "inner" beam and an "outer" beam. With this configuration, each point on the surface is viewed from up to four different azimuth directions – twice by the inner beam looking forward then aft, and twice by the outer beam in the same fashion.

Because the pencil-beam approach employs a single, more compact antenna, it is easier to accommodate on a variety of spacecraft. This is a significant advantage in an era when smaller, lighter spacecraft are mandated. Also, because the pencil-beam approach views the surface at one or two discrete incidence angles, geophysical interpretation of data is simplified and there is no nadir-gap where wind can

not be retrieved [21]. Because of the these and other advantages, NASA has selected the pencil-beam architecture for future Ku-Band scatterometer missions [21, 86].

Whereas the fan-beam approach has been flown on multiple missions over two decades and has been thoroughly studied, there has been significantly less research directed toward the unique aspects of the pencil-beam technique. Although an experimental sensor was flown on Skylab in the early 1970's and several proposals for flying a pencil-beam instrument have been advanced over the years, it is only relatively recently that serious plans have been made to fly such a system [48, 58, 64]. As the advantages of this promising approach become apparent in the Earth science community, there is a strong need for further research in the area of pencil-beam scatterometer design theory.

1.4 Problem Definition, Contributions, and Dissertation Overview

This dissertation addresses the need for a detailed study of the pencil-beam scatterometer problem. Here, a comprehensive methodology is developed for the design and performance optimization of advanced conically-scanning scatterometer systems. This represents the first instance in which the pencil-beam approach has been treated in a comprehensive fashion, and expands the existing body of radar remote sensing theory to cover this increasingly important case. As a key component of this study, the utility of this methodology is demonstrated with "real world" design examples. These include contributions made to the development of the *SeaWinds* scatterometer system, which has been successfully demonstrated in orbit. Further, the design framework established here is used as a basis to propose new pencil-beam techniques which significantly improve upon the resolution and accuracy achieved with previous scatterometer systems.

1.4.1 Contributions

A list of the key contributions from this study is summarized below:

1. An integrated summary of design issues and tradeoffs which are unique to conically-scanning pencil-beam scatterometers is presented. Addressing each

of these issues in turn, a design framework which facilitates the development of advanced scatterometer instruments is developed.

2. A generalized expression for the spatial response function (SRF) of a conically scanning radar is formulated. The SRF is demonstrated to be a valuable tool in analyzing the resolution and measurement accuracy performance of a variety of pencil-beam scatterometer implementations. (Results are reported in *IEEE Transactions on Geoscience and Remote Sensing* [87].)

3. Methods are established for improving the measurement accuracy of beamwidth-limited scatterometers by employing transmit pulse modulation techniques. These methods were adopted by NASA in the original design of the *SeaWinds* instrument. (Results are reported in *IEEE Transactions on Geoscience and Remote Sensing* [53, 81].)

4. Techniques are developed for improving the spatial resolution of pencil-beam scatterometers by utilizing range discrimination processing. The specific range discrimination SRF used in the final design version of the *SeaWinds* instrument is derived. (Results are reported in *IEEE Transactions on Geoscience and Remote Sensing* [84].)

5. A general expression is developed for the measurement variance associated with a real-aperture pencil-beam scatterometer. This expression was used for optimizing the performance of the *SeaWinds* design, and in the *SeaWinds* ground data processing algorithms. (Results are reported in *IEEE Transactions on Geoscience and Remote Sensing* [84].)

6. A characterization of the effects of nadir return contamination and rain contamination on Ku-Band pencil-beam scatterometer measurements is presented. (Results reported at *IEEE International Geoscience and Remote Sensing Symposium* [83].)

7. A system design framework, error model, and measurement variance equation are presented for a polarimetric pencil-beam scatterometer system. (Results

reported in *IEEE Transactions on Geoscience and Remote Sensing* and at *IEEE Aerospace Conference* [86, 93].)

8. The application of synthetic-aperture techniques to a pencil-beam scatterometer in order to significantly improve the spatial resolution is evaluated. Equations are derived to facilitate the design of advanced, high-resolution pencil-beam scatterometers which employ combined range/Doppler processing. (Results reported in *IEEE Transactions on Geoscience and Remote Sensing* and at *IEEE International Geoscience and Remote Sensing Symposium.* [85, 87].)

1.4.2 Dissertation Outline

Chapter 2 begins by reviewing the current state-of-the-art in scatterometer instrument design. Here, the characteristics of the fixed-antenna fan-beam scatterometer approach are summarized. Also included is a discussion of how both real- and synthetic-aperture techniques have been applied to previous fixed-antenna radars. This chapter is intended to serve as background material, and provides motivation for the new problems addressed in the dissertation.

In Chapter 3 a general design framework addressing the unique issues encountered with pencil-beam scatterometers is developed. First, the overall architecture and governing constraints of the pencil-beam approach are discussed. In order to evaluate spatial resolution performance, a generalized expression for the spatial response function (SRF) of a conically-scanning radar is derived. Also presented are generalized expressions for calculating signal-to-noise ratio (SNR), measurement variance, and radar timing solutions. Finally, the impacts of rain and specular-point reflections on the pencil-beam measurement are evaluated. This chapter provides the theoretical "building blocks" for the analysis in the rest of the dissertation.

Chapters 4-7 address a range of pencil-beam techniques, starting with the simplest and ending with the most sophisticated. In Chapter 4 the most basic pencil-beam scatterometer design – the "beamwidth-limited" approach where the spatial resolution is determined by the dimensions of the antenna footprint on the surface – is treated in detail. The use of transmit pulse modulation is demonstrated to

significantly improve the measurement accuracy of beamwidth-limited systems. An overall description of the *SeaWinds* scatterometer system, the first in a series of pencil-beam systems developed by NASA, is provided. Trade-offs involving the application of transmit modulation techniques to the original beamwidth-limited version of the *SeaWinds* design are described.

In Chapter 5 the real-aperture resolution approach is treated. The real-aperture approach involves the application of range discrimination to improve the spatial resolution, and represents an increase in capability over the beamwidth-limited technique discussed in Chapter 4. Again, the *SeaWinds* instrument is used as a example of how real-aperture methods are applied to an actual pencil-beam scatterometer system. Theoretical expressions for the *SeaWinds* measurement accuracy, spatial response function, and calibration parameters are derived.

As an extension of the material in Chapters 4 and 5, Chapter 6 introduces the concept of a polarimetric scatterometer. The addition of polarimetric capability has the potential to significantly improve scatterometer wind retrieval performance. Here, a new design framework is presented for the analysis of a pencil-beam system employing polarimetric detection and processing. This framework is applied to illustrate how a *SeaWinds*-class design may be augmented to include the polarimetric function.

In Chapter 7 the adaptation of synthetic-aperture techniques to a pencil-beam scatterometer is analyzed in detail. Synthetic-aperture techniques are proposed as a means to dramatically improve the spatial resolution of future scatterometer systems, and consequently expand the utility of spaceborne scatterometer data to a variety of new applications. Expressions for the best theoretical resolution of a pencil-beam scatterometer are derived.

Finally, Chapter 8 summarizes the conclusions and contributions of this research, and discusses the implications these results have for future scatterometer development efforts. Appendices then follow which provide auxiliary results and derivations used in the main body of the dissertation.

Chapter 2

Review of Current Fan-Beam Scatterometer Techniques

In this chapter, a review of current fan-beam scatterometer systems is presented. The fan-beam approach has been implemented on several previous missions for the measurement of ocean winds, and is a mature, well-understood technique. The two methods for achieving spatial resolution with a fan-beam system – Doppler discrimination and range discrimination – are described. The important issues of scatterometer measurement variance and calibration accuracy are also discussed. This review provides important background material as well as motivation for the discussion of rotating pencil-beam techniques in the succeeding chapters.

Although the emphasis in this chapter is on multi-antenna, wind scatterometer systems, a brief discussion of synthetic-aperture radar (SAR) is also included. While generally used for imaging applications, SAR systems do in fact function as high resolution scatterometer devices when sufficient amplitude calibration is performed. Like fan-beam scatterometers, SAR systems typically employ fixed antennas that look to the side of the spacecraft. The inclusion of SAR is thus important for a complete overview of the state-of-the-art in scatterometer system design. This chapter concludes with a discussion of the shortcomings of current fixed-antenna scatterometer techniques.

2.1 Fan-Beam Wind Scatterometer Systems

As the wind blows over the ocean, centimeter-scale capillary waves are formed on the surface. These capillary waves are responsible for a Bragg resonance

scattering phenomenon when illuminated with a radar signal [95]. Because the magnitude of this scattering is a function of both the surface wind speed and direction, it has been recognized for several decades that a radar scatterometer can be used to measure ocean surface wind vectors [71, 78]. The first full demonstration of this theory from space was performed in 1978 with the Ku-Band Seasat-A Scatterometer System (SASS) [4]. The success of the SASS instrument spawned the development of the Ku-Band NASA scatterometer (NSCAT), launched in 1997, as well as the C-Band European Remote Sensing (ERS) series of scatterometers first launched in 1996 [3, 64]. All of these systems are "fan-beam" systems where multiple, fixed, broad-beam antennas are employed to make the required measurements of ocean backscatter. In addition to ocean winds, these systems have also proven useful in land and ice studies [49, 100]. In this subsection, the overall system design features of fan-beam scatterometers are described. Included is a discussion of measurement geometry, spatial resolution, and radiometric accuracy.

2.1.1 Fan-Beam Measurement Geometry

The fundamental requirement for any wind scatterometer system is that the backscatter cross section, σ^o, be measured at the same point on the ocean surface from multiple azimuth angles. Only in this way can both the wind speed and direction be unambiguously determined [64]. In Fig. 2.1, the fan-beam approach to making these multiple measurements is shown. (Although only the NSCAT system geometry is displayed in Fig. 2.1, the technique is similar for any fan-beam implementation.) Here, three antenna beams are broadcast at the surface on each side of the spacecraft: one beam illuminates the surface looking forward, one beam looking aft, and a third beam positioned between these two. For instance, on the right side of the NSCAT instrument a given point on the ocean surface is viewed from azimuth angles of 45°, 115°, and 135° as the spacecraft flies past.

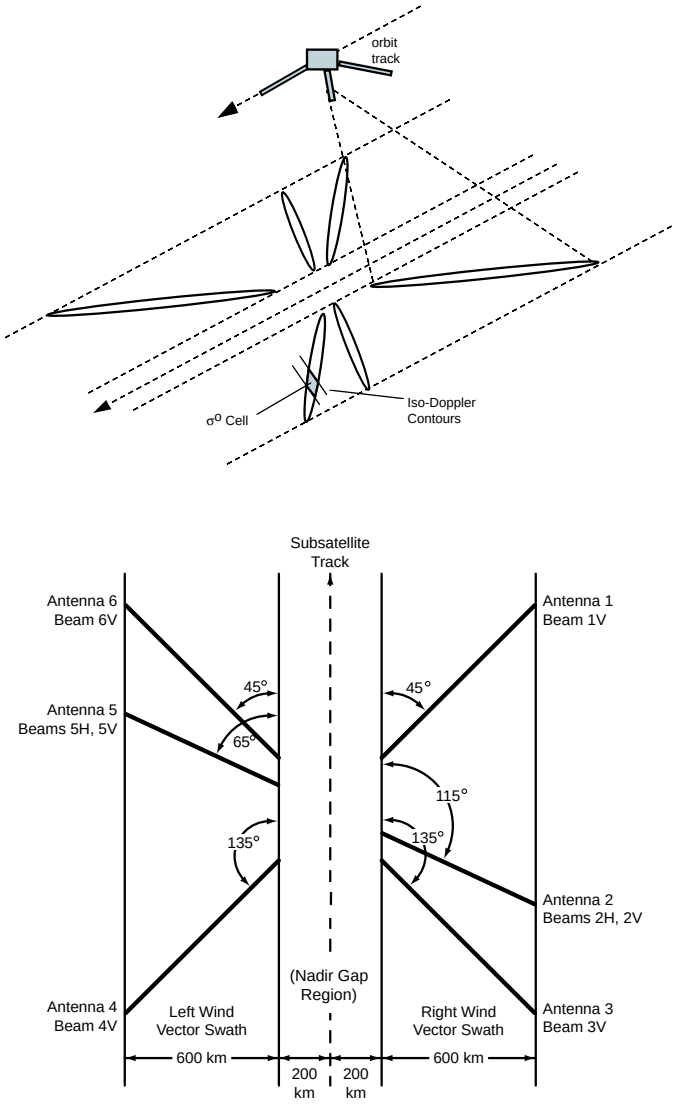

Figure 2.1: The NSCAT measurement geometry. Here, three fan-beam antenna footprints are broadcast to either side of the host spacecraft.

In order to insure that sufficient coverage of the ocean is obtained, the antenna beam is designed to be extremely broad in one dimension and narrow in the other – hence the term "fan-beam." The measurement swath formed by these elongated footprints on each side of the spacecraft is 600 km for the NSCAT instrument. The swath width is selected to obtain maximum Earth coverage in the shortest period of time. Typically for scatterometers, it is desirable to cover the entire Earth in one or two days.

Another feature of the fan-beam design is that a wide range of surface incidence angles are illuminated. In the NSCAT inner swath region, which corresponds to a cross-track distance of 200 km from the sub-satellite ground track, the surface is viewed with a measurement incidence angle of approximately 20°. At the outer edge of the swath, the incidence angle is near 60°. The influence of the Bragg resonance phenomenon, and consequently the scatterometer sensitivity to wind direction, breaks down at incidence angles below 20° because of the increasing dominance of quasi-specular scattering effects [95]. Because of this, there is a "nadir gap" region where wind vectors can not be retrieved. The nadir gap region for NSCAT is a 400 km wide region centered on the sub-satellite track (see Fig. 2.1).

The use of three antenna beams was adopted for the NSCAT and the ERS scatterometers because the original use of two beams on the SASS mission was demonstrated to be insufficient to resolve wind direction ambiguities inherent to the wind retrieval process [3, 9, 64]. The major differences between the NSCAT and ERS beam geometry are: (1) the ERS center beam is positioned at 90° azimuth, rather than the 115° chosen for NSCAT (for reasons explained in the next subsection), and (2) the ERS scatterometer uses three antennas instead of six, and consequently only forms a swath on one side of the spacecraft.

Another important consideration for a wind scatterometer is the polarization. As concluded from the Ku-Band SASS data, the use of multiple polarizations improves the wind direction retrieval performance [64]. As indicated in Fig. 2.1, NSCAT makes both V and H-polarized backscatter measurements. The C-Band ERS scatterometer employs only V polarization.

2.1.2 Fan-Beam Measurement Resolution

For the design of any scatterometer, spatial resolution is an important consideration. In general, the resolution should be consistent with the scale of the geophysical phenomena of interest. For instance, if global-scale winds for long-term climate studies are desired, scatterometer resolution on the order of 25-100 km is acceptable. If small-scale features such as hurricanes are to be observed, however, resolution on the order of 10 km or less is required. In general, the spatial resolution is defined by the dimensions of the σ^o measurement cell (or pixel, as it is often called in imaging radar applications).

For fan-beam scatterometers, the *azimuth* resolution of the σ^o cell is defined by the narrow dimension of the antenna footprint. Resolution in *elevation* is achieved by using radar processing techniques to discriminate specific regions along the broad dimension of the antenna footprint. The two primary techniques used to obtain elevation resolution are Doppler discrimination and range discrimination. Post-processing resolution enhancement algorithms may also be applied to improve the utility of the data.

Doppler Discrimination

The Doppler discrimination approach was employed on both the SASS and NSCAT scatterometers. The nature of this technique is illustrated in Fig. 2.2. The azimuth width of the resolution cell, δ_{az}, is

$$\delta_{az} = R\beta_{az}, \tag{2.1}$$

where R is the range from the spacecraft to the measurement cell and β_{az} is the 2-way 3 dB beamwidth across the narrow dimension of the fan-beam antenna pattern. As an example, the 3-meter long slotted waveguide antennas used by the NSCAT instrument form a narrow beam pattern which is approximately 0.4° wide. This leads to σ^o cells which vary in width from seven kilometers in the inner portion of the swath to 9 kilometers in the outer swath [64].

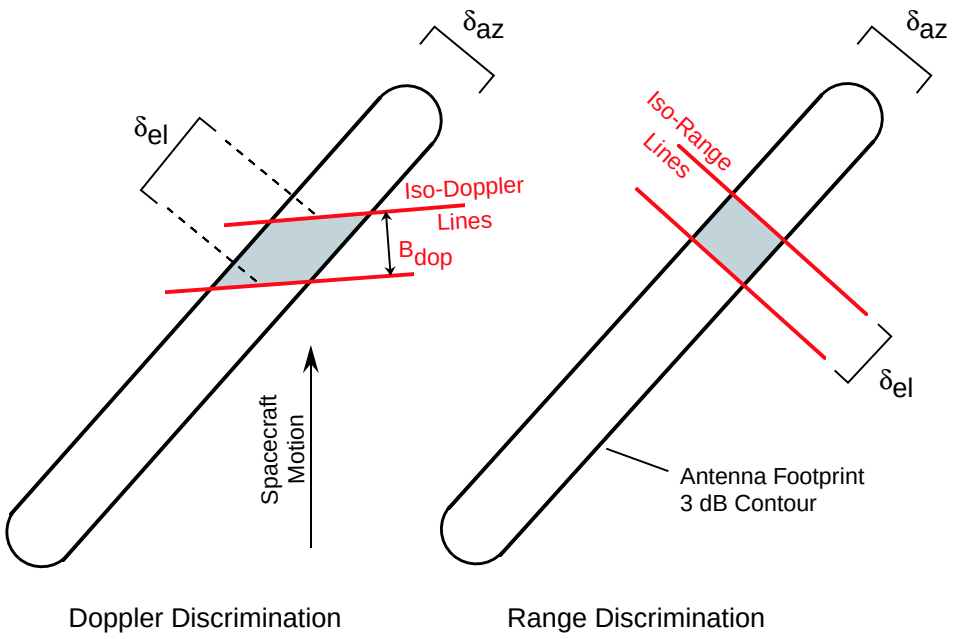

Figure 2.2: Conceptual diagram of fan-beam resolution approaches which use Doppler discrimination (left) and range discrimination (right). In both cases, the resolution cell is indicated by the shaded area, and the azimuth resolution, δ_{az}, is given by the narrow dimension of the antenna footprint. In the elevation dimension the length of the σ^o cell is δ_{el}. The iso-Doppler or iso-range lines associated with the radar processing are used to "cut out" a series of resolution cells from the long dimension of the footprint.

Because the Doppler shift due to spacecraft motion (and, to a lesser extent, Earth rotation) varies over the length of the fan-beam footprint, Doppler information can be used to discriminate different regions along the broad portion of the antenna pattern [4, 15, 64, 95]. With the Doppler discrimination approach, a CW radar pulse is transmitted and the return echo is processed with a filter bank that selects the signal corresponding to a specific Doppler shift [45]. Thus Doppler discrimination effectively "slices" the broad fan-beam footprint into smaller σ^o cells.

The elevation width of the σ^o cell, δ_{el}, is a function of the Doppler bandwidth of the filter, B_{dop}. The relationship between δ_{el} and B_{dop} can be expressed as

$$\delta_{el} = kB_{dop}, \tag{2.2}$$

where the parameter k varies as a function of orbit altitude, beam azimuth, and measurement cell position on the broad beam pattern. For SASS and NSCAT, k varies from about 2.5 km/kHz for the inner portion of the swath, to about 12 km/kHz for the outer edge of the swath. Doppler filtering may be implemented as a fixed filter bank, as in the case of SASS, or as an FFT of the return signal, as implemented in NSCAT. The FFT approach has the advantage of easily adapting to the change in the Earth rotation Doppler component as a function of latitude [45]. With NSCAT, the filter bandwidths were set to maintain a constant $\delta_{el} = 25$ km. Note that, when Doppler discrimination is used, all of the fan-beams must be "squinted" either somewhat forward or backward from an exact side-looking direction (i.e., away from an azimuth angle of 90°). This is because for a fan-beam positioned at an azimuth of 90°, the iso-Doppler lines are parallel to the long dimension of the footprint, and consequently Doppler filtering does not provide sufficient elevation resolution [95].

Range Discrimination

Range discrimination is an alternate technique to sub-divide the broad fan-beam footprint into resolution cells. The ERS series of scatterometers use this approach. As shown in Fig. 2.2, the azimuth resolution associated with this technique is again given by the narrow dimension of the antenna footprint [as in Eq. (2.1)]. The elevation dimension of the σ^o cell, however, is determined by the range resolution associated with the transmit pulse. The inherent elevation resolution, δ_{el}, is thus given by

$$\delta_{el} = \frac{c}{2B_t \sin\theta_{inc}}, \tag{2.3}$$

where B_t is the bandwidth of the transmitted pulse and θ_{inc} is the incidence angle at the center of the measurement cell. For the ERS scatterometer system, 3-meter long antennas are used in combination with range processing to form resolution cells of approximately 25×25 km [69]. Note that for scatterometers employing range discrimination, the iso-range contours are always perpendicular to the broad dimension of the fan-beam footprint. Thus, the center beam of the ERS scatterometer may be (and, in the actual implementation, is) positioned at an azimuth angle of 90°.

Fan-beam scatterometers which employ range resolution are a sub-class of instruments called *real-aperture* radars. With a generic real-aperture system, one dimension of the resolution cell is determined by the antenna beamwidth, and the other is determined by range resolution. In addition to multi-beam scatterometer instruments, single-beam real-aperture systems have been widely employed on aircraft as imaging radars [15, 95].

Resolution Enhancement Techniques

Although adequate for ocean wind studies, the resolution of current fan-beam systems is too coarse for many emerging land and ice applications of the scatterometer data set [13, 49, 69]. In both the Doppler and range discrimination cases, the resolution is fundamentally limited by the azimuth beamwidth of the antenna pattern. In order to improve the resolution, the antenna would have to grow larger. This is problematic because the 3-meter long antennas currently employed are already difficult to accommodate on many spacecraft systems.

To improve the effective resolution of current fan-beam scatterometer systems, several resolution enhancement algorithms have been developed. With these techniques, multiple overlapping σ^o measurements are used to solve for the underlying surface backscatter scene at higher resolution than achieved by the beamwidth-limited instantaneous measurements [13, 49, 69]. These algorithms are applied as a post-processing step, and effectively deconvolve the blurring effect of the finite-width resolution cells initially generated by the scatterometer. Because these techniques usually involve multiple observations of the same point on the surface – either from the multiple fan-beams or multiple orbit passes – the surface must typically be assumed temporally stable and azimuthally isotropic. These resolution enhancement techniques have been successfully applied to the SASS, NSCAT, and ERS fan-beam scatterometer data sets. The resulting higher-resolution backscatter measurements have been used in land and ice studies [50, 55, 72].

2.1.3 Fan-Beam Radar Equation and Measurement Accuracy

Equal in importance to spatial resolution is the issue of scatterometer measurement accuracy. Backscatter measurements are "noisy" due to the random effects of radar fading and receiver thermal noise. Additional measurement error is imparted by calibration uncertainties associated with the radar electronics and antenna. The greater the σ^o measurement error, the larger the uncertainty in the geophysical parameter of interest. Thus, a consideration of the measurement accuracy is critically important in the analysis of any scatterometer design.

With a scatterometer, an estimate of σ^o is obtained using the *radar equation* [44, 80, 95]

$$\sigma^o = \frac{E_s}{X}. \tag{2.4}$$

Here, E_s is the measured energy in the echo return for a given cell, and X is a calibration factor defined by

$$X = \frac{\lambda^2 E_t}{(4\pi)^3 L} \int d\overline{r}\ \frac{G^2(\overline{r})F(\overline{r})}{R^4(\overline{r})}, \tag{2.5}$$

where λ is the transmit wavelength, L is the total system loss, $\overline{r}$ is the location of each point on the surface, $G(\overline{r})$ is the antenna gain pattern on the surface, $F(\overline{r})$ is the effective response of either Doppler or range filtering, $R(\overline{r})$ is the slant range to each surface element, and the integral is performed over the illuminated region. Because the echo energy is measured in the presence of thermal noise, an unbiased estimated of E_s is given by

$$E_s = E_{s+n} - E_{no}, \tag{2.6}$$

where E_{s+n} is the measurement of the echo signal plus the noise energy and E_{no} is an independent estimate of the "noise-only" energy. The noise-only measurement is obtained by observing the system noise floor either during a time, or in a frequency band, where the echo signal is not present [53, 64]. Note from Eq. (2.4) that the error in the estimation of σ^o can be decomposed into: (1) the error associated with the measurement of E_s, which, for historical reasons is referred to as *communication noise*; and (2) the error associated with the determination of X, referred to as *calibration error*.

Communication noise results from the random effects of radar fading and system thermal noise. The normalized standard deviation of this error term is defined as K_{pc}, where

$$K_{pc} = \frac{\sqrt{\mathrm{Var}[E_s]}}{\mathcal{E}[E_s]}. \tag{2.7}$$

Here, "$\mathcal{E}$" and "Var" are the expectation and variance operators respectively. A goal of scatterometer design, therefore, is to minimize the value of K_{pc}.

The K_{pc} for a fan-beam scatterometer employing Doppler filtering has been a topic of several detailed studies [17, 45]. A useful approximation for this case is given by

$$K_{pc} = \frac{1}{\sqrt{B_{dop}T_p}} \left\{ 1 + \frac{2}{\mathrm{SNR}} + \frac{1}{\mathrm{SNR}^2} \left(1 + \frac{T_g B_{dop}}{T_n B_n} \right) \right\}^{\frac{1}{2}}, \tag{2.8}$$

where B_{dop} is the Doppler bandwidth of the σ^o measurement cell, T_p is the transmit pulse length, T_g is the range gate "open" time for the measurement of the signal+noise energy, and B_n and T_n are the bandwidth and integration times for the noise-only estimate respectively [17, 45, 84]. The measurement signal-to-noise ratio is defined as

$$\mathrm{SNR} = \frac{\mathcal{E}[E_s]}{\mathcal{E}[E_{no}]}, \tag{2.9}$$

where $\mathcal{E}[E_{no}]$ is given by $B_n T_n N_o$, and N_o is defined to be the thermal noise power spectral density. Equation (2.8) was used to calculate K_{pc} for the SASS system, which performed Doppler filtering using analog components. A significantly more complex equation was developed for the digital processing used by NSCAT, and is described in [45]. [The NSCAT K_{pc} expression, however, is reasonably well approximated by Eq. (2.8).]

For the ERS-1 scatterometer, which employs range discrimination, K_{pc} is given by

$$K_{pc} = \frac{1}{\sqrt{M}} \left(1 + \frac{1}{\mathrm{SNR}} \right) \tag{2.10}$$

where M is the equivalent number of range "looks" on the surface – i.e., the number of individual range cells averaged to form one σ^o cell. Here the expression is approximated as a linear function of 1/SNR rather than the quadratic given in Eq. (2.8) due

to the very high SNR that the ERS scatterometer typically maintains, allowing the noise subtraction step to be neglected [30].

In addition to the random errors associated with the estimation of E_s, there are also errors in the determination of the calibration parameter X. This calibration error is the result of the combined uncertainty in all the radar systems parameters listed in Eq. (2.5), such as uncertainties in the antenna pattern, systems loss, etc. Similar to K_{pc}, it is convention to quantify this error as a normalized value, K_{pr}, given by

$$K_{pr} = \frac{\Delta X}{X}, \tag{2.11}$$

where ΔX is the calibration error associated with the determination of X ($\Delta X = X(actual) - X(estimated)$). To the extent that ΔX can be assumed to be a random quantity, the total σ^o error is expressed as $\sqrt{K_{pc}^2 + K_{pc}^2}$. A key goal of scatterometer design is the minimization of this total measurement error. The concepts expressed by Eqs. (2.1)-(2.11) have been used extensively to accomplish design optimization for fan-beam systems [30, 45].

2.2 Synthetic-Aperture Techniques

In addition to wind scatterometers, the other major class of spaceborne sensor which has been employed to measure σ^o is synthetic-aperture radar (SAR). The primary advantage of the SAR technique is that spatial resolutions on the order of meters can be obtained – dramatically better than that achievable with real-aperture fan-beam systems described above – although at a cost of significant additional instrument complexity. The first spaceborne SAR system flew on the same groundbreaking Seasat satellite as the first fan-beam scatterometer, and operated at L-Band [43]. Since then, spaceborne SAR's have been operated at C- and X-Band as well. In the following subsections, a brief description of the nature of the SAR technique, capabilities, and accompanying system requirements is provided.

2.2.1 Synthetic-Aperture Resolution

A SAR operates by using the motion of the spacecraft to synthesize an effective aperture much longer than the "real" azimuth length of the antenna. This is accomplished by coherently combining echo pulses during the time that the region to be measured resides in the antenna beam footprint [11, 15, 95]. An equivalent way to view SAR is as a radar which simultaneously resolves the surface scene in both range and Doppler, as shown in Fig. 2.3 [15]. The range resolution of a SAR is equivalent to that given in Eq. (2.3). It can be shown that the best azimuth resolution of a SAR, however, is given by

$$\delta_{az} = \frac{l_{az}}{2}, \tag{2.12}$$

where l_{az} is the length of the azimuth dimension of the antenna. This is a theoretical result which, for reasons discussed in the next subsection, is rarely achieved by actual spaceborne systems. Equation (2.12) nevertheless illustrates the potential resolving power of the synthetic-aperture technique. With the SAR approach, resolution on the order of the antenna physical length – typically on the order of meters – is possible.

2.2.2 Synthetic-Aperture System Requirements

There are a number of considerations that make SAR systems much more complex than the fan-beam scatterometer systems discussed in the previous section [11, 95]. A key complexity for spaceborne SAR systems is the antenna *minimum area constraint*. This constraint is based on range and Doppler ambiguity considerations and provides a bound on the minimum size of the antenna necessary to successfully perform synthetic-aperture resolution processing on the echo return signal [15, 19]. When ambiguity contamination below -20 dB is desired, the constraint can be summarized as

$$l_{az} l_{el} \geq \frac{10 \lambda v_{sc} R \tan \theta_{inc}}{c}, \tag{2.13}$$

where l_{az} and l_{el} are the azimuth and elevation dimensions of the antenna respectively, λ is the radar wavelength, v_{sc} is the spacecraft velocity, R is the average slant range to the illuminated region, and θ_{inc} is the average incidence angle across the illuminated

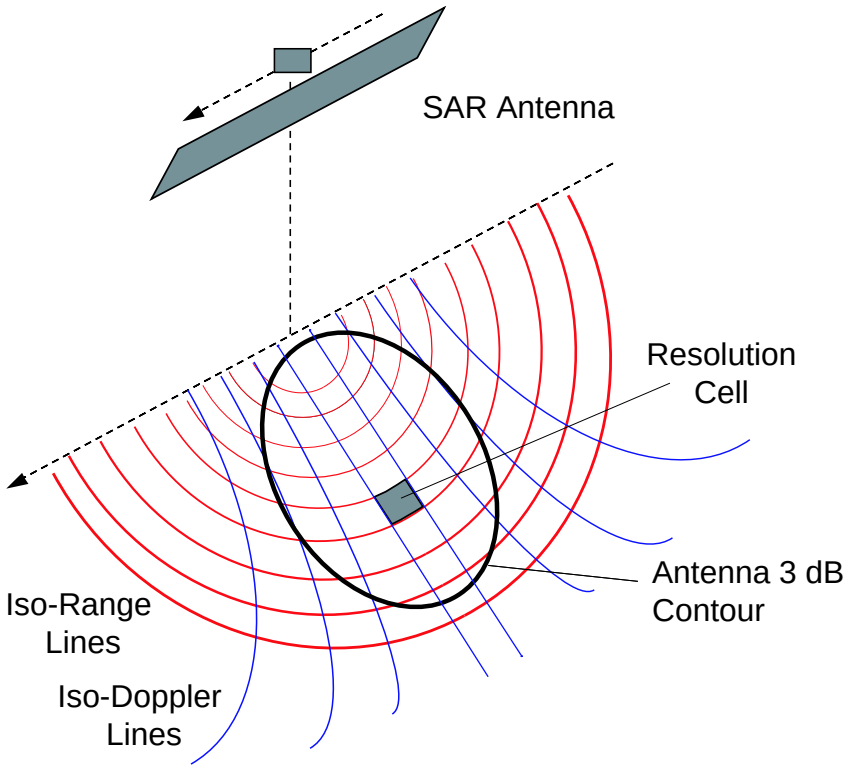

Figure 2.3: Conceptual illustration of spaceborne SAR system. Here, the dark oval represents the illuminated region. The resolution cell (shaded region) is defined by the intersection of iso-Doppler and iso-range contours as projected on the Earth's surface.

region. It follows from Eq. (2.13) that SAR antennas must be quite large. The Seasat SAR, for example, required an approximately 2×11 meter deployable phased-array antenna (see Fig. 2.4).

A corollary to Eq. (2.13) is that because the antenna is required to be larger, the illuminated region on the surface is actually quite small. With the Seasat SAR, the swath width was only 100 km, much smaller than the 500 km swath of the Seasat fan-beam scatterometer system. Thus, although 25 m resolution was achieved by the Seasat SAR, only a very small region of the Earth could be covered at a given time. The limitations imposed by the narrow SAR swath have been overcome somewhat by the recent use of SCANSAR techniques, where a single beam is electronically scanned to different elevation positions in order to increase the effective swath width. The

SCANSAR technique, however, requires an even larger and more complex antenna [60].

2.3 Disadvantages of Fan-Beam and SAR Scatterometer Techniques

The scatterometer techniques discussed in this section have been used successfully over the past two decades, providing measurements which have greatly expanded understanding of many geophysical processes. Despite these successes, however, there are disadvantages to these systems which must be overcome to meet future scatterometer science objectives.

Fan-beam scatterometers – which employ multiple fixed antennas and require wide fields-of-view – are difficult to accommodate on spacecraft, and necessitate complex deployment mechanisms to allow the antennas to fold into the spacecraft shroud during launch. A more compact instrument would consequently have many more opportunities to fly at considerably less expense. In addition, the nature of the fan-beam measurement geometry produces measurements at many different incidence angles. Because the scattering phenomenology (and hence the geophysical interpretation of the σ^o measurements) changes as a function of incidence angle, this feature makes fan-beam measurements difficult to calibrate and interpret. As shown in Fig. 2.1, there is even a region of the fan-beam swath where the incidence angles are so low that wind vectors can not be retrieved at all. Finally, because the resolution of fan-beam systems is strictly limited by the antenna beamwidth, only spatial features on the order of 20 km can realistically be resolved.

The use of SAR to obtain measurements of surface backscatter is a well known solution to resolution problem, but it suffers to an even greater extent in terms of implementation complexity, spacecraft accommodation, and cost. SAR systems typically require large, deployable, phased-array antennas, which, for SCANSAR applications, must be electrically steerable. Because of this, it is extremely difficult to utilize multiple SAR antennas placed in different azimuth positions for the measurement of ocean wind vectors. Thus, SAR measurements can only feasibly be performed at one azimuth angle to obtain non-wind measurements over land and

ice. Finally, even when a SCANSAR approach is adopted, it is difficult to obtain the wide-swath Earth coverage necessary for many global scatterometer applications. Given the listed drawbacks of conventional fixed-antenna scatterometer systems, it is desirable to investigate alternative design approaches.

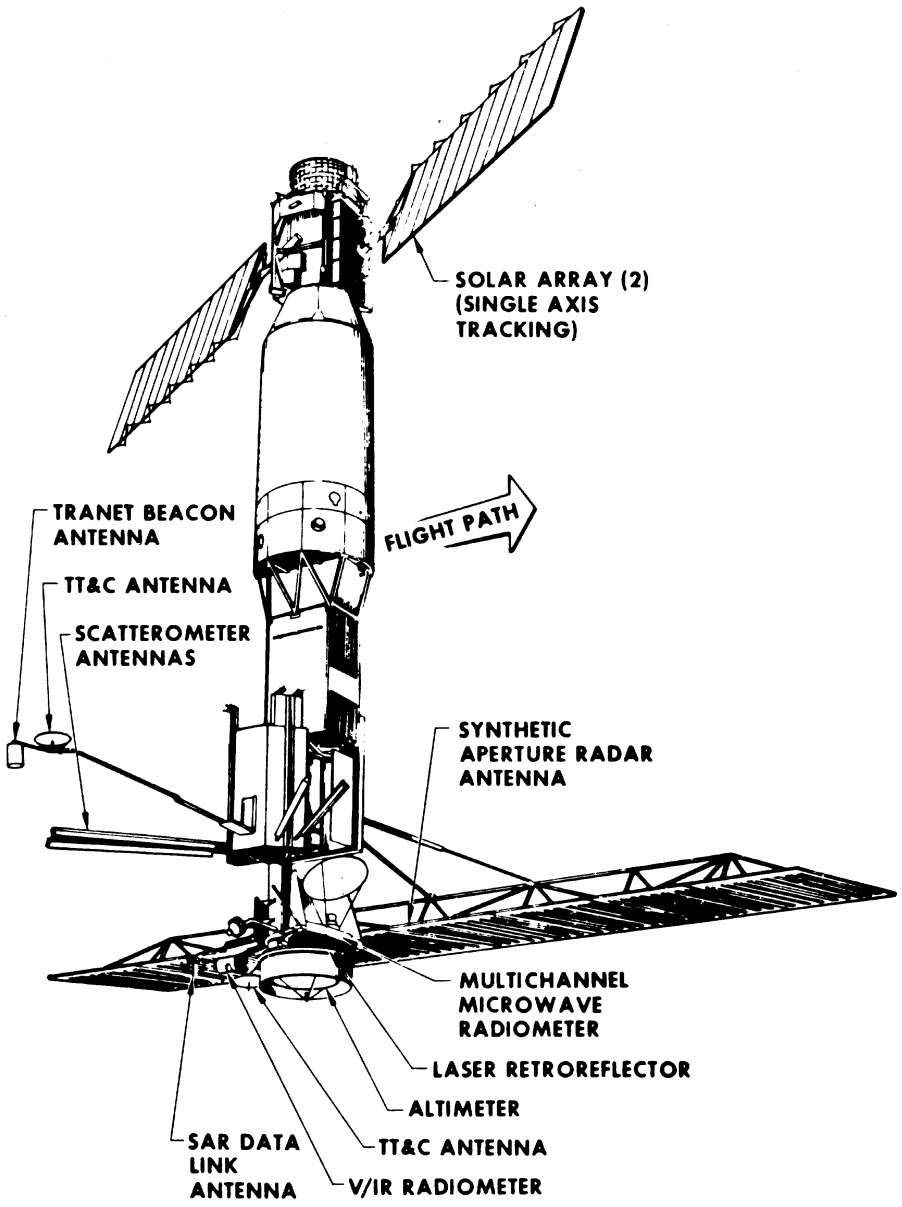

Figure 2.4: Diagram of the very large Seasat-A spacecraft showing the position and size of the various microwave instruments onboard. Particularly noteworthy for the present discussion are the size and configuration of the fan-beam scatterometer and SAR antennas. For scale, the scatterometer antennas are approximately 3 m long, and the SAR antenna is approximately 11 m long

Chapter 3

Fundamental Theory and Design Considerations for a Pencil-Beam Scatterometer

In the preceding chapter, the well-established theory of conventional fixed-antenna, fan-beam scatterometers was summarized. Such systems have demonstrated utility in measuring ocean winds and in obtaining other important geophysical measurements of the Earth's surface. These systems nevertheless have recognized deficiencies. An alternative scatterometer approach which eliminates many of the deficiencies associated with conventional systems is to use a conically-scanning pencil-beam antenna. Key features of the pencil-beam approach that are advantageous for a number of applications include: (1) a single rotating antenna is more easily accommodated on spacecraft than several fixed antennas, (2) the conical scan allows a wide swath of measurements to be obtained at a constant incidence angle, which is desirable for many geophysical retrieval algorithms, and (3) multiple polarizations and/or frequencies are more easily accomplished with this antenna design [15, 21, 84, 93]. Because of these advantages, the pencil-beam approach has been adopted for future NASA wind scatterometers [86].

Although the basic concept of a pencil-beam scatterometer is not new – an experimental system was flown on Skylab in the 1970's and various pencil-beam systems have been proposed to replace fan-beam systems since then – it is only recently that such systems have been seriously pursued for actual spaceborne implementation [26, 48, 58]. Whereas much has been written about design procedures for conventional fixed-antenna systems, such as the fan-beam scatterometers and

SARs discussed in the previous chapter, no equivalent design framework currently exists for the pencil-beam case. The development of a new design framework is necessary to address the unique issues presented by the conical geometry and rapid scanning motion of the pencil-beam case. In this chapter, key results useful for the design of pencil-beam systems are developed. These results form a set of analysis tools which are applied in later chapters where specific pencil-beam implementations are treated in detail.

This chapter is organized by topic, addressing each major pencil-beam design consideration in turn. First the overall pencil-beam measurement geometry is described, and important terms and constraints are defined. Secondly, techniques for achieving spatial resolution with a pencil-beam system are addressed. Here, the concept of the spatial response function (SRF) is introduced, and a formulation for the SRF of a conically-scanning radar is derived. The issue of backscatter measurement accuracy is then discussed, and a generalized framework for the analysis of pencil-beam scatterometer measurement variance is presented. Finally, additional error sources that are particularly problematic with the pencil-beam geometry – specular nadir return and rain contamination – are discussed.

3.1 Pencil-Beam Geometry, Definitions, and Constraints

3.1.1 Pencil-Beam Measurement Geometry

The overall geometry of the pencil-beam measurement is shown in Fig. 3.1. The instrument is at altitude h above the surface. The antenna beam boresight is pointed at an angle θ_{nad} from the spin axis, which is in the direction of nadir. The antenna beam intersects the surface at a constant incidence angle θ_{inc}, which is greater than θ_{nad} due to the Earth curvature effects. The distance along the Earth's surface from the nadir point to the center of the measurement is given by d, and thus the total swath width is $2d$. The slant range to the measurement point is R. Assuming that the Earth's surface is locally spherical, an assumption sufficiently accurate for high level system analysis, the relationship between these geometrical parameters is

given by the equations

$$R = \left((r_e)^2 + (r_e + h)^2 - 2r_e(r_e + h)\cos(\tfrac{d}{r_e})\right)$$
$$\theta_{inc} = \arcsin\left(-\tfrac{(r_e+h)}{R}\sin(\tfrac{d}{r_e})\right)$$
$$\theta_{nad} = \theta_{inc} - \tfrac{d}{r_e}, \tag{3.1}$$

where r_e is the radius of the Earth.

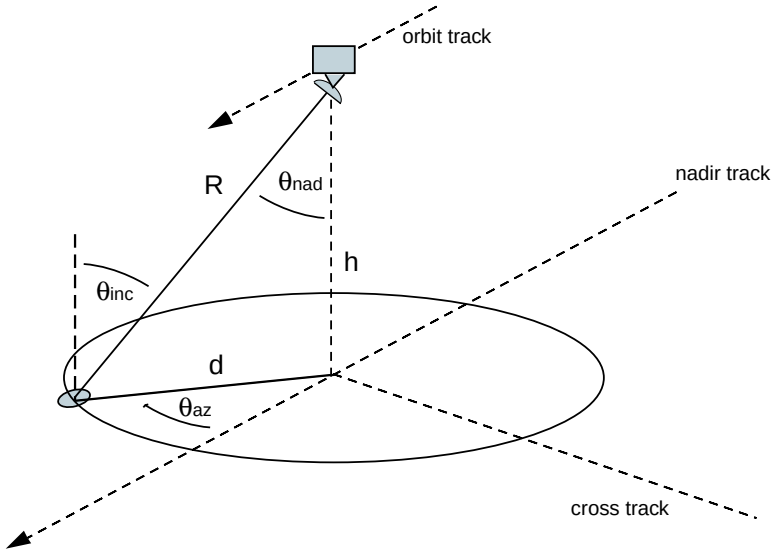

Figure 3.1: Pencil-beam measurement geometry. Shown is the spacecraft and instrument in orbit at height h above the Earth. The antenna boresight is conically scanned making an angle θ_{nad} with the nadir vector. The antenna footprint on the surface is represented by a small oval.

With pencil-beam systems, the antenna is continuously rotated about the nadir axis. The instantaneous azimuth position of the antenna beam, θ_{az}, is measured clockwise relative to the forward direction. The antenna spins at a rate of Ω rotations per second, where

$$\Omega = \frac{1}{2\pi}\frac{d\theta_{az}}{dt}. \tag{3.2}$$

The scanning motion causes the antenna footprint to sweep over the surface, where

the local speed of the footprint motion, γ, is given by

$$\gamma = 2\pi d\Omega. \tag{3.3}$$

Another important geometric consideration is how the Doppler shift, which is created by the motion of the satellite relative to the Earth, varies over the surface. In Fig. 3.2, contours of the Doppler shift are plotted on the Earth's surface for a typical scatterometer orbit. Two important implications of the Doppler shift are manifest in Fig. 3.2. First, note that the Doppler frequency of the footprint center varies as the antenna rotates, imparting a continuously varying frequency shift on the echo return. This effect must be taken into account in the signal processing design of the system. Secondly, note that the contours describe a mapping between the delay/Doppler coordinate system and the various spatial coordinates that can be used to express location on the Earth's surface.

3.1.2 Antenna Footprint Coordinates

The antenna footprint is defined to be the antenna pattern two-way 3 dB contour projected on the Earth's surface. It is convenient to define a set of perpendicular coordinates that are fixed relative to the antenna footprint as it moves over the surface. The *azimuth* axis is defined to be in the direction of footprint motion due to the rotation of the antenna. Perpendicular to this is the *elevation* axis, which is in the direction of increasing range from the sensor along the surface. These coordinates are illustrated in Fig. 3.3.

From an examination of Fig. 3.2, it is noted that the transformation between delay/Doppler coordinates and the local footprint coordinates varies as a function of the scan angle θ_{az}. When the antenna is scanned to the side-looking direction ($\theta_{az} = 90^\circ$ or $\theta_{az} = 270^\circ$), the iso-delay and iso-Doppler contours are locally parallel to the elevation and azimuth axes respectively. When the antenna is scanned to the foreword or aft looking directions ($\theta_{az} = 0^\circ$ or $\theta_{az} = 180^\circ$) however, both the iso-delay and iso-Doppler lines are parallel to the azimuth axis but perpendicular to the eleva-

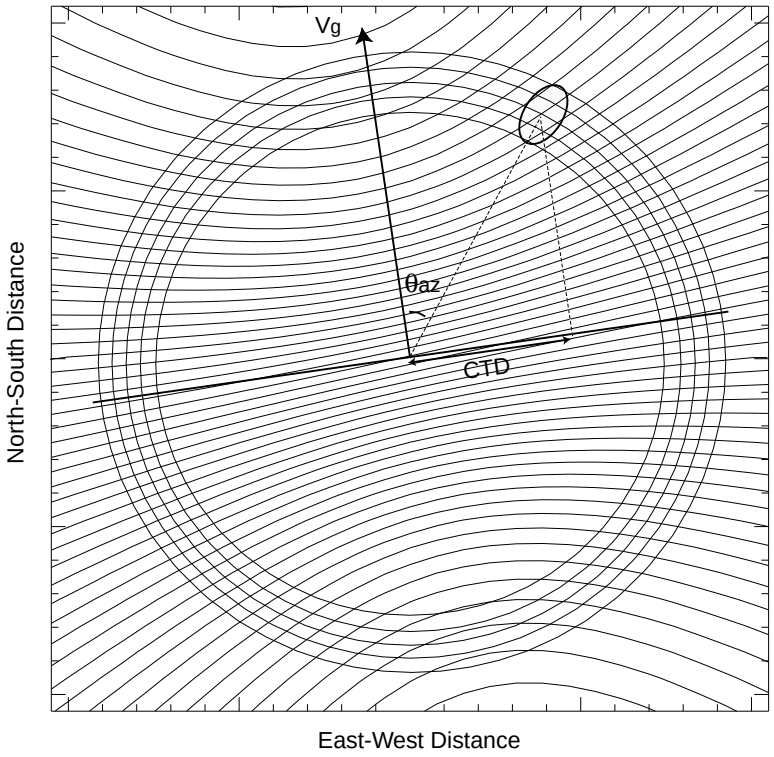

Figure 3.2: Iso-Doppler and iso-range (delay) contours on the surface for an 800 km sun-synchronous orbit. The antenna footprint is represented by an oval. Iso-Doppler lines are hyperbolic and spaced at 20 kHz intervals. (The slight tilt in the iso-Doppler contours is due to the Earth rotation Doppler effect.) Iso-range (or, equivalently, iso-delay) contours associated with the footprint dimensions are shown as concentric circles on the surface. Only iso-range contours associated with the antenna footprint are shown. The cross-track distance (CTD) is defined as the position of the measurement projected on the axis perpendicular to the spacecraft motion.

tion axis. These variations in mapping between delay/Doppler and elevation/azimuth spaces will be of importance in succeeding chapters.

For a pencil-beam scatterometer, the azimuth and elevation widths of the footprint, x_{az} and x_{el}, can be written as

$$x_{az} = \beta_{az} R \tag{3.4}$$

and

$$x_{el} = \frac{\beta_{el} R}{\cos\theta_{inc}}, \tag{3.5}$$

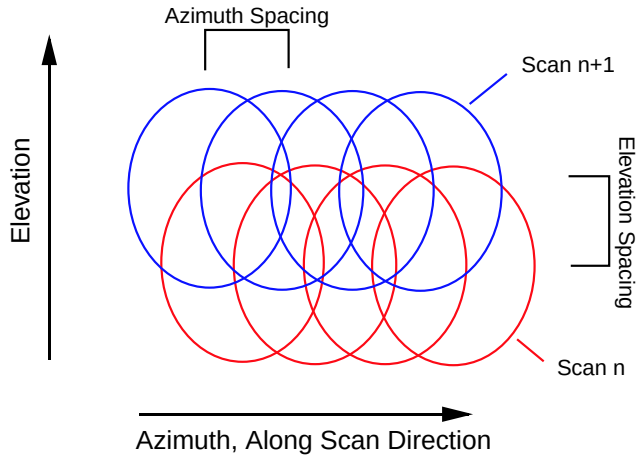

Figure 3.3: Diagram illustrating succession of the pencil-beam footprint locations on the surface. The azimuth and elevation axes are shown. The azimuth spacing is due to the scanning motion of the antenna and the radar sampling interval. The elevation spacing is due to the motion of the spacecraft, with successive rows of footprints due to successive rotations (or scans) of the antenna.

where β_{az} and β_{el} are the 3 dB beamwidths of the azimuth and elevation dimensions of the antenna pattern respectively. Note that in the case of the elevation width there is an elongation effect (given by $\cos\theta_{inc}$) due to the oblique projection of the pattern on the surface.

3.1.3 Measurement Continuity Constraints

An important issue for pencil-beam systems is the spatial continuity of measurements. In order to insure that complete coverage is obtained over the swath with no gaps, neighboring measurement footprints must either overlap (as shown Fig. 3.3) or at least touch. The *along-track continuity constraint* states that during one rotation of the antenna, the spacecraft must not move a distance more than the elevation width of the footprint. This insures that adjacent measurements will be contiguous in elevation. This constraint can be summarized in equation form as

$$\Omega \geq \frac{v_g}{x_{el}}, \tag{3.6}$$

where v_g is the velocity of the spacecraft projected on the Earth's surface.

The *along-scan continuity constraint* insures that the measurement footprints will be contiguous in the along-scan or azimuth direction. Here, the constraint is that

$$\text{MRI} \leq \frac{x_{az}}{\gamma}, \tag{3.7}$$

where MRI represents the measurement repetition interval, or the rate at which measurements are taken as the footprint moves in the azimuth direction. Both Eqs. (3.6) and (3.7) are minimum criteria in the sense that often substantial overlap, and not just simple continuity, are desired for adjacent measurement footprint regions (as will be addressed in later chapters).

3.2 Pencil-Beam Resolution

A key consideration which governs the design of any remote sensing device is spatial resolution. The resolution of an instrument is generally defined by the smallest spatial feature that can be distinguished on the surface. For a radar, the achievable resolution is a function of both the antenna gain pattern and the signal processing scheme employed. With a pencil-beam scatterometer, there are essentially four techniques for achieving spatial resolution [95]. These methods are illustrated in Fig. 3.4 (a)-(d), and are discussed in detail in the following sub-sections.

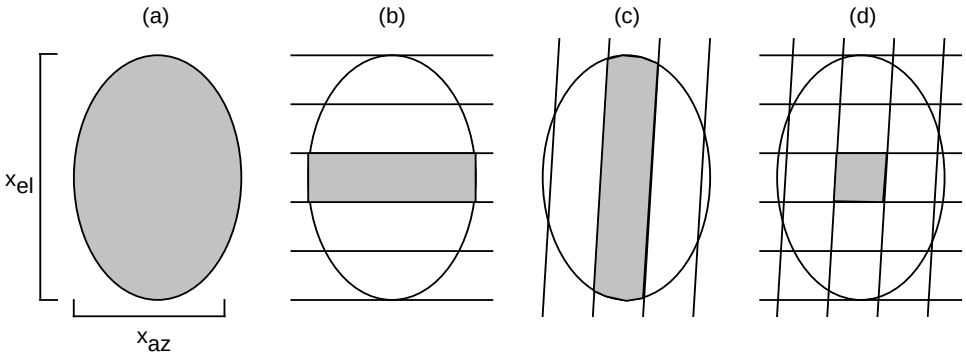

Figure 3.4: Techniques for pencil-beam scatterometer resolution: a) Beamwidth-limited resolution, b) range (delay) discrimination only (lines are iso-range contours), c) Doppler discrimination only (lines are iso-Doppler contours), d) simultaneous range and Doppler discrimination. The shaded region indicates the resolution cell or "pixel."

3.2.1 Beamwidth-Limited Resolution

As shown in Fig. 3.4(a), the beamwidth-limited resolution is defined as the two-way 3 dB contours of the antenna pattern as projected on the surface – i.e., the elevation and azimuth resolution are simply x_{el} and x_{az} as given by Eqs. (3.4) and (3.5) respectively. With this technique, higher resolution is obtained in either dimension simply by making the antenna larger, thus narrowing the beam pattern. The key advantage of the beamwidth-limited approach is its simplicity. The radar signal processing is designed only to detect the total power in the echo return. No effort is made to resolve regions smaller than the antenna footprint itself.

A generic processor for the beamwidth-limited resolution approach is shown in Fig. 3.4(a). Here, the incoming return pulse of bandwidth B_t is filtered, square-law detected, and integrated to form an estimate of the total echo energy E. The integration period T is generally given by

$$T = T_p + \Delta T_{fp}, \tag{3.8}$$

where T_p is the transmit pulse length and ΔT_{fp} is the time required to fill the antenna footprint in the elevation dimension. Although the resolution analysis for the beamwidth-limited case is quite simple, there are additional subtleties relating to measurement accuracy which are discussed in more detail in Chapter 4.

3.2.2 Range and Doppler Discrimination Techniques

If spatial resolution finer than the dimensions of the antenna footprint is required, regions of the surface within the footprint may be discriminated by range (equivalent to round-trip signal delay), Doppler shift, or both. In the case of range resolution, the footprint is divided into iso-range "slices" as shown in Fig. 3.4(b). Here the narrow dimension of the measurement cell is defined by the range processing, and the long dimension of the cell by the azimuth width of the antenna footprint. In a similar fashion, discrimination by Doppler shift can be used to make one-dimensional slices through the footprint. In both cases, however, the limiting resolution is still the antenna beamwidth. If both range and Doppler discrimination are employed

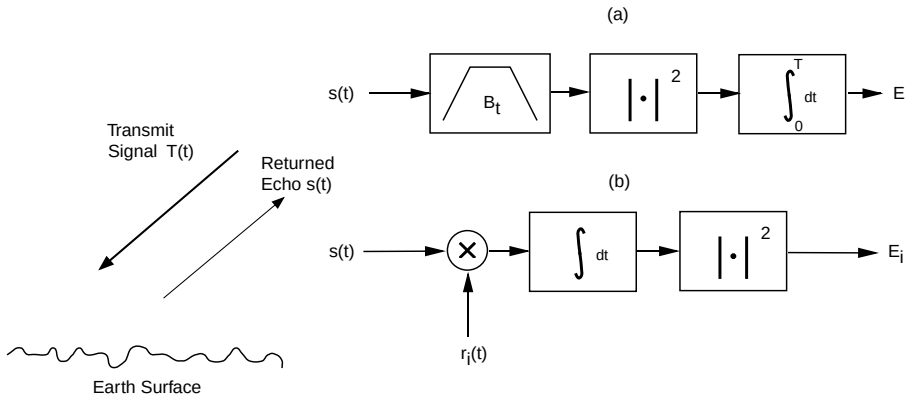

Figure 3.5: Generic signal processing techniques for a) beamwidth-limited systems where total power square-law detection is performed, and b) correlation detection for range delay discrimination, Doppler shift discrimination, or both. In b), the signal r_i is a reference function used in a correlation operation to discriminate the energy, E_i, returning from the ith measurement region.

simultaneously, as in Fig. 3.4(d), the footprint can be sub-divided in two dimensions yielding the best spatial resolution.

For all three of these cases, the discrimination technique involves a correlation (or, equivalently, matched filter) detection scheme. As shown in Fig. 3.5(b), a modulated transmit signal is broadcast. Then, to extract the energy returning from the ith region of the footprint, the echo signal is correlated with a reference function which has the same Doppler and/or range characteristics as the region to be discriminated. Because this process must be repeated for each region within the footprint, signal processing is more complicated than for the beamwidth-limited case.

3.2.3 Spatial Response Function (SRF) for Pencil-Beam Scatterometer Systems

To perform detailed analysis for the range and/or Doppler discrimination methods discussed above, the concept of the *spatial response function* (SRF) is introduced. The SRF is a two dimensional function which quantitatively represents the characteristics of the σ^o measurement cell on the surface given the antenna pattern, scan rate, and transmit pulse modulation. Because the SRF is a general tool that can

be applied to any radar geometry, it is particularly useful in the analysis of the pencil-beam case, where the orientation of the footprint with respect to the range/Doppler coordinates is continuously changing. The SRF is frequently employed in subsequent chapters of this dissertation.

To derive the pencil-beam SRF, we begin by assuming a transmit signal of the general form

$$T(t) = m(t)e^{j\omega t}, \tag{3.9}$$

where $m(t)$ contains the amplitude and phase modulation imparted to the transmit pulse and ω is the transmit carrier frequency. The echo return from a distributed target can be treated as a collection of returns from many infinitesimal surface patches [95]. The echo return from the ith patch is given by a time-delayed, frequency shifted version of the transmit signal with an additional random phase term

$$\xi_i \sqrt{\sigma_{0,i}} \sqrt{\delta A_i} c_i a_i^{tx}(t) a_i^{rx}(t) m(t - t_i) e^{j\omega_i t} e^{j\omega t} e^{j\psi_i}, \tag{3.10}$$

where ξ_i is a Rayleigh distributed random variable such that $\mathrm{E}[\xi_i^2] = 1$, $\sigma_{0,i}$ is the normalized backscatter cross-section at the patch, δA_i is the area of the patch, t_i is the round-trip flight time of the transmit pulse to the surface patch, ω_i is the Doppler shift of the patch, and ψ_i is a random phase term distributed uniformly over $[0 - 2\pi]$. The terms a_i^{tx} and a_i^{rx} represent the normalized antenna amplitude gain response in the direction of the patch during transmit and receive respectively. They are functions of time because the antenna is rotating during pulse transmission and reception. Two different functions (indicated by "tx" and "rx") are used to represent the antenna because either (1) a single antenna beam rotates to a different position during the round trip flight of the pulse, or (2) separate transmit/receive beams are used to avoid scan loss (see Section 3.3.2). The antenna power gains on transmit and receive, g_i^{tx} and g_i^{rx}, are defined as $|a_i^{tx}|^2$ and $|a_i^{rx}|^2$ respectively. The term c_i represents the other system gain terms for the ith patch, and is given by

$$c_i^2 = \frac{P_t G_p^2 \lambda^2}{(4\pi)^2 L r_i^2}, \tag{3.11}$$

where P_t is the transmit pulse power, G_p is the peak antenna power gain, λ is the radar wavelength, L_i is the atmospheric and system losses, and r_i is the slant range.

The echo return from a collection of infinitesimal patch scatterers, representing the distributed target, can thus be written

$$R(t) = \sum_{i \in \mathcal{F}} \xi_i \sqrt{\sigma_{0,i}} \sqrt{\delta A_i} c_i a_i^{tx}(t) a_i^{rx}(t) m(t - t_i) e^{j\omega_i t} e^{j\omega t} e^{j\psi_i}, \tag{3.12}$$

where the summation is performed over all patch scatterers in the radar field-of-view, $\mathcal{F}$.

For a correlation detector, the echo return is multiplied by the reference function

$$m^*(t - t_0) e^{-j\omega_0 t} e^{-j\omega t}, \tag{3.13}$$

where t_0 and ω_0 are the time delay and Doppler frequency coordinates for which maximum response is desired. Integrating, and then computing the magnitude, the detected signal energy, E, is

$$E = \left| \int_{-\infty}^{\infty} dt \ \sum_{i \in \mathcal{F}} \xi_i \sqrt{\sigma_{0,i}} \sqrt{\delta A_i} c_i m(t - t_i) m^*(t - t_0) e^{j(\omega_i - \omega_0)t} e^{j\psi_i} \right|^2. \tag{3.14}$$

The measured energy is a random variable (due to the random variables ξ and ϕ). To assess the mean behavior of the detection process, the expected value of E must be determined. Using

$$\left| \int f(t) dt \right|^2 = \left(\int f(t) dt \right) \left(\int f^*(t') dt' \right) \tag{3.15}$$

and

$$e^{j\psi} e^{-j\psi} = 1, \tag{3.16}$$

and assuming that the scattering patches are uncorrelated with one another, i.e.,

$$\begin{aligned} \mathcal{E}(\xi_m \xi_n) &= 1 \quad \text{for} \quad m = n \\ \mathcal{E}(e^{j\phi_m} e^{-j\phi_n}) &= 0 \quad \text{for} \quad m \neq n, \end{aligned} \tag{3.17}$$

(where $\mathcal{E}$ is the expectation operator), $\mathcal{E}$[E] becomes

$$\mathcal{E}[E] = \sum_{i \in \mathcal{F}} \sigma_{0,i} \delta A_i c_i^2 \left| \int_{-\infty}^{\infty} dt \ a_i^{tx}(t) a_i^{rx}(t) m(t - t_i) m^*(t - t_0) e^{j(\omega_i - \omega_0)t} \right|^2. \tag{3.18}$$

In order to evaluate how various regions of the target scene are resolved, it is convenient to define the spatial response function, $|\chi|^2$, as the energy detected per unit area at each surface patch location:

$$|\chi(t', \omega')|^2 = c_i^2 \left| \int_{-\infty}^{\infty} dt \; a_i^{tx}(t) a_i^{rx}(t) m(t - t') m^*(t - t_0) e^{j(\omega' - \omega_0)t} \right|^2, \tag{3.19}$$

where ω' and t' are the Doppler and delay coordinates of the ith scattering patch. Note that the SRF can be transformed into $|\chi(x, y)|^2$, where the Doppler and delay coordinates have been replaced by elevation and azimuth coordinates (x and y) using the mapping described in Section 3.1.1.

An important decomposition of Eq. (3.19) is obtained by assuming that the radar parameter c_i is constant (i.e., $c_i = K$) over the footprint, and that a^{tx} and a^{rx} can be assumed constant in time. Defining the variables $t_d = t_0 - t'$ and $\omega_d = \omega_0 - \omega'$ as the differential delay and Doppler frequencies respectively, the SRF can be re-written as

$$|\chi(t_d, \omega_d)|^2 = K^2 \; |\chi_{ant}(t_d, \omega_d)|^2 \; |\chi_{raf}(t_d, \omega_d)|^2. \tag{3.20}$$

Here, $|\chi_{ant}|^2$ represents the weighting of the antenna gain pattern on the response function and is given by

$$|\chi_{ant}(t_d, \omega_d)|^2 = g^{tx}(t_d, \omega_d) g^{rx}(t_d, \omega_d) \tag{3.21}$$

(where again a notational change is made from indexing the surface element location with "i," to locating it in delay/Doppler space). The transmit and receive antenna gain functions are thus specified as projections in delay/Doppler space via the mapping illustrated in Fig. 3.2.

Returning to Eq. (3.20), the term $|\chi_{raf}|^2$ is

$$|\chi_{raf}(t_d, \omega_d)|^2 = \left| \int_{-\infty}^{\infty} m(t) m^*(t - t_d) e^{j(\omega_d t)} \right|^2. \tag{3.22}$$

Here, $|\chi_{raf}(t_d, \omega_d)|^2$ represents the resolving capabilities inherent to the the modulated transmit signal $T(t)$. The function $\chi_{raf}(t_d, \omega_d)$ is equivalent to the *radar ambiguity function* [53, 74, 95]. The ambiguity function is central to many concepts in this dissertation and will appear repeatedly in subsequent analyses.

It is instructive to apply Eq. (3.20) to examine the resolution characteristics associated with several example transmit waveforms. In the following subsections, sample SRF's for an interrupted CW pulse, a chirped pulse, a periodic pulse train, and a pulse with pseudo-random phase modulation are given.

Single Long ICW Pulse for Doppler Discrimination

An interrupted continuous-wave (ICW) pulse is defined as

$$T(t) = \begin{cases} e^{i\omega t} & \text{if } 0 \leq t < T_p \\ 0 & \text{otherwise} \end{cases} ,$$

where T_p is the pulse length. In Fig. 3.6, the SRF for the ICW pulse is computed. The underlying contour plot is the ambiguity function ($|\chi_{raf}|^2$), and the oval represents an idealized antenna footprint function ($|\chi_{ant}|^2$) projected in the delay/Doppler plane for a side-looking geometry. For the purposes of this discussion, the footprint function is assumed to have a value of one within the oval and a value of zero outside the oval. Note that a long ICW pulse is able to discriminate Doppler quite well, with the Doppler resolution, δ_{dop}, approximately equal to $\frac{1}{T_p}$. Thus the longer the ICW pulse, the better the Doppler resolution. The resolution along the delay axis, δ_{del}, however, is given by $\delta_{del} = T_p$, and consequently becomes worse as the pulse duration is lengthened. Long ICW pulses are typically employed in situations where only resolution in the Doppler dimension is desired.

Linearly Chirped Pulse for Range Discrimination

A linear FM chirped waveform is employed when high range resolution is desired using a relative low power. A single linearly chirped pulse has a waveform given by

$$T(t) = \begin{cases} e^{\frac{1}{2}j\alpha t^2} e^{j\omega t} & \text{if } 0 \leq t < T_p \\ 0 & \text{otherwise} \end{cases} ,$$

where α is the "chirp rate." With a linear chirp, the frequency is linearly increasing (or decreasing) with time over the length of the pulse. An example SRF for such

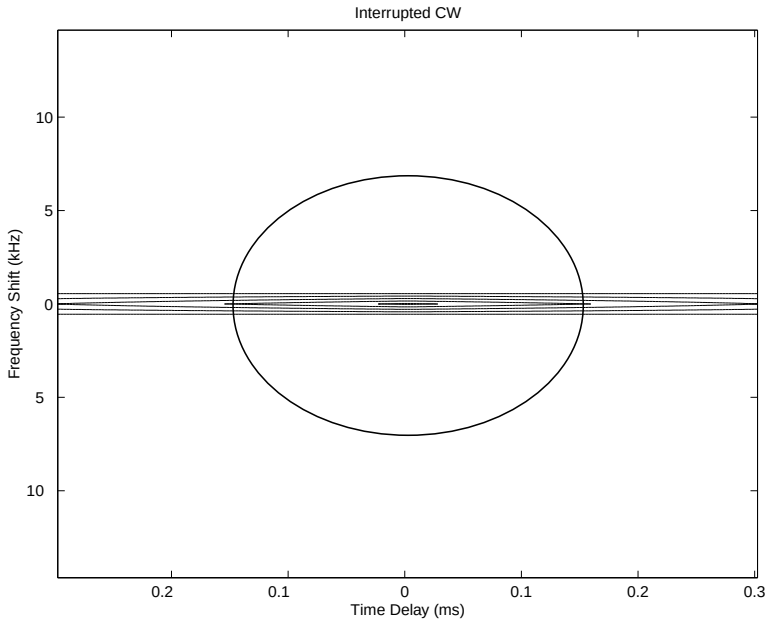

Figure 3.6: SRF for single long ICW pulse. The contours are the ambiguity function response ($|\chi_{raf}|^2$) for the ICW pulse, and the oval represents the antenna footprint as projected in delay/Doppler space for a side-looking antenna azimuth. Inside the oval, $|\chi_{ant}|^2$ is assumed to have a value of one, outside the oval $|\chi_{ant}|^2$ is assumed 0. This modulation scheme is primarily used to resolve the antenna footprint in the Doppler dimension.

a waveform is shown in Fig. 3.7. Note that, again, the single pulse resolves a one-dimensional slice across the antenna footprint. With the linear chirp modulation, however, the discrimination in primarily in the delay dimension. The time delay resolution is approximately given by $\delta_{del} = \alpha T_p$. Thus, the higher the chirp rate, the finer the delay resolution achievable. The pronounced tilt to the ambiguity function "blade" or "slice" indicates that the waveform is not purely discriminating in range. This tilt is the result of the coupling between the chirp waveform and the Doppler shift on the surface. As addressed in more detail in Chapters 4 and 5, the tilt of the blade can be adjusted by changing the chirp rate, α.

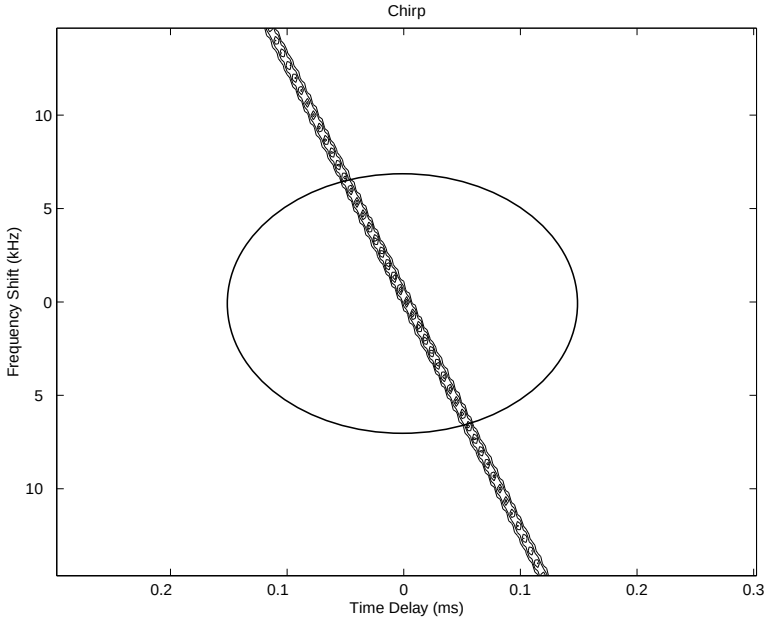

Figure 3.7: SRF for single linear FM chirped pulse. The contours are the ambiguity function response ($|\chi_{raf}|^2$) associated with the waveform, and the oval represents the antenna footprint as projected in delay/Doppler space. Inside the oval, $|\chi_{ant}|^2$ is assume to have a value of one, outside the oval $|\chi_{ant}|^2$ is assumed 0. This modulation scheme is primarily used to resolve the antenna footprint in the delay (or range) dimension, although there is a Doppler component to the response (manifested by the pronounced tilt of the "blade" formed by the ambiguity function) due to coupling between the chirp and the Doppler frequency variation on the surface.

Periodic Pulse Train for Simultaneous Range and Doppler Discrimination

In the two previous examples, the resolution is improved by forming one-dimensional slices through the antenna footprint. Although this narrows the width of the σ^o resolution cell, the length is still determined by the real dimensions of the antenna pattern. These approaches are therefore referred to as *real-aperture* techniques. To further improve the resolution of the measurement cell, a narrower antenna beam must be used. Because a narrow antenna beam implies a larger antenna aperture, there are often practical limitations on how much resolution can be improved. It is therefore desirable to achieve resolution in both delay and Doppler simultaneously, effectively sub-dividing the footprint in two dimensions.

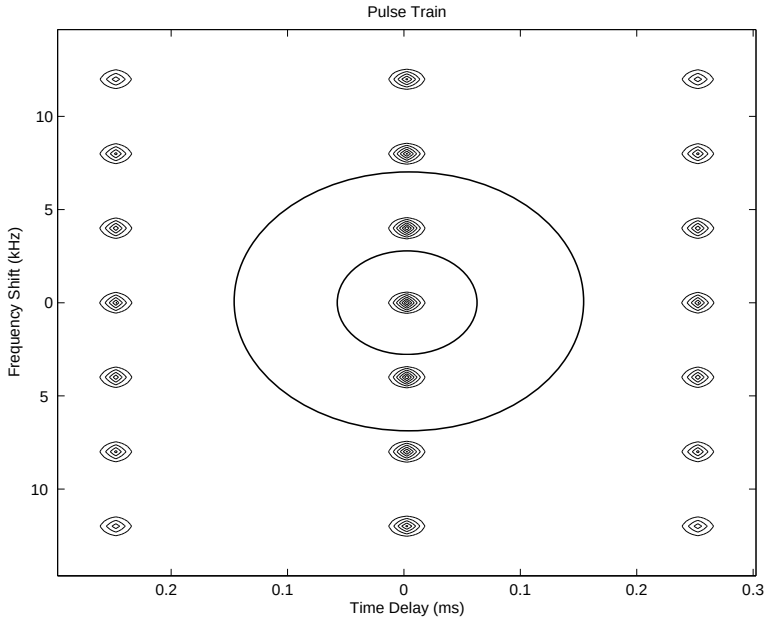

Figure 3.8: SRF for example periodic pulse train. The underlying contour plot is for the ambiguity function response for the periodic train waveform. The ovals represent example antenna footprints as projected in delay/Doppler space. Two ovals are shown in order to highlight the concept of ambiguity rejection: i.e., in order to achieve unambiguous two-dimensional resolution, the antenna pattern must isolate only one peak of the ambiguity function. Here, the small antenna footprint achieves this, whereas the larger footprint does not.

A well known technique to achieve two-dimensional resolution is to transmit a periodic pulse train of the form

$$T(t) = \begin{cases} e^{i\omega t} & \text{if } n\tau_p \leq t < n\tau_p + T_p \\ 0 & \text{otherwise} \end{cases} ,$$

where τ_p is the period of the pulse repetition and n is the pulse index [95]. The SRF for such a pulse train is plotted in Fig. 3.8. Note that the radar ambiguity function, $|\chi_{raf}|^2$, appears as a "bed-of-nails," with sharp two-dimensional responses spaced at multiples of τ_p in the delay dimension and multiples of $1/\tau_p$ in the Doppler dimension [95]. Each "nail" in this function is called an "ambiguity." In order to achieve two-dimensional resolution, the antenna pattern (the $|\chi_{ant}|^2$ term in the SRF) must isolate only one ambiguity. This concept is illustrated in Fig. 3.8 by showing two antenna

pattern contours. The outer contour encompasses three Doppler ambiguities, and thus is too wide to unambiguously resolve a single region of the surface. The inner antenna pattern is just narrow enough to reject all ambiguities but the desired central point. Thus, when a pulse train is employed to achieve two-dimensional resolution of the antenna footprint, care must be taken to insure that the antenna beams are sufficiently narrow (as will be discussed in detail in Chapter 7).

Pseudo-random Phase Shift Modulation

The periodic behavior of the ambiguity function in the previous example results because the original transmitted pulse train is periodic. Two-dimensional resolution of the footprint is successfully achieved provided that the antenna beamwidth is sufficiently narrow. To avoid the antenna beamwidth constraint associated with the use of this waveform, an ambiguity function with only one central peak is ideally desired. An ambiguity function of this type can be realized if the modulation within the waveform occurs at random, rather than periodic, intervals. An example of such a waveform is the so-called pseudo-random phase-shift keying signal, given by

$$T(t) = \begin{cases} e^{j\phi_c(t)}e^{j\omega t} & \text{if } 0 \leq t < T_p \\ 0 & \text{otherwise} \end{cases},$$

where the phase term $\phi_c(t)$ shifts randomly between the discrete values $\frac{\pi}{2}$ and $-\frac{\pi}{2}$ at the *chip period* τ_c [38]. The SRF of this waveform is shown in Fig. 3.9. Note that there is, as desired, one central peak. Rather than additional peaks spaced periodically, however, there is a background level of many smaller ambiguity sidelobes spread evenly over delay/Doppler space. This function shape is typically referred to as a "thumbtack" ambiguity function [74].

Although Fig. 3.9 appears to contain a promising solution for our desire to obtain two-dimensional resolution without any constraints on the antenna beamwidth, consider the fact that the energy returned to the sensor is the *integrated* value of the SRF [see Eq. (3.18)]. When the sidelobe pedestal region is integrated over the illuminated footprint region, the resulting value may be equal to or greater than the response due to the central peak. This explains why this waveform is typically

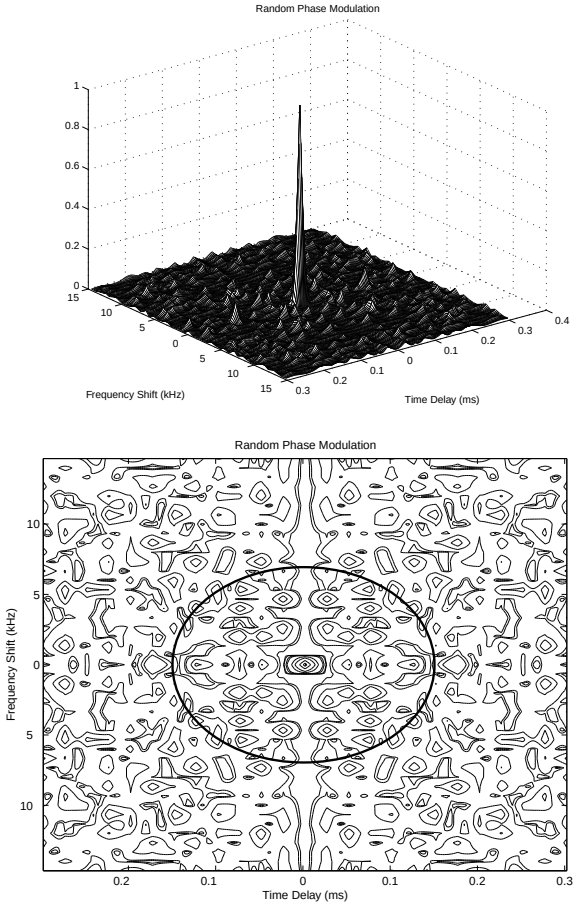

Figure 3.9: SRF for pseudo-random phase modulation. The contours are the ambiguity function response plotted in delay/Doppler space. Note that the ambiguity function consists of a high central peak, surrounded by a lower "pedestal" region. The oval represents a sample antenna footprint as projected in delay/Doppler space.

used for point targets, such as airplanes, and not distributed targets, such as the Earth's surface. Consequently, in the majority of remote sensing cases, a shaper two-dimensional resolution is obtained by employing the periodic pulse train methods of the previous example. The features associated with the pseudo-random phase waveform, however, will prove useful in the performance optimization of beamwidth-limited resolution systems, as is discussed in Chapter 4.

3.3 Measurement Error Considerations

As previously noted for fan-beam systems in Chapter 2, a consideration equal in importance to spatial resolution is that of measurement accuracy. Errors in the measurement of σ^o show up as errors in the wind or other geophysical parameters of interest. To address the pencil-beam case, new expressions for these measurement error sources must be developed.

3.3.1 Random Error, K_{pc}

To determine σ^o, an estimate of the energy backscattered from the surface, E_s, must first be obtained. However, the signal incident on the radar receiver consists of both echo and thermal noise components. Because the combined signal plus noise energy, E_{s+n}, is what is actually detected, a separate estimate of the noise-only energy, E_{no}, must subtracted in order to obtain an unbiased value for E_s. The most general equation for determining the echo energy is given by,

$$E_s = \alpha_1 E_{s+n} - \alpha_2 E_{no}. \tag{3.23}$$

The measurements E_{s+n} and E_{no}, in turn, are given by

$$\begin{aligned} E_{s+n} &= \int_{T_1}^{T_2} |x(t)|^2 \, dt \\ E_{s+n} &= \int_{T_1}^{T_2} |x_o(t)|^2 \, dt, \end{aligned} \tag{3.24}$$

where the signals $x(t)$ and $x_o(t)$ are the outputs of the signal+noise and noise-only processing respectively, and the integration is over the range gate "open" time $T_1 \rightarrow T_2$ (see Fig. 3.10).

Because both E_{s+n} and E_{no} are random variables, the estimate of the backscattered energy E_s is likewise a random variable. The variance of the estimate E_s determines the random error associated with the measurement of σ^o. As in the case of fan-beam systems, the random "noise" associated with the estimate of E_s is quantified by the parameter K_{pc}, where

$$K_{pc} = \frac{\sqrt{\mathrm{Var}[E_s]}}{\mathcal{E}[E_s]}, \tag{3.25}$$

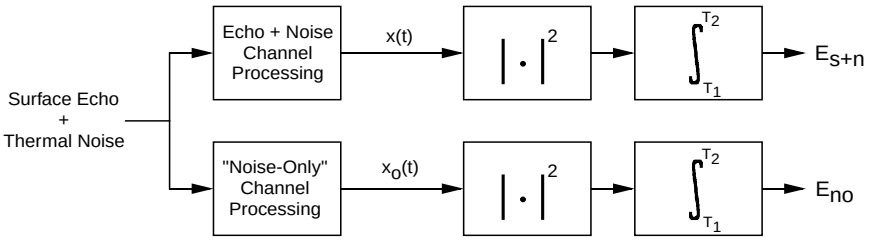

Figure 3.10: Generalized signal processing diagram for pencil-beam systems. The signal+noise processing yields the signal $x(t)$ which contributes to the energy estimate E_{s+n}. This signal contains the echo energy as well as the thermal noise energy present in the echo band. The noise-only processing produces the signal $x_o(t)$. This signal typically contains a wide bandwidth thermal noise component, and may also contain a portion of the echo energy.

and "Var" and "$\mathcal{E}$" are the variance and expectation operators respectively. Note that K_{pc} is the normalized standard deviation of the backscattered energy measurement. A key goal of scatterometer design is the minimization of K_{pc}.

The calculation of K_{pc} for a specific scatterometer design may be quite complex, and is a function of the pulse modulation and signal processing employed (see, for example, [45]). As discussed in Chapter 2, expressions for K_{pc} have been derived for a variety of fan-beam cases. In Chapters 4-7, K_{pc} expressions are derived for pencil-beam cases of interest. It is instructive, however, to consider a generic case in order to highlight the functional form of the K_{pc} parameter.

Utilizing the definition of variance, $\mathrm{Var}[E_s]$ is expanded to

$$\mathrm{Var}[E_s] = \alpha_1^2 \mathrm{Var}[E_{s+n}] + \alpha_2^2 \mathrm{Var}[E_{no}] - 2\alpha_1\alpha_2 \mathrm{Cov}[E_{s+n}E_{no}]. \tag{3.26}$$

Note that with fan-beam scatterometers, the term $\mathrm{Cov}[E_{s+n}E_{no}]$ is usually zero because the signal+noise and noise-only measurements are made at different, non-overlapping times, and hence are uncorrelated. Because the pencil-beam footprint is scanning rapidly over the surface causing the noise floor to be non-stationary, however, it is highly desirable to make the E_{s+n} and E_{no} measurements simultaneously [53, 81]. Consequently, the potential correlation between E_{s+n} and E_{no} must be taken into account for the pencil-beam case.

To evaluate Eq. (3.26), the term $\mathrm{Var}[E_{s+n}]$ defined by

$$\mathrm{Var}[E_{s+n}] = \mathcal{E}[E_{s+n}^2] - \mathcal{E}^2[E_{s+n}] \tag{3.27}$$

is first addressed. For either the square-law or matched-filter detection approach, the output of the signal+noise processing, $x(t)$, can be written as

$$x(t) = \sqrt{\bar{E}_s}s(t) + \sqrt{\bar{E}_n}\eta(t). \tag{3.28}$$

Here, $\bar{E}_s$ and $\bar{E}_n$ are the expected echo and noise energies respectively, and $s(t)$ and $\eta(t)$ are normalized such that

$$\int_{T_1}^{T_2} \mathcal{E}\left[|s(t)|^2\right]\, dt = \int_{T_1}^{T_2} \mathcal{E}\left[|\eta(t)|^2\right]\, dt = 1. \tag{3.29}$$

Both $s(t)$ and $\eta(t)$ are Gaussian random processes. This is true for the echo because it is the composite return from many randomly oriented scatterers on the surface [17, 53, 95]. Receiver noise can likewise be modeled as a filtered white Gaussian noise process [38]. An estimate of the signal+noise energy is thus obtained by

$$E_{s+n} = \int_{T_1}^{T_2} |x(t)|^2\, dt. \tag{3.30}$$

Addressing the second term in Eq. (3.27), we have that

$$\mathcal{E}[E_{s+n}] = \bar{E}_s + \bar{E}_\eta. \tag{3.31}$$

The first term of Eq. (3.27) is somewhat more involved. Inserting Eq. (3.28) into Eq. (3.30), expanding, assuming the echo and noise are uncorrelated, and applying a well-known identity for the forth-order moment of a set of Gaussian random variables [67], we have that

$$\begin{aligned}
\mathcal{E}[E_{s+n}^2] \;=\; & \bar{E}_s^2 \int_{T_1}^{T_2}\int_{T_1}^{T_2} |R_s(t,\tau)|^2\, dt\, d\tau \\
& + 2\bar{E}_s\bar{E}_n \mathrm{Re}\left[\int_{T_1}^{T_2}\int_{T_1}^{T_2} R_s(t,\tau)R_n^*(t,\tau)\right]\, dt\, d\tau \\
& + \bar{E}_n^2 \int_{T_1}^{T_2}\int_{T_1}^{T_2} |R_n(t,\tau)|^2\, dt\, d\tau \\
& + \bar{E}_s^2 + 2\bar{E}_s\bar{E}_n + \bar{E}_n^2
\end{aligned} \tag{3.32}$$

where $R_s(t,\tau)$ and $R_n(t,\tau)$ are the correlation functions of the processes $s(t)$ and $\eta(t)$ respectively (given by $\mathcal{E}[s(t)s^*(\tau)]$ and $\mathcal{E}[\eta(t)\eta^*(\tau)]$). From Eq. (3.27), we then have

$$\begin{aligned}\mathrm{Var}[E_{s+n}^2] &= \bar{E}_s^2 \int_{T_1}^{T_2}\int_{T_1}^{T_2} |R_s(t,\tau)|^2 \, dt \, d\tau \\ &\quad +2\bar{E}_s\bar{E}_n \mathrm{Re}\left[\int_{T_1}^{T_2}\int_{T_1}^{T_2} R_s(t,\tau)R_n^*(t,\tau)\right] \, dt \, d\tau \\ &\quad +\bar{E}_n^2 \int_{T_1}^{T_2}\int_{T_1}^{T_2} |R_n(t,\tau)|^2 \, dt \, d\tau.\end{aligned} \tag{3.33}$$

In order to evaluate the second and third terms in Eq. (3.26), we first define $x_o(t)$ as

$$x_o(t) = \sqrt{k_1\bar{E}_s}s_o(t) + \sqrt{k_2\bar{E}_n}\eta_o(t), \tag{3.34}$$

where k_1 and k_2 represent the percentage of echo or noise energy contained in $x_o(t)$ relative to $x(t)$, and the processes $s_o(t)$ and $\eta_o(t)$ are normalized in the same manner described by Eq. (3.29). The mean value of the noise-only energy is then

$$\mathcal{E}[E_{no}] = k_1\bar{E}_s + k_2\bar{E}_n. \tag{3.35}$$

Inserting Eq. (3.35) together with Eq. (3.31) into Eq. (3.23), α_1 and α_2 must be

$$\begin{aligned}\alpha_1 &= \frac{k_2}{k_2 - k_1} \\ \alpha_2 &= \frac{1}{k_2 - k_1}\end{aligned} \tag{3.36}$$

in order to achieve an unbiased estimate of E_s

A full evaluation of Eq. (3.26) proceeds in a similar manner as shown for the first term given in Eqs. (3.30)-(3.33). The tedious algebra is omitted here, and only the result is presented. First, the following definitions are established:

$$\begin{aligned}a &= \int_{T_1}^{T_2}\int_{T_1}^{T_2} |R_s(t,\tau)|^2 \, dt \, d\tau \\ b &= \int_{T_1}^{T_2}\int_{T_1}^{T_2} \mathrm{Re}\left[R_s(t,\tau)R_n(t,\tau)\right] \, dt \, d\tau \\ c &= \int_{T_1}^{T_2}\int_{T_1}^{T_2} |R_n(t,\tau)|^2 \, dt \, d\tau \\ a' &= \int_{T_1}^{T_2}\int_{T_1}^{T_2} |R_{so}(t,\tau)|^2 \, dt \, d\tau \\ b' &= \int_{T_1}^{T_2}\int_{T_1}^{T_2} \mathrm{Re}\left[R_{so}(t,\tau)R_{no}(t,\tau)\right] \, dt \, d\tau\end{aligned} \tag{3.37}$$

$$
\begin{aligned}
c' &= \int_{T_1}^{T_2}\int_{T_1}^{T_2} |R_{no}(t,\tau)|^2 \; dt \; d\tau \\
a'' &= \int_{T_1}^{T_2}\int_{T_1}^{T_2} |R_{sso}(t,\tau)|^2 \; dt \; d\tau \\
b'' &= \int_{T_1}^{T_2}\int_{T_1}^{T_2} \mathrm{Re}\left[R_{sso}(t,\tau)R_{nno}(t,\tau)\right] \; dt \; d\tau \\
c'' &= \int_{T_1}^{T_2}\int_{T_1}^{T_2} |R_{nno}(t,\tau)|^2 \; dt \; d\tau,
\end{aligned}
$$

where $R_{so}(t,\tau) = \mathcal{E}[s_o(t)s_o^*(t)]$, $R_{sso}(t,\tau) = \mathcal{E}[s(t)s_o^*(t)]$, etc. Further, we define

$$
\begin{aligned}
A &= \alpha_1^2 a + \alpha_2^2 k_1^2 a' - 2\alpha_1\alpha_2 k_1 a'' \\
B &= 2\alpha_1^2 b + 2\alpha_2^2 k_1 k_2 b' - 4\alpha_1\alpha_2\sqrt{k_1 k_2}\, b'' \\
C &= \alpha_1^2 c + \alpha_2^2 k_2^2 c' - 2\alpha_1\alpha_2 k_2 c'',
\end{aligned}
\tag{3.38}
$$

and the signal-to-noise ratio in the signal+noise channel, SNR, as

$$
SNR = \frac{\bar{E}_s}{\bar{E}_n}. \tag{3.39}
$$

Utilizing Eqs. (3.25) and (3.26) and the above definitions, K_{pc} can be written in the form

$$
K_{pc} = \left(A + \frac{B}{\mathrm{SNR}} + \frac{C}{\mathrm{SNR}^2}\right)^{\frac{1}{2}}. \tag{3.40}
$$

Thus, K_{pc} – or, equivalently, the percentage measurement error due to random effects – is a quadratic in 1/SNR. This functional form is the same for all scatterometer systems, and is consequently a general expression which applies to pencil-beam as well as fan-beam systems. The coefficients A, B, and C are related to the correlation statistics associated with a particular instrument, transmit modulation, and processor implementation.

The expressions for the coefficients A, B, and C represented by Eqs. (3.37) and (3.38) are somewhat involved. Fortunately, there is a simplification that will apply to most of the K_{pc} related analyses in this dissertation. Typically the noise-only measurement is made over a much wider bandwidth than the signal+noise measurement. This has two important implications. First, that $k_2 \gg k_1$. Thus when α_1 and α_2 are defined as in Eq. (3.36), all terms of $O(\frac{1}{k_2})$ are approximately 0. Secondly,

because $\eta_o(t)$ is a wide bandwidth process, $c \gg c'$ and $c \gg c''$. When these approximations are applied, the coefficients in Eq. (3.40) become $A = a$, $B = b$, and $C = c$. This simplification will be utilized repeatedly in Chapters 4, 5, 6 and 7.

A particularly informative case to examine is when SNR $\gg 1$, and Eq. (3.40) becomes $K_{pc} = \sqrt{A}$. Here, the term $1/A$ is equivalent to the number of independent samples or "looks" associated with the resolution cell [11, 95]. One intuitive way to view the concept of independent radar looks is to recognize that the number of looks is equal to the number of unique segments into which the cell may be resolved. Because the achievable resolution is given by the spatial response function, there is an important relationship between the SRF and the coefficient A. The precise mathematical relationship between the SRF and A is explored in detail in Section 4.1.4. A key result which derives from this analysis is that

$$\frac{1}{A} \approx \frac{\int\int |\chi_{ant}(t_d, \omega_d)|^2 \, dt_d \, d\omega_d}{\int\int |\chi_{ant}(t_d, \omega_d)|^2 |\chi_{raf}(t_d, \omega_d)|^2 \, dt_d \, d\omega_d}. \tag{3.41}$$

where the integrals are performed over the extent of the measurement cell. The righthand side of Eq. (3.41) is the ratio of the cell area to smallest resolvable surface area, or, equivalently, the number of surface segments which can be independently discriminated by the ambiguity function within the backscatter cell. Thus, the higher the inherent resolution associated with the radar ambiguity function χ_{raf}, the more independent regions the backscatter cell may be divided into, and the greater the number of independent looks.

Another useful way to consider the concept of radar looks is as the time-bandwidth product associated with the measurement of the return echo. The higher the bandwidth and the longer the integration time associated with the return echo signal, the better the averaging statistics and the lower the noise variance of the signal energy estimate. For instance, the time bandwidth product appears explicitly in Eq. (2.8) for the Doppler fan-beam system. This representation of equivalent looks is important because it highlights a potential disadvantage of pencil-beam systems. Whereas fan-beam systems use the spacecraft motion to move the footprint along the surface, pencil-beam systems use the rapid scanning motion of the antenna. Because

the pencil-beam footprint motion is much more rapid (i.e., $\gamma \gg v_g$), the available integration time is much shorter than for the fan-beam case. Thus, in order to obtain measurement performance equal to fan-beam systems, techniques must be devised to improve the effective signal bandwidth. These techniques are addressed in detail in Chapters 4 and 5.

3.3.2 SNR for Pencil-Beam Systems, Scanning Loss

Because the signal-to-noise ratio appears explicitly in the expression for K_{pc} [see Eq. (3.40)], it is important to have a convenient expression for SNR in conducting scatterometer design studies. For conventional side-looking radar systems, the SNR is well approximated by [74, 95]

$$\text{SNR} = \frac{P_t G^2 A_c \lambda^2 \sigma^o}{(4\pi)^3 R^4 L N_0}, \tag{3.42}$$

where P_t is the peak transmit power, G is the antenna gain, A_c is the area of the resolution cell, λ is the carrier wavelength, R is the slant range, L is the total system loss, and N_0 is the system noise power spectral density. This approximation is valid for pencil-beam systems as well with one important exception: the antenna gain in the direction of the measurement cell (G) is no longer a constant value, but varies with time as the pencil-beam footprint is rapidly scanned. The rapid motion of the antenna gain pattern effectively creates an additional signal loss, termed *scanning loss*, which must be taken into account in the computation of pencil-beam SNR [62].

During the round-trip flight time of the radar pulse to the surface and back, the rotating antenna beam sweeps away from the region originally illuminated. Scanning loss is defined as the loss of signal power that occurs because of this antenna pattern shift [62, 81]. Assuming that the slant range, R, is approximately constant over the footprint, the scanning loss, L_{scan}, is defined by

$$L_{scan} = \frac{\int g_{tx}(\overline{r}) g_{rx}(\overline{r})\, dA}{\int g_{tx}^2(\overline{r})\, dA}. \tag{3.43}$$

Here, g_{tx} and g_{rx} are the beam patterns on the surface at the time of transmit and receive respectively, and the integral is performed over the surface footprint region.

For pencil-beam systems, the value of L_{scan} must be included in the total system loss term, L, in evaluating Eq. (3.42).

When $x_{el} \ll d$, the antenna pattern motion during the pulse flight time can be modeled as a simple translation in the azimuth direction, Δx_{scan}, where

$$\Delta x_{scan} = \frac{2R\gamma}{c}. \tag{3.44}$$

Using Eqs. (3.43) and (3.44), the scanning loss as a function of the separation factor, ρ, is calculated and shown in Fig. 3.11. Here, ρ is defined as the azimuth displacement normalized by the two-way azimuth beam-width (i.e., $\rho = \frac{\Delta x_{scan}}{\beta_{az}}$). As expected, scanning loss increases with increasing azimuth separation. The allowable amount of signal loss is dependent on the measurement accuracy requirements for a specific system design.

The scanning loss calculation represented by Eqs. (3.43) and (3.44) applies for the case where the same antenna beam is used for both transmit and receive. If scanning loss, according to Fig. 3.11, becomes too large, it may be necessary to employ separate transmit/receive beams. In the separate beam case, the antenna patterns are steered to different positions in azimuth alternately on transmit and receive so as to compensate for the azimuth separation in Eq. (3.44). Transmit/receive azimuth steering may be accomplished, for example, by switching between two adjacent feeds – one which looks slightly ahead in azimuth and one slightly behind – so as to compensate for the movement of the footprint during the round-trip flight time. In general, such azimuth steering complicates the antenna design and calibration, so it is desirable to use a single beam where possible. Combining Eqs. (3.3) and (3.6) with Eq. (3.44), a constraint on the antenna pattern dimensions such that a single beam may be used for both transmit and receive is

$$\beta_{el}\beta_{az} \geq \frac{4\pi d v_g \cos\theta_{inc}}{cR\rho_{min}}, \tag{3.45}$$

where ρ_{min} is the separation factor that corresponds to the maximum acceptable scanning loss for a given application. Equation (3.45) indicates that higher resolution, higher gain beams also imply more complex antennas where transmit/receive steering is required.

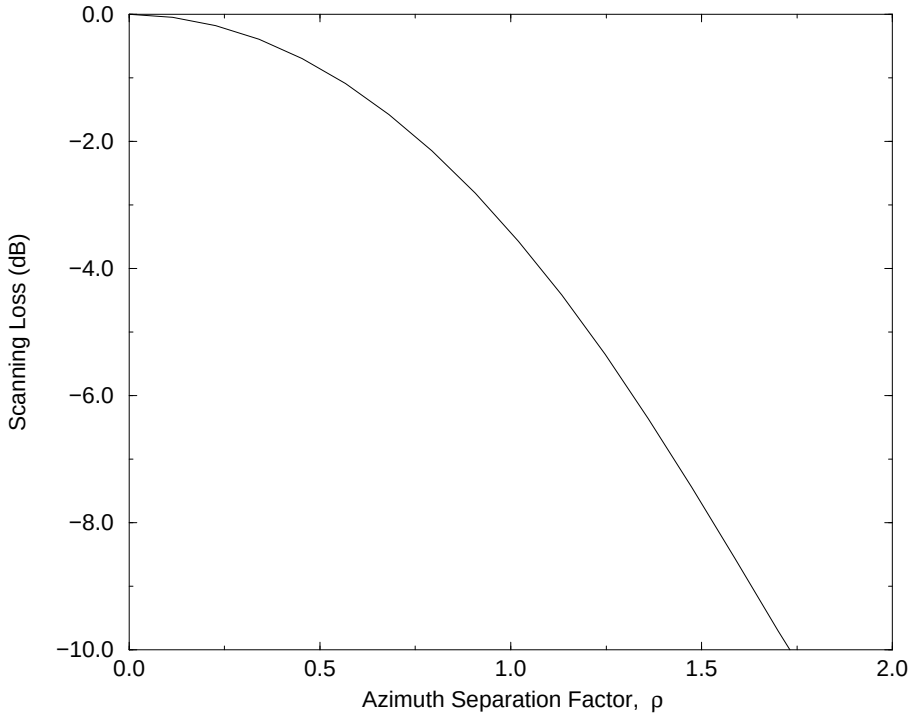

Figure 3.11: An example of scanning loss (in dB) vs. scan separation factor ρ. For the purposes of analysis, the antenna pattern has been modeled as a uniformly illuminated circular aperture. Due to the normalization by the beamwidth in calculating ρ, however, sensitivity to the precise antenna pattern in estimating scanning loss is small (see text).

3.3.3 Pencil-Beam Radar Equation, Calibration Error

As in the fan-beam case, an estimate of σ^o is obtained from the measurement of echo return energy utilizing the radar equation,

$$\sigma^o = \frac{E_s}{X}. \tag{3.46}$$

For the pencil-beam case, however, the expression for X must be modified to take into account the spinning motion of the antenna and the resulting separation of the transmit and receive antenna patterns (as discussed in the context of scanning loss in the previous subsection). The expression for the X of a pencil-beam system is then

[compare to Eq. (2.5)]

$$X = \frac{\lambda^2 E_t}{(4\pi)^3 L} \int d\overline{r}\ \frac{g_{tx}(\overline{r}) g_{rx}(\overline{r}) g_{rp}(\overline{r})}{R^4(\overline{r})}, \tag{3.47}$$

where E_t is the transmit energy, L represents the total system and instrumental losses, g_{tx} and g_{rx} are the beam patterns on the surface at the time of transmit and receive respectively, $g_{rp}(\overline{r})$ is the surface discrimination function due to radar resolution processing, $R(\overline{r})$ is the slant range to each surface element, and the integral is performed over the surface footprint region. The K_{pr} calibration error term is then computed in a similar fashion to that described for the fan-beam system in Section 2.3, the primary difference being that now the uncertainty in scanning loss is also a contributing factor to the overall calibration error.

3.4 Radar Pulse Timing and Nadir Contamination

Fundamental to any radar design is the appropriate selection of transmit pulse and echo return timing. In this section, the basic transmit and receive timing considerations for a pencil-beam scatterometer system are described. Because of the rapid scanning motion of the antenna and the relatively small footprint, the pulse-repetition frequency (PRF) of a pencil-beam system may be much higher than that of a fan-beam system. These higher PRF's, in turn, create more stringent requirements for pulse interleaving and for the rejection of nadir return contamination.

3.4.1 Transmit/Receive Timing Constraints

A generic illustration of spaceborne radar timing is shown in Fig. 3.12. Here, transmit pulses of width T_p are repeated at the pulse repetition interval, PRI (where the PRI is the inverse of the pulse repetition frequency, PRF). The round trip flight time of the echo to the surface and back is given by $\frac{2R}{c}$. The echo return from the ith pulse is shown as a large trapezoid. Note, in the case shown, that there are always two pulses in flight. The small trapezoids in Fig. 3.12 represent the echo returns from the direction of nadir (the effect of which will be considered shortly).

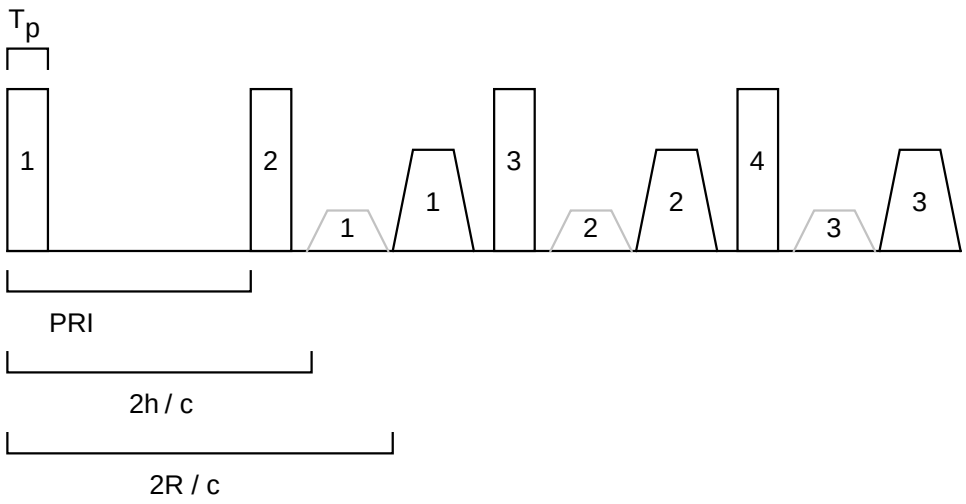

Figure 3.12: Sample radar timing diagram. Shown are transmit events (tall rectangles), echo returns (tall trapezoids), and returns from nadir (small trapezoids). Numbered labels are used to match echoes to the corresponding transmit events.

In general, the PRI is selected to satisfy the required along track sampling, such as that dictated by Eq. (3.7), or to produce desirable ambiguity patterns when two-dimensional resolution is sought, as discussed in Section 3.2.3. The PRI must also be selected to achieve a proper interleaving of transmit and receive events as shown in Fig. 3.12. Quantitatively, this interleaving constraint can be expressed as

$$\left|(n+\frac{1}{2})PRI - \frac{2R}{c}\right| \leq \frac{PRI - 2T_p - \Delta T_{fp} - \Delta T_{marg}}{2}, \tag{3.48}$$

where n is an integer representing the number of pulses in flight, T_p is the pulse length, ΔT_{fp} is the round-trip delay between the inner and outer edges of the footprint, and ΔT_{marg} is timing margin allowed for uncertainties in the precise value of R. For $x_{el} \ll d$, a convenient approximation for ΔT_{fp} is given by

$$\Delta T_{fp} = \frac{2\sin\theta_{inc}}{c} x_{el}. \tag{3.49}$$

Once selected, the PRI limits the allowed length of the transmit pulse, T_p, such that

$$T_p \leq \frac{\mathrm{PRI} - \Delta T_{fp} - \Delta T_{marg}}{2}. \tag{3.50}$$

The higher the PRI, the more difficult it is to find a timing solution which maintains adequate timing margins.

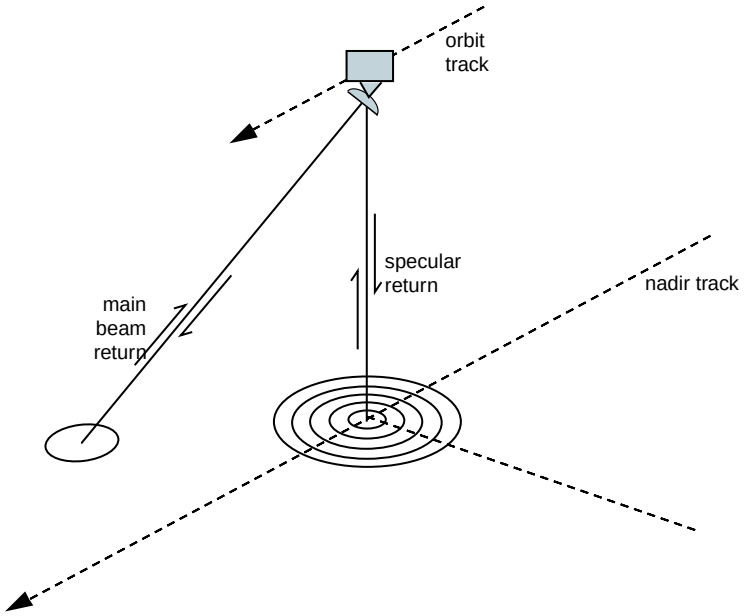

Figure 3.13: Near-nadir return contamination geometry.

3.4.2 Nadir Return Contamination

In addition to the interleaving of transmit and receive events, a timing issue that is of particular concern for pencil-beam scatterometers is the suppression of the unwanted echo reflection from the specular point in the direction of nadir. (These spurious signals are shown as small trapezoids in Fig. 3.12.) As shown in Fig. 3.13, the main beam of the scatterometer instrument illuminates the surface at relatively high incidence angles (47° and 55° in the case of the *SeaWinds* scatterometer described in Chapter 4) where Bragg scattering dominates the ocean return. At these high incidence angles, σ^o values are relatively low, ranging from about -30 dB for 3 m/s winds to -14 dB for 20 m/s winds at Ku-Band. However, the near-nadir region is also illuminated by the antenna sidelobes. In the incidence angle regime near 0°, specular reflection and quasi-specular scattering dominate, and σ^o ranges from around 0 dB for rough surfaces to over 30 dB for very smooth surfaces.

Because of the very large discrepancy in backscatter between the Bragg and specular regimes, and because pencil-beam scatterometers typically have multiple

transmit pulses and return echoes in flight, care must be taken in the scatterometer design to insure that the near-nadir return is sufficiently suppressed so it does not contaminate the main beam measurements. Examining Fig. 3.12, the most desirable solution is to select the timing so that the nadir echo returns at a different time as the main beam, therefore allowing it to be "gated out." This approach, however, severely limits the available timing schemes for future advanced scatterometers. In particular, if a higher PRF (corresponding to a higher sampling rate on the Earth's surface) is desired, it becomes increasingly difficult to find acceptable solutions where the nadir return can be gated out. With higher PRF's, it is likely that a return from the nadir region will appear in the same gate as the desired off-nadir return. While Doppler filtering may also be used to eliminate the near-nadir return, this strategy does not work when the antenna beam is scanned to $+/-90^\circ$ azimuth where the Doppler shift is near zero Hz. The best way to alleviate the specular region contamination problem is to insure that the antenna side-lobe levels in the direction of nadir sufficiently suppress this signal.

To assess the level of contamination from regions outside the main measurement footprint, the contamination ratio, Γ, is defined as

$$\Gamma = \frac{P_{out}}{P_{main}}. \tag{3.51}$$

Here, P_{main} and P_{out} are the returned powers from inside and outside the main beams respectively. The power returned from a given region of the surface, $\mathcal{R}$, is expressed as

$$P_{\mathcal{R}} = \frac{P_t \lambda^2}{(4\pi)^3 L} \int_{\mathcal{R}} d\overline{r}\ \frac{G^2(\overline{r})\sigma^o(\overline{r})}{R^4(\overline{r})}, \tag{3.52}$$

where P_t is the transmit power, λ is the wavelength, and L is the total system loss. Here, the integral is performed over the selected illuminated surface region $\mathcal{R}$ (either the main beam or elsewhere in the pattern).

In general, a comparison of the power from the main beam region to the return from all areas outside of the main beam is desired. For this analysis, however, the very strong contamination due to the specular region is of primary interest.

Assuming that the specular region is many beamwidths away from the antenna boresight, several simplifications may be applied to Eqs. (3.51) and (3.52). First, for the main beam return it is assumed that the beamwidth is sufficiently narrow so that σ^o and R may be set as constant over the footprint. P_{main} may then be expressed

$$P_{main} = \frac{P_t \lambda^2 G_p^2 A_{eff} \sigma^o_{main}}{(4\pi)^3 R^4_{main} L}. \tag{3.53}$$

Here, G_p is the peak antenna gain, A_{eff} is the effective two-way illuminated area, and σ^o_{main} and R_{main} are the backscatter cross-section and range at the main beam defined footprint.

For the near-nadir return, the primary simplification made is that the antenna pattern in this region may be modeled as a constant value, G_{nad}. This assumption will yield an upper-bound on the allowable sidelobe level in the far region of the antenna pattern. P_{nad} can thus be approximated as

$$P_{nad} = \frac{P_t \lambda^2 G^2_{nad}}{(4\pi)^3 L_{sys}} \int_{\mathcal{N}} \frac{\sigma^o_{nad}(r)}{R^4(r)} \; r \; dr d\theta. \tag{3.54}$$

Here, the Earth's surface in the vicinity of nadir is approximated as flat, and the integration has been changed to polar coordinates where r and θ are the radial distance and angle of the surface scatter relative to the nadir point. It is also assumed that σ^o_{nad} is only a function of the radial distance from the nadir point. (This is equivalent to assuming that σ^o_{nad}, on average, is only a function of incidence angle.) Note that in Eq. (3.54) the integration is performed over the nadir region, $\mathcal{N}$, only. The extent of the nadir region is determined by the radius over which contamination is significant.

Combining Eqs. (3.51), (3.53) and (3.54),

$$\Gamma = \frac{G^2_{nad} R^4_{main}}{G_p^2 A_{eff} \sigma^o_{main}} \int_{\mathcal{N}} \frac{\sigma^o_{nad}(r)}{R^4(r)} \; r \; dr d\theta. \tag{3.55}$$

This expression can then be evaluated for different σ^o_{main} in order to determine the nadir interference as a function of wind speed, and in order to determine the required side lobe level, G_p/G_{nad}. As an example, consider the case of a Ku-Band scatterometer system operating at the *SeaWinds* measurement geometry (h = 800 km, $\theta_{inc} = 55°$). First, it is assumed that a Γ value of -10 dB provides sufficient suppression of the

nadir contamination. Evaluating Eq. (3.60) for σ^o_{main} = -32 dB, which corresponds to a very low wind speed, and with a "worst-case" profile for $\sigma^o_{nad}(r)$, which is derived and presented in Appendix B, it is determined that $\frac{G_{nad}}{G_p}$ = -44 dB is required. This level is readily achievable in hardware.

3.5 Rain Contamination

The purpose of a scatterometer is to obtain a very accurate measurement of the surface backscatter cross-section. To the extent that the intervening atmosphere is not completely transparent to the microwave signal, an error in the measurement will result. The dominant error source at frequencies up to Ku-Band (14 GHz) is the presence of rain. Previous analyses have addressed the impact of rain on fan-beam scatterometer systems [61]. These studies, however, have only emphasized the signal attenuation produced by atmospheric liquid water. For pencil-beam scatterometers, which operate at high incidence angles where the surface backscatter cross-section is very small, the backscatter from the rain itself may be significant. In this section, a model for rain contamination which includes the influence of volume scattering from raindrops is developed. Using actual rain profiles, the effect of these errors is characterized for a Ku-Band system.

3.5.1 Rain Contamination Model

Atmospheric rain has two effects on the measurement of surface σ^o. First, the radar signal which passes through the rain is attenuated. Secondly, backscatter from the rain itself adds unwanted echo power to the return signal. These combined effects can be described by

$$\sigma^m = \alpha\sigma^o + \sigma^r, \tag{3.56}$$

where σ^m is the measured cross-section, σ^o is the actual surface cross-section, α is the effective path attenuation, and σ^r is the "rain equivalent backscatter cross-section" which represents the increase in apparent backscatter due to scattering from the rain. (Strictly speaking, both atmospheric water vapor and clouds may cause attenuation

even when rain is not present. These effects, however, are much smaller than those due to rain [94].)

Figure 3.14 illustrates the geometry assumed for the calculation of α and σ^r. Note that, in addition to the direct scattering paths from the rain and surface to the sensor, multi-path components which reflect off both the surface and the rain also exist. In general these multi-path terms will increase the value of σ^r relative to that calculated using only the direct scattering term. Here, because of the complexity in estimating the multi-path components, this contribution is assumed small, and thus our calculation will represent a lower bound on σ^r.

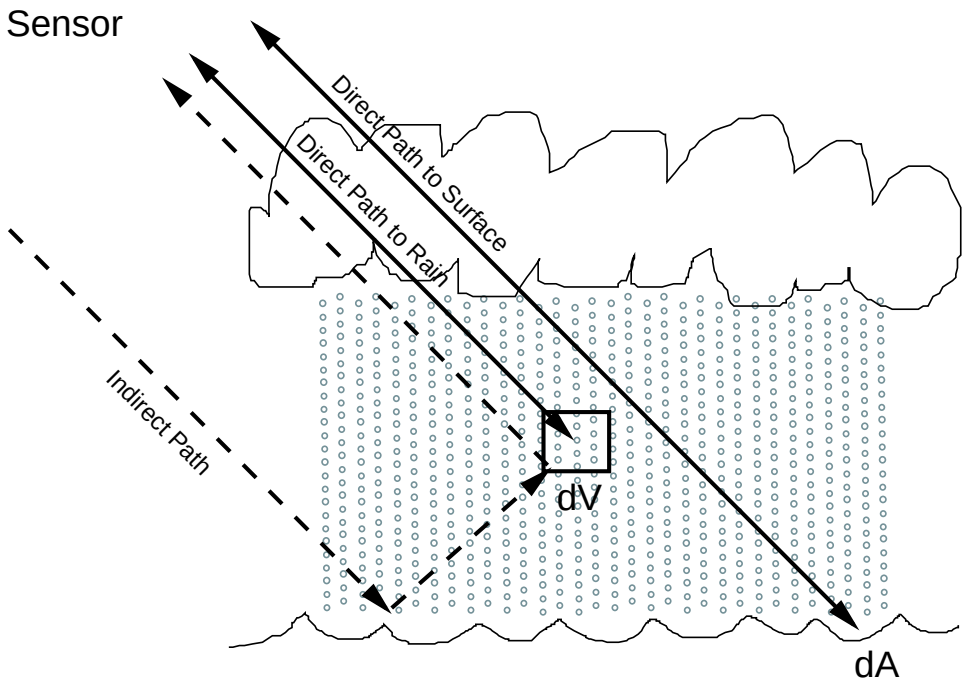

Figure 3.14: Rain contamination geometry.

In building the rain contamination model, it is convenient to first define the function $\mu(x, y, z)$, which quantifies the two-way attenuation from the sensor to a point at (x, y, z) located within the rain layer and back:

$$\mu(x, y, z) = 2 \int ds \;\; \kappa(x', y', z'). \tag{3.57}$$

Here, $\kappa(x, y, z)$ is the attenuation per unit path length and the integral is performed over the line from the point (x, y, z) to the sensor. With μ so defined, the total attenuation α is written

$$\alpha = \frac{1}{A_{eff}} \int dA \;\; G(x, y, z)\mu(x, y, z), \tag{3.58}$$

where A_{eff} is the effective area of the antenna footprint, $G(x, y, z)$ is the total gain function associated with the measurement, and the integral is performed over the Earth's surface. The rain-equivalent backscatter, σ^r, is given by

$$\sigma^r = \frac{1}{A_{eff}} \int dV \;\; G(x, y, z)\mu(x, y, z)\sigma^v(x, y, z), \tag{3.59}$$

where $\sigma^v(x, y, z)$ is the volume backscattering coefficient of the rain and the integral is performed over the raining volume.

3.5.2 Rain Errors

In order to evaluate Eqs. (3.57)-(3.59) and obtain a quantitative assessment of rain contamination effects, it is desirable to use realistic values for $\mu(x, y, z)$ and $\sigma^v(x, y, z)$. An ideal source for these functions is the Tropical Rainfall Mapping Mission Precipitation Radar (TRMM-PR). This instrument directly measures these parameters a Ku-Band. Using the TRMM-PR data, α and σ^r are calculated for a variety of actual rain conditions. Inserting these values into Eq. (3.56), the error in the measurement of σ^o due to rain contamination, $\Delta\sigma^o$, is given by

$$\Delta\sigma^o = 10 \log \left(\frac{\sigma^m}{\sigma^o} \right). \tag{3.60}$$

In Fig. 3.15, parametric curves for this error as a function of average column rain rate – the vertically integrated rain rate averaged over the scatterometer footprint – are derived for different assumed values of surface σ^o. Note that for low to moderate values of σ^o (-30 and -20 dB which correspond to winds from 3 to 10 m/s), the scattering from the rain dominates, and rain actually *increases* the apparent surface cross-section. For higher values of σ^o, attenuation is the dominant effect and the measured values are lower than expected. Due to the relatively high incidence angles

at which pencil-beam systems operate, the majority of the σ^o's encountered over the ocean fall into the -30 to -20 dB range. Because of this, rain is predicted to generally increase the apparent cross-section for most measurements. (This effect is indeed what is observed from an analysis of the *SeaWinds* data [39].)

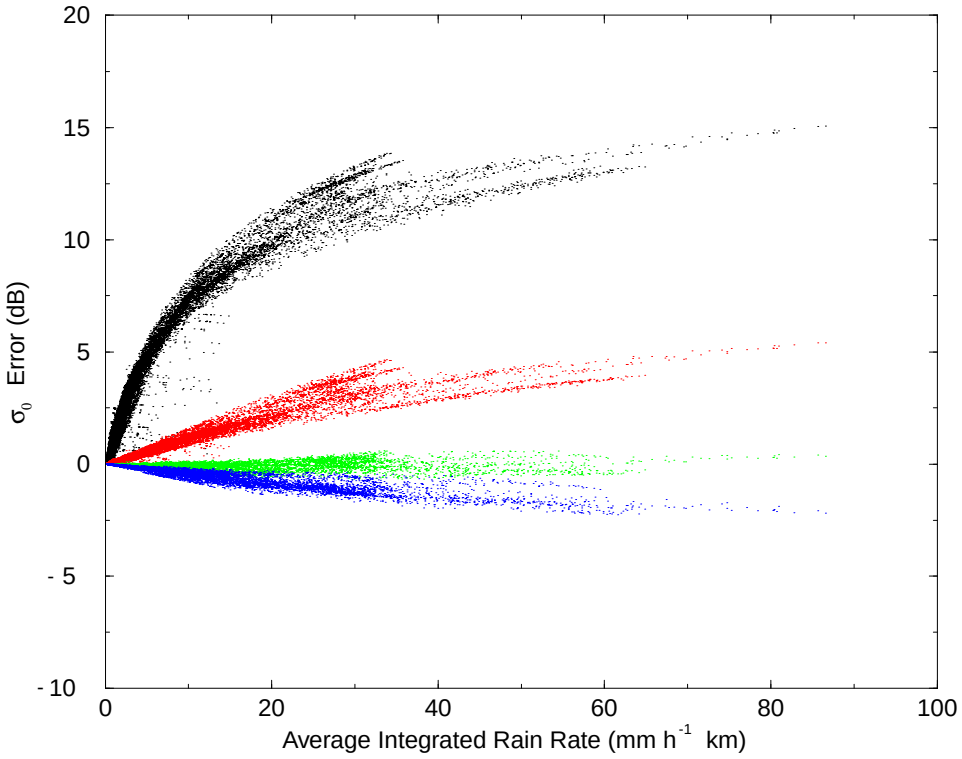

Figure 3.15: Scatterometer measurement error as a function of average column rain rate for four values of surface σ^o: -30 dB (black, corresponding to very low wind), -20 (red, corresponding to moderate wind), -14 dB (green, corresponding to high wind), and -10 dB (blue, corresponding to extremely high wind).

To further illustrate the effects of rain contamination, consider the example in Figs. 3.16 and 3.17. Here, TRMM PR data has been used to calculate the total attenuation, α, and the rain-equivalent backscatter cross-section, σ^r, over hurricane Floyd which formed in September, 1999. Also, in Fig. 3.18, the percentage of the detected signal which is coming from the surface, as opposed to the rain, is calculated.

An examination of Fig. 3.18 indicates that in heavily raining regions, such as the main hurricane bands, most of the backscattered signal is actually coming from the rain and not the surface. In such situations it is impossible to accurately retrieve the surface σ^o. Thus, it is critically important in the planning of Ku-Band scatterometer systems to be able to flag raining regions. This may be accomplished using a separate radiometer system located on the spacecraft platform or by identifying the signature of rain in the backscattered signal itself [39, 61]. When lower scatterometer frequencies, such as C-Band or L-Band, are used, rain contamination is of significantly less concern [25].

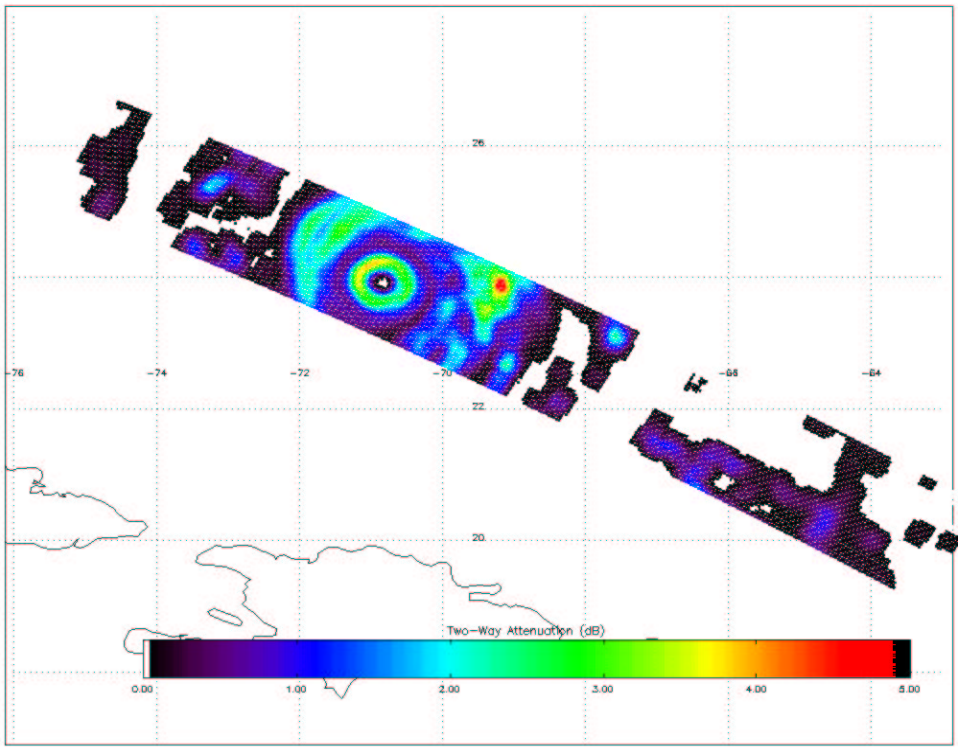

Figure 3.16: Two-way rain attenuation (α) calculated from TRMM-PR data over Hurricane Floyd, September 1999.

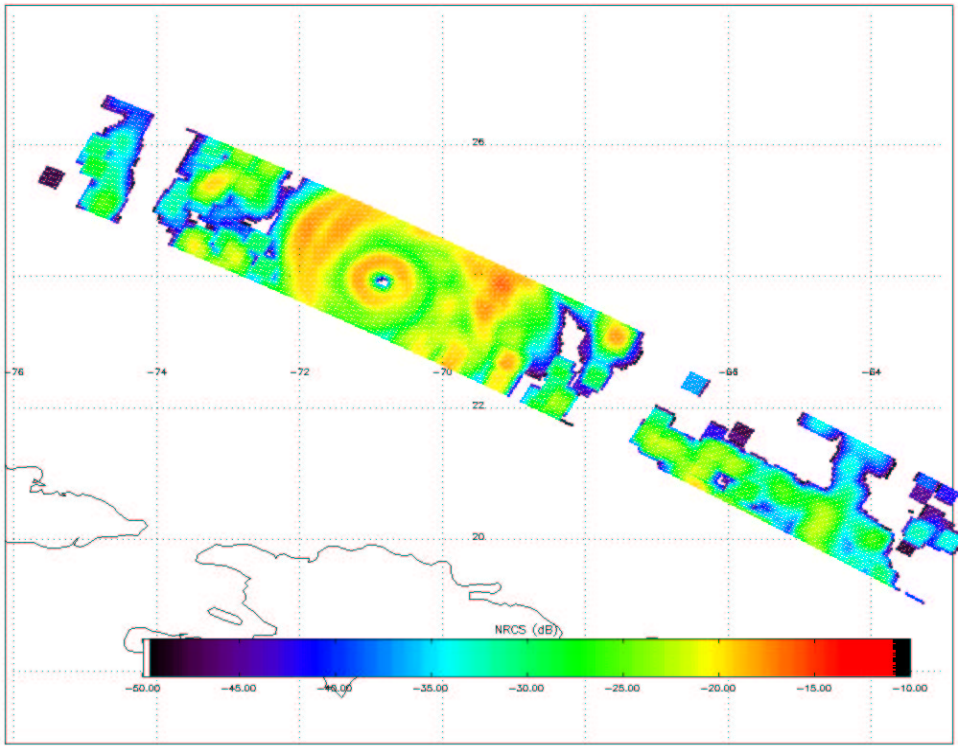

Figure 3.17: Rain equivalent cross-section (σ^r) calculated from TRMM-PR data over Hurricane Floyd, September 1999.

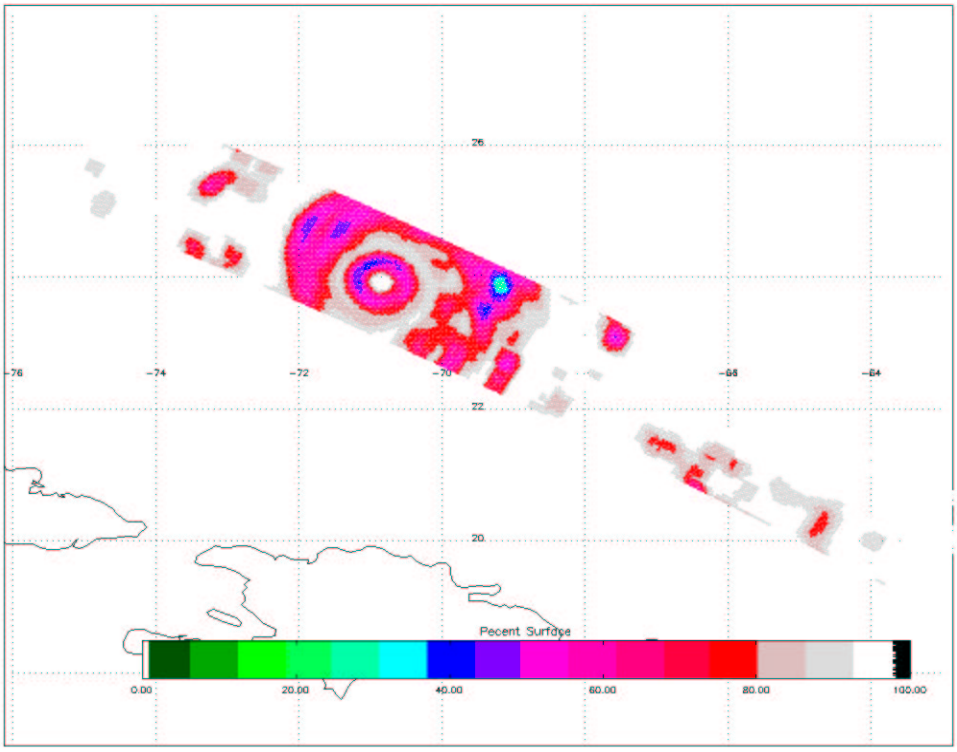

Figure 3.18: Percent of total echo energy actually coming from surface, calculated from TRMM-PR data over Hurricane Floyd, September 1999.

Chapter 4

Measurement Accuracy Optimization for Beamwidth-Limited Pencil-Beam Scatterometer Systems

In this chapter pencil-beam systems which employ the beamwidth-limited resolution approach are treated in more detail. These systems are easy to implement in hardware because they typically use band-pass filtering and square-law power detection, as opposed to more complex correlation detection approaches treated in succeeding chapters. As discussed in Chapter 3, the spatial resolution of a beamwidth-limited scatterometer is simply determined by the dimensions of the antenna footprint as projected on the surface. Once an antenna design which meets the spatial resolution requirement has been specified, the major design issue associated with beamwidth-limited systems is the minimization of backscatter measurement error.

Previous authors have addressed the measurement accuracy issue for spaceborne scatterometers and considered only the case where an unmodulated interrupted CW signal was transmitted [17]. It is demonstrated in this chapter that by appropriate modulation of the transmit signal, the measurement variance for beamwidth-limited systems can be significantly improved. In general, modulating the transmit signal to a higher bandwidth improves the equivalent number of independent looks obtained. Increasing the transmit bandwidth of the pulse, however, lowers the SNR. These competing effects must be carefully traded-off in order to achieve optimal performance.

This chapter is divided into two main parts. In Section 4.1, a signal processing framework for the beamwidth-limited case is described. General expressions are developed for the measurement variance when transmit modulation is employed,

and a discussion is provided concerning which modulation formats are optimum for a given application. In Section 4.2, these measurement variance optimization strategies are applied to the real-world example of the *SeaWinds* instrument, NASA's first pencil-beam scatterometer. It is shown how, using the methodology developed in Section 4.1, an optimal transmit modulation was selected for the initial beamwidth-limited version of the *SeaWinds* design.

4.1 Signal Processing Framework for Beamwidth-Limited Scatterometer Systems

In this section the signal processing for the general beamwidth-limited scatterometer case is described. Equations are presented which allow the unbiased estimation of signal energy given the signal+noise and noise-only measurements. Next, the issue of backscatter measurement variance is addressed. Uses the equations developed in Section 3.3.1, expressions are derived for the normalized measurement error (K_{pc}) when arbitrary transmit modulation is employed. Finally, the advantages and disadvantages of four different transmit modulation formats are discussed.

4.1.1 Beamwidth-Limited Echo Detection Approach

The overall signal detection approach for a beamwidth-limited scatterometer system is shown in Fig. 4.1. The input signal, which consists of both the echo return from the surface and thermal noise, is passed through a band-pass filter of bandwidth B_r. The resulting filtered output echo-plus-noise signal, represented by $s(t) + \eta(t)$, is squared and then integrated over the receive gate period $T_1 \rightarrow T_2$ to estimate the echo-plus-noise energy, E_{s+n}. To obtain information necessary to remove the thermal noise component in E_{s+n}, a separate "noise-only" measurement is made over a wider bandwidth, B_n. The output of this noise-only filtering process is represented by $s_o(t) + \eta_o(t)$. As described in Section 3.3, an estimate of E_s is then formed by

$$E_s = \alpha_1 E_{s+n} - \alpha_2 E_{no}. \tag{4.1}$$

Note that in Fig. 4.1 the noise-only energy is integrated over the same period as the signal+noise energy ($T_1 \rightarrow T_2$). For pencil-beam systems it is advantageous to perform the noise-only integration simultaneous with the signal+noise measurement, rather than at a different time as typically done with fan-beam systems. This is because the footprint is scanned over the surface at an effective speed that is much greater than the spacecraft motion. Consequently, the scene brightness temperature, which contributes to the noise power energy to be subtracted in Eq. (4.1), may change quickly. Thus, a simultaneous integration insures that $\eta(t)$ and $\eta_o(t)$ are filtered versions of the same process, and eliminates errors caused by non-stationarity.

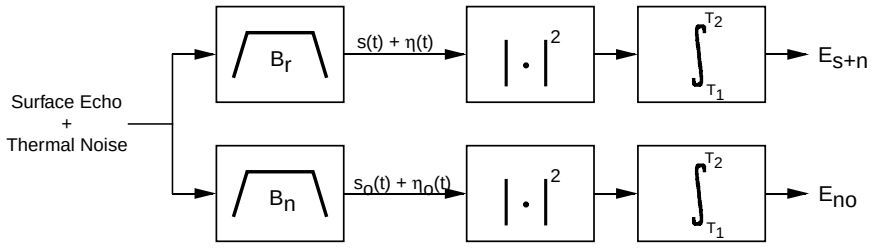

Figure 4.1: Signal processing approach for beamwidth-limited scatterometer systems. The combined echo and system noise signals are band-passed filtered to bandwidth B_r for the "signal+noise" channel, and B_n for the "noise-only" channel. (Note that the term "noise-only" is used for historical purposes. In reality, the noise-only measurement can contain some or all of the echo energy as well.) The energy in the two channels is detected by magnitude squaring and integrating the detected voltages.

In Fig. 4.2, a frequency domain representation of the processing in Fig. 4.1 is shown. The thermal noise spectrum is assumed to be a white noise process with a constant power spectral density over the frequencies of interest. The echo return has a narrowband spectrum of width B_s centered on the transmit carrier frequency (plus or minus the Doppler shift due to the relative motion of the satellite and the Earth). Superimposed on these spectra are the signal+noise and noise-only bandpass filter operations. Indicated are two approaches for the noise-only filtering: a non-

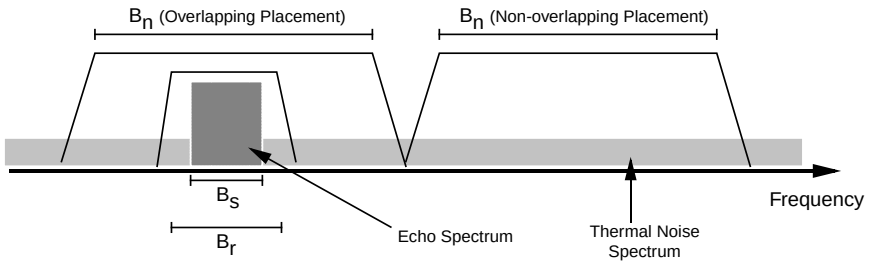

Figure 4.2: Signal processing of Fig. 4.1 shown from the perspective of the frequency domain. The echo signal spectrum and thermal noise floor are shown. As described in the text, the noise-only filtering pass-band may or may not overlap the echo spectrum.

overlapping placement of the bandpass region which rejects the echo spectrum, and an overlapping placement of the bandpass region which includes the echo spectrum.

When the noise-only filtering rejects the entire echo spectrum this is termed the "non-overlapping" case for which

$$\begin{aligned} \mathcal{E}[E_{s+n}] &= \bar{E}_s + B_r(T_2 - T_2)N_o \\ \mathcal{E}[E_{no}] &= B_n(T_2 - T_2)N_o, \end{aligned} \tag{4.2}$$

where $\bar{E}_s$ is the total energy in the echo, B_r is the effective bandwidth of the signal+noise channel, B_n is the effective bandwidth of the noise-only channel, and N_o is the thermal noise power spectral density. In order for Eq. (4.1) to yield an unbiased estimate of the echo energy, the coefficients α_1 and α_2 for this idealized case become

$$\begin{aligned} \alpha_1 &= 1 \\ \alpha_2 &= \frac{B_r}{B_n}. \end{aligned} \tag{4.3}$$

Using the notation of Section 3.3.1, this is equivalent to setting $k_1 = 0$ (because there is no signal component in the noise-only channel) and $k_2 = \frac{B_n}{B_r}$.

For the "overlapping" case, often easier to implement in hardware, the noise-only filter includes the echo, and we have that

$$\begin{aligned} \mathcal{E}[E_{s+n}] &= \bar{E}_s + B_r(T_2 - T_2)N_o \\ \mathcal{E}[E_{no}] &= \bar{E}_s + B_n(T_2 - T_2)N_o, \end{aligned} \tag{4.4}$$

and consequently

$$\begin{aligned} \alpha_1 &= \frac{\frac{B_n}{B_r}}{\frac{B_n}{B_r} - 1} \\ \alpha_2 &= \frac{1}{\frac{B_n}{B_r} - 1}. \end{aligned} \tag{4.5}$$

For large values of $\frac{B_n}{B_r}$, the coefficients for the two filtering strategies approach the same value. Note that Eqs. (4.2)-(4.5) are exact only for the "ideal" spectral shapes and filter responses shown in Fig. 4.1. These equations are adequate for initial performance modeling purposes, consistent with the primary goals of this section, but may require small modifications for realistic signals where not all of the echo signal is passed by the signal+noise filter (see Section 4.2.2).

4.1.2 Measurement Variance for Interrupted CW Transmit Signal

The bandwidth of the received echo, B_s, is a function of the nature of the transmit pulse. The simplest transmit signal is a single interrupted CW (ICW) pulse (see Section 3.2.3). The RADSCAT scatterometer flown on the Skylab mission, an experimental pencil-beam scatterometer and the precursor to modern systems, utilized this approach [17]. The measurement variance associated with the echo from an ICW transmit pulse is treated in a straightforward manner utilizing standard stochastic signal processing theory. The resulting equation for K_{pc} is discussed here to motivate the need for more sophisticated transmit signal modulation addressed in the following section. This development also provides some simplifying results that are of use in these later discussions.

The transmit bandwidth, B_t, of an ICW pulse is given by $B_t = 1/T_p$, where T_p is the pulse length. The Doppler shift bandwidth covered by the antenna beam footprint is defined as Δf_d. When $\Delta f_d \gg B_t$, the bandwidth of the echo return is approximately $B_s = \Delta f_d$. Furthermore, when the transmit pulse length is much longer than the beam fill time [i.e., $T_p \gg \Delta T_{fp}$ where ΔT_{fp} is defined as in Eq. (3.52)], the echo return can be modeled as a stationary band-limited white-noise process with bandwidth B_s [17]. Assuming that the power spectral density of the

echo is rectangular in shape (as illustrated in Fig. 4.3) the correlation function of $s(t)$ is given by [38]

$$R_s(t,\tau) = \frac{1}{T_p}\text{sinc}(2B_s(t-\tau)). \tag{4.6}$$

When $T_pB_s \gg 1$, which is typically the case for a single long transmit pulse, the a term in Eq. (3.37) is well approximated as [17]

$$a = \frac{1}{T_p^2}\int_{T_1}^{T_2}\int_{T_1}^{T_2}\text{sinc}^2(2B_s(t-\tau))\,dt\,d\tau \approx \frac{1}{T_pB_s}. \tag{4.7}$$

Note that the thermal noise is a band-limited white noise processes. When $B_r = B_s$ and the receive gate is set such that $T_2 - T_1 = T_p$, then $R_n(t,\tau) = R_s(t,\tau)$ and

$$\begin{aligned} b &\approx \frac{2}{T_pB_s} \\ c &\approx \frac{1}{T_pB_s}. \end{aligned} \tag{4.8}$$

With scatterometer systems, it is possible to have a very wide bandwidth for the noise-only measurement. This is desirable because a wide bandwidth reduces the noise-only contribution to the overall measurement variance. When $B_n \gg B_r$, then $k_2 \gg k_1$, and the simplifications discussed at the end of Section 3.3.1 apply (i.e., $A = a$, $B = b$, and $C = c$). Also, when B_n is large, $\alpha_1 \approx 1$ for the overlapping bandwidth case. Utilizing these approximations with Eqs. (4.7) and (4.8), the best achievable K_{pc} for the interrupted CW transmit pulse becomes

$$K_{pc} = \frac{1}{\sqrt{T_pB_s}}\left(1 + \frac{2}{\text{SNR}} + \frac{1}{\text{SNR}^2}\right)^{\frac{1}{2}}, \tag{4.9}$$

where the signal-to-noise ratio is given by

$$\text{SNR} = \frac{\bar{E}_s}{T_pB_sN_o}. \tag{4.10}$$

Equation (4.9) has important implications for motivating the advanced pencil-beam scatterometer measurement techniques discussed in the following sections. In this expression a key factor determining the measurement variance is the time-bandwidth product, T_pB_s, which effectively sets the number of independent looks achieved for the measurement. With pencil-beam systems employing ICW pulses,

however, there are fundamental limits on how large this term can be. The signal bandwidth is limited by the Doppler range associated with the size of the antenna footprint on the surface, Δf_d. Larger footprints leading to larger Doppler bandwidths can be employed, but at the expense of degraded resolution, an unacceptable option for many applications. The available pulse length, T_p, is even more strictly limited by the timing constraints as discussed in Section 3.4. Because the pencil-beam footprint is moving so quickly over the surface, there is much less integration time available compared to the fan-beam case. All these effects serve to limit the achievable $T_p B_s$ once a given antenna beamwidth has been selected. Therefore, to further improve K_{pc} it is necessary to consider methods which may involve more sophisticated transmit pulse modulations than the interrupted CW case discussed thus far.

4.1.3 K_{pc} for Beamwidth-Limited Pencil-Beam Systems Employing Modulated Transmit Pulses

Although the integration time for pencil-beam systems is tightly limited by the rapid scanning motion of the antenna, it is possible to increase the effective number of looks by transmitting a wider bandwidth signal than that created by the Doppler shift alone. This may be accomplished by modulating the transmit pulse in a variety of different ways. For a modulated signal, however, the echo return does not have same simple stochastic description as that presented in Eqs. (4.6) and (4.7). A new, more general formulation for the coefficients a, b, and c (and consequently A, B and C) must be derived.

In general, the transmit signal can be written in the form

$$T(t) = \sqrt{E_t}\, m(t) e^{j\omega_c t}, \tag{4.11}$$

where E_t is the total energy in the transmit pulse and $m(t)$ is the complex modulation imparted to the transmit pulse which is normalized so that

$$\int_0^{T_p} |m(t)|^2 \, dt = 1. \tag{4.12}$$

The return echo is the sum of returns from infinitesimal scattering patches on the ocean surface. The return from each patch can be represented as a Doppler shifted,

range delayed, phased shifted, and path attenuated replica of the transmitted signal. In this analysis, it is convenient to locate the position of each patch by its coordinates in delay/Doppler space as illustrated in Fig. 3.2. When the dimensions of the footprint are small compared to the scan radius (i.e., $d \gg x_{el}, x_{az}$) these coordinates uniquely locate each point within the antenna footprint.

Assuming that the backscatter cross-section over the footprint is constant, the combined echo return, $S(t)$ can be written

$$\begin{aligned} S(t) &= \sqrt{\frac{E_t G_p^2 \lambda^2 \sigma^o}{(4\pi)^3 \bar{r}^4}} \int_{t_d,\omega_d} \xi(\omega_d, t_d) g(\omega_d, t_d) m(t - t_d) \\ &\quad \cdot e^{j\omega_c} e^{j\omega_d} e^{j\psi(\omega_d, t_d)} \sqrt{\delta A(\omega_d, t_d)}\, d\omega_d\, dt_d \end{aligned} \tag{4.13}$$

where G_p is the net peak gain of the combined transmit/receive antenna beam patterns, $\bar{r}$ is the average range over the footprint, the integral is performed over all Doppler (ω_d) and delay (t_d) positions within the footprint region, $g(\omega_d, t_d)$ is the net normalized gain pattern at the position of the patch, and $\delta A(\omega_d, t_d)\, d\omega_d\, dt_d$ is the infinitesimal surface area associated with the scattering patch at location (ω_d, t_d). The terms ξ and ψ represent the random amplitude and phase due to the fading (or speckle) from the scattering patch, and have the properties

$$\begin{aligned} \mathcal{E}[\xi^2(\omega_d, t_d)] &= 1 \\ \mathcal{E}[e^{j\psi(\omega_d, t_d)} e^{j\psi(\omega'_d, t'_d)}] &= \delta(\omega_d - \omega'_d, t_d - t'_d). \end{aligned} \tag{4.14}$$

Defining the effective footprint area, A_{eff}, as

$$A_{eff} = \int_{t_d,\omega_d} g^2(\omega_d, t_d) \delta A(\omega_d, t_d)\, d\omega_d\, dt_d, \tag{4.15}$$

Eq. (4.13) is rearranged into the form used in Section 3.3.1 by writing

$$S(t) = \sqrt{\bar{E}_s}\, s(t), \tag{4.16}$$

where the expected total energy in the echo return is given by

$$\bar{E}_s = \frac{E_t G_p^2 \lambda^2 A_{eff} \sigma^o}{(4\pi)^3 \bar{r}^4}, \tag{4.17}$$

and thus

$$s(t) = \frac{1}{\sqrt{A_{eff}}} \int_{t_d,\omega_d} \xi(\omega_d, t_d) g(\omega_d, t_d) m(t - t_d) \cdot e^{j\omega_c t} e^{j\omega_d t} e^{j\psi(\omega_d, t_d)} \sqrt{\delta A(\omega_d, t_d)}\; d\omega_d\; dt_d. \tag{4.18}$$

The correlation function of the signal $s(t)$ is

$$R_s(t,\tau) = \frac{1}{A_{eff}} \int\int m(t - t_d) m^*(\tau - t_d) g^2(t_d, \omega_d) \cdot e^{j\omega_d(t-\tau)} \delta A(\omega_d, t_d)\; dt_d\; d\omega_d. \tag{4.19}$$

When the signal+noise and noise-only filtering operations are approximated as ideal bandpass filters, we have that

$$R_n(t,\tau) = \frac{1}{(T_2 - T_1)} \text{sinc}(2B_r(t - \tau)) \tag{4.20}$$
$$R_{no}(t,\tau) = \frac{1}{(T_2 - T_1)} \text{sinc}(2B_n(t - \tau)).$$

For the non-overlapping noise-only filtering case of Fig. 4.2, the correlation function definitions given in Eqs. (4.18)-(4.20) allow a complete solution to the K_{pc} equation when inserted into Eqs. (3.37)-(3.40). (This is true because $k_1 = 0$ and $R_{nno}(t,\tau) = 0$). When the signal+noise filter bandwidth is wide enough to pass the entire echo return signal, and the noise-only filter overlaps the echo, then $R_{so}(t,\tau) = R_{sso}(t,\tau) = R_s(t,\tau)$ and $R_{nno}(t,\tau) = R_n(t,\tau)$. These functions can also be used with Eqs. (3.37)-(3.40) to obtain a general solution for K_{pc}.

4.1.4 Simplified Analysis of Transmit Modulation Strategies

Exact solutions to K_{pc} based on the general expressions given in Eqs. (4.18)-(4.20) may be calculated numerically, but yield little insight into what transmit modulation is best for minimizing measurement variance. In this subsection, an approximate formulation for K_{pc} is used to provide a more intuitive assessment for the effect of transmit modulation.

We begin by assuming that the antenna beam footprint can be approximated by a rectangular region on the surface, where

$$g(t_d, \omega_d) = \begin{cases} 1 & t_d, \omega_d \in \text{illuminated rectangle} \\ 0 & \text{otherwise.} \end{cases}$$

This idealized rectangular antenna pattern is illustrated in Fig. 4.3. Note that as the antenna is scanned in azimuth, the delay and Doppler lines assume a different geometry relative to the antenna pattern (compare to Fig. 3.2). To assess the effect of this varying geometry, two cases are considered: (1) the case of the antenna scanned to a side-looking azimuth ($\theta_{az} = 90°$), where the iso-Doppler and iso-range lines are perpendicular; and (2) the forward-looking case ($\theta_{az} = 0°$), where the iso-Doppler and iso-range contours are parallel.

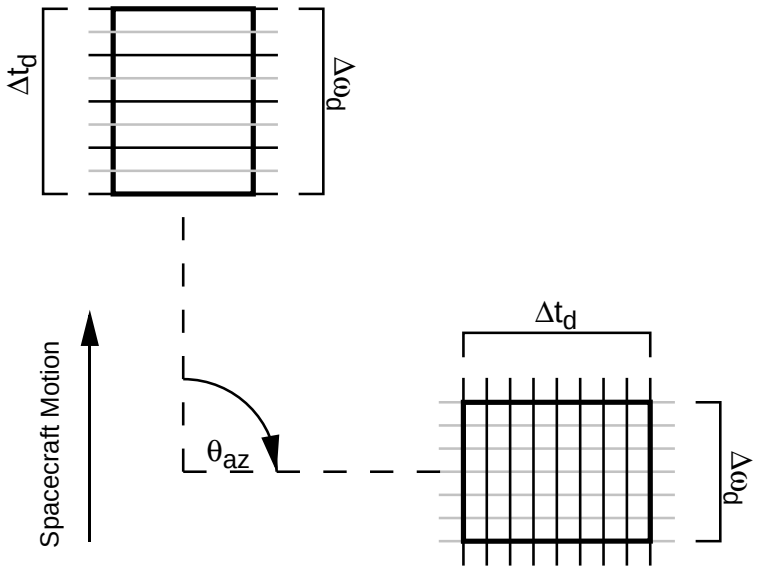

Figure 4.3: Simplified antenna geometry. The bold rectangles are idealized shapes of the antenna footprint on the surface. Δt_d and $\Delta\omega_d$ are the delay and Doppler widths of the footprint respectively. The lines of iso-range are shown in black, and the lines of iso-Doppler are shown in gray (compare to Fig. 3.2).

Case 1: Side-Looking Geometry

For the side-looking geometry case, the dimensions of the rectangular antenna pattern in delay/Doppler space are given by $\Delta t_d = t_{d,2} - t_{d,1}$ and $\Delta\omega_d =$

$\omega_{d,2} - \omega_{d,1}$ respectively. Consequently, the elemental area term in Eq. (4.15) is given by

$$\delta A(r, \omega_d) = \frac{A_{eff}}{\Delta t_d \Delta \omega_d}. \tag{4.21}$$

Applying this definition and the idealized antenna pattern assumption discussed above, the correlation function $R_s(t, \tau)$ becomes

$$\begin{aligned} R_s(t,\tau) &= \frac{1}{\Delta t_d \Delta \omega_d} \int_{t_{d,1}}^{t_{d,2}} \int_{\omega_{d,1}}^{\omega_{d,2}} m(t - t_d) m^*(\tau - t_d) \\ &\quad \cdot e^{j\omega_d(t-\tau)}\, dt_d\, d\omega_d. \end{aligned} \tag{4.22}$$

Inserting Eq. (4.22) into the expression for a, Eq. (3.37) becomes

$$\begin{aligned} a &= \frac{1}{\Delta t_d^2 \Delta \omega_d^2} \int_{T_1}^{T_2} \int_{T_1}^{T_2} \int_{t_{d,1}}^{t_{d,2}} \int_{t_{d,1}}^{t_{d,2}} \int_{\omega_{d,1}}^{\omega_{d,2}} \int_{\omega_{d,1}}^{\omega_{d,2}} m(t - t_d) m^*(\tau - t_d) \\ &\quad \cdot m^*(t - t'_d) m(\tau - t'_d) e^{j(\omega_d - \omega'_d)(t-\tau)} dt_d\, d\omega_d\, dt'_d\, d\omega'_d\, dt\, d\tau. \end{aligned} \tag{4.23}$$

As a simplification, consider the integral

$$\int_{T_1}^{T_2} m(\tau - t'_d) m^*(\tau - t_d) e^{j(\omega'_d - \omega_d)}\, d\tau. \tag{4.24}$$

Utilizing the substitutions $y = \tau - t'_d$ and $\rho = t_d - t'_d$, this becomes

$$e^{j(\omega'_d - \omega_d)t'_d} \int_{T_1 - t'_d}^{T_2 - t'_d} m(y) m^*(y - \rho) e^{j(\omega'_d - \omega_d)y}\, dy. \tag{4.25}$$

When the range gates are sufficiently wide to admit the entire echo signal, the integration limits in Eq. (4.24) may be set at infinity without changing the value. The integral in Eq. (4.24) thus becomes the radar ambiguity function as defined in Section 3.2.3. Equation (4.23) can now be written

$$a = \frac{1}{\Delta t_d^2 \Delta \omega_d^2} \int_{t_{d,1}}^{t_{d,2}} \int_{t_{d,1}}^{t_{d,2}} \int_{\omega_{d,1}}^{\omega_{d,2}} \int_{\omega_{d,1}}^{\omega_{d,2}} \left| \chi_{raf}(t_d - t'_d, \omega_d - \omega'_d) \right|^2 dt_d\, d\omega_d\, dt'_d\, d\omega'_d. \tag{4.26}$$

If the ambiguity function is symmetric in time and frequency, a very good assumption for most transmit signals used in remote sensing, Eq. (4.26) can then be written

$$a = \frac{1}{\Delta t_d^2 \Delta \omega_d^2} \int_{-\Delta t_d}^{\Delta t_d} \int_{-\Delta \omega_d}^{\Delta \omega_d} (\Delta t_d - |t_d|)(\Delta \omega_d - |\omega_d|) \left| \chi_{raf}(t_d, \omega_d) \right|^2 dt_d\, d\omega_d\, . \tag{4.27}$$

Equation (4.27) is a key result. It demonstrates that the a term, which is related to the number of independent looks obtained over the measurement footprint, can be approximated by a weighted integral over the radar ambiguity function.

It is useful to consider solutions to the integral in Eq. (4.27) for three idealized ambiguity function shapes (illustrations of which can be found in Section 3.2.3):

Doppler Resolving "Blade": When the ambiguity function is a blade-like function which is much longer than Δt_d in the delay dimension, but much shorter $\Delta\omega_d$ in the Doppler dimension; the value of a in Eq. (4.27) is approximately the ratio of the Doppler width of the blade to the Doppler width of the antenna footprint.

Delay Resolving "Blade": When the ambiguity function is a blade-like function which is much longer than $\Delta\omega_d$ in the Doppler dimension, but much shorter Δt_d in the delay dimension; the value of a in Eq. (4.27) is approximately the ratio of the delay width of the blade to the delay width of the antenna footprint.

Doppler/Delay "Spike": When the ambiguity function is a "spike" narrow in both the Doppler and delay dimensions relative to the dimensions of the footprint, the value of a in Eq. (4.27) is approximately the ratio of the area under the spike to the area of the footprint in delay/Doppler space.

Given the above approximations, one intuitive interpretation for the concept of "independent looks" is the number of independent regions into which the ambiguity function can divide the footprint.

Case 2: Forward-Looking Geometry

For the forward-looking geometry case, the iso-Doppler and iso-range lines are parallel, and consequently a change in delay is equivalent to a change in Doppler. Defining $\beta = \frac{\Delta\omega_d}{\Delta t_d}$, we have that $\omega_d = \beta t_d$. Making this substitution, Eq. (4.23) becomes

$$\begin{aligned} a &= \frac{1}{\Delta t_d^2}\int_{T_1}^{T_2}\int_{T_1}^{T_2}\int_{t_{d,1}}^{t_{d,2}}\int_{t_{d,1}}^{t_{d,2}} m(t-t_d)m^*(\tau-t_d) \\ &\quad \cdot\, m^*(t-t'_d)m(\tau-t'_d)e^{j\beta(t_d-t'_d)(t-\tau)}dt_d\; dt'_d\; dt\; d\tau. \end{aligned} \tag{4.28}$$

Utilizing similar substitutions applied to a obtain Eq. (4.27),

$$a = \frac{1}{\Delta t_d^2} \int_{-\Delta t_d}^{\Delta t_d} (\Delta t_d - |t_d|) \left|\chi_{raf}(t_d, \beta t_d)\right|^2 \, dt_d. \tag{4.29}$$

Equation (4.29) is a weighted line integral through delay/Doppler space of the ambiguity function. This is consistent with the fact that as the antenna is scanned toward the forward-looking direction, the shape of the antenna pattern footprint projected in delay/Doppler space gradually collapses from a rectangle to a line. As the a value for the side-looking case can be approximated by ratios of the ambiguity function area to the footprint area, the a value for forward looking case can be approximated a ratio of lengths along $(t_d, \beta t_d)$ through ambiguity space.

4.1.5 Evaluation of Specific Modulation Formats

In this subsection, Eqs. (4.27) and (4.29) are applied to four specific transmit modulation examples to illustrate strategies for minimizing the measurement variance of a beamwidth-limited scatterometer. Here, it is initially assumed that the SNR is high, and therefore $K_{pc} = 1/\sqrt{a}$. (A discussion of how the results change for lower SNR is provided in the following Section 4.2.) Interrupted CW, narrow-bandwidth FM chirp, high-bandwidth FM chirp, and pseudo-random phase modulation formats are addressed in turn below. In all of these examples, the Doppler width of the footprint is assumed to be 10 kHz, the delay width 0.3 ms, and the length of the transmit pulse is assumed to be $T_p = 1.5$ ms. (These parameters are the same as for the *SeaWinds* design discussed later in this chapter.)

Interrupted CW Pulse Modulation

The ambiguity function for an ICW pulse is conceptually shown in Fig. 4.4(a). Here, the dark band represents the "blade" in delay/Doppler space that results from a CW pulse 1.5 ms long. The black-outlined square is a representation of the idealized antenna footprint projected in delay/Doppler space when the antenna is side-looking (scanned to $\theta_{az} = 90°$). This is the region over which the integration in Eq. (4.27) is performed. The red-outlined linear region is a representation of the idealized antenna

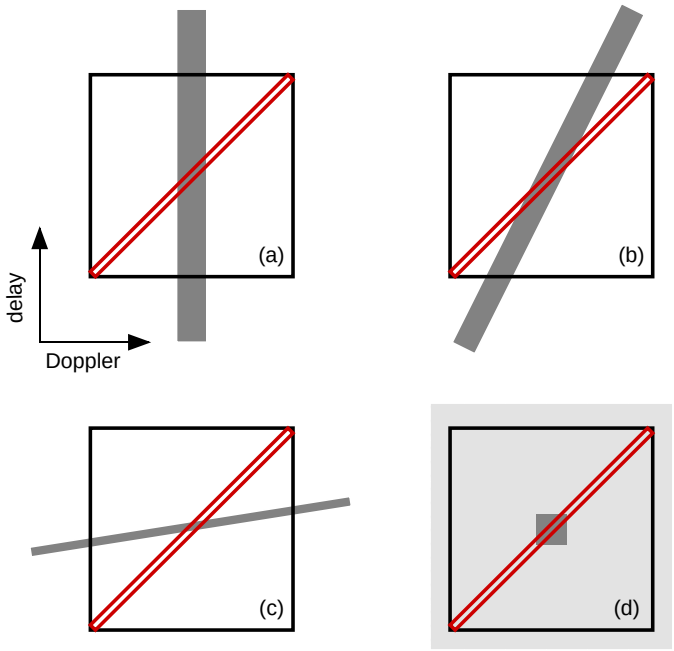

Figure 4.4: Conceptual illustration of ambiguity functions and integrations regions associated with the evaluation of Eqs. (4.27) and (4.29). An idealized ambiguity function is shown for a) Interrupted CW [compare with Fig. 3.6], b) Narrow-Band FM chirp [compare with Fig. 3.7], c) Wide-Band FM chirp [also compare with Fig. 3.7], and d) Pseudo-random phase modulation [compare with Fig. 3.9]. In each case, the shaded region shows the non-negligible portion of the idealized ambiguity function response where white represents $|\chi_{raf}|^2 = 0$, and the dark gray represents $|\chi_{raf}|^2 = 1$. The pedestal region of the pseudo-random phase modulation case is shown in light gray and has a small average value. The black square represents the idealized antenna footprint projected in delay/Doppler space for the side-looking case over which the integral in Eq. (4.27) is performed. The red-outlined linear region is the idealized antenna footprint projected in delay/Doppler space for the forward-looking case over which the integral in Eq. (4.29) is performed.

footprint for the forward-looking geometry projected in delay/Doppler space. This is the line over which the integral in Eq. (4.29) is performed. Evaluating high-SNR K_{pc} for the side-looking and forward-looking cases, the results listed in Table 4.1 are obtained. Note that for this modulation scheme example, K_{pc} is only a function of the Doppler resolution and is independent of azimuth angle.

Narrow-Bandwidth FM Linear Chirp Modulation

The ambiguity function for an FM linear chirp of bandwidth 40 kHz is conceptually shown in Fig. 4.4(b). Note that the relatively low bandwidth imparted to the signal means that a significant tilt in the Doppler dimension is imparted to resulting ambiguity blade. The high-SNR K_{pc} associated with this signal is shown in Table 4.1. Here, the side-looking K_{pc} is comparable to the interrupted CW case, but the forward-looking value is somewhat worse. Examining Fig. 4.4(b), this is because the line integral required to evaluate Eq. (4.29) is almost parallel to the tilt direction of the blade, consequently picking up a larger value. In fact, if the tilt direction of the blade had been the same as the integration path, the value of K_{pc} would become unity.

Wide-Bandwidth FM Linear Chirp Modulation

The ambiguity function for an FM linear chirp of bandwidth 400 kHz is conceptually shown in Fig. 4.4(c). There are two important differences to note relative to the low bandwidth case. First, there is a much less pronounced tilt in the Doppler direction, and the blade is consequently more purely resolving the surface in the delay dimension. Secondly the width of the blade is much narrower. Both of these effects lead to much smaller values of K_{pc} as shown in Table 4.1.

Pseudo-random Phase Modulation

As a final example, the ambiguity function of a pseudo-random phase modulated pulse of bandwidth 40 kHz is illustrated conceptually in Fig. 4.4(d). Here the small, dark square region represents the central ambiguity "spike" where the ambiguity function has a value of one. The lighter shaded region is the ambiguity "pedestal" where the ambiguity function has a much smaller value (an average ambiguity level of approximately 0.01 in this particular example). Note from Table 4.1 that the K_{pc} value for the side-looking case is approximately the same as for the high-bandwidth linear FM modulation, but the forward-looking geometry yields performance more similar to the CW and low-bandwidth chirp signals.

The significant difference between the side-looking and forward-looking geometries in this example is intuitively explained from a closer examination of Fig. 4.4(d). The proportion of the ambiguity "spike" which lies within the side-looking integration region is smaller than the proportion which contributes to the forward-looking line integral. This feature yields the observed increase in K_{pc} for this modulation scheme as the antenna is scanned to 0° azimuth.

Table 4.1: High-SNR values of K_{pc} for the transmit modulation schemes shown in Fig. 4.4.

Modulation	K_{pc} for $\theta_{az} = 90°$	K_{pc} for $\theta_{az} = 0°$
Interrupted CW	0.26	0.26
Narrow-Bandwidth Chirp	0.23	0.31
Wide-Bandwidth Chirp	0.13	0.14
Pseudo-random Phase	0.13	0.27

4.1.6 Comparison of Beam-Limited Pulse Modulation Formats

The combined results summarized in Table 4.1 allow a comparison of the various pulse modulation formats which may be applied to a beamwidth-limited scatterometer design. Clearly, of the options examined, the best is the wide-bandwidth FM chirp. For the detection scheme shown in Fig. 4.1, however, the maximum SNR available is given by $\bar{E}_s/T_pB_sN_o$, where B_s is the bandwidth of the signal. This means that a larger bandwidth signal has associated with it a *lower* SNR. Thus, to achieve the high-SNR conditions assumed by Table 4.1, the high-bandwidth chirp signal must be generated with a higher transmit power. Because of power limitations aboard the spacecraft, this could be problematic.[1] An alternate approach to achieve a more bandwidth efficient improvement in K_{pc} is to employ the pseudo-random phase

[1] This conclusion is based exclusively on the simple "unmatched" filtering shown in Fig. 4.1. When pulse compression matched filtering is employed with high-bandwidth pulses, as will be discussed in Chapter 5, a net SNR gain is realized, and a wide-bandwidth FM chirp remains the superior performance choice.

modulated signal. This approach allows an improvement in K_{pc} with a narrower-band transmit signal, albeit with a degradation in performance as the antenna is scanned to the forward-looking position.

4.2 The *SeaWinds* Scatterometer: Beam-Limited Design Version

The utility of the results presented in the previous section can be illustrated by considering the real-world design example of the *SeaWinds* scatterometer. *SeaWinds* is NASA's first conically-scanning pencil-beam scatterometer, and was developed to replace the fan-beam NSCAT system. Although, as described in the next chapter, the final *SeaWinds* design implementation uses a range-discrimination resolution approach, an initial *SeaWinds* design concept used the beamwidth-limited resolution approach treated in this chapter [21, 81]. The signal processing framework developed in Section 4.1 was applied in the design of this initial beamwidth-limited concept. In this section, the tradeoffs performed by the author to select an optimum modulation scheme for the initial beamwidth-limited version of *SeaWinds* are described.

4.2.1 Overview of the *SeaWinds* Design

Before addressing the analysis performed in support of the *SeaWinds* effort, the overall characteristics of the *SeaWinds* instrument are first described. The *SeaWinds* measurement approach is illustrated in Fig. 4.5. *SeaWinds* is operates at an orbital altitude of 800 km. The antenna illuminates the surface with two beams: an outer beam using V-polarization, and an inner beam using H-polarization. Because the beams have different scan radii, each point within 700 km of the nadir track is viewed from four different azimuth angles; twice by the outer beam looking forward then aft, and twice by the inner beam in the same fashion. The multiple azimuth views insure that ocean surface wind vectors can be accurately retrieved.

An overriding consideration which governed the design of the *SeaWinds* instrument was the desire to keep the instrument compact. For this reason a one meter scanning dish antenna was selected. The beamwidth-limited resolution associated

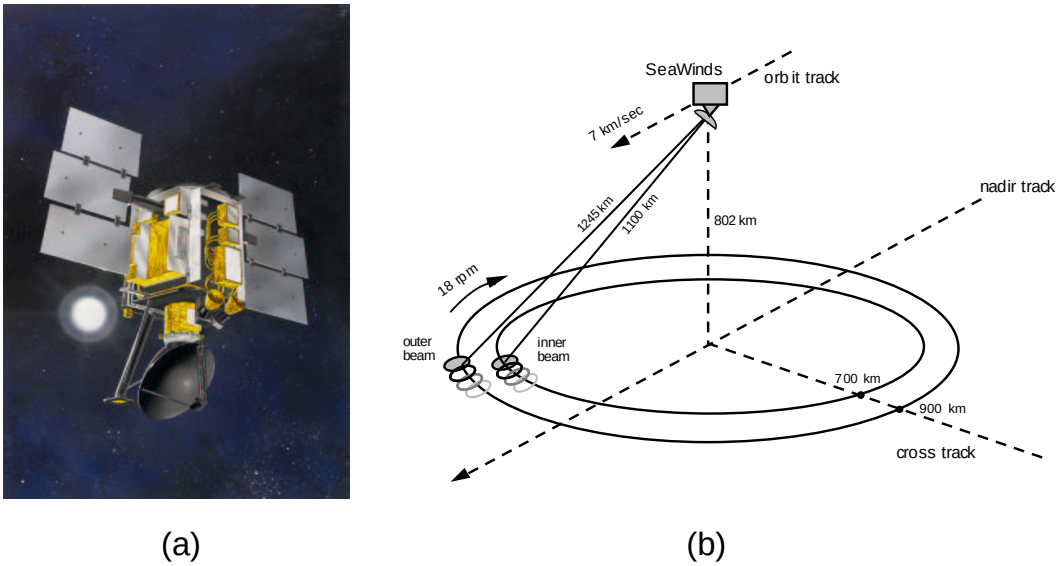

Figure 4.5: (a) The *SeaWinds* instrument aboard the QuikSCAT spacecraft which was launched in June, 1999. (b) The overall geometry of the *SeaWinds* measurement showing both the inner and outer antenna beam footprints.

with the *SeaWinds* antenna footprints is approximately 25 km (azimuth) by 35 km (elevation). In order to meet the along-track continuity constraint with a 30% overlap, a rotation rate of 18 rpm is selected [see Eq. (3.6)]. The antenna and measurement geometry parameters are summarized in Table 4.2.

Figure 4.6 depicts the basic design of the SeaWinds radar electronics and shows the transmit, receive, and processing functions. Upon command from the timing controller, the transmitter issues a 1.5 ms duration Ku-Band pulse. Available Ku-Band amplifier technology limits the peak power of the pulse to 110 Watts (an issue of significance in this and the following chapters). The pulse is routed to either the inner or the outer beam through an RF rotary joint to the spinning section of the antenna assembly.

The echo return is likewise directed to the receiver where it is amplified, downconverted, and detected. Details of the transmit pulse and echo detection timing are shown in Fig. 4.7. The transmit events occur every 5.4 ms and alternate

Table 4.2: *SeaWinds* beam geometry and antenna parameters.

Parameter	Inner Beam	Outer Beam
Polarization	H	V
Elevation Angle	40°	46°
Surface Incidence Angle	47°	55°
Slant Range	1100 km	1245 km
3 dB Beam Widths (az × el)	1.8° × 1.6°	1.7° × 1.4°
Two-Way 3 dB Footprint Dimensions (az × el)	24 × 31 km	26 × 36 km
Peak Gain	38.5 dBi	39 dBi
Rotation Rate	18 rpm	
Along Track Spacing	22 km	22 km
Along Scan Spacing	15 km	19 km

between the inner and outer beams. This produces a PRF of 92.5 Hz on each beam individually and 185 Hz overall. The range gate length (or signal sampling interval) is approximately 2 ms long. During this time, both the signal+noise and noise-only measurements are made. The PRF was selected to insure that adequate surface sampling is achieved (see Section 3.1.3), and that the strong nadir return arrives outside the sampling interval (see Section 3.4.2). A summary list of the key radar parameters is given in Table 4.3.

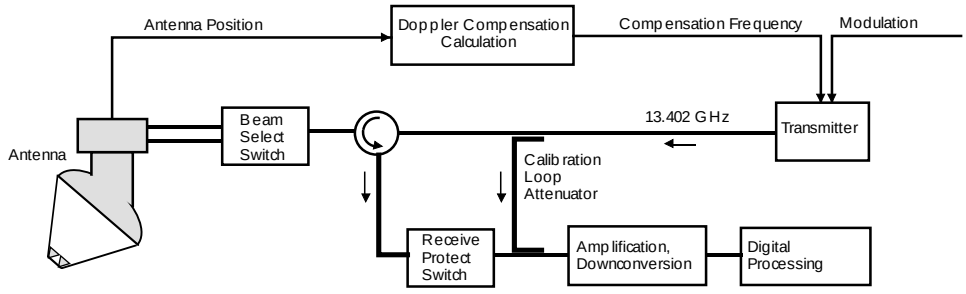

Figure 4.6: Diagram of the *SeaWinds* radar electronics showing transmit, receive, Doppler compensation, and calibration loop functions.

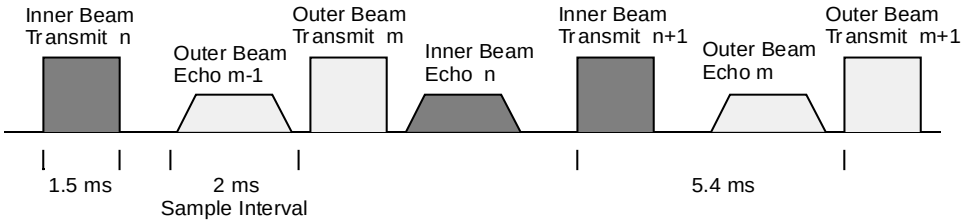

Figure 4.7: Diagram showing *SeaWinds* radar timing. The dark shaded rectangles and trapezoids are transmit pulse and receive echo events which occur on the inner beam. The light shaded areas are the same events which occur for the outer beam.

Table 4.3: *SeaWinds* radar electronics and timing parameters

Parameter	Value
Transmit Frequency	13.402 GHz
Transmit Power	110 Watts
Transmit PRF	186 Hz (93 Hz each beam)
Transmit Pulse Length	1.5 ms
Receive Gate Length	2.0 ms
Receive Gate Delay	7.3 ms (inner beam), 8.3 ms (outer beam)
System Noise Temperature	740°K

Due to the motion of the satellite relative to the Earth, a Doppler shift between ± 500 kHz is imparted to the echo return signal. When the antenna is pointing forward or behind relative to the spacecraft motion, the Doppler shift is at a maximum or minimum. When the antenna is scanned perpendicular to the spacecraft ground-track, the shift is near zero. In the *SeaWinds* design, the Doppler shift is pre-compensated by tuning the transmit carrier frequency to 13.402 GHz minus f_{dop}, where f_{dop} is the expected frequency shift to be imparted to the return signal (see Fig. 4.6). The compensation frequency is computed by the SeaWinds on-board processor using the measured antenna position, orbit location, spacecraft velocity, and Earth rotation. Pre-compensating the transmit pulse for Doppler shift produces an echo signal that always occurs at the same center frequency, simplifying the RF downconversion and detector electronics.

An important feature of any scatterometer system is the accurate calibration of the transmit power and receiver gain [80]. In the SeaWinds instrument design, these parameters are measured simultaneously by periodically injecting the transmit pulse, attenuated by a known amount, into the receiver. To avoid corruption by spurious leakage power during a "loop-back" calibration event, a high loss receive protect switch is enabled.

4.2.2 K_{pc} Trade-Offs for the Beam-Limited *SeaWinds* Design

With the high-level system parameters decided, the next major design consideration for a beamwidth-limited system is the identification of a pulse modulation which minimizes the value of K_{pc}. Here, the framework derived in Section 4.1 is applied to obtain optimum signal processing parameters for the specific case of the *SeaWinds* scatterometer.

Modulation Format Selection

The signal processing for the initial beamwidth-limited version of the *SeaWinds* design is the same as that shown in Fig. 4.1. In general, the *SeaWinds* hardware is flexible enough to implement any pulse modulation scheme. In Section 4.1, it was shown that pseudo-random phase modulation provides measurement accuracy performance better than a simple interrupted CW pulse, and yet still utilizes a relative small bandwidth. For this reason, pseudo-random phase modulation was selected for the beamwidth-limited version of the *SeaWinds* instrument.

Thus far in this dissertation, only *binary* phase modulation, where the phase is toggled randomly between 0° and 180°, has been considered. This format was assumed in generating Fig. 3.9 and in the calculation of the values in Table 4.1. Nearly identical K_{pc} enhancement results can be obtained with *quadrature* phase modulation, where the phase is toggled randomly between 0°, 90°, 180°, 270°. Because the phase transitions are less abrupt, quadrature phase modulation leads to lower spectral sidelobes in the signal spectrum, and thus is somewhat more desirable than binary schemes. A specific form of quadrature modulation known as multiple

phase-shift keying (MSK), widely used in communications applications, was selected for use with the beamwidth-limited version of the *SeaWinds* scatterometer. The characteristics and performance of the MSK modulation approach are addressed in the following subsections.

Relationship Between Signal+Noise Bandwidth and MSK Modulation Bandwidth

With the modulation scheme chosen, the remaining design decisions necessary to optimize measurement accuracy performance are the selection of a modulation bandwidth, B_{msk}, a signal+noise channel bandwidth, B_r, and a noise-only channel bandwidth, B_n. The spectrum of the MSK modulation transmit signal is given by [38]

$$S_{msk}(\omega) = 16\pi^2 E_t T_b \left[\frac{\cos T_b\omega}{4\tau_c^2\omega^2 - \pi^2}\right]^2, \tag{4.30}$$

where E_t is the total energy in the transmit pulse and τ_c is the modulation "chip" period. The 3 dB bandwidth of the transmit pulse, B_{msk}, is approximately given by

$$B_{msk} = \frac{0.6}{\tau_c}. \tag{4.31}$$

The spectrum of the echo return, $E(\omega)$, is somewhat different from that of the transmit pulse. The spectrum of the echo is a result of the interaction of the transmit signal with the ocean surface over the illuminated footprint. The echo energy spectrum is a summation of replicas of the transmit energy spectrum weighted by the antenna pattern and shifted by the Doppler frequency. The echo return spectrum can be written as a frequency domain convolution of the transmit spectrum and the footprint Doppler spectrum, $D(\omega)$,

$$E(\omega) = S_{msk}(\omega) * D(\omega), \tag{4.32}$$

where the Doppler spectrum represents the degree to which the transmit signal is spread in frequency due to the Doppler shift encountered over the illuminated area.

Figure 4.8 is a graphical example of how the echo spectrum is formed. Here, the transmit spectrum was computed from Eq. (4.30) assuming $B_{msk} = 40$ kHz. The

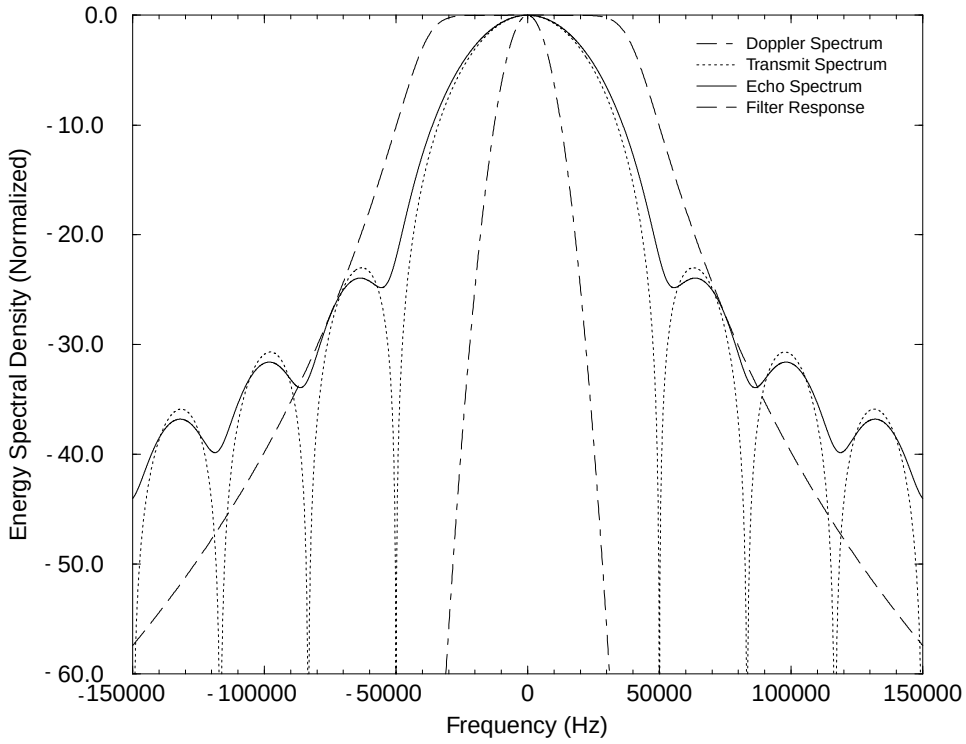

Figure 4.8: Sample plot of transmit spectrum ($B_{msk} = 40$ kHz), the Doppler spectrum associated with the *SeaWinds* antenna footprint, and the resulting echo return spectrum. Also plotted, for comparison, is a sample signal+noise filter response where $B_r = 80$ kHz.

Doppler spectrum shown is for the *SeaWinds* footprint parameters given in Table 4.2, and has a 3 dB bandwidth of approximately 10 kHz. The resulting baseband echo spectrum was computed from Eq. (4.32). All spectra were normalized to a peak value of unity. Note that for the case shown, and indeed in all cases where $B_{msk} > B_{dop}$, the transmit spectrum is the dominant factor in determining the bandwidth of the echo return.

The signal+noise filter bandwidth, B_r, must be sufficiently wide to accommodate the echo return spectrum, yet as narrow as possible to minimize the amount of thermal noise passed. In the *SeaWinds* design process, two metrics are employed to assess the performance of the signal+noise filter: the fraction of the echo energy passed by the filter, and the Doppler compensation error. The fraction of the echo

energy passed, ρ_E, is given by

$$\rho_E = \frac{\int |H_r(\omega)|^2 E(\omega)\ d\omega}{\int E(\omega)\ d\omega}, \tag{4.33}$$

where $|H_r(\omega)|^2$ is the magnitude response of the signal+noise filter. The Doppler compensation error is caused by inexact pre-compensation of the transmit carrier for echo Doppler shift. Nominally, the Doppler shift imparted to the return signal is perfectly pre-compensated and the echo spectrum is centered in the signal+noise filter. In reality, antenna position uncertainty and spacecraft attitude uncertainty lead to errors in Doppler tracking. The resultant error in detecting the echo energy, Δ_E, is given by

$$\Delta_E = \int |H_r(\omega)|^2 E(\omega)\ d\omega - \int |H_r(\omega)|^2 E(\omega - \omega_{err})\ d\omega, \tag{4.34}$$

where ω_{err} is the error associated with an inexact nulling of the Doppler center frequency, leading to an offset in the baseband echo spectrum. The filter bandwidth must be sufficiently wide to accommodate this "jitter" in the echo center frequency, without producing excessive error.

In examining the performance of the signal+noise filter, "filter overhead" is defined as $B_r - B_{msk}$, or the additional bandwidth of the filter over the 3 dB bandwidth of the transmit pulse. In Figs. 4.9 and 4.10, ρ_E and Δ_E are calculated for five different values of B_{msk} as a function of filter overhead. Note that in the case of $B_{msk} = 0$ kHz, the transmit signal is the unmodulated carrier and the echo spectrum is the same as the Doppler spectrum. The filter magnitude response is a 5th order Butterworth type, an example of which for $B_r = 80$ kHz is shown in Figure 4.8. In computing Δ_E, the Doppler compensation error was fixed at 10 kHz ($\omega_{err} = 2\pi \times 10^4$ rad/sec), the anticipated maximum value for the SeaWinds design.

From Figs. 4.9 and 4.10, a relationship between the transmitted B_{msk} and the required B_r can be determined. To insure that a sufficient fraction of the echo energy is passed, it is required that the filter be wide enough to pass 90% of the echo energy. To minimize frequency jitter induced errors in the measurement of echo return energy, it is required that $\Delta_E < 0.15$ dB. Applying these criteria to Figs. 4.9

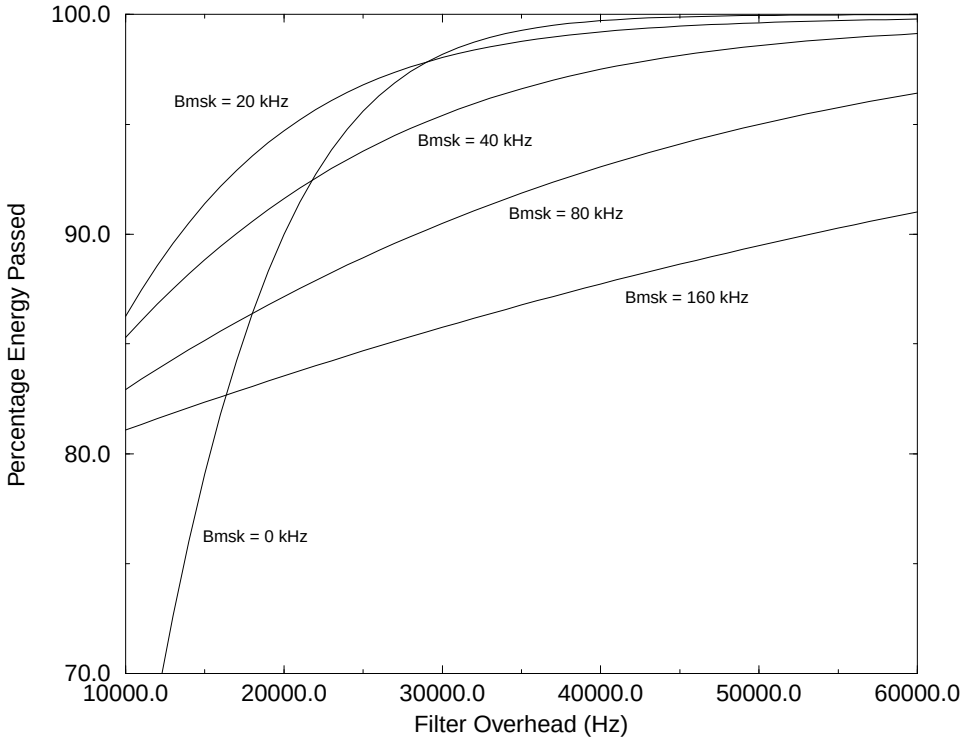

Figure 4.9: Plot of the percentage of echo energy passed, ρ_E, by the signal+noise band-pass filtering operation for different values of B_{msk} and filter "overhead" ($B_r - B_{msk}$).

and 4.10, it is observed that they are satisfied for a filter overhead of between 30 kHz and 50 kHz, depending on which B_{msk} is examined; the Doppler induced error being the primary factor for low values of B_{msk} and the percentage energy requirement being more important for large values of B_{msk}. In trade-off analyses to find the optimum modulation bandwidth, it is useful to have a generalized relationship between B_{msk} and B_r. Such a relationship is:

$$B_r = B_{msk} + 40 \text{ kHz}. \tag{4.35}$$

Thus, the bandwidth of the signal+noise filter is sized to be 40 kHz larger than the 3 dB bandwidth of the transmit pulse spectrum.

The role of the noise-only filter is to provide a separate measurement so that the thermal noise component can be subtracted from the signal+noise. As discussed in

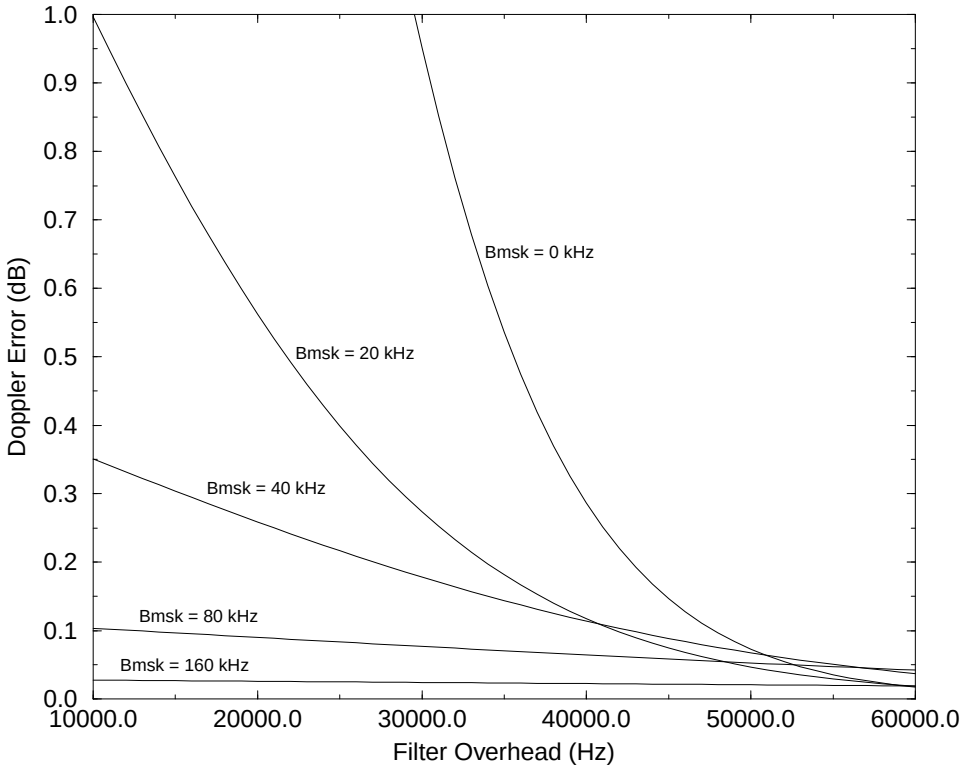

Figure 4.10: Plot of the Doppler compensation error, Δ_E, in dB for different values of B_{msk} and filter "overhead" $(B_r - B_{msk})$.

Section 3.3.1, the contribution to K_{pc} due to the noise-only measurement is minimized for $B_n >> B_r$. For the range of B_{msk} and B_r considered in the SeaWinds trade-off analyses ($B_{msk} = 0$ to 160 kHz, $B_r = 40$ to 200 kHz), a noise-only filter bandwidth of $B_n \geq 1$ MHz meets this condition. In general, however, the precise selection of the noise-only filter parameters is a less critical one than the selection of the signal+noise filter parameters.

Selection of B_{msk} for Optimization of K_{pc}

Given B_n and the relationship between B_{msk} and B_r, the value of B_{msk} which provides optimum measurement variance performance is considered. Recall that K_{pc} is given by

$$K_{pc} = \left(A + \frac{B}{\mathrm{SNR}} + \frac{C}{\mathrm{SNR}^2} \right)^{\frac{1}{2}}, \tag{4.36}$$

where, for this case,

$$\text{SNR} = \frac{E_s}{(T_2 - T_1)N_o B_r}. \tag{4.37}$$

The parameters A, B, and C can be evaluated using Eqs. (4.19) and (4.20). These equations are computed for the example case of $B_n = 10$ MHz, $B_{msk} = 40$ kHz and $B_r = 80$ kHz in Fig. 4.11. Note that, as predicted in Section 4.1.5, the value of the A term varies with antenna azimuth angle for the pseudo-random phase modulated transmit pulse. The terms B and C, however, are primarily dependent on the noise statistics which do not vary with azimuth angle.

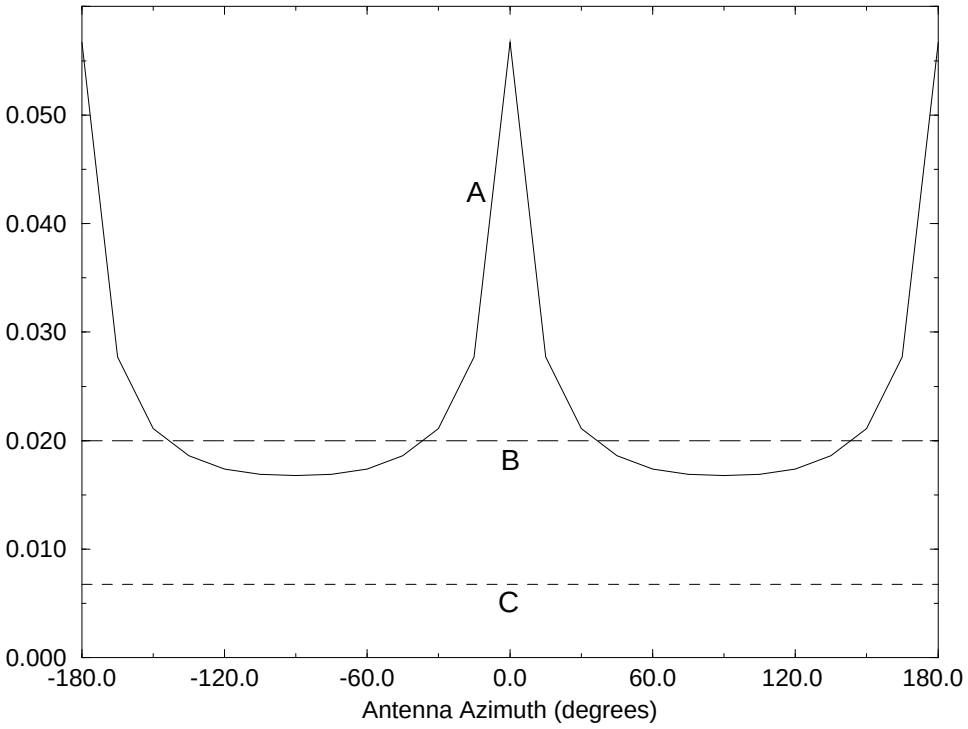

Figure 4.11: Sample values of the K_{pc} coefficients A, B, and C, calculated for B_{msk} = 40 kHz, $B_r = 80$ kHz, and $B_n = 1$ MHz.

In general, as the bandwidths B_{msk} and B_r increase, the values of A, B, and C decrease. This is because the wider bandwidth signals produce a narrower correlation function, and, consequently, lower variance estimations of the signal+noise

and noise-only energies. As these bandwidths go up, however, the SNR associated with the measurement goes down via Eq. (4.37). From Eq. (4.36), it is observed that a decreasing SNR forces K_{pc} to go up. Consequently there is a trade-off associated with selecting a modulation bandwidth which gives the lowest value of A, B, and C, without generating too low of an SNR. This trade-off is complicated by the fact that the design optimization must be valid for a wide range of ocean surface σ^o values. In Table 4.4, the values of σ^o for a range of ocean surface conditions and the resulting echo return energies calculated from the *SeaWinds* design parameters are shown.

Table 4.4: Expected *SeaWinds* echo energies for low (3 m/s), medium (8 m/s) and high (20 m/s) ocean wind speeds.

	Inner Beam		Outer Beam	
Wind Speed	σ^0 (dB)	E_s (dBJoules)	σ^0 (dB)	E_s (dBJoules)
3 m/s	-32	-184	-27	-179
8 m/s	-23	-175	-20	-172
20 m/s	-14	-167	-14	-167

Utilizing the values in Table 4.4 and Eqs. (4.36) and (4.37), K_{pc} is calculated as a function of antenna azimuth angle for low, medium, and high wind speed conditions and for a range of values of B_{msk} and displayed in Fig. 4.12. Note that for high wind speeds (20 m/s) where SNR is inherently high, increasing B_{msk} up to 160 kHz leads to a monotonic reduction in K_{pc} for both the *SeaWinds* inner and outer beams. For low wind speeds (3 m/s), however, increasing B_{msk} leads to a higher value of K_{pc} on the inner beam as the SNR is reduced due to the larger value of B_r that is required. For the beamwidth-limited version of the *SeaWinds* design, values of $B_{msk} = 40$ kHz and $B_r = 80$ kHz were chosen to yield the best overall performance at all wind speeds.

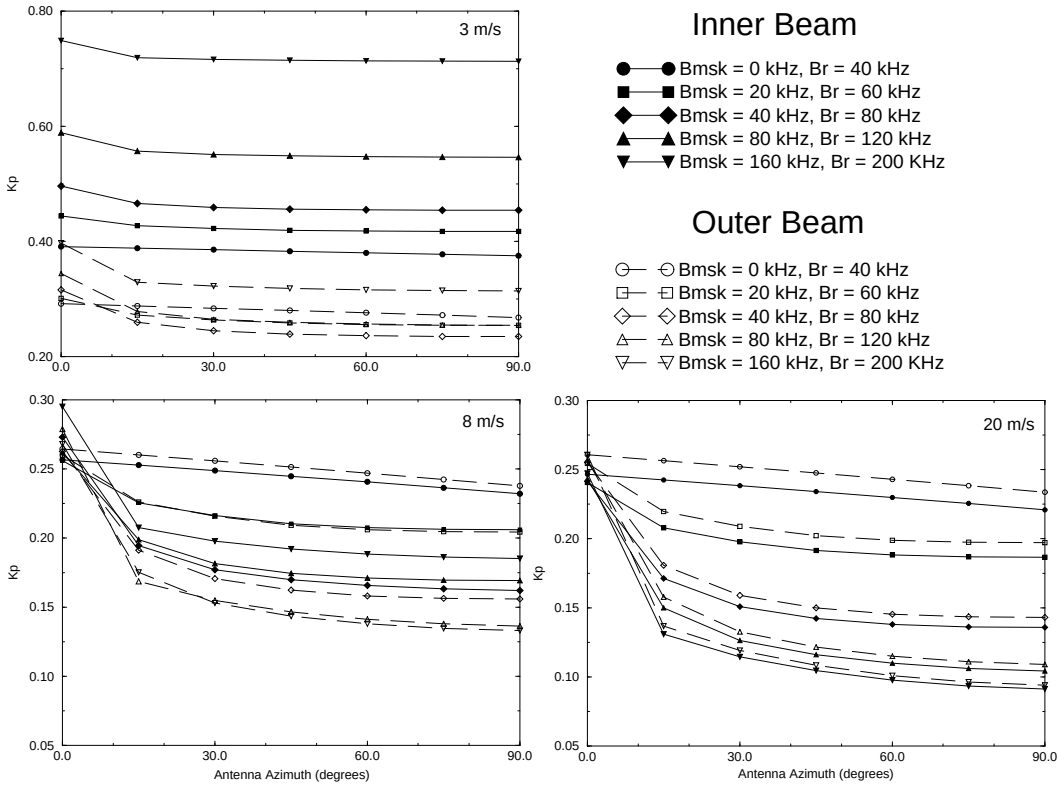

Figure 4.12: Calculated values of K_{pc} for three wind speeds (3, 8, and 20 m/s) shown as a function of antenna azimuth angle and for different B_{msk} and B_r combinations.

4.3 Conclusions Concerning Beam-Limited Scatterometer Design

In this chapter, the trade-offs involved in the design of beamwidth-limited scatterometer systems have been addressed, and a new signal processing framework for the utilization of transmit modulation has been developed. As an illustration of this methodology, the tradeoffs performed for an initial design version of the *SeaWinds* scatterometer have also been presented. The major conclusion from both the theory and the design example is that by careful selection of the transmit modulation, the measurement error performance of beamwidth-limited systems can be optimized. Using this novel technique, the limitations imposed by the short integration times associated with pencil-beam systems may be overcome.

Chapter 5

Real-Aperture Pencil-Beam Scatterometer Systems

In the previous chapter the beamwidth-limited resolution approach, which represents the simplest pencil-beam scatterometer design, was treated. In this chapter real-aperture approaches which "slice" the antenna footprint into smaller resolution cells in either the range or Doppler dimension are considered. These techniques represent a medium level of complexity in pencil-beam scatterometer design in that they improve upon the resolution capability of beamwidth-limited systems, but do not obtain the fine two-dimensional resolution achieved with the synthetic-aperture technique discussed in Chapter 7.

To illustrate the utility of the real-aperture concepts developed in this chapter, the real-world design example of the *SeaWinds* scatterometer is once again invoked. Based in part on the arguments presented here, NASA decided to change the design of *SeaWinds* from a beamwidth-limited system to a real-aperture system. This was the design version that was ultimately launched on the *QuikSCAT* satellite in June 1999. Many of the concepts and equations developed by the author here were adopted for use by the SeaWinds project. Although discussed primarily in the context of *SeaWinds*, these contributions apply to the analysis of any real-aperture pencil-beam scatterometer system.

5.1 Desire for Higher Resolution Scatterometer Techniques

Although the resolution achieved with beamwidth-limited designs is adequate for measuring large scale (> 25 km) wind and land features, many geophysical applications benefit from finer spatial resolution. These include the study of mesoscale

wind features, such as coastal zone winds and hurricanes; cryospheric phenomena, such as sea ice extent and the Greenland ice sheet; and terrestrial processes, such as rain forest depletion and soil moisture monitoring.

A technique which has been demonstrated to significantly improve the resolution, and hence utility, of scatterometer measurements is *enhanced resolution imaging* (ERI). With ERI, multiple, overlapping scatterometer measurements from the same region are combined to solve for backscatter images that have higher spatial resolution than the original measurements. Examples of ERI algorithms that have been successfully employed to achieve resolution enhancement include Backus-Gilbert inversion and scatterometer image reconstruction and filtering (SIRF) [13, 49].

As observed with the SIRF algorithm, the practical resolution achievable with ERI is roughly equivalent to the *narrowest* dimension of the backscatter measurement cell. For example, the beamwidth-limited version of the *SeaWinds* instrument has an azimuth resolution of 25 km (see Table 4.2). By employing either range or Doppler resolution techniques, however, a resolution "slice" is created through the footprint, and a resolution cell results which is much narrower in one dimension (see Section 3.2.3). For a *SeaWinds*-class system, the narrow dimension of such a slice is much smaller than 25 km, and consequently would allow a dramatic improvement in resolution when ERI is employed. This improvement in resolution must be traded-off against the increased measurement noise inherent to smaller measurement cells. In the following sections, the issues and tradeoffs associated with modifying the original beamwidth-limited version of the *SeaWinds* instrument to yield higher resolution backscatter measurements are addressed in detail.

5.2 Doppler vs. Range Discrimination for the *SeaWinds* System

In this section, options for improving the *SeaWinds* spatial resolution are examined. The approximate dimensions of the antenna two-way 3 dB footprint contour, along with the associated two-way iso-range and iso-Doppler lines are conceptually illustrated in Fig. 5.1. Two representative cases are shown: the case where the beam is scanned to an azimuth angle of 0° (beam looking in the direction of spacecraft

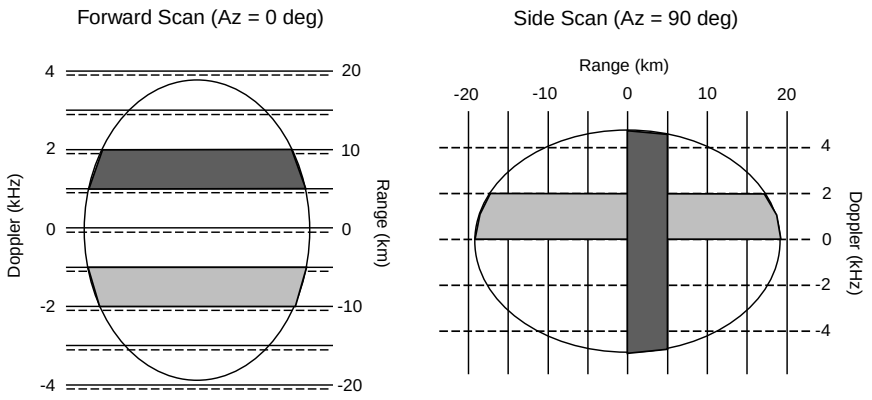

Figure 5.1: Conceptual diagram of *SeaWinds* 3-dB antenna footprint projected on the surface (oval) with two-way iso-range (solid) and iso-Doppler (dashed) contours. Shaded areas illustrate range-filtered (dark) and Doppler-filtered (light) resolution elements.

motion), and the case where the beam is scanned to an azimuth of 90° (beam looking perpendicular to spacecraft motion). Note that for the 0° azimuth case, the iso-range and iso-Doppler lines are approximately parallel, whereas in the 90° case they are nearly perpendicular. Other azimuth angles yield various intermediate states of these two cases, with the range and Doppler lines slanting with respect to each other.

Ideally, a processing scheme which resolves the footprint in two dimensions, such as the periodic pulse train discussed in Section 3.2.3, is desired. This approach yields the highest possible resolution, and would effectively make the scatterometer a conically-scanning SAR system (as discussed in Chapter 7). Unfortunately, the ambiguity rejection constraint required for two-dimensional resolution can not be satisfied with the *SeaWinds* instrument parameters. As an alternative, simple range filtering or simple Doppler filtering, which form spatial slices through the antenna footprint, are considered to improve the resolution in one dimension. Idealized slices, formed either by range or Doppler discrimination, are illustrated in Fig. 5.1. As discussed in Section 5.1, the sharpening of resolution in at least one dimension is of benefit, particularly for land and ice images constructed with ERI. To determine whether range or Doppler filtering should be employed for *SeaWinds*, two issues are

considered: the backscatter measurement variance and the geometrical orientation of the resultant σ^o cells.

The measurement variance tradeoff can be addressed by calculating the number of independent looks achieved with either the range or Doppler resolution approach (see Section 3.3.1). In the Doppler filtering case, the maximum number of "looks" available is related to the Doppler frequency resolution achieved with the transmit signal. For the selected *SeaWinds* timing, the maximum integration time on each scene is 1.5 ms, implying a best Doppler resolution of $1/(1.5 \text{ ms}) = 666$ Hz. Given that the total Doppler bandwidth of the illuminated region is about 10 kHz, the footprint could theoretically be resolved into as many as $10,000 \div 666 = 15$ separate elements, each constituting one independent look at the surface. If the footprint is equally divided into four resolution slices, each slice would thus contain the equivalent of 3.75 independent looks, corresponding to a normalized measurement standard deviation of 52% ($1/\sqrt{3.75} = 0.52$) of the actual σ^o value. Measurement variance can not be further reduced without improving the Doppler resolution by lengthening the transmit pulse, which is not allowed by the *SeaWinds* timing constraints.

In the range filtering case, however, the inherent resolution is a function of the bandwidth of the modulated transmit pulse. If the transmit pulse is modulated with a linear chirp at a rate of 250 kHz/ms, the resulting pulse has a bandwidth of 375 kHz, corresponding to a time delay resolution of $1/(375 \text{ kHz}) = 2.7$ μs. This in turn corresponds to a surface distance resolution of about 0.7 km for the outer beam. If the 36 km long outer beam footprint is divided equally into four 9 km slices, this implies $9 \div 0.7 = 12.86$ looks per slice, or a measurement standard deviation of 28% ($1/\sqrt{12.86} = 0.28$) of the true σ^o value. If SNR is sufficiently high, the measurement variance can be further improved in the range filtering case by increasing the bandwidth of the transmitted pulse. The flexibility to improve the measurement accuracy of the slices, and consequently the accuracy of geophysical products such as winds and surface images, by adjusting the transmit modulation bandwidth is a key advantage of the range filtering approach.

A rough, intuitive assessment of the comparative wind performance for different modulation approaches may be made by considering the variance when all backscatter measurements are combined in the wind retrieval. For wind estimates at 25 km resolution, all σ^o slices from all azimuth directions which fall in a 25 km box or "wind vector cell" on the ocean surface are used in the wind retrieval. If each footprint is divided into four slices, the *SeaWinds* PRF and scan rate dictates that there are, on average, about 40 slices available for each wind measurement. In a simplified sense, the wind *speed* accuracy achievable can be estimated by considering the standard deviation that results when all forty σ^o measurements are averaged. For the Doppler resolution case discussed above, the effective combined standard deviation is thus 8% ($1/\sqrt{40 \times 3.75} = 0.08$) or, equivalently, 0.33 dB of the true value. For the range resolution case, the corresponding standard deviation is is 4% ($1/\sqrt{40 \times 12.86} = 0.04$) or 0.17 dB about the actual value. Measurements of high wind speed are most sensitive to errors in σ^o. For a 20 m/s wind, a 0.33 dB or 0.17 dB backscatter error translates into a 1.7 m/s or 0.9 m/s wind speed error respectively. Thus, the use of range filtering has the potential to improve wind performance by at least a factor of two over Doppler filtering for the original *SeaWinds* design.

A secondary consideration is the orientation of the σ^o slices. Because ERI algorithms utilize many overlapping σ^o measurements, possibly from multiple orbits, it is generally desirable to have the slices oriented at different angles so that resolution may be enhanced effectively in all directions. As shown in Fig. 5.1, this requirement favors range filtering because the orientation of the cells rotate with azimuth angle, as opposed to Doppler filtering where the cells are oriented roughly perpendicular with the direction of flight. Because of the above described advantages in measurement variance and cell orientation, the range discrimination approach was chosen for the real-aperture *SeaWinds* design ultimately adopted by NASA.

5.3 *SeaWinds* Range Filtering Approach

The final, real-aperture version of the *SeaWinds* instrument is identical to the initial beamwidth-limited design described in the previous chapter except for the

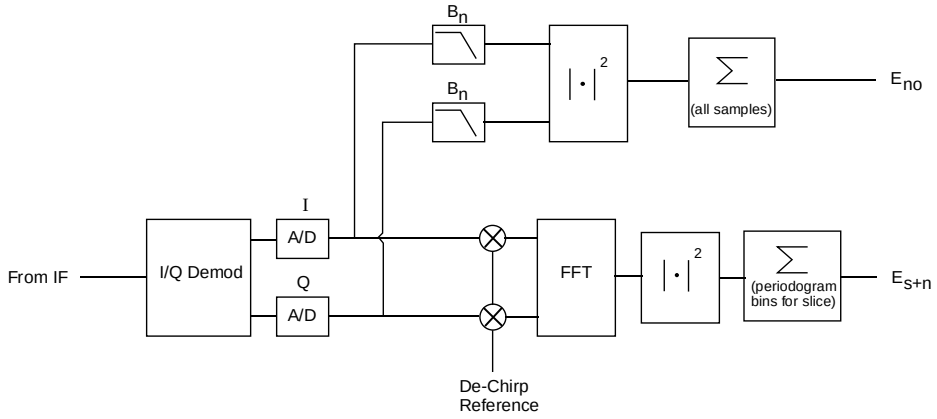

Figure 5.2: Functional diagram of *SeaWinds* digital range processing and "noise-only" processing. The range processing is achieve by multiplying by a chirped reference signal (or "de-ramping"), and then performing an FFT to extracted the range information from each region of the antenna footprint.

addition of range processing. Instead of an MSK modulated signal, a 1.5 ms FM linear chirped pulse is transmitted. In the receiver, the band-pass filter and square-law detection approach is replaced with a signal processing scheme capable of extracting the range information from the echo return. The new receiver implementation is shown in Fig. 5.2. After downconversion to baseband, the echo is digitally sampled. The total echo return, which is the sum of all the echo returns from scatterers across the illuminated region, is then digitally "deramped" by mixing with a chirped reference single. This operation effectively converts range delays into frequency shifts. To extract the range information, a DFT (implemented as an FFT) is performed on the deramped signal and a periodogram is formed by applying a magnitude squared operation. The periodogram bins are then summed into twelve range slice energy measurements to be telemetered to the ground. The deramp/FFT implementation has been extensively employed with altimeter systems (see [105]).

To illustrate further, Fig. 5.3 shows a conceptual plot of the deramped power spectral density (shaded region) and slice bandwidths. For the selected *SeaWinds* chirp rate of 250 kHz/ms, the deramped spectral density has a 3 dB bandwidth (B_{3dB}) of approximately 40 kHz. The returned energy for the qth slice, E_{s+n}^{q}, is formed

by summing adjacent periodogram bins over the slice bandwidth, B_s. For *SeaWinds* it was decided to construct σ^o cells which resolve the surface to approximately 7 km in the range dimension. For the given chirp rate, this corresponds to $B_s = 8.3$ kHz. This bandwidth is used for the ten innermost slices. The two outermost slices are termed "guard slices" and are assigned a somewhat larger bandwidth. The total bandwidth spanned by all twelve slices, B_e, is approximately 200 kHz, and is designed to capture the entire deramped echo spectrum. As in the beamwidth-limited design, a wide-band "noise-only" measurement, E_{no}, is made by passing the return echo and system noise through a filter with bandwidth $B_n = 1$ MHz, square-law detecting, and then integrating. This measurement is used in determining the thermal noise background component to E^q_{s+n} which must be subtracted off before σ^o can be estimated.

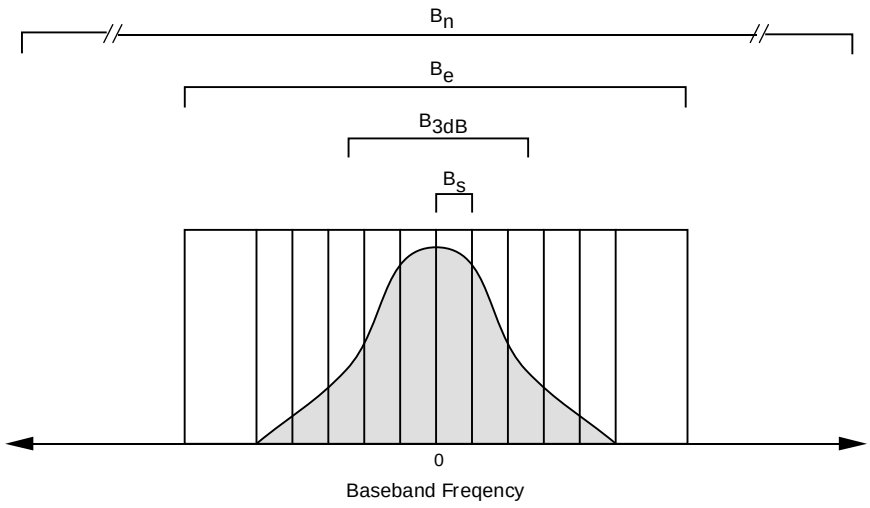

Figure 5.3: Conceptual diagram illustrating deramped echo spectrum (shaded), frequency "slices," and other bandwidths used in processing. The energy in the qth spectral slice is accumulated to form the measurement E^q_{s+n}.

5.4 Characterization of Measurement Accuracy for *SeaWinds* with Range Filtering

As described in Section 3.3, the estimation of σ^o is essentially a two-step process. First, an estimate of the thermal noise contribution in each slice, E^q_n, must

be subtracted from the signal+noise estimate in each slice to yield the signal-only energy, E_s^q:

$$E_s^q = E_{s+n}^q - E_n^q, \tag{5.1}$$

where E_n^q is obtained from E_{no} using the methods discussed in Section 4.1.1. Secondly, σ^o for each slice is then calculated by applying the calibration factor X^q

$$\sigma^o = \frac{E_s^q}{X^q}. \tag{5.2}$$

Here, X^q incorporates all instrumental and geometrical parameters necessary to define the relationship between the detected energy and the surface backscatter cross-section. The overall backscatter measurement accuracy is thus the combination of the uncertainties associated with determining E_s^q and X^q.

In general, achieving the desired measurement accuracy is more difficult with σ^o cells formed by "range slicing" than in the beamwidth-limited case, and requires the introduction of new formulations for the radar equation and backscatter measurement variance calculation. The following subsections provide the necessary analytical framework for addressing the issue of σ^o accuracy for the real-aperture version of *SeaWinds*, and address several of the trade-offs that must be conducted to optimize performance. First, a formulation for X^q and the associated calibration error are provided. Following this, an expression for the K_{pc} of the range-filtered case is presented.

5.4.1 Derivation of X^q for *SeaWinds* and Associated Calibration Errors

The first step in the calibration of the instrument involves the development of an expression for the parameter X^q. In deriving X^q, the radar signal is followed through its interaction with the surface and the subsequent echo signal processing.

The transmitted signal can be written as

$$T(t) = \sqrt{E_t} p(t) e^{j2\pi[f_c + f_{dc} + \frac{1}{2}\mu t]t}, \tag{5.3}$$

where t is time from transmit pulse onset, E_t is the total energy in transmit pulse, $p(t)$ is the transmit pulse power envelope such that $\int p^2(t) = 1$, f_c is the transmit carrier frequency, f_{dc} is the Doppler compensation frequency, and μ is the chirp rate.

The echo return from the surface can be treated as the summation of returns from many independent scattering "patches", each with a different range delay and Doppler shift (see Section 3.2.3). It is assumed that each patch is large relative to the correlation length of the surface, but sufficiently small so that the Doppler shift and slant range do not vary significantly over its dimensions. The echo return from the ith scattering patch is expressed as

$$R_i(t) = \xi_i \sqrt{\sigma_i^o} K B_i(t) e^{j2\pi \left\{ [f_c + f_{dc} + f_{d,i} + \frac{1}{2}\mu(t - t_{d,i})](t - t_{d,i}) + \phi_i \right\}}. \tag{5.4}$$

Here, σ_i^o is the normalized backscatter cross section at the scattering patch, ξ_i is a uni-variant Rayleigh random variable for the signal amplitude due to fading, ϕ_i is a uniform random variable (over 0 - 2π) for the random phase of the return from the patch, $f_{d,i}$ is the Doppler shift of the patch, and $t_{d,i}$ is the round trip flight time to the patch given by $t_{d,i} = 2r_i/c$ where r_i is the slant range to the patch.

The value K in Eq. (5.4) is defined such that

$$K^2 = \left(\frac{\lambda^2}{(4\pi)^3} \right) \left(\frac{E_t G_r G_p^2}{L_{sys}} \right), \tag{5.5}$$

where λ is the transmit wavelength, G_r is the receiver gain, G_p is the peak antenna gain, and L_{sys} is total two-way system loss. The echo return is windowed by the function $B_i(t)$

$$B_i(t) = p(t - t_{d,i}) \left(\frac{\delta A_i}{r_i^4} \right)^{\frac{1}{2}} [g_i(t) g_i(t - t_{d,i})]^{\frac{1}{2}}, \tag{5.6}$$

where δA_i is the area of the scattering patch, and $g_i(t)$ is the normalized antenna pattern gain in the direction of the ith scattering patch at time t. The term $g_i(t)g_i(t - t_{d,i})$ reflects the fact that the antenna gain is changing as a function of time as the antenna rotates.

The composite return over the entire footprint, $R(t)$, is given by

$$R(t) = \sum_{i \in \mathcal{F}} R_i(t), \tag{5.7}$$

where the summation is over all contiguous, unique patches in the illuminated region $\mathcal{F}$. In this analysis, discrete summation over the illuminated region, rather than the more conventional integral representation, is used for clarity and to reflect the

fact that X is evaluated numerically in practice. As with all numerical integrations, the size of δA_i and the extent of $\mathcal{F}$ are ultimately selected such that acceptable convergence is achieved.

At the receiver, the signal is downconverted and deramped by multiplying $R_i(t)$ with

$$M(t) = \exp\{-\pi\mu j(t - t_g)(t - t_g)\}, \tag{5.8}$$

where t_g is the reference delay, to yield

$$R_d(t) = R(t)M(t) = K\sum_{i\in\mathcal{F}} \xi_i\sqrt{\sigma_i^o}B_i(t)\exp\{2\pi j f_{b,i}t + j\psi_i\}. \tag{5.9}$$

Here, $f_{b,i}$ is the baseband frequency of the return from the ith patch and is given by

$$f_{b,i} = f_{d,i} + f_{dc} + \mu(t_g - t_{d,i}). \tag{5.10}$$

The new phase term ψ_i is a function of ϕ_i, but is still a random variable uniformly distributed over (0 - 2π). Examining Eq. (5.9) and Eq. (5.10) it is evident that the deramped echo is a composite of many scaled, windowed, single frequency tones with random phase. (Fig. 5.4 is provided to illustrate this summation over the scattering patches.) Each tonal frequency is determined by the range delay *and* Doppler shift associated with each scatterer. Note, then, that the processing does not represent pure range filtering because the iso-baseband frequency lines on the surface are somewhat tilted with respect to the iso-range lines, the magnitude of the tilt being a function of the chirp rate μ.

The deramped signal is digitally sampled and gated to form the sequence, $d[n]$

$$d[n] = K\sum_{i\in\mathcal{F}} \xi_i\sqrt{\sigma_i^o}G(t_n)B_i(t_n)\exp\{2\pi j f_{b,i}(t_n) + j\psi_i\}. \tag{5.11}$$

Here, the sample time, t_n, is equal to $t_{gs} + nT$, where t_{gs} is the time associated with the first sample input to the DFT, n is the sample number, and T is the sample period. $G(t)$ is a rectangular window function representing the range gate ($G = 1$ for signal "on" or $G = 0$ for signal "off").

To form the slice measurement E_s^q, a DFT is applied to the sample sequence, the Fourier domain sequence is magnitude squared, and then the appropriate

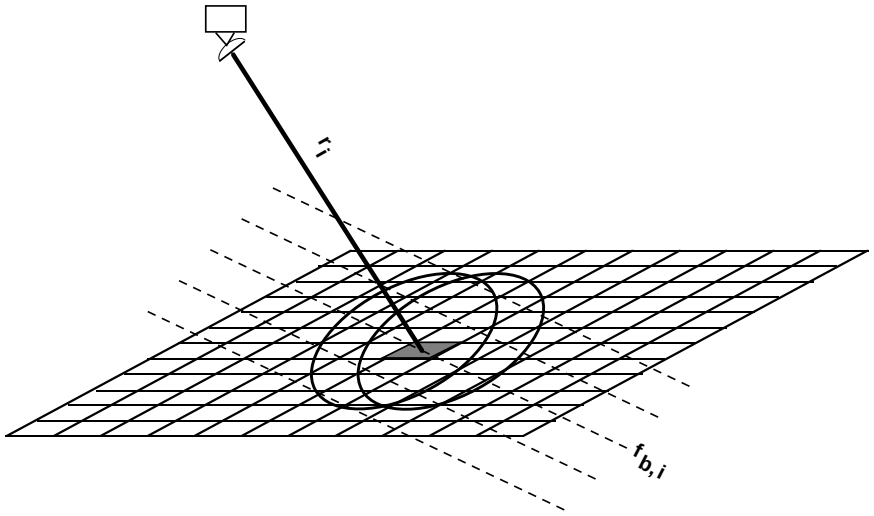

Figure 5.4: X parameter calculation geometry. Shaded region represents ith surface element with incremental area δA_i. Dotted lines represent lines of constant base-band frequency, with baseband frequency of ith element $f_{b,i}$. Offset ovals represent antenna footprint position at time of transmit and receive. Range from ith element to sensor is r_i.

periodogram bins are summed. Also, it is assumed that the backscatter cross section is constant over the slice to obtain

$$E_s^q = \sigma^o K^2 \sum_{k=k_s}^{k_e} \left| \sum_{n=0}^{N-1} \left[\sum_{i \in \mathcal{F}} \xi_i G(t_n) B_i(t_n) \exp\{2\pi j f_{b,i}(t_n) + j\psi_i\} \right] \exp\{-2\pi j \frac{kn}{N}\} \right|^2 , \tag{5.12}$$

where k_s and k_e are the start and end bin numbers (corresponding to the bounding frequencies from Fig. 5.3) of the qth slice and N is the total number of samples input to the DFT (i.e., the FFT size).

Because E_s^q is a random quantity, the expected value is taken to find X:

$$\mathcal{E}[P_s^q] = \sigma^o K^2 \sum_{k=k_s}^{k_e} \sum_{i \in \mathcal{F}} \left| \sum_{n=0}^{N-1} G(t_n) B_i(t_n) \exp\{2\pi j (f_{b,i} T - \frac{k}{N}) n\} \right|^2 , \tag{5.13}$$

where, to eliminate the random variables and reorder the summations, it is assumed that separate scattering patches are uncorrelated (i.e., that $\mathcal{E}[e^{j\psi_m} e^{-j\psi_n}] = 0$ for $m \neq n$). Referring to Eq. (5.2), it is concluded that

$$X^q = K^2 \sum_{k=k_s}^{k_e} \sum_{i \in \mathcal{F}} \left| \sum_{n=0}^{N-1} G(t_n) B_i(t_n) \exp\{2\pi j (f_{b,i} T - \frac{k}{N}) n\} \right|^2 . \tag{5.14}$$

Equation (5.14) is a general expression for X for a rotating antenna with digital range filtering.

Under certain conditions (which apply in the case of *SeaWinds*) the computation of X may be simplified somewhat. If the transmit pulse envelope is rectangular, we write

$$\begin{aligned} p(t) &= \frac{1}{\sqrt{T_p}} \quad \text{for} \quad t_{ps} \le t < t_{ps} + T_p \\ p(t) &= 0 \qquad\quad \text{otherwise,} \end{aligned} \tag{5.15}$$

where t_{ps} is the time of transmit pulse start. If it is further assumed that the antenna gain in the direction of a given surface patch is constant during the pulse period, then

$$B_i(t_n) = p(t_n - t_{d,i}) \left(\frac{\delta A_i}{r_i^4} \right)^{\frac{1}{2}} \left[g_i(t_{trs}) g_i(t_{rec}) \right]^{\frac{1}{2}}, \tag{5.16}$$

where $g_i(t_{trs})$ is the gain in the direction of the ith patch at the time of transmit, and $g_i(t_{rec})$ is the gain in the direction of the ith patch at the time of receive after the antenna has rotated during the pulse round-trip flight time $t_{d,i}$. The above two assumptions are equivalent to assuming that the echo return from a given scatterer is flat, and is not modulated by either the pulse envelope or the rotating antenna beam. The sampled signal values thus correspond to a rectangular window whose length is determined by the overlap between the delayed return pulse and the range gate window.

Employing Eqs. (5.15) and (5.16), Eq. (5.14) can be written as

$$X^q = \frac{K^2}{T_p} \sum_{k=k_s}^{k_e} \sum_{i \in \mathcal{F}} \left(\frac{\delta A_i g_i(t_{trs}) g_i(t_{rec})}{r_i^4} \right) \left| \sum_{n=n_{s,i}}^{n_{s,i}+N_{p,i}} \exp\{2\pi j (f_{b,i} T - \frac{k}{N}) n\} \right|^2 . \tag{5.17}$$

Here, $n_{s,i}$ is the sample in the sequence $d[n]$ associated with the leading edge of the gated echo from the ith patch. $N_{p,i}$ is the length of the echo from the ith patch (expressed in number of samples) captured by the range gate. $N_{p,i}$ is given by

$$N_{p,i} = \text{int} \left(T_p \sum_{n=0}^{N-1} p_r(t_n - t_{d,i}) G(t_n) \right). \tag{5.18}$$

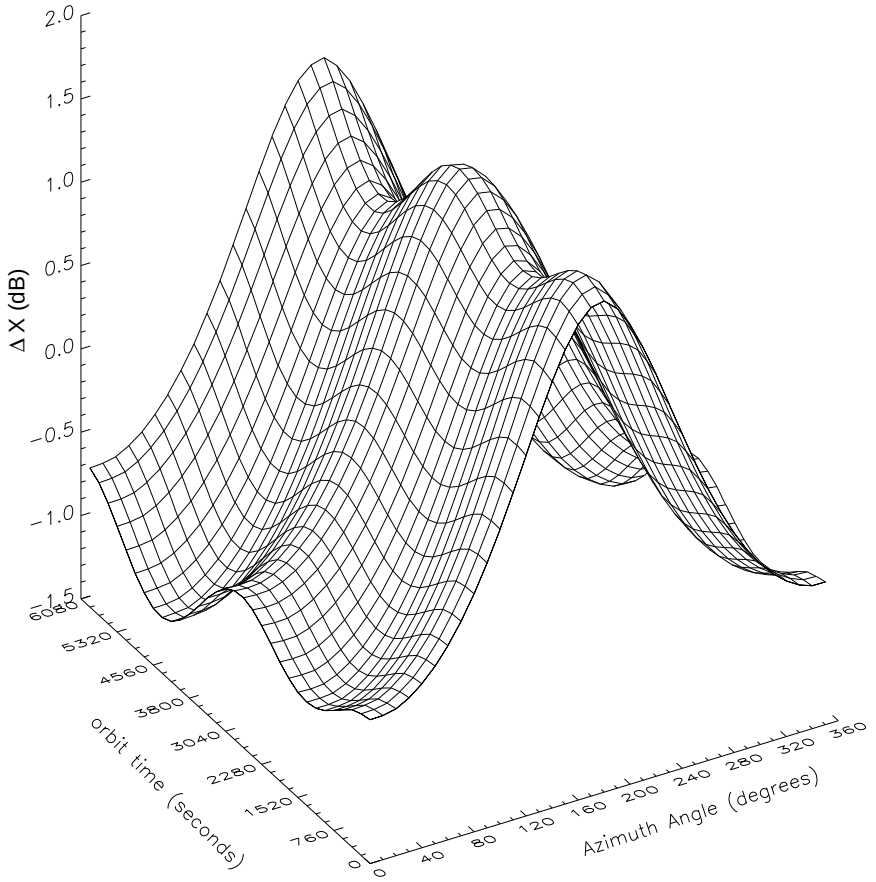

Figure 5.5: X parameter for example "slice" vs. orbit time (one complete orbit = 6080 seconds) and antenna scan azimuth angle. Here X has been normalized by its mean value.

It is convenient, particularly for the analysis of measurement variance, to define the DFT term in Eq. (5.17) as the function β, where

$$\beta(i,k) = \sum_{n=n_{s,i}}^{n_{s,i}+N_{p,i}} \exp\{2\pi j(f_{b,i}T - \frac{k}{N})n\}. \tag{5.19}$$

Evaluating Eq. (19) we have that

$$\beta(i,k) = \left(\frac{\exp[j\pi(N_{p,i}+2n_{s,i})(f_{b,i}T - \frac{k}{N})]}{\exp[j\pi(f_{b,i}T - \frac{k}{N})]}\right)\left(\frac{\sin[\pi N_{p,i}(f_{b,i}T - \frac{k}{N})]}{\sin[\pi(f_{b,i}T - \frac{k}{N})]}\right). \tag{5.20}$$

Note that because the complex phase term in $|\beta(i,k)|^2$ cancels, we can always sum from 0 to $N_{p,i}$ in the DFT regardless of the pulse position in the range gate. Equation

(5.17) then becomes,

$$X^q = \frac{K^2}{T_p} \sum_{i \in \mathcal{F}} \left\{ \left(\frac{\delta A_i g_i(t_{trs}) g_i(t_{rec})}{r_i^4} \right) \sum_{k=k_s}^{k_e} \left[\frac{\sin^2[\pi N_{p,i}(f_{b,i}T - \frac{k}{N})]}{\sin^2[\pi(f_{b,i}T - \frac{k}{N})]} \right] \right\}. \tag{5.21}$$

Using Eq. (5.21), X^q for a sample slice is plotted versus orbit position and antenna azimuth angle for the expected *QuikSCAT* orbit in Fig. 5.5. Note that the value of X varies significantly as a function of orbit position and azimuth. Despite the simplifications embodied in Eq. (5.21), X^q is still too computationally expensive to compute repeatedly for each individual pulse during ground data processing. Where the satellite orbit is very stable, as is expected for both the *QuikSCAT* and ADEOS-II spacecraft, X^q may be precomputed in tabular form which is then interpolated in azimuth and orbit position to obtain values for each pulse and slice [1].

Spatial Response Function (SRF) and Surface Sampling

It is insightful to view the X parameter as an integration of the instrument spatial response function (SRF) on the Earth's surface. The SRF can be constructed from Eq. (5.21) by taking the energy contribution to the slice from each scattering patch, and then normalizing by the area of the patch. Utilizing the notational convention established in Section 3.2.3,

$$|\chi(x_i, y_i)|^2 = \frac{K^2 g_i(t_{trs}) g_i(t_{rec})}{T_p r_i^4} \sum_{k=k_s}^{k_e} \left[\frac{\sin^2[\pi N_{p,i}(f_{b,i}T - \frac{k}{N})]}{\sin^2[\pi(f_{b,i}T - \frac{k}{N})]} \right], \tag{5.22}$$

where x_i and y_i are the surface position coordinates (in latitude and longitude, for instance) of the ith patch.

In Fig. 5.6 the SRF is displayed for two cases. In Fig. 5.6(a), the response for the beamwidth-limited case (no range filtering) is shown. In Fig. 5.6(b), the response for an example range slice of width 7 km (B_s =8.3 kHz for μ = 250 kHz/ms) is shown. In Fig. 5.6(b), note the sharp drop-off of the response function in the range direction. Such a sharp edge in the spatial response preserves high frequency information in the spatial frequency domain, and thus is a highly desirable property for enhanced resolution image reconstruction purposes. Note also the tilt in the orientation of the slice due to Doppler shift across the footprint. In Fig. 5.7, the surface

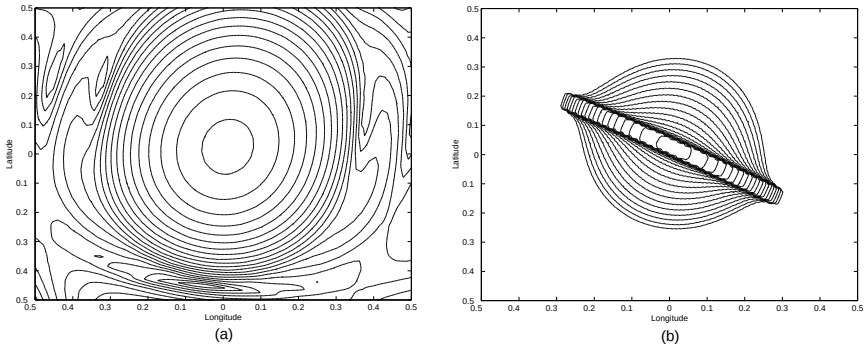

Figure 5.6: (a) Example σ^o cell spatial response for beamwidth-limited (no range filtering) case. (b) Example σ^o cell spatial response for center range slice. Contour spacing is at 1 dB intervals.

sampling achieved by the center eight slices for several consecutive pulses is shown. The eight center slices correspond approximately to the extent of the antenna main beam, and thus are the slices expected to yield measurements of sufficient accuracy. Here the σ^o cell outlines are delineated by plotting the approximate 3 dB contour of the slice response. As is evident, the measurements form a very dense sampling of the surface with many overlapping cells. This is another property favorable for ERI [13], as well as higher resolution wind retrieval.

Errors in X^q

Regardless of the care taken in deriving an expression for X^q, the calibration accuracy can only be as good as our knowledge of the various instrumental and geometric parameters comprising X^q. The parameter K in Eq. (5.21) embodies all radiometric components of X^q. Although there is potential for error in determining the value of K, this error is likely to be a constant bias for all measurements and should not contribute significantly to relative calibration error. This is because the determination of transmit power and receiver gain through periodic "loop-back" calibration measurements relies on a very stable, thermally controlled waveguide coupler. Furthermore, the antenna gain and system losses are likewise expected to be quite constant because of reliance on equally stable passive RF components. What can

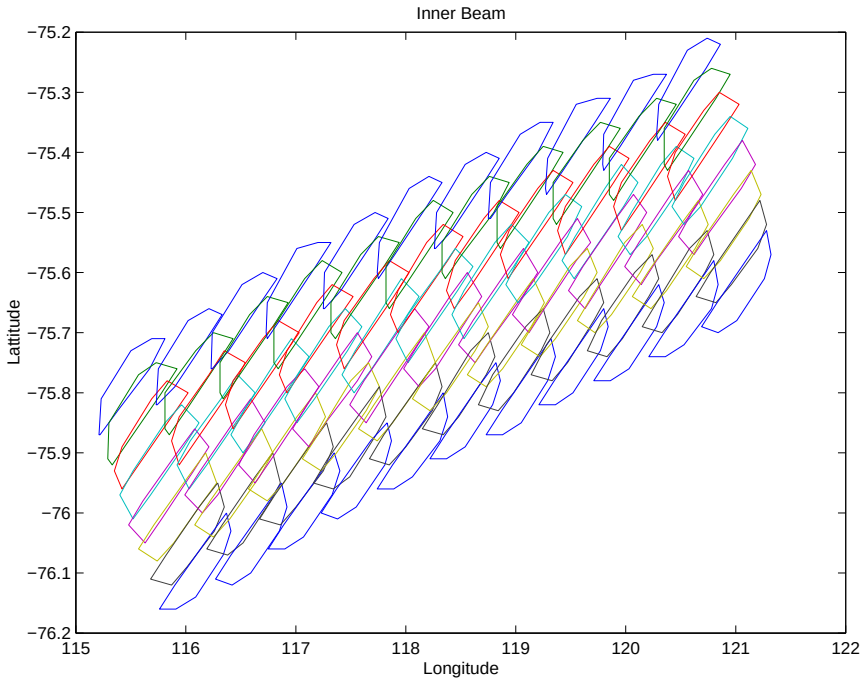

Figure 5.7: Center eight slice outlines for eleven consecutive transmit pulses for the inner antenna beam. Slice outlines are given by approximations to the 3 dB spatial response contour.

change on-orbit, however, is the measurement geometry, primarily through variations in the spacecraft attitude. In fact, attitude knowledge errors were observed to constitute the dominant source of relative calibration error for both the SEASAT-A and NSCAT scatterometers [40, 80].

As the attitude changes, the antenna pattern shifts with respect to the lines of constant baseband frequency on the Earth which form the slice edges. If the attitude change is unknown, an error in X^q, and consequently an error in σ^o, results. The magnitude of this error can be evaluated by taking the ratio of X^q calculated at the true attitude to the estimated attitude. In general, there is much more sensitivity to attitude variations which change the elevation angle than to those which change the azimuth angle. In Fig. 5.8, the error in σ^o is plotted vs. the error in elevation angle for different slices. The slices are numbered according to their position in the antenna beam: Slice 1 being an "inner" slice near the peak of the antenna pattern as

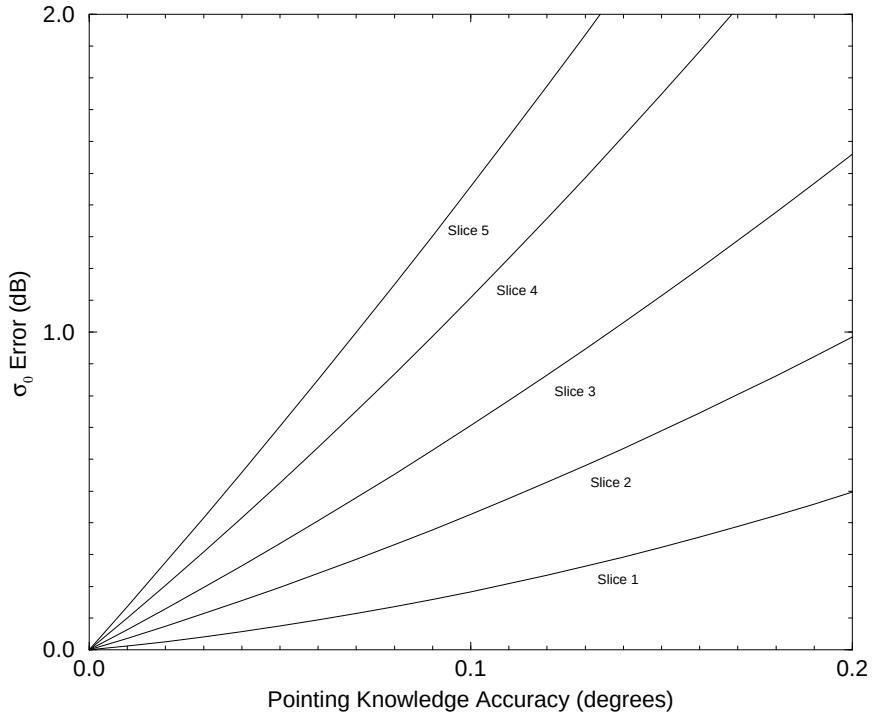

Figure 5.8: The σ^o calibration error (or, equivalently, X^q error) as a function of antenna pointing elevation angle knowledge accuracy. As labeled, "Slice 1" is the slice nearest the center of the frequency spectrum in Fig. 5.3, and "Slice 5" is on the right outer edge of the spectrum. Similar curves apply for the slices to the left side of the center of the spectrum.

projected on the surface, and Slice 5 an "outer" slice further down on the main beam. It is evident that slices near the peak where the antenna pattern is varying slowly are relatively insensitive to changes in pointing, whereas the outer slices where the pattern is changing rapidly are quite sensitive to pointing errors. Thus attitude knowledge becomes a key design consideration for improved resolution measurements that did not exist for the low resolution case. To achieve the desired calibration accuracy for all slices requires spacecraft pointing knowledge on the order of 0.02 degrees. Calibration goals can still be met on the inner slices, however, if less ambitious attitude control techniques are employed.

5.4.2 Measurement Variance of E_s^q

Measurements of the detected energy, E_s^q, are "noisy" due to radar fading and the presence of system thermal noise. The random variations in E_s^q place a fundamental limit on the instrument precision. For the selected range filtering implementation, however, measurement precision is optimized by careful selection of the transmit chirp rate and slice bandwidth. Similar to the analysis presented in previous chapters, the measurement variance is quantified by the parameter K_{pc}, where, in the case of range filtering,

$$K_{pc} = \frac{\sqrt{\mathrm{Var}[\sigma^o]}}{\mathcal{E}[\sigma^o]} = \frac{\sqrt{\mathrm{Var}[E_s]}}{\mathcal{E}[E_s]}, \tag{5.23}$$

where the slice index "q" has been dropped for notational simplicity. As discussed in previous chapters, a key goal of the signal processing design is the minimization of K_{pc}. From Eq. (5.1), the variance of P_s^q is

$$\mathrm{Var}[E_s] = \mathrm{Var}[E_{s+n}] + \mathrm{Var}[E_n] + 2(\mathcal{E}[E_{s+n}]\mathcal{E}[E_n] - \mathcal{E}[E_{s+n}E_n]). \tag{5.24}$$

As discussed in Chapters 3 and 4, when $B_n \gg B_s$, the second and third terms of Eq. (5.24) are much smaller than $\mathrm{Var}[E_{s+n}]$. For *SeaWinds*, because $B_n = 1$ MHz and $B_s = 8.3$ kHz, this condition applies and allows us to assume

$$K_p = \frac{\sqrt{\mathrm{Var}[E_{s+n}]}}{\mathcal{E}[E_s]}. \tag{5.25}$$

As discussed in Section 3.3.1, K_{pc} is written as

$$K_{pc} = \left(A + \frac{B}{SNR} + \frac{C}{SNR^2}\right)^{\frac{1}{2}}. \tag{5.26}$$

Where, for the range filtered case,

$$SNR = \frac{X^q \sigma^o}{T_g B_s N_0}. \tag{5.27}$$

Here T_g is the range gate length and N_0 is the noise floor power spectral density expressed in suitable units. The parameters A, B, and C for the range filtered case are derived in Appendix B, and are given by

$$A = \frac{1}{X^2} \sum_k \sum_h \sum_i \sum_l c_i^2 c_l^2 \beta(i,k)\beta^*(i,h)\beta^*(l,k)\beta(l,h)$$

$$B = \frac{2}{MN_\nu X}\sum_k\sum_h\sum_i c_i^2 \frac{e^{j\pi\frac{(k-h)}{N}(N_\nu+2n_\nu)}\sin(\pi\frac{(k-h)}{N}N_\nu)}{e^{j\pi\frac{(k-h)}{N}}\sin(\pi\frac{(k-h))}{N})}\beta(i,k)\beta^*(i,h)$$

$$C = \frac{1}{M^2N_\nu^2}\sum_k\sum_h\sum_{n=0}^{N_\nu-1}\sum_{m=0}^{N_\nu-1} e^{j\frac{2\pi}{N}(k-h)(m-n)}, \tag{5.28}$$

where $\beta(i,k)$ is as defined in Eq. (5.20), n_ν is the sample number in the series $d[n]$ corresponding to the opening of the range gate, N_ν is the duration (in number of samples) of the range gate open time, M is the total number of periodogram bins summed to form the slice, and c_i is defined as

$$c_i = \frac{K^2\delta A_i g_i(t_{trs})g_i(t_{rec})}{T_p r_i^4}. \tag{5.29}$$

Equation (5.28) can be approximated in a form more suited to intuitive analysis by making the following three assumptions: 1) the echo return is nearly stationary – i.e. the pulse length T_p (1.5 ms for *SeaWinds*) is much greater than the time it takes the fill the entire antenna beam (about 0.5 ms for *SeaWinds*), 2) $B_{3dB} \gg B_s$, and 3) $T_pB_s \gg 1$. Under these conditions, which apply for *SeaWinds*, A, B, and C are approximated by (see Appendix B)

$$\begin{aligned} A &= \frac{1}{B_sT_p} \\ B &= \frac{2}{B_sT_g} \\ C &= \frac{1}{B_sT_g}. \end{aligned} \tag{5.30}$$

Note that the K_{pc} for each slice is thus approximately the same as for a bandlimited white-noise process as discussed in Section 4.1.2. Again, the "A" term is the contribution to the variance due to radar signal fading alone, with B_sT_p approximating the number of independent looks associated with a given measurement slice. Assuming that T_p is fixed due to timing and sampling constraints, the term A can only be reduced by increasing the bandwidth of the slice measurement, B_s. The slice bandwidth is, in turn, related to the narrow (range) dimension of the slice spatial response on the surface and the transmit chirp rate. For the *SeaWinds* orbit altitude of 800 km,

$$B_s \approx W\sqrt{2\times10^{-5}\mu^2 + 0.14}, \tag{5.31}$$

where B_s is the slice bandwidth in kHz, μ is the transmit pulse chirp rate in kHz/ms, and W is the mean range dimension of the slice in kilometers. Thus, for a given slice dimension the bandwidth is increased by increasing the chirp rate. As discussed in Chapter 4, it is desirable to make B_s as large as possible for a scanning scatterometer to compensate for the relatively short integration times (as opposed to the longer dwell times available with non-scanning, fan-beam systems).

As in Chapter 4, a trade-off exists because as B_s is increased, SNR decreases [see Eq. (5.27)], and the second and third terms of Eq. (5.26) increases. In other words, the benefits of a larger measurement bandwidth must be balanced with the effects of allowing more thermal noise to enter the measurement. This analysis is governed by a consideration of the backscatter strength from ocean winds, which generally have lower SNR than land targets. A chirp rate of μ =250 kHz/ms was selected for *SeaWinds*. This strikes a balance in K_{pc} performance for high wind speeds, which have high inherent SNR ($>$ 6 dB) and hence benefit from larger measurement bandwidths, and low wind speeds, which have low SNR ($<$ 0 dB) and where the variance may be made worse by increasing the measurement bandwidth.

5.4.3 Measurement Variance of Combined Slices

For some applications it is desirable to combine individual range slices into "composite" σ^o cells. The formation of a composite cell can be viewed in two ways: (1) The σ^o's are retrieved from each slice separately, and a weighted average is constructed to form the composite using the X^q's as weights; or (2) The detected energy from several slices is summed, and a composite value of X is applied. Both approaches lead to the same result for the composite backscatter, σ_c^o,

$$\sigma_c^o = \frac{\sum E^q}{\sum X^q}, \tag{5.32}$$

where the summations are performed over the N slices which are used to form the composite, and the individual slice values are again indexed by "q."

An expression for the composite value of K_{pc} is next derived. First, from Eq. (5.23) we can write

$$\mathrm{Var}[E^q] = \frac{(K_{pc}^q)^2}{\mathcal{E}^2[E^q]}, \tag{5.33}$$

where K_{pc}^q is the K_{pc} for each individual slice within the composite. If it is assumed that the energy estimates are uncorrelated from slice to adjacent slice, a good assumption when many (> 10) periodogram bins are summed into each cell, then

$$\mathrm{Var}\left[\sum E^q\right] = \sum \mathrm{Var}[E^q]. \tag{5.34}$$

The total composite K_{pc} then becomes

$$K_{pc}^2 = \frac{\sum \mathcal{E}^2[E^q](K_{pc}^q)^2}{\left(\sum \mathcal{E}[E^q]\right)^2}. \tag{5.35}$$

To mirror previous analyses, it is desirable to write the composite K_{pc} in the form

$$K_{pc}^2 = A_c + \frac{B_c}{SNR_c} + \frac{C_c}{{SNR_c}^2}, \tag{5.36}$$

where the subscript "c" indicates an effective value of these parameters for the composited cell. Letting N_0 equal the expected noise energy in a given slice, then

$$SNR^q = \frac{\mathcal{E}[E^q]}{N_0}. \tag{5.37}$$

Assuming that each slice has the same bandwidth and that the noise power spectral density is constant over the cells, SNR_c becomes

$$SNR_c = \frac{\sum \mathcal{E}[E^q]}{NN_0}. \tag{5.38}$$

Solving for the parameters in Eq. (5.36) by using Eqs. (5.33), (5.34), and (5.35),

$$\begin{aligned} A_c &= A\frac{\sum \mathcal{E}^2[E^q]}{\left(\sum \mathcal{E}[E^q]\right)^2} \\ B_c &= \frac{B}{N} \\ C_c &= \frac{C}{N}. \end{aligned} \tag{5.39}$$

Note in Eq. (5.39) that it is necessary to know $\mathcal{E}[E^q]$ for each slice to compute A_c. This is acceptable for the simulation case where the values of the $\mathcal{E}[E^q]$'s

are known in advance. When K_{pc} is to be estimated from actual data, the values of $\mathcal{E}[E^q]$ will be noisy. If it is known a priori that σ^o is uniform over the composite cell, or if the fundamental variance in the estimate of $\mathcal{E}[E^q]$ is larger than the change in σ^o between slices to be composited, it is acceptable to substitute X^q for $\mathcal{E}[E^q]$ in Eq. (5.39) to yield

$$A_c = A\frac{\sum (X^q)^2}{\left(\sum X^q\right)^2}. \tag{5.40}$$

Because X^q is not a random variable, this may improve the estimate of A_c. If the variance in σ^o between slices is larger than the variance in E^q, however, it is more accurate to use E^q as an estimate of $\mathcal{E}[E^q]$.

5.5 Enhanced-Resolution Imaging Performance

As one example of how the addition of range filtering capability expands the utility of SeaWinds, in this section the resulting ERI land/ice imaging performance is examined. As previously noted, Ku-band scatterometer σ^o measurements have proved to be very useful in land and ice studies; hence the desire to maintain a long time series of such measurements. While the original design of *SeaWinds* would have provided usable measurements, the modified design provides σ^o measurements with significantly improved resolution. This is expected to extend the utility of the *SeaWinds* measurements in land/ice science studies as well as for the primary wind observation mission. Here, the land/ice imaging resolution of the original and modified *SeaWinds* designs are compared using conventional gridding and a particular ERI technique known as the Scatterometer Image Reconstruction with Filtering (SIRF) [13].

To make the performance comparison, both beamwidth-limited and range sliced σ^o cells are used. Simulated backscatter measurements are generated with the aid of a synthetic image of the surface σ^o [see Fig. 5.9(a)], which is similar to that used in [49]. For each beamwidth-limited footprint or range slice, the effective σ^o measurement is computed as the weighted average of the pixels of the synthetic image, where the weighting is the spatial response function described earlier. Then,

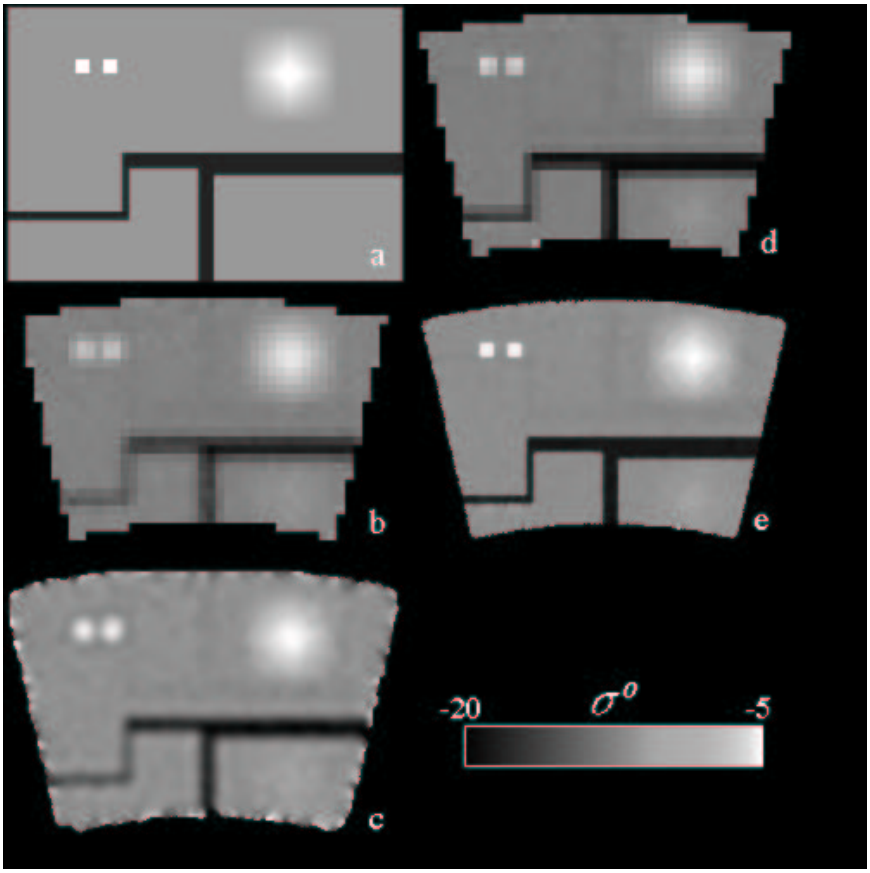

Figure 5.9: Simulated images from *QuikSCAT/SeaWinds*. a) Simulated truth image. b) Gridded image [25 km grid] using beamwidth-limited footprint [no range slicing]. c) SIR-enhanced resolution image using beamwidth-limited footprint. d) Gridded image using the 10 inner slices [25 km grid]. e) SIRF-enhanced resolution image using range slices. Pixel resolution is 4.5 km. The area is a small, synthetic region in Wilkes Land in Antarctica [hence the odd shape which is a box in lat/lon space but is mapped using a Lambert projection to a flat map].

K_{pc} is computed and Monte Carlo noise is added to generate a simulated noisy σ^o measurement. For this analysis, calibration errors are neglected.

In order to simulate the Earth location and orientation of the measurements, the synthetic test image was located over Wilkes Land in Antarctica. The test region is approximately 1000 km $\times$ 800 km and is centered at 74.5° S and 128.5° W. Over a one day period, at least part of the test site is observed during 5 passes of *QuikSCAT*. The imaging results for a number of cases are compared in Fig. 5.9. Using

the simulated σ^o measurements, images were computed using a (non-enhanced) gridding approach and the SIRF resolution enhancement technique for both beamwidth-limited cells and slices. The non-enhanced grid images have a pixel resolution of approximately 25 km while the SIRF images have a pixel resolution of approximately 4.5 km.

To generate the non-enhanced images, each σ^o measurement is assigned to the grid element in which its center falls. The average σ^o is then computed and assigned to the associated pixel. The SIRF images were generated with a modified form of the SIRF algorithm [13]. While the original SIRF algorithm (described in [49]) is bi-variate, estimating both the incidence angle normalized σ^o and the incidence angle dependence of σ^o, the algorithm used here is modified to image only σ^o, similar to the radiometer version of the algorithm [13, 54].

Subjectively, the addition of range resolution capability is observed to significantly improve the effective two dimensional resolution of land/ice images produced from the simulated SeaWinds measurements whether or not resolution enhancement is applied. This is true, even though range filtering resolves the footprint in just one dimension, because of the different orientations of the σ^o cells contributing to each pixel. Using the SIRF algorithm further improves the image resolution over the gridding approach. Because the SeaWinds measurements densely overlap, reasonable images can be made from only one day of data in this polar region. However, the noise level in the images can be reduced if multiple days are combined and the surface is temporally stable.

5.6 Considerations for Single-Pass Resolution Enhancement

In the previous section, the performance of a multi-pass resolution enhancement algorithm applied to the *SeaWinds* data was evaluated. By "multi-pass" it is meant that σ^o measurements from both the forward and aft portions of the antenna scan, as well as from different orbits, are combined to yield the higher resolution images. The theory and performance of such multi-pass techniques, where the spatial sampling of the data is often irregular and the orientation of the σ^o cells is variable,

is addressed in detail in [13]. The multi-pass approach has been applied to previous scatterometer data sets such as NSCAT [49].

A significant limitation of the multi-pass approach is that the target scene must be assumed temporally stable over the integration period, in order to allow multiple orbits to be combined, and azimuthally isotropic, to allow measurements from the entire 360° scan of the antenna to be combined. These assumptions are invalid for ocean wind measurements, which are distinctively anisotropic and vary over short time scales. Further, these assumptions are also problematic for fast-varying land and ice phenomena, such as freeze/thaw events and flooding. It is therefore desirable to achieve higher resolution within a single-pass of the target scene. In this section single-pass resolution enhancement of real-aperture radar data is briefly addressed, and fundamental deconvolution theory is applied to establish rules-of-thumb for the limits on the performance of such algorithms.

5.6.1 One Dimensional Signal Deconvolution and Restoration Concepts

The surface sampling associated with real-aperture scatterometer measurements is shown conceptually in Fig. 5.10. Note that the elevation dimension of the measurement cell, δ_{el}, is much narrower than the azimuth dimension, δ_{az}. Indeed, the elevation resolution can be made arbitrarily narrow by utilizing a wider bandwidth transmit pulse (as described by Eq. 2.3), and consequently the azimuth resolution is typically the limiting factor. The single-pass resolution enhancement problem, then, reduces to the one-dimensional problem of improving the azimuth resolution. Furthermore, when the σ^o cells are uniformly spaced in azimuth, as they are for a single rotation of the antenna, this case simplifies to a uniformly-sampled, one-dimensional signal reconstruction problem. Thus, for the discussion here, we consider only a one-dimensional deconvolution approach.

For a specific elevation location, the *measured* surface σ^o, b, as a function of azimuth position, x, can be written

$$b(x) = h(x) * s(x), \tag{5.41}$$

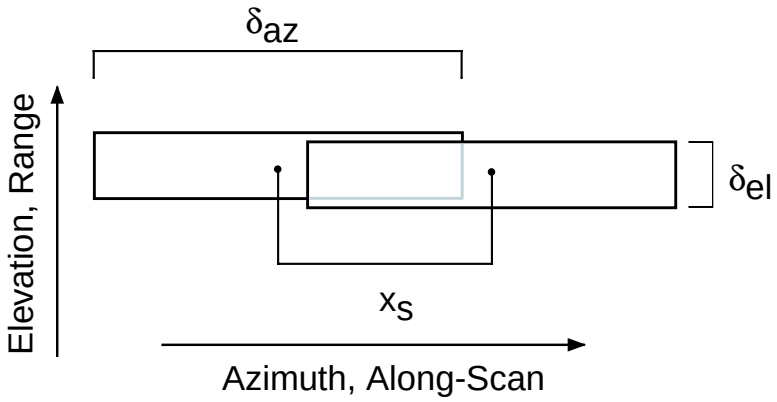

Figure 5.10: Conceptual diagram of surface sampling with a real aperture radar system. The thin rectangles represent real-aperture measurement cells (or slices) with elevation dimension δ_{el} and azimuth dimension δ_{az}. Successive cells are placed on the surface at regular intervals of x_s in azimuth, and correspond to individual transmit pulse events.

where $s(x)$ is the *actual* surface σ^o as a function of azimuth, $h(x)$ is the antenna aperture function, and the asterisk indicates that a convolution operation is performed. This formulation is equivalent to many signal reconstruction problems where the observed scene is the convolution of the "channel" response and the original scene, with the measured scene being a low-pass filtered or "blurred" version of the original.

In practice, the scene is sampled at discrete points, so that a series of measurements, $m[n]$, is obtained where

$$m[n] = b[n] + \eta[n]. \tag{5.42}$$

Here, $b[n] = b(nx_s)$, where n is the measurement number index and x_s is the spatial sampling interval. The noise on each measurement is represented by $\eta[n]$. In the Fourier domain, this becomes

$$M(\omega) = H(\omega)S(\omega) + N(\omega), \tag{5.43}$$

where the capital letters represent the discrete Fourier transforms of the above series.

The ultimate goal is to recover an estimate of the actual surface, $\hat{S}$. To this end, a generalized inverse filtering operation denoted by $\hat{H}^{-1}$ is applied:

$$\hat{S} = \hat{H}^{-1}HS + \hat{H}^{-1}N, \tag{5.44}$$

where the dependence on discrete angular frequency, ω, is now implied. Note that the operation $\hat{H}^{-1}$ is intended to be our best attempt to "un-do" the smoothing effect of H. The ideal inverse filter is one where $\hat{H}^{-1}H = 1$, but this is rarely realizable due to zero crossings in H, or desirable due to noise amplification problems (as discussed further when Wiener filtering is addressed in Section 5.6.3).

The new effective aperture function, $h_e(x)$, is given by the inverse Fourier transform of the product $\hat{H}^{-1}H$. The width of the aperture function in the spatial domain is inversely proportional to the width of its spectrum in the spatial frequency domain. As a metric of the spatial resolution improvement associated with the application of the inverse filter the *resolution enhancement factor* (RIF) is defined as

$$\text{RIF} = \frac{\int |\hat{H}^{-1}H|}{\int |H|}, \tag{5.45}$$

where the integration is performed from 0 to π in the discrete angular frequency domain. As $\hat{H}^{-1}$ restores the original backscatter scene with higher and higher fidelity (equivalent to the recovery of more and more of the original frequency content), the value of the RIF will increase.

A well know problem with inverse filtering operations, however, is noise amplification [27]. When the noise on the measurements is modeled as an additive process, the ratio of the inverse-filtered noise power to the original noise power present in the measurements is given by

$$\frac{\int_0^\pi \mathcal{N}(\omega)|\hat{H}^{-1}(\omega)|^2 d\omega}{\int_0^\pi \mathcal{N}(\omega) d\omega},$$

where $\mathcal{N}(\omega)$ is the noise power spectral density. This ratio is equivalently the average increase in the noise variance due to the inverse filtering process. As a metric of the increased measurement error due to noise, it is convenient to consider the increase in noise standard deviation. In the scatterometer case, the measurement noise is

typically a white process where each noise realization is uncorrelated with all others. Consequently, $\mathcal{N}$ becomes a constant with frequency, and thus a *noise amplification factor* (NAF) can be defined as

$$\text{NAF} = \left(\frac{1}{\pi} \int |\hat{H}^{-1}(\omega)|^2 \right)^{\frac{1}{2}}. \tag{5.46}$$

A key goal of single-pass resolution enhancement is thus to maximize RIF while minimizing NAF.

5.6.2 Single-Pass Resolution Enhancement Analysis

To generate a quantitative assessment of how a single-pass resolution enhancement algorithm will perform, it is first necessary to model the aperture function and its spectrum. It is assumed that the antenna pattern in the azimuth dimension can be give by the square of a first-order Bessel function. An example aperture function is shown in Fig. 5.11. The magnitude of the Fourier transform of this aperture function is shown in Fig. 5.12. Note that because the spatial function is approximately Gaussian, the transform is approximately Gaussian of the form

$$|H(f)| = \exp[-4\ln(2)\beta^2 f^2], \tag{5.47}$$

where f is the spatial frequency and β is the two-way 3 dB width of the antenna aperture function. When the surface is sampled at a spatial sampling rate of f_s, corresponding to a sample spacing on the surface of x_s (where $f_s = \frac{1}{x_s}$), the discrete spatial frequency response becomes

$$|H(\omega)| = \exp\left[-\ln(2) \left(\frac{\beta}{x_s} \right)^2 \left(\frac{\omega}{\pi} \right)^2 \right], \tag{5.48}$$

where the necessary periodicity in 2π is implied.

For analysis purposes, the Gaussian form assumed for H allows us to construct a very simple inverse filter given by

$$\begin{aligned} \hat{H}^{-1} &= \tfrac{1}{H} \quad \text{for} \quad \omega \leq \omega_c \\ \hat{H}^{-1} &= 0 \quad \text{for} \quad \omega > \omega_c \end{aligned} \tag{5.49}$$

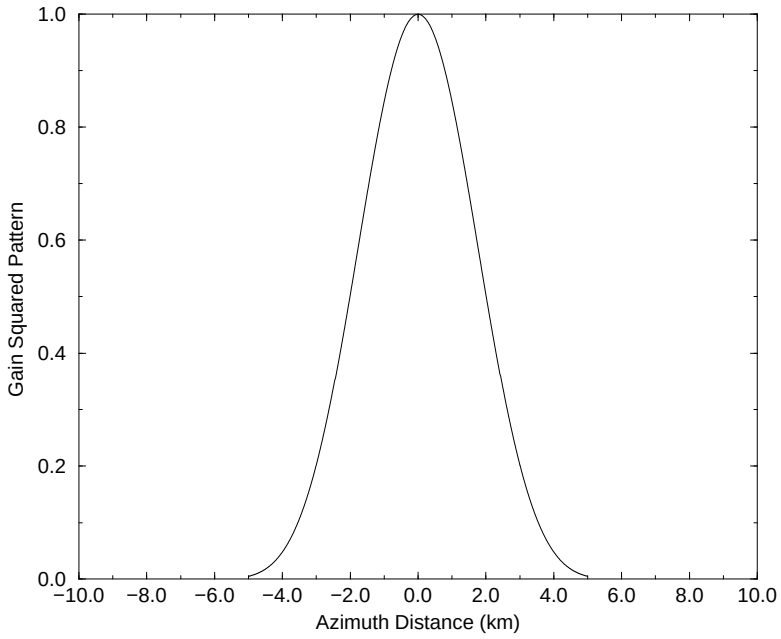

Figure 5.11: Example azimuth aperture function in the spatial domain. Here an antenna 2-way 3 dB width of 4 km on the ground is assumed.

where ω_c is a cutoff frequency above which no information about the scene is obtained. In practice, the actual filter might be of the modified Wiener form which does not have such sharp frequency cutoffs and thus is more implementable (see the following discussion in Section 5.6.3), but this form is adequate for evaluating the approximate enhanced resolution performance of a given system. An additional consideration with this inverse filter formulation is the possibility for alias contamination. The requirement is to sample at a sufficiently high frequency such that

$$\frac{|H(\omega_c)|}{|H(\omega_c - 2\pi)|} > thresh, \tag{5.50}$$

where $thresh$ is some threshold value so that unacceptable amplification of alias power does not occur.

Using the above expressions, curves of NAF versus RIF are constructed by varying ω_c from 0 to π. This is performed for different sampling rates in Fig. 5.13.

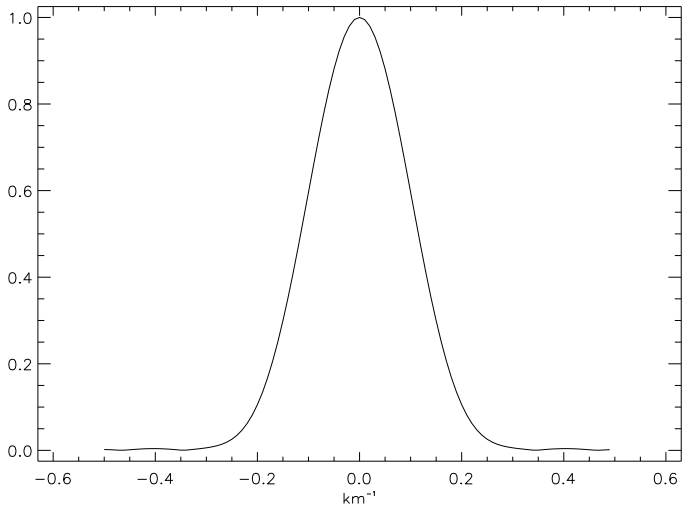

Figure 5.12: Magnitude of Fourier transform of aperture function shown in Fig. 5.11.

Here the sampling rate is expressed as β/x_s, which is the fraction of the beamwidth at which the surface is sampled. A reasonable Nyquist rate given the scatterometer spectrum is $x_s = \beta/2$. In general, as reconstructions at higher frequencies are attempted, RIF improves, but a higher value of NAF results. At the Nyquist sampling rate of $\beta/2$, a factor of 1.5 resolution enhancement is achieved at a cost of a factor of two increase in the noise. Beyond this, the noise as well as aliasing increase dramatically. As the sampling rate increases, aliasing is no longer a problem and better NAF performance is obtained for a given RIF due to the averaging effect.

5.6.3 Example Single-Pass ERI Implementation: Modified Wiener Filter

In the preceding discussion, an ideal inverse filter was assumed. In reality, such a filter will have a very long impulse response due to the spectral "spikes" as shown in Fig. 5.14. A more implementable filter is a modified Wiener filter approach, where

$$\hat{H}^{-1} = H_{bp}\left(\frac{H^*}{|H|^2 + \kappa}\right). \tag{5.51}$$

Here, H_{bp} is an ideal bandpass filter with cutoff frequency ω_c, and the parameter κ is selected to smooth the transition between the rapidly growing response at higher

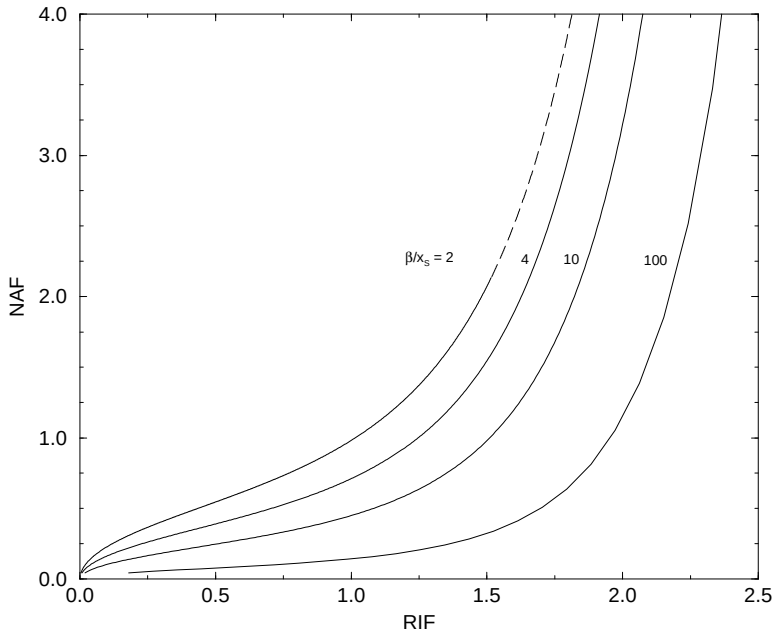

Figure 5.13: Plots of NAF versus RIF for various surface sampling rates. Here, the sampling rate is expressed as β/x_s. The dotted line represents a region of the curve where significant aliasing may occur.

frequencies and the passband cutoff. Such smoothing in the spectral domain will insure a stable and implementable filter. As an example, Fig. 5.15 shows the modified Wiener inverse filter constructed from the response in Fig. 5.14. In Fig. 5.16, the impulse response function of this filter is shown.

As an example of how this filter is employed, consider Fig. 5.17. Here the original one-dimensional scene, $s(x)$, is a step function. The dotted line is the aperture smoothed measured function, $m(x)$ [in this case noise-free]. After inverse filtering, the reconstructed scene, $\hat{s}$, is given by the dashed line. Note the sharpening of the 3 dB boundary consistent with approximately a factor of two improvement in resolution. (As indicated by Fig. 5.13, it is possible to obtain more resolution enhancement if sufficiently dense sampling is obtained. For the purposes of analysis of a *SeaWinds*-class system, however, this example represents typical performance.)

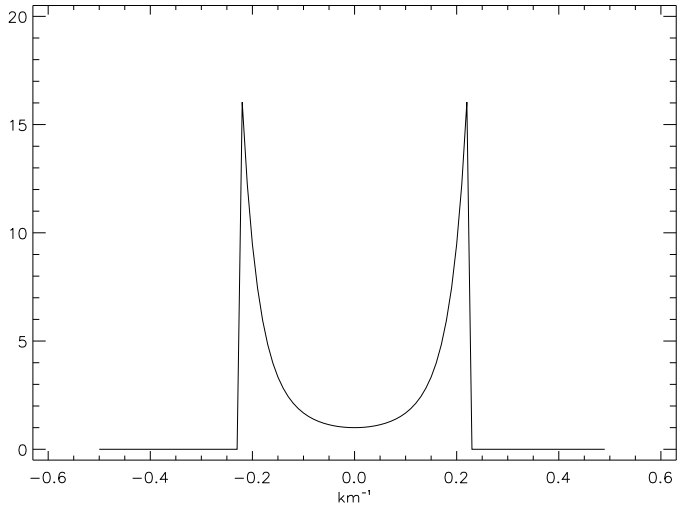

Figure 5.14: Ideal inverse filter spectral response.

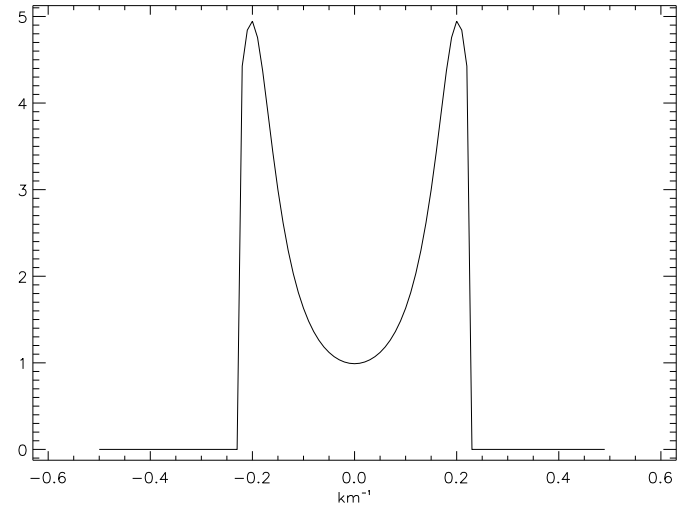

Figure 5.15: Modified Wiener inverse filter spectral response.

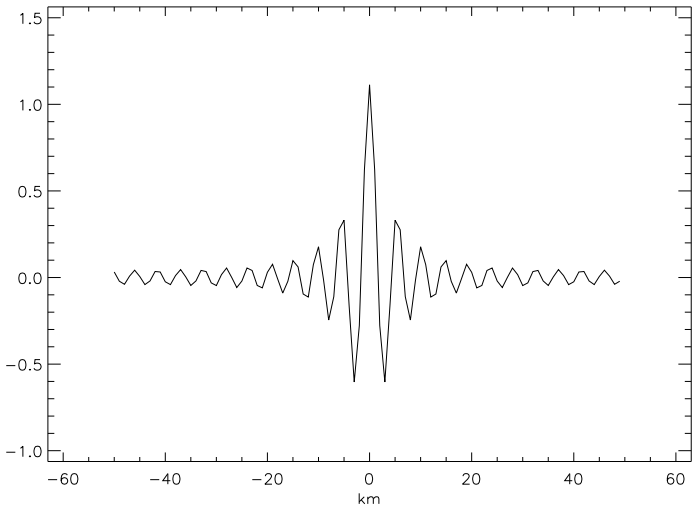

Figure 5.16: Impulse response of filter in Fig. 5.14.

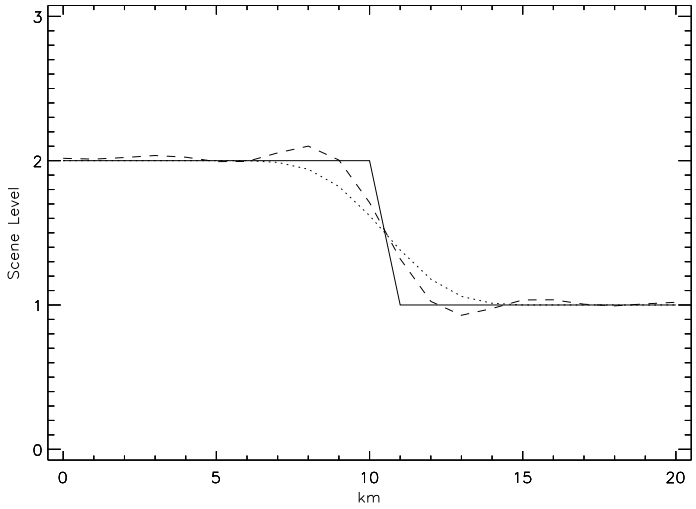

Figure 5.17: Example reconstruction of a 3 dB step function (solid). The dotted line is the aperture smoothed measured function, and the dashed line the inverse filter reconstructed version.

5.7 Summary and Conclusions

In this chapter, a framework for the design of pencil-beam scatterometers employing the real-aperture resolution approach has been presented. As discussed, range filtering is generally preferred over Doppler filtering because of lower measurement variance and more favorable geometric orientation of the σ^o cells. Although range discrimination by deramp processing is a relatively straightforward approach, its implementation must be accompanied by a careful accounting of calibration factors in order to meet backscatter measurement accuracy goals. This involves a formulation for the SRF and radar equation which includes digital processing and antenna rotation effects, as well as a consideration of spacecraft attitude variations. Trade-offs to obtain minimum measurement variance by optimizing the chirp rate and detection bandwidth for the available signal-to-noise ratio must also be conducted to obtain the best performance.

It was shown how the spatial resolution performance of *SeaWinds* has been significantly improved by the addition of a range filtering scheme. This was demonstrated to be particularly useful for land and ice images constructed using multi-pass enhanced resolution imaging algorithms. Range slicing of the antenna footprint, coupled with the application of ERI, is thus an economical way of extending the capabilities of small, scanning pencil-beam scatterometers such as *SeaWinds*. The application of single-pass resolution techniques was also examined. While multi-pass techniques achieve resolution on the order of the narrow elevation dimension of the σ^o cell, a reasonable bound for the single-pass resolution improvement is approximately a factor of 0.5 - 0.7 times the azimuth dimension of the σ^o cell when the surface is sampled at a minimum Nyquist rate. When a more dense sampling is achieved, the spatial resolution can be further improved.

Chapter 6

A Design Framework for Polarimetric Scatterometer Systems

Scatterometer instruments discussed thus far in this dissertation have been based on the *co-polarized* backscatter measurement (i.e., the transmit and receive signals have the same polarization). In remote sensing applications, it is often useful to also detect the *cross-polarized* return (i.e., the transmit and receive signals have orthogonal polarization) [29]. The cross-polarized signal contains additional information about the surface properties, and may contribute to improved retrieval of geophysical parameters of interest. Scatterometers which measure both the co- and cross-polarized returns are termed *polarimetric* systems.

Of particular interest in wind scatterometry is the mathematical correlation of the co-polarized and cross-polarized returns [93, 104]. Theoretical studies have demonstrated that whereas both the co-polarized and cross-polarized backscatter from the ocean surface are odd functions of illumination azimuth angle, the correlation between the co- and cross-polarized signals is an even function of azimuth. The orthogonal symmetry of this correlation term consequently has potential to further constrain the wind direction solution and thus improve wind retrieval accuracy [93]. As with conventional co-polarized scatterometers, the ability of the co-pol/cross-pol correlation term to contribute meaningfully to wind retrieval is related to the measurement accuracy achieved. A concern for spaceborne scatterometer systems, however, is that because the cross-polarized return is so weak, the resulting SNR may be too small for a statistically meaningful measurement to be made. This, and other problems associated with designing a spaceborne polarimetric scatterometer have not been previously addressed.

In this chapter, key design issues for a polarimetric scatterometer are addressed. A generalized signal processing framework is presented which facilitates the analysis of polarimetric scatterometer systems, and allows the quantification of measurement errors encountered with this advanced technique. Finally, a new expression for the measurement variance associated with the co-pol/cross-pol correlation term is derived. This expression is used to demonstrate that statistically meaningful measurements may be obtained with a polarimetric system, even when the cross-polarized return is very weak.

6.1 Utility of Polarimetric Scatterometry

With a co-polarized measurement, a specific polarization is transmitted and the backscattered energy in that same polarization is measured. On the *SeaWinds* outer beam, for instance, vertical polarization (V-pol) radiation is transmitted and the backscattered V-pol power is then measured. For this case, the normalized backscatter cross-section is proportional to the detected power in the like-polarized echo signal, or

$$\sigma_{VV} \propto \langle s_{VV} s_{VV}^* \rangle. \tag{6.1}$$

Here, the VV subscript indicates that V-Pol is transmitted and received, s_{VV} is the like-polarized return signal, and the brackets indicate that a time average is performed.

The cross-polarized backscatter cross-section is, in turn, proportional to the power in the cross-polarized signal. For the case where V-pol is transmitted, but H-pol is received,

$$\sigma_{HV} \propto \langle s_{HV} s_{HV}^* \rangle, \tag{6.2}$$

where the subscript HV indicates the polarization sense of the measured and transmitted signals respectively. Examples of σ_{VV} and σ_{HV} for an 8 m/s ocean wind speed at 54° incidence angle are shown in Fig. 6.1. Note that (1) both the co- and cross-polarized signals are similar even functions of wind direction, and (2) the cross-polarized return is around 15 dB below the co-polarized return. Because of these

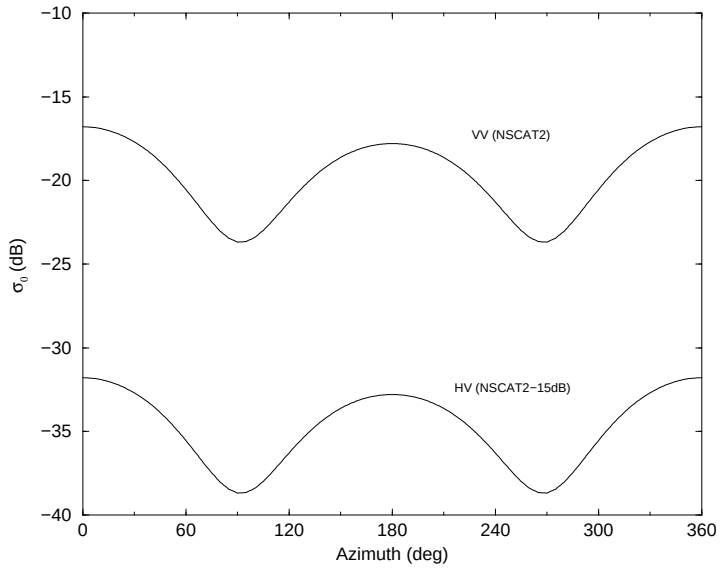

Figure 6.1: Co-pol and Cross-pol model functions for 8 m/s wind at 54° incidence angle. The co-polarized curve was generated using the NSCAT-2 model function. The cross-polarized curve was generated by taking the co-polarized curve and subtracting 15 dB, representing the theoretical difference between the co- and cross polarized backscatter (see [86]).

characteristics, the addition of the cross-polarized backscatter cross-section, by itself, adds little to the wind retrieval process.

A different phenomenology emerges when the correlation of the co- and cross-polarized signals is taken. Here,

$$\sigma_{hvvv} \propto \langle s_{HV} s_{VV}^{*} \rangle \tag{6.3}$$

represents the *polarimetric correlation cross-section* associated with the HV and VV signals. Similar cross-sections can be defined for any combination of polarizations [see Eq. (6.5)]. As shown in Fig. 6.2, unlike the co- and cross-pol cross-sections, the correlation cross-section is an odd function of wind speed. This symmetry is orthogonal to the even symmetry of the traditional scatterometer co-pol measurements, and consequently adds new information to the wind retrieval process [93]. The measurement of polarimetric correlation cross-section is an important capability being considered for future scatterometer systems [86].

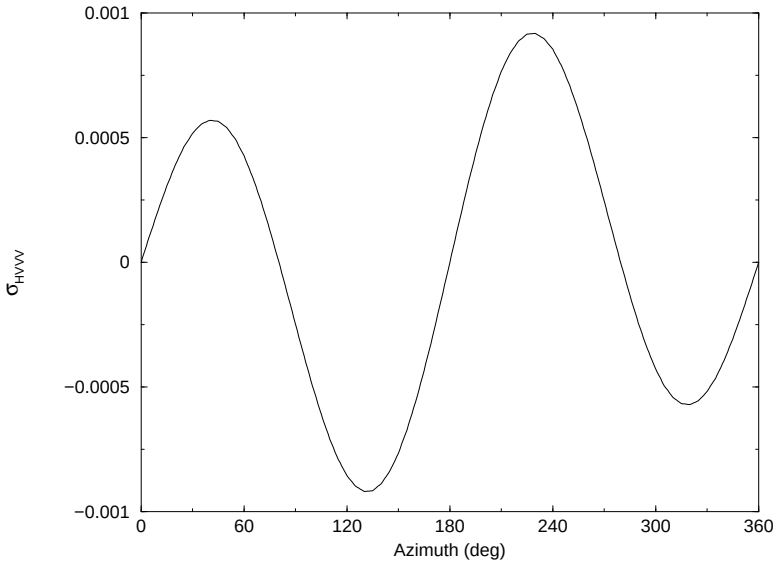

Figure 6.2: Co-pol/Cross-pol correlation cross-section for 8 m/s wind at 54° incidence angle. This curve is computed from a theoretical model of backscatter from periodic surfaces [93].

6.2 Polarimetric Instrument Modifications

A modified pencil-beam radar schematic, which includes the capability to make polarimetric measurements is shown in Fig. 6.3 (compare to the *Seawinds* design in Fig. 4.6). Here a single transmitter generates a pulse that is either routed to the inner or outer beam by switch S1. The transmit signal crosses the rotary joint interface to the moving antenna. Switches S2 and S3 are used to control which polarization is transmitted by routing the signal to the appropriate port of an orthomode transducer and antenna feed horn assembly.

As on transmit, the receive function alternates between the two beams. When the echo for a given beam returns, switches S2 and S3 are set so that both the co-polarized return and cross-polarized return may be passed by the two channel rotary joint to two separate receivers. Here, the signals are downconverted and digitally sampled in quadrature to form two complex data streams. In general, the design described involves only a moderate expansion of the current non-polarimetric *SeaWinds* architecture; the key differences being the addition of dual polarized antenna feed

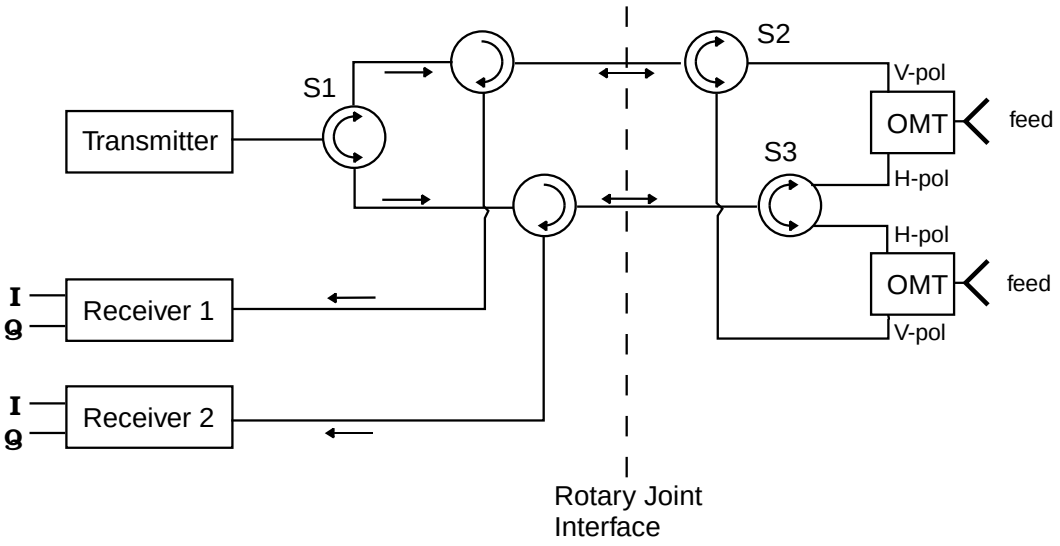

Figure 6.3: Representative polarimetric scatterometer schematic (compare to Fig. 4.6). Relative to a conventional scatterometer, the polarimetric design implements an additional receiver for simultaneous detection of the cross-pol return and additional switches for routing the two signals.

horns, some additional switching on the rotating side of the antenna subsystem, and an addition receiver chain. It is emphasized that this is just one representative implementation of the polarimetric capability.

6.3 Polarimetric Signal Description

In this section a general formulation for analyzing the polarimetric signal measurement process is developed. The echo signal amplitude detected in the H-pol and V-pol channels, R_H and R_V, at time t from a single scatterer located at position $\bar{r}$ is represented by

$$\begin{bmatrix} R_H(t,\bar{r}) \\ R_V(t,\bar{r}) \end{bmatrix} = \frac{\lambda}{(4\pi)^{3/2}|\bar{r}|^2} \left\{ \begin{bmatrix} h^r_{HH}(\bar{r}) & h^r_{HV}(\bar{r}) \\ h^r_{VH}(\bar{r}) & h^r_{VV}(\bar{r}) \end{bmatrix} \begin{bmatrix} \mathcal{S}_{HH}(\bar{r}) & \mathcal{S}_{HV}(\bar{r}) \\ \mathcal{S}_{VH}(\bar{r}) & \mathcal{S}_{VV}(\bar{r}) \end{bmatrix} \right.$$
$$\left. \begin{bmatrix} h^t_{HH}(\bar{r}) & h^t_{HV}(\bar{r}) \\ h^t_{VH}(\bar{r}) & h^t_{VV}(\bar{r}) \end{bmatrix} \begin{bmatrix} T_H(t-\frac{2|\bar{r}|}{c})e^{i\omega_d(\bar{r})t} \\ T_V(t-\frac{2|\bar{r}|}{c})e^{i\omega_d(\bar{r})t} \end{bmatrix} \right\}. \quad (6.4)$$

Here, T_H and T_V are the transmit signals generated for the H- and V-pol channels. The echo from each scattering element is delayed by $2|\bar{r}|/c$ and Doppler shifted by ω_d. The h^t_{ij}'s and h^r_{ij}'s are the total amplitude gains for transmission and reception through the radar system. In general, all the h_{ij}'s are complex, and take into account the antenna pattern, RF component gains and losses, phase shifts, and all cross-talk between the two channels. When reciprocity conditions apply, $h_{HV} = h_{VH}$ in both the transmit and receive gain matrices. The $\mathcal{S}_{ij}$'s are complex random variables and form a scattering matrix defined such that

$$\langle \mathcal{S}_{ij}(\bar{r})\mathcal{S}^*_{kl}(\bar{r}')\rangle = \sigma_{ijkl}\delta(\bar{r}-\bar{r}'). \quad (6.5)$$

The total signal received in each channel is the combination of echo returns from all scatters, plus thermal noise:

$$\begin{aligned} C_H(t) &= \int d^2\bar{r}\ R_H(t,\bar{r}) + \nu_H(t) \\ C_V(t) &= \int d^2\bar{r}\ R_V(t,\bar{r}) + \nu_V(t), \end{aligned} \quad (6.6)$$

where the integral is performed over the illuminated ocean surface and the noise components in each channel (ν_H and ν_V) may be partially correlated due to cross-talk.

6.3.1 The Co-Pol Measurement

As an example of how the above framework can be used, consider the case of the conventional measurement of the co-polarized backscatter cross-section – either σ_{VVVV} or σ_{HHHH} (which are abbreviated as σ_{VV} and σ_{HH}). This process was described in previous chapters, and is reexamined here in light of the expression for the fully polarimetric system described by Eq. (6.4).

Assuming that only a V-polarized signal is generated by the transmitter, then $T_H = 0$. Because $h_{VV} \gg h_{HV}$ and $\sigma_{VV} \gg \sigma_{HV}$, it is typical to assume that all cross terms in the matrices of Eq. (6.4) are negligible. Noting that the signal and noise are uncorrelated, the total integrated power in the V channel is

$$\langle |C_V|^2 \rangle = X\sigma_{VV} + \langle |\nu_V|^2 \rangle, \tag{6.7}$$

where dependence on t has been dropped for notational convenience. It is assumed that the wind, and hence backscatter, is constant over the illuminated footprint. The parameter X is thus defined as

$$X = \frac{\lambda^2}{(4\pi)^3} \int d^2\bar{r}\ \frac{|h^t_{VV}|^2 |h^r_{VV}|^2}{|\bar{r}|^4}. \tag{6.8}$$

An estimate of σ_{VV} is then obtained from

$$\widetilde{\sigma_{VV}} = \frac{\langle |\widetilde{C_V}|^2 \rangle - \langle |\widetilde{\nu_V}|^2 \rangle}{X}, \tag{6.9}$$

where the tilde indicates that an estimate of an inherently random quantity is obtained. Typically, an estimate of the channel noise power is obtained by observing the noise floor at a time or in a bandwidth when the signal is not present. (Note that this is identical, although with somewhat different notation, to the process described in Section 3.3.3.)

For scatterometer performance evaluation, it is also important to know the variance of the cross-section estimate. For the co-polarized return case, this has been derived in Chapters 4 and 5. Assuming that the echo return has a Doppler bandwidth B_s and a pulse duration T_p, and that the time-bandwidth product of the noise-only estimate is $\gg B_s T_p$, the cross-section estimate variance may be approximated as

$$\mathrm{Var}[\widetilde{\sigma_{VV}}] = \frac{\sigma_{VV}}{T_p B_s} \left(1 + \frac{2}{\mathrm{SNR}_{VV}} + \frac{1}{\mathrm{SNR}^2_{VV}} \right), \tag{6.10}$$

where the signal-to-noise ratio is defined as

$$\mathrm{SNR}_{VV} = \frac{X\sigma_{VV}}{\langle |\nu_V|^2 \rangle}. \tag{6.11}$$

Similar results are obtained for the measurement of σ_{HH}.

6.3.2 Polarimetric Signal Detection

To obtain the correlation cross-section σ_{HVVV} discussed in Section 6.1, a correlation of the return from the two polarization channels must be performed. For the measurement of σ_{HVVV}, from Eqs. (6.4) and (6.6) we have that

$$\langle C_V C_H^* \rangle = X_1 \sigma_{HVVV} + X_2 \sigma_{VVVV} + \ldots + \langle \nu_V \nu_H^* \rangle, \tag{6.12}$$

where the term $X_1 \sigma_{HVVV}$ contains the desired information with

$$X_1 = \frac{\lambda^2}{(4\pi)^3} \int d^2\bar{r} \; \frac{|h_{VV}^t|^2 h_{VV}^r h_{HH}^{r*}}{|\bar{r}|^4}, \tag{6.13}$$

and the largest "cross-talk" term is $X_2 \sigma_{VVVV}$ with

$$X_2 = \frac{\lambda^2}{(4\pi)^3} \int d^2\bar{r} \; \frac{|h_{VV}^t|^2 h_{VV}^r h_{HV}^{r*}}{|\bar{r}|^4}. \tag{6.14}$$

The "$+\ldots$" in Eq. (6.12) represents all 14 other cross-talk terms with the appropriate X's similarly defined. Note that when the cross-terms in the gain matrices are small, the contribution of the cross-talk power to Eq. (6.12) is small as well. The term $\langle \nu_V \nu_H^* \rangle$ represents the potential for the noise in the channels to be partially correlated due to cross-talk effects.

An estimate of σ_{HVVV} is thus obtained from

$$\widetilde{\sigma_{HVVV}} = \frac{\langle \widetilde{C_V C_H^*} \rangle - \left(X_2 \widetilde{\sigma_{VVVV}} + \ldots + \langle \widetilde{\nu_V \nu_H^*} \rangle \right)}{X_1}. \tag{6.15}$$

Note that in order to estimate σ_{HVVV}, an estimate of both the signal and noise cross-talk powers must be obtained and subtracted from the channel correlation measurement. In the case of the noise correlation term, this is accomplished in a manner analogous to the co-pol "noise-only" calibration where periodic observations of the noise floor are performed. For the signal cross-talk terms, it is most desirable to design the system so that the cross-talk gains are very small, thus making the cross-talk power negligible. If this can not be achieved, then the cross-talk contamination may be subtracted out by a thorough calibration of all system gains in Eq. (6.12).

As an example of how strong the cross-talk terms may be, consider the case of V-Pol transmitted and incident on the surface at 54° (the incidence angle

for the *SeaWinds* outer beam). If the wind is blowing at 8 m/s, then $\sigma_{VV} = 0.012$ and $\sigma_{HVVV} = 0.0006$ – indicating that the cross-section of the co-pol return is 13 dB higher than the correlation cross-section. This creates the potential for significant contamination from the first and largest cross-talk term in Eq. (6.12). If, however, the h^r_{HV} term in Eq. (6.14) provides sufficient attenuation relative to the h^r_{HH} term in Eq. (6.13), this cross-talk is reduced. Let us now assume that $|h^r_{HV}|/|h^r_{HH}| < -20$dB for all $\bar{r}$. This then implies $|X_2|/|X_1| < -20$dB, and thus the total cross-talk contamination is 7 dB below the desired signal power.

6.4 Polarimetric Signal Variance

Because of the existence of the cross-talk terms and the correlations between them, the variance analysis for the estimate of σ_{HVVV} is quite complicated. An analytic expression for the measurement variance and its sensitivity to signal-to-noise ratio, however, is critical for instrument concept design and performance simulation. A derivation of the measurement variance for a polarimetric scatterometer system is provided here for the first time. Two simplified cases are examined: a) where no cross-talk contamination is assumed, and b) where some in-phase cross-talk contamination is allowed.

6.4.1 Measurement Variance With No Cross-Talk

In this analysis the case is addressed where pure V-polarization is transmitted and where both V-pol (co-pol or "VV") and H-pol (cross-pol or "HV") are received [i.e., $T_H = 0$ in Eq. (6.4)]. This can easily be extended to the case where pure H-pol is transmitted. Because it is also assumed that the instrument has been designed such that cross-talk is negligible, then all cross-gains in Eq. (6.4) are zero and consequently

$$\begin{aligned} C_H(t) &= \frac{\lambda^2}{(4\pi)^3} \int d^2\bar{r}\, \frac{h^r_{HH} \mathcal{S}_{HV} h^t_{VV}}{|\bar{r}|^2} T_V(t - \frac{2|\bar{r}|}{c}) e^{i\omega_d t} + \nu_H(t) \\ C_V(t) &= \frac{\lambda^2}{(4\pi)^3} \int d^2\bar{r}\, \frac{h^r_{VV} \mathcal{S}_{VV} h^t_{VV}}{|\bar{r}|^2} T_V(t - \frac{2|\bar{r}|}{c}) e^{i\omega_d t} + \nu_V(t), \end{aligned} \tag{6.16}$$

which can be notationally simplified to

$$\begin{aligned} C_H(t) &= s_{HV}(t) + \nu_H(t) \\ C_V(t) &= s_{VV}(t) + \nu_V(t). \end{aligned} \tag{6.17}$$

If we further make the assumption that $h^r_{HH} = h^r_{VV} = h^t_{VV}$ (i.e., transmit and receive gains for each channel have the same magnitude and phase), then

$$\begin{aligned} \sigma_{VV} &= \frac{\langle s_{VV} s^*_{VV} \rangle}{X} \\ \sigma_{HV} &= \frac{\langle s_{HV} s^*_{HV} \rangle}{X} \\ \sigma_{HVVV} &= \frac{\langle s_{VV} s^*_{HV} \rangle}{X}, \end{aligned} \tag{6.18}$$

where

$$X = \frac{\lambda^2}{(4\pi)^3} \int d^2\bar{r} \; \frac{|h^t_{VV}|^4}{|\bar{r}|^4}. \tag{6.19}$$

The no cross-talk condition also implies

$$\langle \nu_V \nu^*_H \rangle = 0. \tag{6.20}$$

In general, $s_{HV}(t)$, $s_{VV}(t)$, $\nu_H(t)$, and $\nu_V(t)$ are complex random processes. The "in-phase" condition guarantees that

$$\mathrm{Im}\,\{\mathcal{E}[s_{VV}(t) s^*_{HV}(t')]\} = 0$$

and

$$\mathrm{Im}\,\{\mathcal{E}[\nu_V(t) \nu^*_H(t')]\} = 0$$

for all t and t'. Each process is Gaussian distributed – the ν's because they are generated by thermal noise, and the s's because they are generated by a summation over many random surface scatterers. In this development, only the variance for an interrupted CW signal is derived, but the results are easily extended to other modulation formats. The bandwidth of the echo, B_s, is determined by the range of Doppler frequencies that are illuminated by the antenna footprint. If filtering is performed to exactly match the signal bandwidth, the normalized power spectral

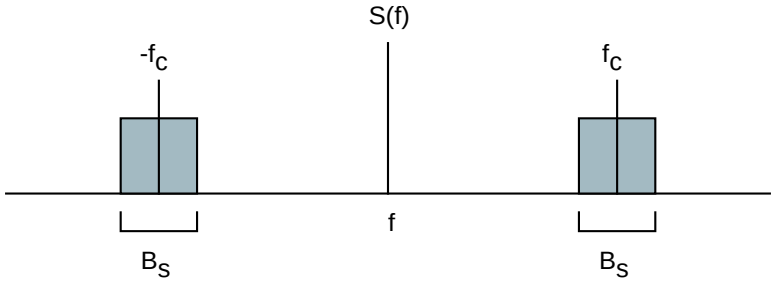

Figure 6.4: Ideal power spectral density assumed for signals in Eq. (6.17). The spectrum is shown before the removal of the carrier frequency f_c.

density, $S(f)$, may be approximated as the same for both the echo and noise processes. This is illustrated in Fig. 6.4.

Using Eqs. (6.16)-(6.20), Eq. (6.15) becomes

$$\mathrm{Var}\left[\sigma_{\widetilde{HVVV}}\right] = \frac{\mathrm{Var}\left[\langle \widetilde{C_V C_H^*} \rangle\right]}{X^2}, \tag{6.21}$$

where

$$\mathrm{Var}\left[\langle \widetilde{C_V C_H^*} \rangle\right] = \mathcal{E}\left[\langle \widetilde{C_V C_H^*} \rangle^2\right] - \mathcal{E}^2\left[\langle \widetilde{C_V C_H^*} \rangle\right]. \tag{6.22}$$

Because the likely system design employs digital processing, we now treat the estimation problem in the discrete time domain. Due to our "in-phase" assumption, an estimate of the correlation between the two channels can be constructed as

$$\langle \widetilde{C_V C_H^*} \rangle = \frac{1}{N} \sum_{n=0}^{N-1} \mathrm{Re}\left\{C_V(n) C_H^*(n)\right\}, \tag{6.23}$$

where n is the discrete sample index. The real part of the correlation is taken because σ_{HVVV} is real [104], and X is real under the assumptions of this analysis.

Equation (6.23) can be expanded as

$$\begin{aligned} \langle \widetilde{C_V C_H^*} \rangle = \frac{1}{N} \sum_{n=0}^{N-1} \; & s_{VV}^R(n) s_{HV}^R(n) + s_{VV}^I(n) s_{HV}^I(n) \\ & + s_{VV}^R(n) \nu_H^R(n) + s_{VV}^I(n) \nu_H^I(n) \\ & + s_{HV}^R(n) \nu_V^R(n) + s_{HV}^I(n) \nu_V^I(n) \\ & + \nu_V^R(n) \nu_H^R(n) + \nu_V^I(n) \nu_H^I(n). \end{aligned} \tag{6.24}$$

Where the "R" and "I" denote the real and imaginary components of the signals respectively. Using the fact that the thermal noise is uncorrelated with the signal, and assuming the signals are stationary, we drop dependence on the sample index in the expectation, and

$$\mathcal{E}\left[\langle C_V \widetilde{C}_H^* \rangle\right] = \mathcal{E}[s_{VV}^R s_{HV}^R] + \mathcal{E}[s_{VV}^I s_{HV}^I]. \tag{6.25}$$

Because $\mathcal{E}[s_{VV}^R s_{HV}^R] = \mathcal{E}[s_{VV}^I s_{HV}^I]$, then

$$\mathcal{E}\left[\langle C_V \widetilde{C}_H^* \rangle\right] = 2\mathcal{E}[s_{VV}^R s_{HV}^R]. \tag{6.26}$$

To complete the variance calculation, we next evaluate

$$\mathcal{E}\left[\langle C_V \widetilde{C}_H^* \rangle^2\right] = \frac{1}{N^2}\mathcal{E}\left[\sum_{n=0}^{N-1} \mathrm{Re}\left\{C_V(n)C_H^*(n)\right\} \sum_{m=0}^{N-1} \mathrm{Re}\left\{C_V(n)C_H^*(n)\right\}\right]. \tag{6.27}$$

To expand this equation, the following relations and properties are applied to reduce the number of terms:

- $\mathcal{E}[abcd] = \mathcal{E}[ab]\mathcal{E}[cd] + \mathcal{E}[ac]\mathcal{E}[bd] + \mathcal{E}[ad]\mathcal{E}[bc]$ for real Gaussian random variables.
- The noise in the co-pol channel is uncorrelated with the noise in the cross-pol channel.
- The signal is uncorrelated with the noise in either channel.
- All imaginary components are uncorrelated with all real components (see [38]).

The remaining terms from an expansion of Eq. (6.27) are

$$\begin{aligned}
\mathcal{E}\left[\langle C_V \widetilde{C}_H^* \rangle^2\right] \;=\; & \frac{1}{N^2}\sum_{n=0}^{N-1}\sum_{m=0}^{N-1} \mathcal{E}[s_{VV}^R(n)s_{HV}^R(n)s_{VV}^R(m)s_{HV}^R(m)] \\
& + \mathcal{E}[s_{VV}^R(n)s_{HV}^R(n)s_{VV}^I(m)s_{HV}^I(m)] + \mathcal{E}[s_{VV}^I(n)s_{HV}^I(n)s_{VV}^R(m)s_{HV}^R(m)] \\
& + \mathcal{E}[s_{VV}^I(n)s_{HV}^I(n)s_{VV}^I(m)s_{HV}^I(m)] + \mathcal{E}[s_{VV}^R(n)\nu_H^R(n)s_{VV}^R(m)\nu_H^R(m)] \\
& + \mathcal{E}[s_{VV}^I(n)\nu_H^I(n)s_{VV}^I(m)\nu_H^I(m)] + \mathcal{E}[s_{HV}^R(n)\nu_V^R(n)s_{HV}^R(m)\nu_V^R(m)] \\
& + \mathcal{E}[s_{HV}^I(n)\nu_V^I(n)s_{HV}^I(m)\nu_V^I(m)] + \mathcal{E}[\nu_V^R(n)\nu_H^R(n)\nu_V^R(m)\nu_H^R(m)] \\
& + \mathcal{E}[\nu_V^I(n)\nu_H^I(n)\nu_V^I(m)\nu_H^I(m)].
\end{aligned} \tag{6.28}$$

Equation (6.28) can be further reduced by again applying the forth order moment expansion for Gaussian random variables, and by recognizing that $\mathcal{E}[a(n)b(m)] = 0$ when $n \neq m$. This second property is a result of the fact that when rectangular spectra are sampled at exactly the Nyquist rate, the samples are uncorrelated. (Our ultimate result, of course, only requires that the signal be sampled at the Nyquist rate or higher. The assumption of the exact Nyquist rate, however, makes the mathematics of this problem easier.) Applying these simplifications, Eq. (6.28) becomes

$$\begin{aligned}\mathcal{E}\left[\langle \widetilde{C_V C_H^*}\rangle^2\right] &= 4\mathcal{E}[s_{VV}^R s_{HV}^R] + \frac{2}{N}\mathcal{E}^2[s_{VV}^R s_{HV}^R] + \frac{2}{N}\mathcal{E}[s_{VV}^R s_{VV}^R]\mathcal{E}[s_{HV}^R s_{HV}^R] \\ &\quad + \frac{2}{N}\mathcal{E}[s_{VV}^R s_{VV}^R]\mathcal{E}[\nu_H^R \nu_H^R] + \frac{2}{N}\mathcal{E}[s_{HV}^R s_{HV}^R]\mathcal{E}[\nu_V^R \nu_V^R] \\ &\quad + \frac{2}{N}\mathcal{E}[\nu_V^R \nu_V^R]\mathcal{E}[\nu_H^R \nu_H^R],\end{aligned} \tag{6.29}$$

where it is again assumed that stationarity and the statistical equivalence of the real and imaginary components hold.

Subtracting off the square of the expected value from Eq. (6.29),

$$\begin{aligned}\mathrm{Var}\left[\langle \widetilde{C_V C_H^*}\rangle\right] &= \frac{2}{N}\left(\mathcal{E}^2[s_{VV}^R s_{HV}^R] + \mathcal{E}[(s_{VV}^R)^2]\mathcal{E}[(s_{HV}^R)^2]\right. \\ &\quad + \mathcal{E}[(s_{VV}^R)^2]\mathcal{E}[(\nu_H^R)^2] + \mathcal{E}[(s_{HV}^R)^2]\mathcal{E}[(\nu_V^R)^2] \\ &\quad \left. + \mathcal{E}[(\nu_V^R)^2]\mathcal{E}[(\nu_H^R)^2]\right).\end{aligned} \tag{6.30}$$

Because $2\mathcal{E}[s_x^R s_y^R]$ is equivalent to $\langle s_x s_y^*\rangle$, Eq. (6.30) becomes

$$\begin{aligned}\mathrm{Var}\left[\langle \widetilde{C_V C_H^*}\rangle\right] &= \frac{1}{2N}\left(\langle s_{VV} s_{HV}^*\rangle^2 + \langle s_{VV} s_{VV}^*\rangle\langle s_{HV} s_{HV}^*\rangle + \langle s_{VV} s_{VV}^*\rangle\langle \nu_H \nu_H^*\rangle\right. \\ &\quad \left. + \langle s_{HV} s_{HV}^*\rangle\langle \nu_V \nu_V^*\rangle + \langle \nu_V \nu_V^*\rangle\langle \nu_H \nu_H^*\rangle\right).\end{aligned} \tag{6.31}$$

Defining

$$\mathrm{SNR}_{VV} = \frac{\langle |s_{VV}|^2\rangle}{\langle |\nu_V|^2\rangle} \qquad \text{and} \qquad \mathrm{SNR}_{HV} = \frac{\langle |s_{HV}|^2\rangle}{\langle |\nu_H|^2\rangle}, \tag{6.32}$$

and employing Eq. (6.18), Eq. (6.21) becomes

$$\mathrm{Var}\left[\widetilde{\sigma_{HVVV}}\right] = \frac{1}{2N}\left[\sigma_{HVVV}^2 + \sigma_{VV}\sigma_{HV}\left(1 + \frac{1}{\mathrm{SNR}_{VV}}\right)\left(1 + \frac{1}{\mathrm{SNR}_{HV}}\right)\right]. \tag{6.33}$$

When sampling is limited to the duration of the echo, the value of N is equal to the pulse width, T_p, divided by the sample period. Because the signal is sampled at the

Nyquist rate for quadrature, the sample period is simply the inverse of the signal bandwidth, B_s. Equation (6.33) then becomes

$$\mathrm{Var}\left[\sigma_{\widetilde{HVVV}}\right] = \frac{1}{2T_pB_s}\left[\sigma^2_{HVVV} + \sigma_{VV}\sigma_{HV}\left(1+\frac{1}{\mathrm{SNR}_{VV}}\right)\left(1+\frac{1}{\mathrm{SNR}_{HV}}\right)\right]. \qquad (6.34)$$

Equation (6.34) is a significant result. Note that the variance of the correlation term is a function of both the co- and cross-pol SNR's. Because $\mathrm{SNR}_{VV} \gg \mathrm{SNR}_{HV}$, the variance is dominated by the signal-to-noise ratio in the cross-polarized return. As an example, let us consider the case previously described of a measurement made at an incidence angle of 54° with an 8 m/s wind blowing at an azimuth of 45°. Here, $\sigma_{VV} = 0.012$, $\sigma_{HV} = 0.00038$, and $\sigma_{HVVV} = 0.0006$. For a *SeaWinds*-class scatterometer, these values imply $\mathrm{SNR}_{VV} = 11\mathrm{dB}$ and $\mathrm{SNR}_{HV} = -4\mathrm{dB}$. Also for a *SeaWinds* class instrument, $T_p = 1.5$ ms and $B_s = 40$ kHz. Defining the normalized standard deviation of the correlation as $K_{pc} = \sqrt{\mathrm{Var}[\sigma_{\widetilde{HVVV}}]}/\sigma_{HVVV}$, we have from Eq. (6.34) that $K_{pc} = 54\%$. Because the standard deviation is smaller than the value of the correlation term itself, the measurement may be considered statistically significant.

6.4.2 Variance Calculation: Cross-Talk Present

The preceding analysis addressed the idealized case where the co- and cross-polarized terms were perfectly isolated and the noise components in each channel were independent. In reality this is never exactly the case. In this section, the variance analysis is extended to the situation where cross-correlation between the channels may be significant.

We begin by assuming that the signal in each channel can be approximated as

$$\begin{aligned} C_H(t) &= \frac{\lambda^2}{(4\pi)^3}\int d^2\bar{r}\ \frac{h^r_{HH}\mathcal{S}_{HV}h^t_{VV}}{|\bar{r}|^2}s^t_V(t-\frac{2|\bar{r}|}{c})e^{i\omega_d t} \qquad (6.35)\\ &\quad + \frac{\lambda^2}{(4\pi)^3}\int d^2\bar{r}\ \frac{h^r_{HV}\mathcal{S}_{VV}h^t_{VV}}{|\bar{r}|^2}s^t_V(t-\frac{2|\bar{r}|}{c})e^{i\omega_d t} + \nu_H(t)\\ C_V(t) &= \frac{\lambda^2}{(4\pi)^3}\int d^2\bar{r}\ \frac{h^r_{VV}\mathcal{S}_{VV}h^t_{VV}}{|\bar{r}|}s^t_V(t-\frac{2|\bar{r}|}{c})e^{i\omega_d t} + \nu_V(t). \end{aligned}$$

Equation (6.35) is equivalent to assuming that the dominant cross-talk contamination is from the co-pol (VV) term leaking into the cross-pol (HV) channel. We further assume that $h^r_{HH} = h^r_{VV}$ and that $h^r_{HV}/h^r_{HH} = \alpha$, where α is a real constant for all $\bar{r}$. This is equivalent to saying that the cross-polarized gain of the H-pol channel on receive is identical to the co-polarized gain attenuated by some real constant. By forcing all the signal terms to be "in-phase" a more tractable problem is achieved that also produces a conservative bound on the variance. The noise terms are likewise assumed to be "in-phase." Utilizing the above assumptions, Eq. (6.35) is expressed as

$$\begin{aligned} C_H(t) &= s_{HV} + \alpha s_{VV}(t) + \nu_H(t) \\ C_V(t) &= s_{VV} + \nu_V(t). \end{aligned} \tag{6.36}$$

Next an expression for the variance of $\sigma\widetilde{_{HVVV}}$ is derived. First, it is assumed that the estimate of $\langle \nu_V \nu_H^* \rangle$ – which is now non-zero due to cross talk – is determined by an independent, large band-width measurement, and hence has negligibly low-variance. Secondly, it is noted that $X_1 = X$ and $X_2/X_1 = \alpha$. We then write

$$\begin{aligned} \mathrm{Var}\left[\sigma\widetilde{_{HVVV}}\right] &= \frac{\mathrm{Var}\left[\langle C_V\widetilde{C}_H^* \rangle\right]}{X^2} + \alpha^2 \mathrm{Var}\langle\widetilde{\sigma_{VV}}\rangle \\ &\quad + \frac{2\alpha}{X}\left(\mathcal{E}\left[\langle C_V\widetilde{C}_H^* \rangle\right]\mathcal{E}\left[\langle\widetilde{\sigma_{VV}}\rangle\right] - \mathcal{E}\left[\langle C_V\widetilde{C}_H^* \rangle\langle\widetilde{\sigma_{VV}}\rangle\right]\right). \end{aligned} \tag{6.37}$$

The term $\mathrm{Var}\langle\widetilde{\sigma_{VV}}\rangle$ is given by Eq. (6.10). Using stochastic signal processing techniques similar to that employed for the no cross-talk case, it can be shown, after some tedious algebra, that

$$\begin{aligned} \frac{\mathrm{Var}\left[\langle C_V\widetilde{C}_H^* \rangle\right]}{X^2} &= \frac{1}{2T_pB_s}\left[\sigma^2_{HVVV} + \sigma_{VV}\sigma_{HV} + \frac{\sigma_{VV}\sigma_{HV}}{\mathrm{SNR}_{HV}} + \frac{\sigma_{VV}\sigma_{HV}}{\mathrm{SNR}_{VV}}\right. \\ &\quad + \frac{\sigma_{VV}\sigma_{HV}}{\mathrm{SNR}_{VV}\mathrm{SNR}_{HV}} + 4\chi\sigma_{HVVV}\sigma_{VV} + 2\chi^2\sigma^2_{VV} \\ &\quad + \frac{2\kappa\sigma_{HVVV}\sqrt{\sigma_{VV}\sigma_{HV}}}{\sqrt{\mathrm{SNR}_{VV}\mathrm{SNR}_{HV}}} + \frac{2\kappa\chi\sigma_{VV}\sqrt{\sigma_{VV}\sigma_{HV}}}{\sqrt{\mathrm{SNR}_{VV}\mathrm{SNR}_{HV}}} \\ &\quad \left. + \frac{2\chi\sigma_{HVVV}\sigma_{VV}}{\mathrm{SNR}_{VV}} + \frac{\chi^2\sigma^2_{VV}}{\mathrm{SNR}_{VV}} + \frac{\kappa^2\sigma_{VV}\sigma_{HV}}{\mathrm{SNR}_{VV}\mathrm{SNR}_{HV}}\right], \end{aligned} \tag{6.38}$$

and that,

$$\frac{2\alpha}{X}\left(\mathcal{E}\left[\langle\widetilde{C_V C_H^*}\rangle\right]\mathcal{E}\left[\langle\widetilde{\sigma_{VV}}\rangle\right]-\mathcal{E}\left[\langle\widetilde{C_V C_H^*}\rangle\langle\widetilde{\sigma_{VV}}\rangle\right]\right)=$$
$$\frac{1}{2T_pB_s}\left[-4\alpha\sigma_{VV}\sigma_{HVVV}-4\alpha^2\sigma_{VV}^2-\frac{4\kappa\chi\sigma_{VV}\sqrt{\sigma_{VV}\sigma_{HV}}}{\sqrt{\mathrm{SNR}_{VV}\mathrm{SNR}_{HV}}}\right.$$
$$\left.-\frac{4\alpha^2\sigma_{VV}^2}{\mathrm{SNR}_{VV}}-\frac{4\alpha\sigma_{VV}\sigma_{HVVV}}{\mathrm{SNR}_{VV}}-\frac{4\kappa\chi\sigma_{VV}\sqrt{\sigma_{VV}\sigma_{HV}}}{\mathrm{SNR}_{VV}\sqrt{\mathrm{SNR}_{VV}\mathrm{SNR}_{HV}}}\right]. \tag{6.39}$$

Here, κ is defined as

$$\kappa=\frac{\mathcal{E}[\nu_V\nu_H]}{\sqrt{\mathcal{E}[\nu_V^2]\mathcal{E}[\nu_H^2]}}, \tag{6.40}$$

in order to characterize the inter-channel noise correlation. Note that when $\kappa=0$ and $\alpha=0$, a case equivalent to having no cross-talk between channels, Eqs. (6.37)-(6.40) reduce to Eq. (6.34). Another useful case to examine is when $\kappa=1$, $\alpha=1$, $\sigma_{HV}=\sigma_{VV}=\sigma_{HVVV}$, and $\mathrm{SNR}_{VV}=\mathrm{SNR}_{HV}$. This case is equivalent to a situation where the two terms to be correlated are the same, and is identical to the detection in co-pol scatterometry, where

$$\mathrm{Var}\left[\sigma_{\widetilde{HVVV}}\right]=\frac{\sigma_{VV}^2}{T_pB_s}\left[1+\frac{2}{\mathrm{SNR}_{VV}}+\frac{1}{\mathrm{SNR}_{VV}^2}\right]. \tag{6.41}$$

To assess the impact of cross-talk on the variance, some sample cases are examined. First, the assumption is made that the noise in each channel can be modeled as

$$\begin{aligned}\nu_V &= \nu_V'+\alpha_\nu\nu_H'\\ \nu_H &= \nu_H'+\alpha_\nu\nu_V',\end{aligned} \tag{6.42}$$

where ν_V' and ν_H' represent uncorrelated components of the noise in each channel, and α_ν is the voltage cross-talk attenuation factor between the two channels. If it is further assumed that $\mathcal{E}[\nu_V^2]=\mathcal{E}[\nu_H^2]$, and that α_ν is small, it can be shown that

$$\kappa\approx 2\alpha_\nu. \tag{6.43}$$

Adopting the above assumption, we address the variance for the previously discussed case (where V-Pol is transmitted, the incidence angle on the surface is 54°, the wind speed is 8 m/s, and the wind direction is 45° in azimuth relative to

the illumination direction). To evaluate the effect of cross-talk, it is assumed that $\alpha_\nu = \alpha = 0.03$. This corresponds to a case where the *power* isolation is -30 dB. Evaluating all the terms in Eqs. (6.37)-(6.40), a normalized standard deviation of 57% is calculated, compared to 54% calculated for the no cross-talk example of Section 6.4.1. This represents only a small increase despite the fact that the correlation bias, defined as the ratio of $\alpha\sigma_{VV}$ to σ_{HVVV}, is relatively large. This result is due to the fact that the variance estimate is still primarily determined by the high level of noise in the cross-pol measurement. Thus, the existence of a reasonable level of cross-talk does not effect the measurement variance of σ_{HVVV}.

6.5 Conclusions

In this chapter, a framework for addressing the measurement accuracy for a polarimetric scatterometer was presented, and expressions for the measurement variance of the polarimetric correlation term were derived. It was shown that despite the significantly lower SNR associated with the cross-polarized return, statistically significant measurements can still be made of the polarimetric correlation effect. It was further demonstrated that the deleterious effect of channel-to-channel cross-talk contamination may be sufficiently suppressed for most wind scatterometer applications.

These results are of great significance to future scatterometer systems. A *SeaWinds* class pencil-beam scatterometer instrument can be augmented to make polarimetric measurements by employing an additional receiver, some additional switching, and an antenna which has adequate cross-pol isolation. Because of the superior cross-pol isolation of reflector antennas relative to array antennas, pencil-beam scatterometer systems are uniquely capable of making the polarimetric measurements required for wind retrieval improvement.

Chapter 7

Synthetic Aperture Techniques

In both Chapters 4 and 5, a major limiting factor for the pencil-beam scatterometer resolution was observed to be the width of the antenna beam pattern. As discussed in Chapter 5, this limitation can be overcome somewhat by employing a combination of range processing and enhanced resolution imaging (ERI) techniques. Both multi-pass and single-pass ERI techniques were considered. A shortcoming of multi-pass techniques is that they typically require the scene to be temporally stable and/or azimuthally isotropic. Many natural phenomena violate these assumptions. The primary shortcoming of single-pass techniques is that it is difficult to obtain the approximately 1 km resolution desired for many Earth science applications (see Chapter 1).

As discussed in Section 3.2.3, an established method for improving resolution beyond the real-aperture limit is to employ Doppler discrimination simultaneous with range discrimination in order to obtain a spatial response function which is narrow in two dimensions. This approach is the basis of synthetic-aperture radar (SAR) – widely used in high resolution imaging applications – but has not been previously applied to the conically-scanning scatterometer case. In this chapter, combined range/Doppler discrimination techniques are proposed for the first time as a means to improve the single-pass resolution of future pencil-beam scatterometer systems. The unique considerations associated with the addition of Doppler beam sharpening to a conically scanning radar are described, and expressions for the fundamental performance constraints and best theoretical resolution of such a system are derived. To

illustrate the utility of the combined range/Doppler resolution approach, two conceptual design examples based on pencil-beam scatterometer systems of current interest are provided. It is shown that an order of magnitude improvement in spatial resolution can be achieved by employing the Doppler-sharpening technique, albeit with requirements for a somewhat larger antenna and increased PRF relative to either beamwidth-limited or real-aperture systems.

7.1 Real- vs. Synthetic Aperture Techniques

Figure 7.1 illustrates the two primary techniques for obtaining sub-footprint resolution with a pencil-beam scatterometer system. The real-aperture approach discussed in Chapter 5, where only range discrimination is employed, is shown in Fig. 7.1(b). The resolution cell is indicated by the shaded region. Here, the azimuth resolution is the azimuthal width of the antenna footprint, x_{az}. The elevation resolution, δ_{el}, is achieved by applying range processing to the radar echo return, forming narrow elevation "slices" through the footprint. As previously discussed, the real-aperture approach is relatively easy to implement in hardware and is employed with *SeaWinds* [84]. The key disadvantage of this approach is that large antenna apertures are required to obtain high-resolution. For example, to achieve an instantaneous azimuth resolution of 1 km with a Ku-Band system operating with the same measurement geometry as *SeaWinds*, an antenna length of over 20 meters is required.

In order to obtain improved azimuth resolution without resorting to an unrealistically large rotating antenna, the target scene can be discriminated in both range and Doppler simultaneously. The resulting resolution is shown conceptually in Fig. 7.1(c). In this case, the azimuth width of the resolution cell, δ_{az}, is determined by the Doppler resolution achieved by the instrument and processor design. The technique of employing both range and Doppler discrimination simultaneously will equivalently be referred to as "Doppler-sharpening" in this chapter.

As shown in Section 3.2.3, combined range/Doppler processing can be viewed as a correlation operation applied to an echo pulse train which extracts the backscattered energy from specific locations in range/Doppler space. Key design considerations include the selection of an antenna pattern and PRF which suppress range and Doppler ambiguities, and which yield the desired azimuth resolution and swath width. Such techniques are the foundation of synthetic-aperture radar (SAR), which has been used extensively for high-resolution imaging applications, and form the basis for the improved-resolution scatterometry discussed in this chapter.

Although the application of Doppler techniques to a conically-scanning scatterometer system is similar in principle to the familiar SAR case, there are key differences. SAR systems typically employ array antennas which view the surface at a fixed (usually side-looking) azimuth angle – as in strip-map or scan-SAR – or are steered in azimuth to dwell on a specific target region – as in spotlight-SAR. By contrast, the antenna footprint of pencil-beam scatterometer is continuously rotated away from the target scene at a rate much faster than that generated by the spacecraft motion alone. This dramatically reduces the target dwell time relative to conventional SAR, and thus limits the achievable azimuth resolution. Another consideration for a conically-scanned radar is that the azimuth angle of the measurements varies over the measurement swath. This is equivalent to having a different squint angle for each measurement, and leads to a variation in resolution performance over the swath. In order to address these and other considerations in detail, a new design framework is developed which adapts established Doppler techniques to the unique issues associated with a conically-scanned radar geometry.

7.2 Instrument Design Considerations for Pencil-Beam Scatterometers Employing Simultaneous Range/Doppler Discrimination

In this section, key considerations governing the design and performance of a conically-scanned scatterometer utilizing combined range/Doppler discrimination techniques are addressed. For brevity, familiarity with standard SAR terminology and techniques is assumed (see [11, 18, 95]), and emphasis is therefore on the unique

system design issues posed by such an approach. This analysis results in a set of equations which can be used for conceptual design tradeoffs in the development of future high-resolution pencil-beam scatterometer systems.

7.2.1 Doppler Geometry and Azimuthal Dependent Resolution Effects

When applying Doppler discrimination techniques, a fundamental consideration is the geometrical relationship of the range and Doppler contours over the entire region scanned by the antenna. In Fig. 7.2, contours of iso-range and iso-Doppler are plotted for the example case of an 800 km, sun-synchronous orbit (the same as *SeaWinds*). The antenna beam position is termed "side-looking" when $\theta_{az} = 90°$ or 270°, and "forward-" or "aft-looking" when $\theta_{az} = 0°$ or 180° respectively. Note that the pencil-beam azimuth angle, θ_{az}, is the complement of the squint angle as typically defined for a SAR systems. The cross-track distance, CTD, is defined to be the distance of a given measurement from the spacecraft nadir track.

The above described Doppler geometry has important implications for the achievable azimuth resolution. A spatial resolution cell is delimited by the intersection of range and Doppler bands, where the width of these bands corresponds to the Doppler and range resolution achieved by the radar instrument. When the antenna is pointed to the side-looking direction, the angle between the Doppler and range contours in the vicinity of the footprint is 90°, and the resolution cell is rectangular. As the antenna is scanned (or squinted) toward the forward or aft direction, however, we observe from Fig. 7.2 that the Doppler contours shift from perpendicular to parallel with the range contours. This rotation of the iso-Doppler lines distorts the resolution cells into parallelograms whose azimuth width, δ_{az}, is elongated with respect to the azimuth width for the side-looking geometry. This elongation effect is further enhanced by the fact that the spacing between the iso-Doppler lines on the surface grows wider as the antenna is rotated away from the side-looking direction (again, see Fig. 7.2). The total azimuth resolution degradation relative to the side-looking pointing shall be termed "squint elongation."

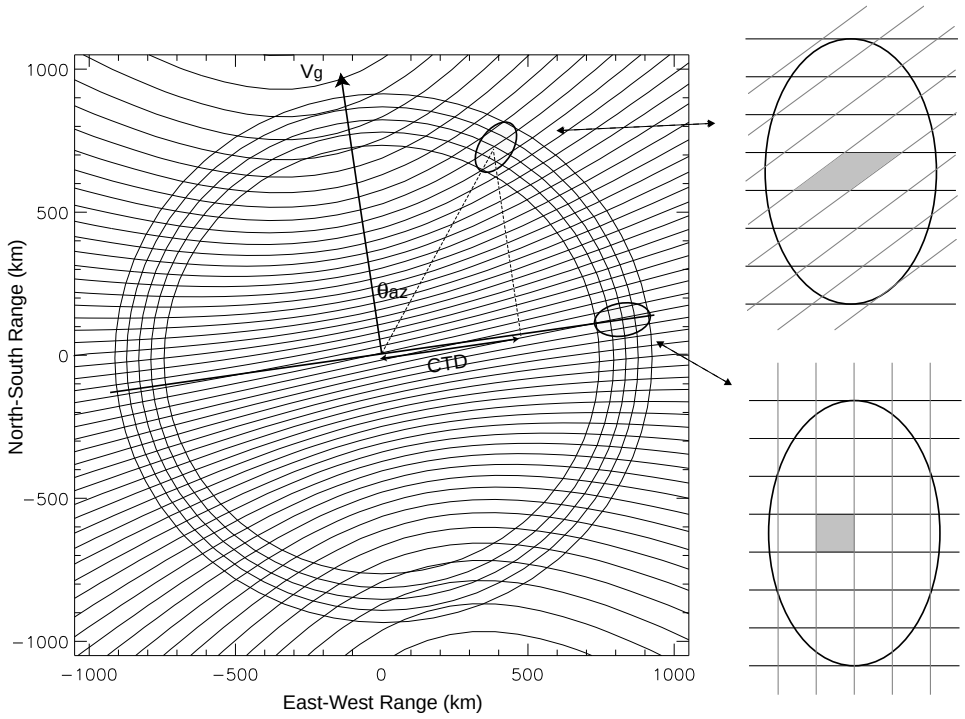

Figure 7.2: Lines of iso-Doppler and iso-range for 800 km sun-synchronous orbit at ascending equator crossing. The hyperbolic iso-Doppler contour spacing is 20 kHz. Also shown are circles representing the iso-range contours associated with the antenna footprint. Other iso-range lines, if plotted, would appear as more concentric circles likewise centered on the nadir point. The sidebar at right illustrates the relationship of the range/Doppler contours local to the antenna footprint for two antenna azimuth positions, with the shaded region representing the resolution cell.

An exact quantification of squint elongation requires a calculation which includes accurate satellite orbit propagation, Earth rotation, and Earth oblateness effects (these are taken into account in producing the iso-Doppler contours of Fig. 7.2). The assumption of a non-rotating, spherical Earth, however, yields results with sufficient accuracy for the concept analysis presented here. Adopting this assumption, the first derivatives of the Doppler shift components along the elevation and azimuth directions in the vicinity of the surface footprint, s'_{el} and s'_{az}, are approximated by:

$$\begin{aligned} s'_{az} &= \left[-2v_{sc}\sin(\theta_{az})\right] / \left[R\lambda\right] \\ s'_{el} &= \left[2v_{sc}\cos(\theta_{az})(1-\sin^2(\theta_{inc}))\right] / \left[R\lambda\right]. \end{aligned} \tag{7.1}$$

Because the iso-range lines are locally parallel to the footprint azimuth axis, the angle between the iso-Doppler and iso-range contours, ψ, is

$$\psi = \arctan\left(\frac{s'_{el}}{s'_{az}}\right), \tag{7.2}$$

and the magnitude of the Doppler frequency gradient along the surface of the Earth, s', is given by

$$s' = \sqrt{(s'_{el})^2 + (s'_{az})^2}. \tag{7.3}$$

Using these definitions, the "angular" component of the elongation, $f_{ang}(\theta_{az})$, due to the rotation of the iso-Doppler lines is

$$f_{ang}(\theta_{az}) = \frac{1}{\cos\psi}, \tag{7.4}$$

and the additional elongation due the Doppler contour spacing, $f_{sp}(\theta_{az})$, is

$$f_{sp}(\theta_{az}) = \frac{s'(\theta_{az})}{s'(\theta_{az} = 90°)}. \tag{7.5}$$

In Fig. 7.3, the angular and Doppler spacing elongation effects, as well as the combined elongation effect given by $f(\theta_{az}) = f_{ang}(\theta_{az})\ f_{ang}(\theta_{az})$, are plotted vs. CTD for the geometry corresponding to Fig. 7.2. (Similar curves apply for other orbit and scan geometries.) The significance of Fig. 7.3 for the present analysis is that, unlike the conventional real-aperture or SAR case where azimuth resolution is essentially a constant value over the measurement swath, the azimuth resolution for the Doppler-sharpened pencil-beam scatterometer case is highly dependent on cross-track position. As an illustration, consider that a system design capable of achieving 1 km azimuth resolution at a cross-track distance of 800 km (side-looking case), can only obtain an azimuth resolution of 2 km at a cross-track distance of 400 km, and 4 km at 200 km cross-track. The azimuth resolution quickly degrades near the nadir track, ultimately becoming the same as that achieved by a real-aperture system. The variation in azimuth resolution over the swath must be taken into account when assessing the performance of a high-resolution pencil-beam design.

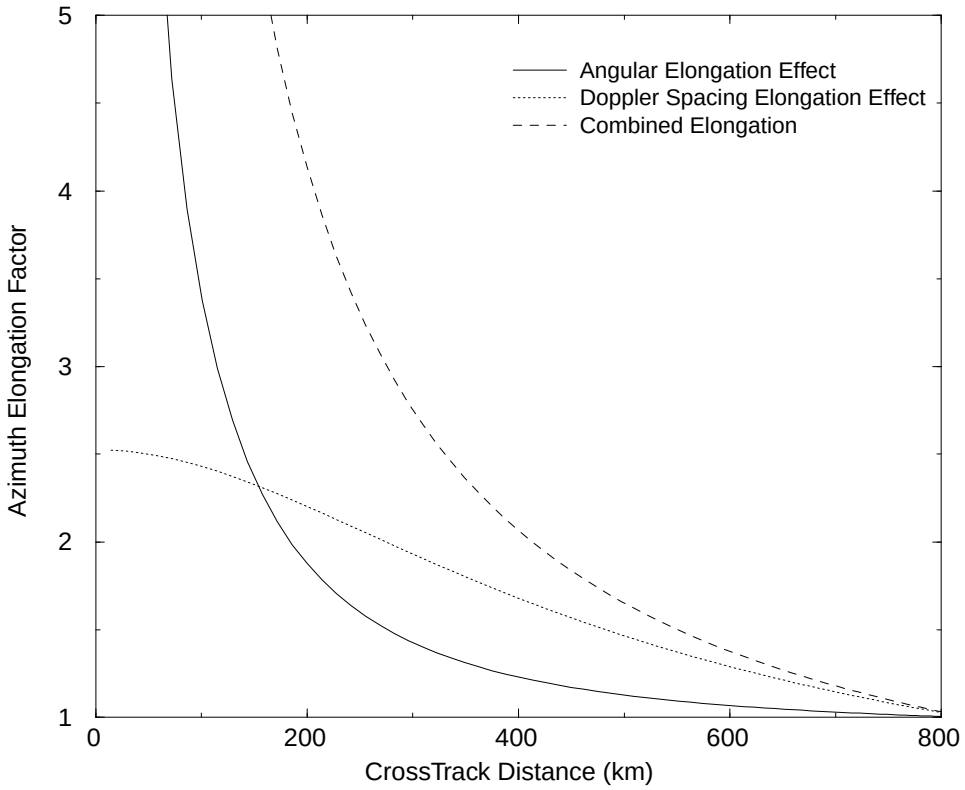

Figure 7.3: Angular, Doppler spacing, and combined elongation effect for scan geometry of Fig. 7.2.

7.2.2 Range/Doppler Ambiguity Considerations

As discussed in Section 3.2.3, another fundamental consideration is the suppression of range and Doppler ambiguities associated with the transmitted waveform. Ambiguity rejection constraints limit the allowable dimensions of the antenna footprint, and hence strongly impact the overall resolution performance of the radar design. The ambiguity issue can be visualized and addressed in a variety of ways. Given the rapid scanning motion of the antenna, an analysis based on the radar ambiguity function is found to be particularly useful for the pencil-beam scatterometer case. Our approach here is to first perform an ambiguity function analysis for the side-looking geometry, and then extend these results to the case of arbitrary azimuth angle.

In Fig. 7.4, a conceptual depiction of the ambiguity function of a periodic pulse train is shown. The dark spots represent the location of ambiguities in delay/Doppler space – the center spot representing the location of the desired resolution cell, and the other spots representing locations of unwanted ambiguities spaced at multiples of the pulse repetition frequency (PRF) and the pulse repetition interval (PRI=1/PRF) along the Doppler and delay axes respectively. As illustrated by Fig. 7.2, the local delay/Doppler coordinates may be transformed into elevation/azimuth coordinates, where the transformation is a function of the antenna azimuth position, θ_{az}. For the side-looking case the delay/Doppler axes are parallel to the elevation/azimuth axes.

In order to unambiguously detect the echo at the desired resolution cell, the unwanted ambiguity peaks must be suppressed by appropriate design of the antenna gain pattern. In Fig. 7.4, the effect of the antenna pattern is conceptually illustrated by concentric rectangles which represent contours of the two-way antenna gain pattern as projected on the delay/Doppler plane (or, equivalently for the side-looking case, on the elevation/azimuth plane). The outer rectangle is the contour that produces the desired level of ambiguity suppression. This contour may correspond, for example, to the -20 dB point in the two-way antenna pattern. The inner rectangle represents the "usable" region of the antenna footprint within which individual scatterers can be unambiguously detected. This contour, for instance, could correspond to the -3 dB level of the antenna pattern. The dimensions of the usable footprint in delay/Doppler space are x_{del} and x_{dop}, and are related to the dimensions of the outer contour by the parameters a and b as shown in Fig. 7.4. For the side-looking case, these dimensions are approximately related to the equivalent elevation/azimuth dimensions by

$$x_{el} = \frac{c}{2\sin\theta_{inc}} x_{del}, \tag{7.6}$$

and, utilizing Eq. (7.1) with $\theta_{az} = 90°$,

$$x_{az} = \frac{R\lambda}{2v_{sc}} x_{dop}. \tag{7.7}$$

As discussed in the following subsection, the best azimuth resolution is achieved by *maximizing* the usable footprint size. The relationship between the usable

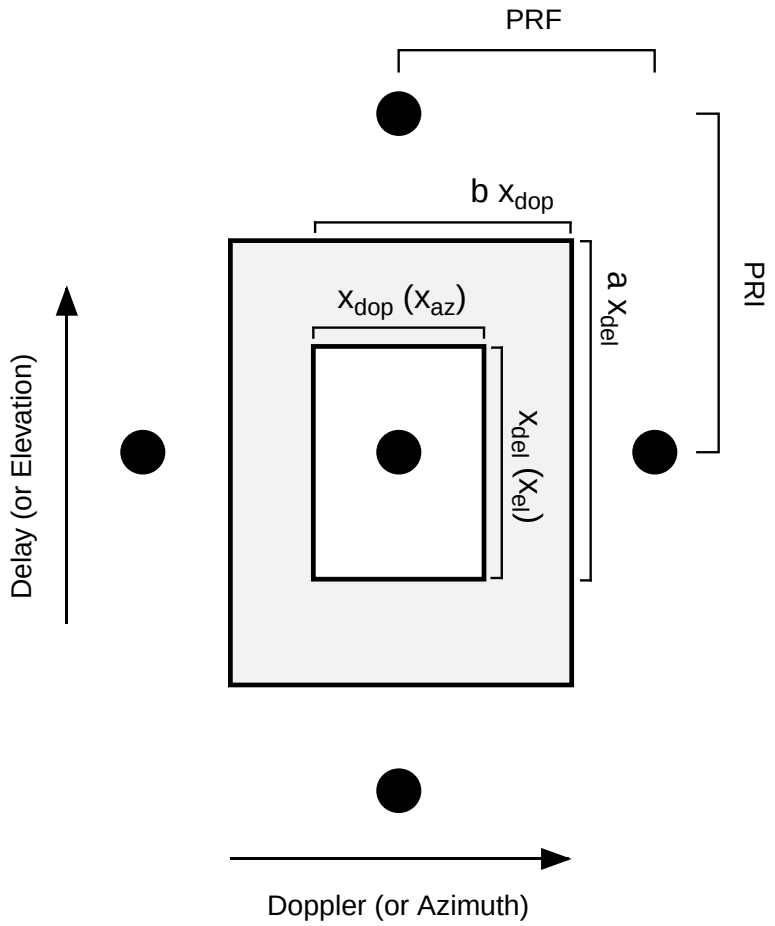

Figure 7.4: Spatial ambiguity diagram for the side-looking geometry. Dark spots represent Doppler/delay ambiguities for side-looking case. Concentric squares represent antenna pattern, with the center region defined as the usable footprint area.

footprint dimensions in delay/Doppler space and the PRF is summarized by

$$\begin{aligned} ax_{del} &\leq \text{PRI} \\ bx_{dop} &\leq \text{PRF}. \end{aligned} \tag{7.8}$$

Recalling that PRF $= 1/\text{PRI}$, we combine the two inequalities in Eq. (7.8) to write

$$x_{del}x_{dop} \leq \frac{1}{ab}. \tag{7.9}$$

Using Eqs. (7.8) and (7.9), when can then write

$$x_{el}x_{az} \leq \frac{cR\lambda}{4abv_{sc}\sin\theta_{inc}}. \tag{7.10}$$

Equation (7.10) is a key result for the current analysis. Based on ambiguity suppression considerations, it establishes a maximum constraint on the usable footprint dimensions.

Strictly speaking, Eq. (7.10) is valid only for the side-looking geometry. As the antenna is scanned forward or backward of this position, the Doppler and azimuth axes are no longer parallel as shown in Fig. 7.4, but are rotated and transformed consistent with Eqs. (7.1)-(7.5). As viewed from the perspective of the elevation/azimuth plane, this transformation neither changes the shape or dimensions of the projected antenna footprint (which is still $x_{el} \times x_{az}$), or the location of the ambiguities on the elevation axis. However, the loci of the ambiguities along the azimuth axis change, with the azimuth spacing between the ambiguities growing larger due to the same geometrical effects which lead to squint elongation discussed in the previous subsection. Consequently, as the antenna position points forward or aft, there is less contamination from the azimuth ambiguities than for the side-looking geometry. Equation (7.10) thus represents the limiting case, and we conclude that if the ambiguity constraint is satisfied for the side-looking case, it is satisfied at all other scan positions as well. (This argument is validated in a more quantitative fashion in Section 7.3.)

An important application of the constraint provided by Eq. (7.10) is the specification of antenna design parameters. In order to illustrate the tradeoffs associated with the antenna beamwidth, usable footprint dimensions, ambiguity level, and the a and b parameters; the design curves in Fig. 7.5 have been constructed. Here, the maximum ambiguity level associated with scatterers within the usable footprint is plotted vs. a (if elevation/range ambiguities are being addressed) or b (if azimuth/Doppler ambiguities are being addressed). Each curve, in turn, represents a different value of the usable footprint width expressed as a fraction of the two-way 3 dB beamwidth. The parameter χ is defined as $\chi_{el} = x_{el} \cos\theta_{inc} / R\beta_{el}$ for the elevation dimension, and $\chi_{az} = x_{az} / R\beta_{az}$ for the azimuth dimension. The ambiguity levels are computed assuming a representative antenna gain pattern roll-off function (Bessel function squared, in this case). As an example of the application of this plot,

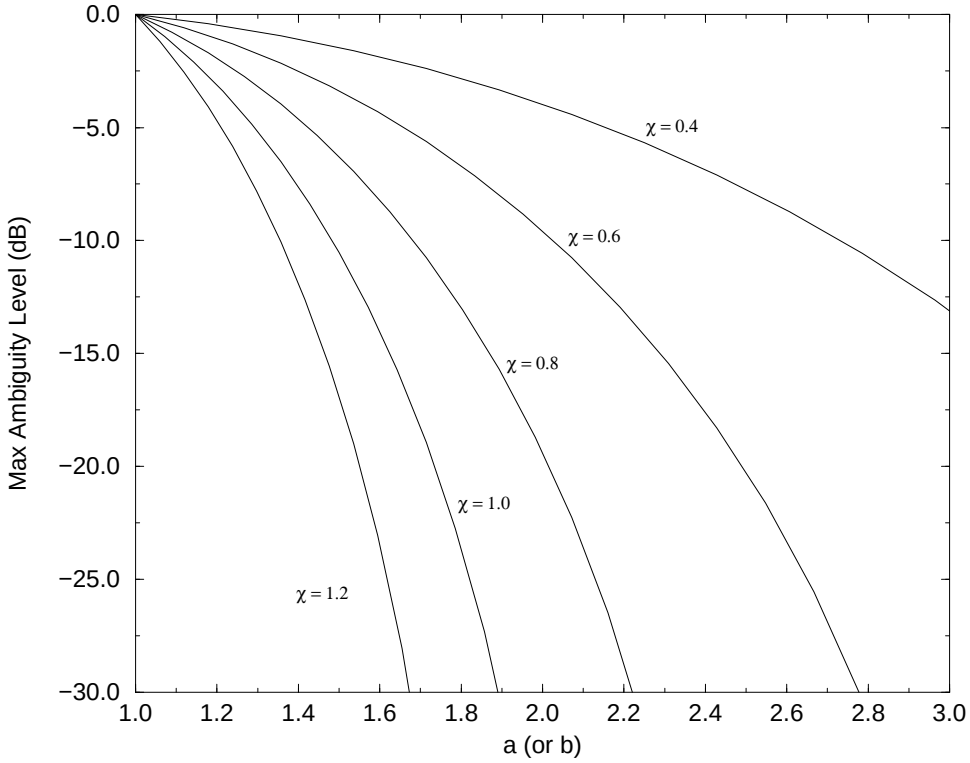

Figure 7.5: Design curves for trading-off antenna beamwidth, ambiguity, and the a and b parameters (see text).

if the requirement for ambiguities is -20 dB and the usable footprint is defined by the two-way 3 dB antenna contour, then $\chi_{el} = \chi_{az} = 1$ and, from Fig. 7.5, $a = b = 1.72$.

Inserting the definitions for χ_{el} and χ_{az} into Eq. (7.10),

$$\beta_{el}\beta_{az} \leq \frac{c\lambda \cot\theta_{inc}}{ab\chi_{el}\chi_{az}Rv_{sc}}. \tag{7.11}$$

Eq. (7.11) represents a constraint on the product of the antenna beamwidths and consequently on the minimum antenna area, and is similar to constraints used in the design of conventional SAR systems [11]. It is important to note that, depending on the requirements for a given application, an antenna with larger beamwidth may be acceptable if either the ambiguity suppression requirement is relaxed or if a smaller footprint can be tolerated [19].

7.2.3 Spatial Resolution

With constraints established for the usable footprint dimensions and antenna spin rate, we return to the topic of spatial resolution. When range discrimination is employed the finest elevation resolution achieved, δ_{el}, is

$$\delta_{el} = \frac{c}{2 \sin \theta_{inc} B_t}, \tag{7.12}$$

where B_t is the bandwidth of the transmit pulses. Note that Eq. (7.12) applies to all remote sensing radars, including real-aperture scatterometer systems and SAR. The key point of departure in the analysis of high-resolution conically-scanning scatterometers is the calculation of azimuth resolution. Due to the rapid scanning motion, commonly used design equations developed for conventional SAR systems do not fully apply.

The fundamental limit on azimuth resolution is determined by the antenna dwell time – i.e., the length of time a given scatterer is observed as the antenna footprint sweeps past. The relationship between the Doppler resolution, δ_{dop}, and the dwell time, τ_d, is approximately $\delta_{dop} = 1/\tau_d$. Employing an approximation similar to that used to obtain Eq. (7.7), the achievable azimuth resolution, δ_{az}, is

$$\delta_{az} = \frac{R\lambda}{2 v_{sc} \tau_d} f(\theta_{az}). \tag{7.13}$$

Here, the first (quotient) term is the azimuth resolution for the side-looking geometry and the term $f(\theta_{az})$ represents the degradation in resolution due to squint elongation effects as discussed in Section 7.2.1.

The maximum available footprint dwell time for a given point on the surface is

$$\tau_d = \frac{x_{az}}{\gamma}, \tag{7.14}$$

where x_{az} is the azimuthal width of the usable footprint, and γ is the azimuthal ground speed of the footprint due to the scanning motion as defined Eq. (3.3). Note that because γ is typically much greater than v_g, the dwell time available is dramatically shorter for the scanning pencil-beam case when compared to the typical SAR case.

The shorter dwell time reduces the azimuth resolution, and is the price paid for the extremely wide swath achieved by the conically-scanned pencil-beam approach.

As discussed in Section 3.1.3, the rotation rate of the antenna, and consequently the available dwell time for obtaining azimuth resolution, is a function of the antenna beamwidth dimensions. The ambiguity suppression constraints discussed in the previous subsection often require the antenna beam to be quite narrow. This has two impacts on the design of the scatterometer system. First, as addressed in Section 3.3.2, the scanning loss will increase. Secondly, as the beamwidth narrows, the rotation rate must increase in order to meet the along-track continuity constraint given by Eq. (3.6). The higher angular momentum that results from faster spin rates is undesirable because it requires a larger and more complex spacecraft attitude control system. In situations where it is undesirable to lengthen x_{el} in order to reduce the spin rate – such as when range ambiguities must be rejected – multiple antenna beams offset in elevation so as to cover a wider elevation range must be used. When this approach is adopted Eq. (3.6) becomes

$$\Omega \geq \frac{v_g}{N_b x_{el}}, \tag{7.15}$$

where N_b is the number of independent elevation beams employed. The term "independent" here means that the beams are sufficiently isolated in space, frequency, or polarization so that ambiguities associated with one beam do not contaminate the adjacent beams.

Inserting Eq. (7.14) into Eq. (7.13), applying both the along-track continuity constraint of Eq. (7.15) and the maximum usable footprint constraint in Eq. (7.10), and making the conservative assumption that $v_g \approx v_{sc}$; the best achievable azimuth resolution is then

$$\delta_{az} \leq \frac{4\pi d v_{sc} \sin\theta_{inc} ab}{N_b c} f(\theta_{az}). \tag{7.16}$$

Equation (7.16) indicates that δ_{az} is not a function of antenna size or carrier frequency, but depends only on the orbit and measurement geometry, the required ambiguity level (via a and b), and the number of independent elevation beams. The example system designs presented in Section 7.3 demonstrate that a value of δ_{az} on the order of

one kilometer can be readily achieved using this approach. This is significantly finer resolution than can realistically be achieved with real-aperture systems, but coarser than that achieved by typical SAR systems.

7.2.4 Transmit Pulse Timing

As discussed in Section 3.4.1, a practical consideration to be addressed in the design process is the selection of a radar timing scheme which insures that the transmission of pulses does not interfere with the reception of echo returns. In the development of Eq. (7.16) it was assumed that a given scatterer is observed for the entire the footprint dwell time – i.e., that the radar is pulsing continuously. This continuous pulse timing scheme is illustrated in Fig. 7.6(a). In addition to meeting the constraints in Eq. (7.8), the PRI must be selected to allow proper interleaving of the transmit events and receive echoes. Utilizing Eqs. (3.48)-(3.50) this interleaving constraint is expressed as

$$\left|(n+\frac{1}{2})\mathrm{PRI}-\frac{2R}{c}\right| \leq \frac{\mathrm{PRI}-2T_p-x_{del}-\Delta T_{marg}}{2}, \tag{7.17}$$

where n is an integer representing the number of pulses in flight, T_p is the pulse length, x_{del} is the round-trip delay between the inner and outer edges of the usable footprint [see Eq. (7.6)], and ΔT_{marg} is timing margin allowed for uncertainties in the precise value of R. The limit on the transmit pulse length is then

$$T_p \leq \frac{\mathrm{PRI}-x_{del}-\Delta T_{marg}}{2}. \tag{7.18}$$

For the wide swath and high incidence angles typically used for pencil-beam scatterometers, however, the constraints of Eq. (7.17) and Eq. (7.18) may be difficult to meet simultaneously. This is particularly true if significant timing margins are required in order to allow for spacecraft attitude variations and for land surface topography. We also see from Eq. (7.18) that, after the beam filling effect and necessary timing margin are taken into account, the available time for the transmit pulse width is limited. One solution to these problems is to adopt a burst pulsing scheme as shown in Fig. 7.6(b). For this timing scheme, a multiple-pulse burst of length τ_{bur} is

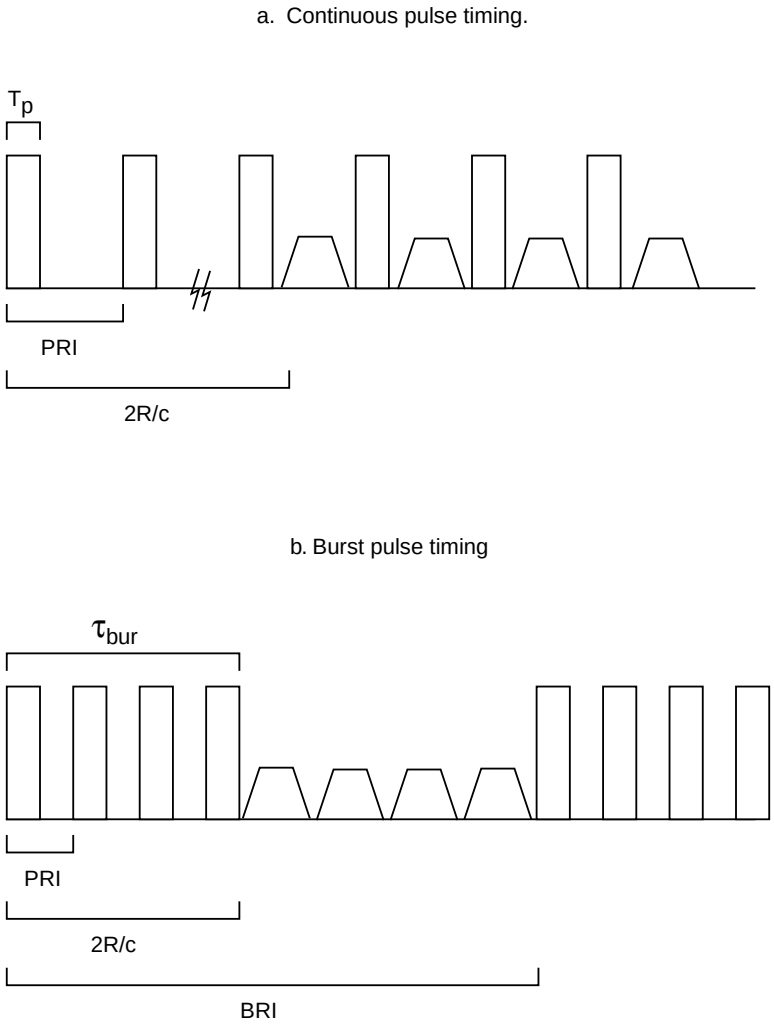

Figure 7.6: Pulse timing schemes: a) Continuous, b) Burst. Rectangles represent transmit events and trapezoids represent return echoes.

repeated at the *burst repetition interval*, BRI. The entire echo burst is then processed to obtain a range/Doppler discriminated "snapshot" of the surface, after which the footprint scans to an adjacent location.

With burst pulsing, however, new factors serve to decrease the available dwell time, and, consequently, the achievable azimuth resolution. Due to the rapid scanning of the antenna, the azimuthal width of the region imaged by a burst of pulses, x'_{az}, is given by

$$x'_{az} = x_{az} - \gamma \tau_{bur}. \tag{7.19}$$

Equation (7.19) indicates that only the surface region within the usable footprint during the entire burst period can be unambiguously measured. The constraint on allowable values of BRI is given by

$$2\tau_{bur} \leq \text{BRI} \leq \frac{x'_{az}}{\gamma}. \tag{7.20}$$

Here the upper bound on BRI results from the necessity to interleave transmit and receive burst events, and the lower bound results from the requirement to achieve azimuthal continuity of imaged regions on the surface. Inserting the definition of x'_{az} from Eq. (7.19) into Eq. (7.20), an expression for the maximum burst length, and hence maximum dwell time, is

$$\tau_d = \tau_{bur} \leq \frac{1}{3}\frac{x_{az}}{\gamma}. \tag{7.21}$$

Note that the maximum available dwell time is one third that of the continuous pulsing case, yielding

$$\delta_{az} \leq \frac{12\pi d v_{sc} \sin\theta_{inc} ab}{N_b c} f(\theta_{az}). \tag{7.22}$$

Thus, the timing simplicity obtained with burst pulsing comes at the price of a factor of three decrease in achievable azimuth resolution. However, the burst timing used here does not require interleaving of transmit and receive events, and thus is freed from the tight constraints imposed by Eq. (7.20) and Eq. (7.21).

Although only two timing schemes are addressed in detail – continuous, interleaved pulsing and non-interleaved burst pulsing – hybrid approaches are possible. One option applicable when more than one independent elevation beam is employed ($N_b > 1$) is to transmit pulse bursts alternately on each beam. In this way inter-beam interference may be avoided. For this case, the reception of the individual pulses within the burst may be interleaved with the transmit events in order to achieve longer integration times than if the scheme illustrated in Fig. 7.6(b) were strictly adhered to. This timing approach is applied to the L-Band design example in Section 7.6.

7.2.5 Scatterometer Measurement Variance

As with the beamwidth-limited and real-aperture systems discussed in previous chapters, it is important to consider the issue of backscatter measurement accuracy. In this section, the system trade-offs associated with minimizing backscatter measurement variance for a system employing simultaneous range/Doppler discrimination are addressed.

An estimate of normalized backscatter cross-section is obtained by subtracting the noise power component from the combined signal-plus-noise value detected by the receiver (as discussed in previous chapters.) Here, we express this process in a notation more consistent with synthetic-aperture analysis as

$$\tilde{\sigma^o} = \tilde{\sigma^o_{sn}} - \tilde{\sigma^o_{ne}} \tag{7.23}$$

where σ^o_{sn} is the apparent value of σ^o due to the combined echo signal and noise, σ^o_{ne} is the noise-equivalent value of σ^o (i.e., the apparent σ^o if no echo is present and only the thermal noise is processed), and the tilde indicates that the value is an estimate of a random quantity. An estimate of σ^o_{ne} is obtained by making an independent measurement of the receiver noise floor in a frequency band separate from the echo band, or at a quiescent time when the echo is not present. This estimate of the noise-only component must be subtracted to insure that estimates of σ^o are not biased high at low signal-to-noise ratios. Utilizing this notation, the signal-to-noise ratio (SNR) is given by σ^o/σ^o_{ne}.

An expression for the normalized measurement variance, K_{pc}, associated with the synthetic-aperture case is developed by extending the results of previous chapters. As discussed in Section 3.3.1, a single resolution element of dimensions $\delta_{el} \times \delta_{az}$ represents one independent look at the surface. In order to lower the measurement variance, it is necessary to average multiple independent looks together. The term A in Eq. (3.40) is consequently the inverse of the total number of $\delta_{el} \times \delta_{az}$ elements which are averaged to form a resolution cell. Defining N_{el} and N_{az} as the number of looks in the elevation and azimuth dimensions respectively, and utilizing the same

assumptions used in the development of Eqs. (4.9) and (6.33),

$$K_{pc} = \frac{\sqrt{\mathrm{Var}[\tilde{\sigma^o}]}}{\sigma^o} = \frac{1}{\sqrt{N_{el}N_{az}}}\left(1 + \frac{2}{\mathrm{SNR}} + \frac{1}{\mathrm{SNR}^2}\right)^{\frac{1}{2}}. \tag{7.24}$$

Note that the formation of multi-look cells degrades the overall elevation and azimuth resolution to $N_{el}\delta_{el}$ and $N_{az}\delta_{az}$ respectively.

A convenient approximation to the SNR achieved by synthetic-aperture systems is given by [95]

$$\mathrm{SNR} = \frac{P_t G^2 \delta_{el}\delta_{az}\lambda^2 (n_p T_p)\sigma^o}{(4\pi)^3 R^4 L N_0}, \tag{7.25}$$

where P_t is the peak transmit power, G is the antenna gain in the direction of the resolution cell, δ_{el} and δ_{az} are the dimensions of the single-look resolution cell, R is the slant range to the cell, L is the total system/path loss (including L_{scan}), N_0 is the thermal noise power spectral density, T_p is the length of an individual transmit pulse, and n_p is the number of coherently integrated pulses processed to form the cell.

Taken together, Eqs. (7.23) and (7.25) describe a key trade-off that must be performed in the design of high-resolution scatterometer systems. In order to minimize the measurement variance, it is generally desirable to average as many independent looks as possible. As discussed in Section 7.3, the ability to achieve fine azimuth resolution given the conically-scanning geometry is somewhat limited. Consequently, the ability to average multiple azimuth looks without significantly degrading the ultimate resolution is limited. There is considerably more flexibility to achieve finer elevation resolution, and hence more elevation looks, by utilizing a higher bandwidth transmit signal [see Eq. (7.12)]. As the elevation resolution decreases, however, there is a commensurate decrease in SNR via Eq. (7.25), which tends to increase the measurement variance as expressed in Eq. (7.24). The key trade-off here, as with the beamwidth-limited and real-aperture systems, is to obtain as many elevation looks as possible without overly degrading SNR.

Another source for additional looks is the overlap in the measurements due to successive rotations of the antenna. The along-track continuity constraint of Eq. (7.15) insures that measurements along the nadir track are just contiguous, but

there may be significant overlap in the measurements in regions of the swath away from nadir. When overlapping resolution cells from successive scans are combined, the total number of looks can be increased without degrading the final resolution associated with the multi-look cell.

7.3 Instrument Design Examples

The application of combined range/Doppler discrimination techniques to pencil-beam scatterometers is illustrated with two system examples of current interest. In each case, the framework described in the previous sections is used to establish high-level instrument design parameters and performance.

7.3.1 Ku-Band Design Example

First, the example of a Ku-Band system operating with the same orbit and measurement geometry as the *SeaWinds* scatterometer is considered (see Table 7.1). Assuming a circular reflector antenna is used, the antenna diameter must be increased from 1 m (current *SeaWinds* design) to 2.5 m in order to satisfy the ambiguity constraints as expressed in Eq. (7.11). The antenna size determines the beamwidth, as well as the footprint dimensions on the surface. These parameters then determine the required PRF via Eq. (7.8), which is 7.5 kHz. If only one elevation beam ($N_b = 1$) is employed, the spin rate must be at least 30 rpm to satisfy the along-track continuity constraint in Eq. (7.15). However, to allow a slower spin rate more comparable to the *SeaWinds* case of 18 rpm, two elevation beams are assumed for this example. Despite being slower, the spin rate combined with the narrow antenna beamwidths still leads a relatively high scanning loss of 8 dB. To compensate for this loss, transmit/receive beam steering must be performed on both elevation beams, complicating the antenna feed design somewhat.

The next major consideration is the pulse timing scheme. Because of the very high PRF required, it is difficult to maintain proper interleaving with a continuous pulsing scheme. A much more robust strategy for this system is to employ the burst pulsing approach, with bursts of 1.5 ms duration repeated every 3.2 ms,

Table 7.1: Example Ku-Band system employing range/Doppler resolution.

Parameter	Value
Frequency	14 GHz
Spacecraft Altitude	800 km
Measurement Incidence Angle	54°
Antenna Diameter	2.5 m
One-Way 3 dB Beamwidth	0.5°
Number of Elevation Beams	2
Rotation Rate	15 rpm
Uncompensated Scanning Loss	-8 dB
PRF	7.3 kHz
Burst Timing	$\tau_d = 1.5$ ms, BRI = 3.2 ms
Resolution ($\theta_{az} = 90°$)	1 km

selected to satisfy the constraint of Eq. (7.20). Utilizing Eq. (7.21), the resulting 1.5 ms dwell time yields an azimuth resolution of 1 km for the side-looking geometry. With the squint elongation effect taken into account, a resolution of between 1-3 km may be obtained over 70% of the total measurement swath, with the resolution rapidly degrading to the real-aperture limit near nadir (see Fig. 7.3). This example demonstrates that an order of magnitude improvement over the current *SeaWinds* resolution of 25 km may be obtained by incorporating the techniques described in this paper. The primary instrument enhancement required to achieve this performance is a larger antenna with a more complex feed system. An increase in antenna size appears readily feasible since spinning reflector antennas with diameters 2 meters or greater are planned for radiometer missions in the near future (such as the AMSR instrument to fly on the ADEOS-II mission in 2002).

7.3.2 L-Band Example

As a second example we address an L-Band system similar to a combined radar/radiometer instrument proposed in [68] for the measurement of soil moisture. For this concept, a six-meter deployable mesh reflector antenna is used at an orbital altitude of 670 km (see Fig. 7.7). As in the Ku-Band example, two elevation beams

are used to reduce the spin rate and consequently the angular momentum that must be compensated for by the spacecraft attitude control system. Unlike the Ku-Band example, however, the scanning loss is only -0.1 dB, a consequence of the wider L-Band beamwidths as well as the lower orbit. The low scanning loss allows a single antenna feedhorn to be used for both transmit and receive, significantly simplifying the feed design.

Table 7.2: Example L-Band system employing range/Doppler resolution.

Parameter	Value
Frequency	1.2 GHz
Spacecraft Altitude	670 km
Measurement Incidence Angle	40°
Antenna Diameter	6.5 m
One-Way 3 dB Beamwidth	2.7°
Number of Elevation Beams	2
Rotation Rate	6 rpm
Uncompensated Scanning Loss	-0.1 dB
PRF	3.5 kHz
Burst Timing	τ_d = 15 ms, BRI = 40 ms
Resolution ($\theta_{az} = 90°$)	1 km

Another beneficial consequence of the frequency and measurement geometry of this example is that a lower PRF (3.5 kHz) is required to perform the high resolution processing, which allows interleaving of transmit and receive events to be achieved more easily. In this design, bursts of 15 ms are alternately transmitted on the inner and outer beams to avoid interbeam interference. As in the previous example, the length of these bursts yields an azimuth resolution of 1-3 km over most of the swath. Again, the major design issue is the antenna size. Deployable mesh antennas larger than 6 m have been utilized for space communications, and the issues associated with spinning such antennas for remote sensing applications have been studied in detail. The L-Band system is currently under serious consideration for an actual mission in the 2005-6 time frame [68].

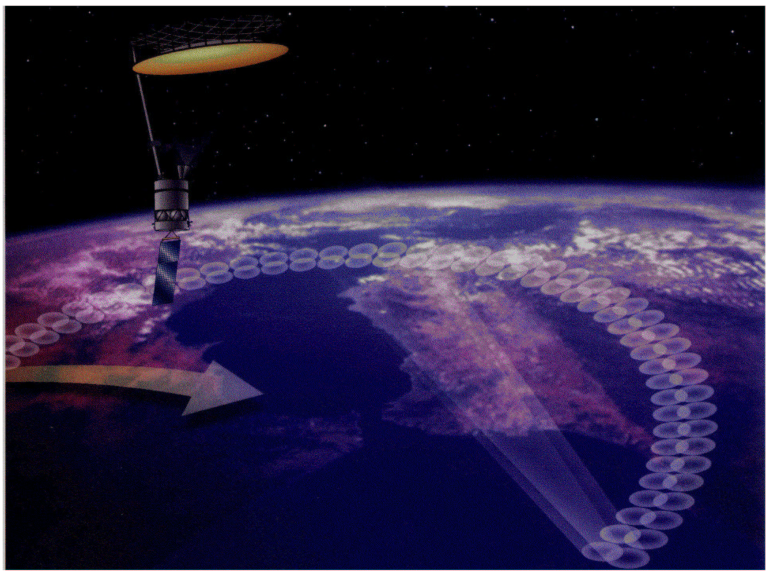

Figure 7.7: Conceptual drawing is shown of L-Band pencil-beam scatterometer utilizing six meter deployable mesh antenna proposed for future NASA mission.

7.4 Point-Target Response and Data Processing

In the preceding sections, Doppler beam-sharpening techniques have been adapted to the scanning pencil-beam scatterometer to yield a set of fundamental design equations and constraints. Although these expressions are sufficient to establish an initial conceptual design, more detailed calculations are required to verify the complex interplay between the Doppler geometry, ambiguities, antenna pattern, and scanning motion. Furthermore, the issue of data processing, which is a major consideration in the design of conventional SAR systems, must also be addressed.

7.4.1 Use of Spatial Response Function as Idealized Point-Target Response

An approach widely used in conventional SAR analysis to assess the combined effects of the instrument and processor design is the point-target response (PTR). The PTR quantifies the processor response at all locations within the scene to a single point scatterer. This concept is comparable to that of the spatial response function (SRF) derived in Section 3.2.3. The SRF represents the magnitude-squared

response to each location in the target scene when a correlation detector is exactly matched or "tuned" to the range/Doppler characteristics of a particular scatterer. The SRF is thus equivalent to the "ideal" PTR achieved if a perfect reference function is employed in the correlation process. Consequently, the SRF is useful to establish the best theoretical performance of the instrument design if a perfect processor is realized.

In Fig. 7.8, the SRF is computed for the Ku-Band example described in the previous section. This plot exhibits the effects discussed previously – including azimuth elongation, range/Doppler ambiguities, cell resolution – as well as important considerations not yet addressed – such as range/Doppler side-lobes. Note that the resolution and ambiguity levels are as predicted by the development in Section 7.2.2, hence validating the use of these design equations. In Fig. 7.9, the 3 dB contour for the SRF is shown for different azimuth angles, and the squint elongation predicted in Section 7.2.1 is evident.

By integrating over the SRF the effects of side-lobes, shown cascading from the central peak in Fig. 7.8, can be calculated. When N_{el} is large, the sidelobes in azimuth become the primary issue. If no windowing of the echo return is employed [equivalent to time domain windowing of the $R(t)$ term in Eq. (3.12)], the integrated side-lobe ratio (ISLR) is only about -10 dB, which may not be acceptable for many applications. Azimuth sidelobes can be minimized by applying a time-domain window function during processing. When a Hamming window is applied over the dwell period τ_d, the ISLR improves to -16 dB. The windowing, however, degrades the effective azimuth resolution and the measurement variance performance by a factor of approximately 1.6.

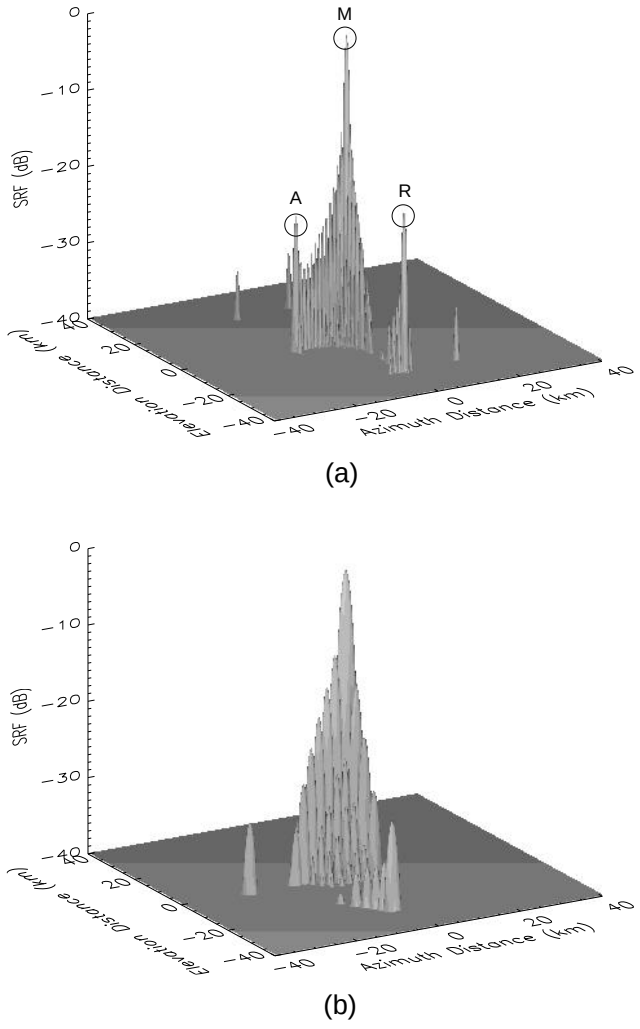

Figure 7.8: SRF diagram for the Ku-Band example of Section 7.3.1: (a) for side-looking geometry. The main ambiguity is indicated by "M", the first azimuth ambiguity by "A", and the first range ambiguity by "R." The SRF for $\theta_{az} = 30°$ is shown in (b). (exactly side-looking) for center pixel.

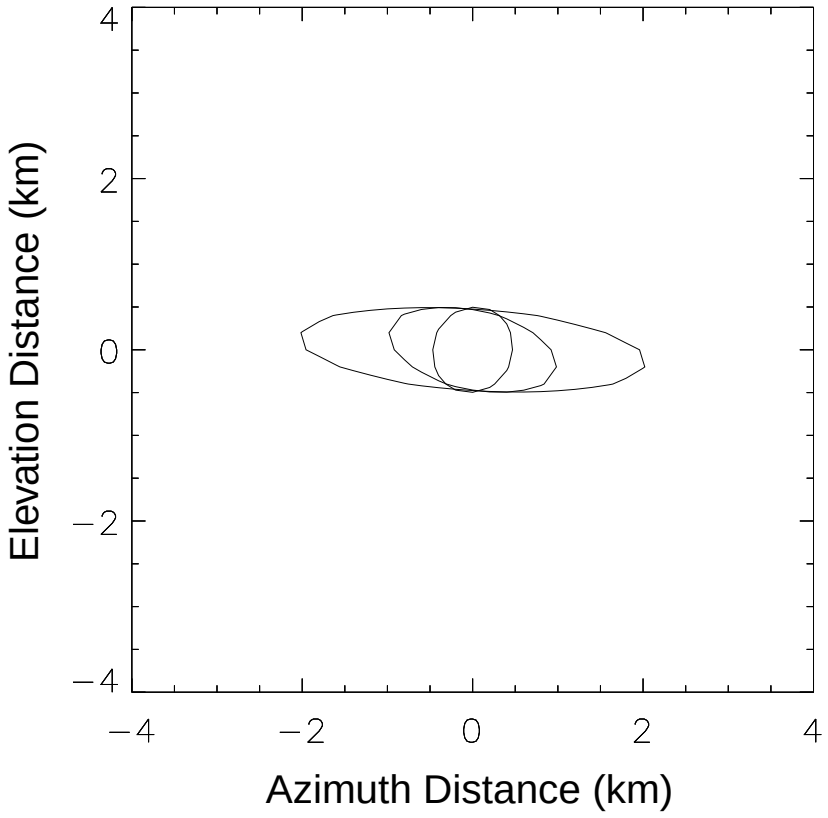

Figure 7.9: Comparison of -3 dB contour regions of the example SRF in Fig. 4.8 for cross-track distance of 800, 400, and 200 km.

7.4.2 Data Processing Issues

The primary goal of this chapter is to address the instrument requirements and theoretical performance of a conically scanning radar employing combined range/Doppler discrimination. However, it is clear that this resolution technique imposes new requirements on data processing beyond what is needed for current real-aperture pencil-beam systems. A treatment of the specific processing algorithms necessary to form the final high-resolution backscatter product is beyond the scope of the present analysis. High-resolution radar processing is an expansive and well studied topic (see [11], for example), and a variety of existing SAR algorithms can be adapted for the pencil-beam scatterometer case. In this subsection, some special processing considerations associated with a conically scanning radar are briefly discussed. In general, because the pencil-beam system achieves a low resolution (order of kilometers) when compared to conventional imaging SAR's, a relatively simple processing approach can be employed. New provisions must be made, however, for unique aspects of the conical geometry which include a continuously varying Doppler centroid and a helical posting pattern on the surface.

An important indication of processor complexity is the degree to which the Doppler shift of a given scatterer changes over the integration time. Using a criterion similar to that described in [95], it is noted that when

$$\frac{R\lambda}{2\delta_{az}^2} = \frac{2v_{sc}^2\tau_d^2}{R\lambda} \ll 1, \tag{7.26}$$

the Doppler shift change during the dwell time is smaller than the Doppler resolution. When Eq. (7.26) holds, an "unfocused" azimuth processing approach may be applied, where the Doppler for each scatterer is essentially assumed constant during the integration time. Because of the relatively short dwell times implied by Eq. (7.14), an unfocused Doppler compression algorithm can usually be applied to the pencil-beam scatterometer case, simplifying the processing.

Just as the Doppler shift of a specific scatterer my vary over the integration time, the range may vary as well. This "range walk" effect is known to be potentially severe for high squint angles [95]. If the range changes a significant fraction of the

range resolution, the range samples must be resampled to the desired locations previous to azimuth compression to avoid a de-focusing effect. To avoid having to correct for range walk, the following condition must hold:

$$\frac{v_g \tau_d}{\delta_{el}} \ll 1 \tag{7.27}$$

Equation (7.27) insures that at high squint angles (i.e., extreme forward or aft looking directions) that the range cell only moves a small fraction of the overall range resolution. Like Eq. (7.26), Eq. (7.27) generally holds for pencil-beam systems because of the very short integration times allowed by the rapidly moving footprint. When both of these conditions apply, a given scatterer may be assumed to be fixed in both range and Doppler, allowing the ideal PTR to be achieved with a relatively simple processing architecture.

As an example, consider the processing necessary for the Ku-Band example summarized in Table 7.1. Assuming that 10 range looks are desired for each 1 km resolution cell, there are a total of 110 single-look range pixels. For the burst integration time of 1.5 ms, a maximum of 11 pulses are used to form a synthetic aperture. Thus, the dimensions of the footprint is 110 by 11 single-look pixels. If, as is likely, a chirped transmit signal is used, range processing may be performed on the samples from each pulse by applying a 128-point forward FFT, multiplying by a de-chirp reference in the Fourier domain, and then applying a 128-point inverse FFT. Because the criteria in Eq. (7.27) is well satisfied for this example, the 110 range lines may be used "as is" (i.e., with no resampling to account for range walk effects). The condition given in Eq. (7.26) is also met for this example, so azimuth processing may be accomplished using a simple unfocused technique. For each range location, 11 sinusoidal reference functions are applied to remove the Doppler centroids. The 11 azimuth pixels are then formed by coherently summing the resultant signals, and then magnitude-squaring to obtain the backscattered power. This process is repeated for each pulse burst.

The above described processing is similar to unfocused algorithms used for conventional SAR [11, 95]. A key deviation for the pencil-beam case is that the

Doppler centroid for each azimuth pixel varies continuously over the antenna scan. When the orbit altitude is repeatable to within 1 km and the spacecraft attitude is known to $< 0.1^\circ$ – which is generally the case for modern satellite systems – these reference functions may be pre-computed and tabularized. The tabularization of computationally intensive aspects of scatterometer processing was used successfully with the *SeaWinds* system [1]. Lastly, it is noted that the natural posting of the pencil-beam pixels is in a helical pattern on the surface. If desired, the final multi-look product can be generated by averaging the Earth-located single-look pixels into "bins" in rectilinear coordinates centered on the spacecraft subtrack.

7.5 Summary and Conclusions

In this chapter, Doppler beam-sharpening techniques are employed with pencil-beam systems to achieve significant improvement in spatial resolution over current systems. A set of design equations have been presented to characterize the performance and facilitate design tradeoffs for such a system. Relative to current scatterometer instruments, the main impact of implementing combined range/Doppler discrimination is the requirement for a somewhat larger and more complex antenna. The required antenna diameters are within the range of what is feasible with today's technology, and are similar to devices which have flown on other scientific or commercial missions. As briefly noted, processing complexity – either on-board the instrument, within the ground data system, or both – also increases with the necessity to perform Doppler compression. Because resolution on the order of 1 km is obtained, with no need for focusing or range migration corrections, the additional processor complexity is modest relative to many conventional SAR systems.

A pencil-beam scatterometer with combined range/Doppler resolution represents an viable alternative to current scatterometer systems. The resolution achieved (order of 1 km) is between the coarse real-aperture resolution of scatterometers (tens of kilometers) and very high-resolution SAR's (tens of meters). Further, these measurements are obtained over a very wide swath – providing the frequent revisit time

necessary for studying global and mesoscale phenomena – and at near constant incidence angle – often simplifying geophysical parameter retrieval. The utilization of a reflector antenna to form the pencil-beam also allows multiple frequencies, multiple polarizations, and passive radiometer channels to be incorporated more easily than with an array design. These capabilities are becoming important as multi-channel techniques are increasingly used to obtain environmental parameters. Thus, with the noted advantages, and with no major theoretical or technological barriers, the improved resolution scatterometer approach addressed in this chapter can be seriously considered for future radar remote sensing missions.

Chapter 8

Summary and Conclusions

In the preceding chapters, a methodology for the design optimization and performance analysis of advanced pencil-beam scatterometers was developed. In Chapter 1, the importance of scatterometer data in a variety of Earth science applications was described. The state-of-the-art in scatterometer instrument theory was then reviewed in Chapter 2, and the shortcomings of current fan-beam scatterometer and side-looking SAR systems were addressed. In Chapter 3, advantages of a conically-scanning pencil-beam scatterometer approach were described. Here, a comprehensive framework was presented for the design of pencil-beam scatterometer systems.

In Chapters 4, 5, 6, and 7, a progression of increasingly advanced pencil-beam scatterometer design strategies was addressed. As shown graphically in Fig. 8.1, these include methods which can be used to improve both the spatial resolution and measurement accuracy of pencil-beam systems. In Chapter 4, it was shown how the addition of transmit signal modulation can be used to improve the measurement accuracy of simple beamwidth-limited scatterometer systems. In Chapter 5, real-aperture systems, where range discrimination processing is added to improve both resolution and measurement performance, were addressed. Results critical to the design and operation of the *SeaWinds* scatterometer were derived. This chapter also included a brief discussion of enhanced resolution processing. The new topic of polarimetric scatterometers, which have the potential to dramatically improve wind retrieval performance, was treated in Chapter 6. Finally, in Chapter 7, the application of synthetic-aperture techniques to obtain the highest possible resolution with a

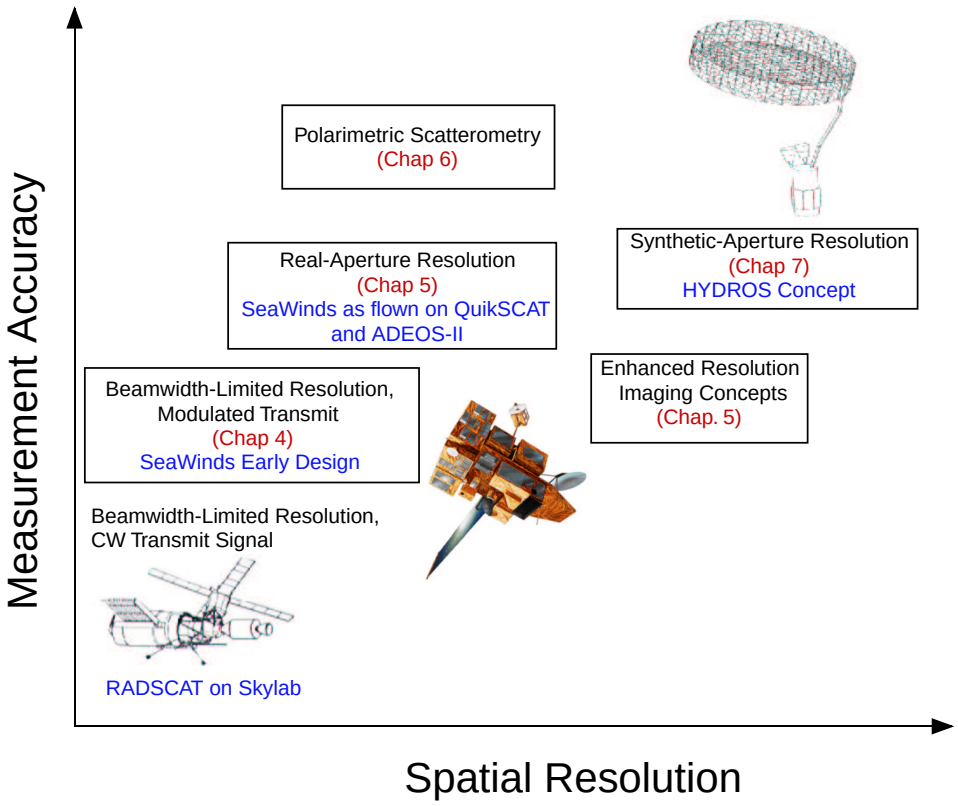

Figure 8.1: Diagram showing how the material in dissertation Chapters 4 through 7 has expanded the understanding of pencil-beam scatterometers. The "X" axis represents improved pencil-beam scatterometer resolution. The "Y" axis represents improved pencil-beam scatterometer measurement accuracy. Note that the boxed items represent areas of contribution from this dissertation.

pencil-beam scatterometer was studied, yielding a set of design formulae applicable to the next generation of scatterometer systems.

8.1 Contributions

This dissertation contains significant contributions to the field of microwave Earth remote sensing. These contributions can be categorized and summarized as follows:

8.1.1 General Pencil-Beam Theory

Side-looking fan-beam scatterometer systems have been extensively studied, with a well-established set of standard design equations available in the remote sensing literature. With the adoption of the pencil-beam approach for future NASA wind scatterometers, however, there is an increased need for a design framework which addresses the conically-scanning radar case. This dissertation fills this need. In Chapter 3, a series of equations are developed which serve as basic design aids in the selection of viewing geometry, antenna beamwidth, rotation rate, and pulse timing for pencil-beam systems. The generalized spatial response function (SRF) for a scanning pencil-beam system was derived. The SRF was shown to be a valuable tool in the analysis of pencil-beam resolution performance as the scan geometry changes.

8.1.2 Measurement Accuracy

Because fan-beam systems utilize fixed antennas, the target dwell time is very long, and the resulting averaging of the random radar echo produces very high measurement accuracy. With pencil-beam systems, however, the rapid scanning of the antenna yields relatively short dwell times. In this dissertation, new techniques are described which use transmit pulse modulation to achieve more independent looks in a shorter period of time. In Chapter 4, the SRF was demonstrated to be valuable in the analysis of pencil-beam measurement accuracy performance. It was concluded that the number of statistically independent looks associated with a measurement is equivalent to the number of independent resolution elements formed by a given modulated transmit signal. This result greatly simplifies scatterometer concept analysis, and was applied to demonstrate how pseudo-random phase modulation provides the best measurement performance with beamwidth-limited resolution systems.

When deramp processing is used to obtain range resolution, as discussed in Chapter 5 in the context of the *SeaWinds* scatterometer, it is shown that a wider bandwidth transmit pulse will improve measurement accuracy for each of the resulting σ^o cells. Finally, addressing the new technique of polarimetric wind scatterometry, an expression for the measurement error of a polarimetric signal in the presence of noise

was derived. It was further demonstrated that statistically significant measurements of the polarimetric signal can indeed by made.

8.1.3 Spatial Resolution

To expand the utility of scatterometer data to a range of new geophysical applications, it is desirable to improve the spatial resolution of the measurements. Previous to this dissertation, only beamwidth-limited pencil-beam scatterometers had been considered. In Chapter 5, it was discussed how range discrimination can be used to improve spatial resolution in the elevation dimension. The resulting formation of long, narrow σ^o slices was demonstrated to be particularly advantageous when multi-pass enhanced resolution imaging (ERI) algorithms are applied. Theoretical results for a single-pass ERI approach are also presented. The demonstration of such techniques is an important contribution because it allows a very simple hardware implementation to achieve a resolution finer than the inherent dimensions of the antenna footprint.

To obtain high resolution directly, without using post-processing methods such as ERI, Chapter 7 addressed how synthetic-aperture techniques can be extended to the pencil-beam scatterometer case. Here, a set generalized design equations for simultaneous range/Doppler discrimination with a conically-scanning radar are presented, and an expression for the highest theoretically achievable resolution of such a system was derived. This work is being employed in advanced NASA radars, such as the planned HYDROS mission.

8.1.4 The *SeaWinds* Mission

Many of the results presented in this dissertation were developed for, and have since been utilized by, NASA's *SeaWinds* scatterometer project – the first pencil-beam wind scatterometer to be flown in space. These results include the derivation of the exact spatial response function necessary for the calibration of the *SeaWinds* instrument, as well as the derivation of the expression for K_{pc} adopted in the *SeaWinds* wind processing algorithm. These results were developed and published previous to

the first flight of *SeaWinds* on the *QuikSCAT* satellite in June, 1999, and have been validated by the successful operation of the *SeaWinds* instrument over the past two years.

8.1.5 Pencil-Beam Measurement Contamination Sources

This dissertation provides an analysis of other unique issues presented by the conically-scanning pencil-beam measurement geometry. In Chapter 3 (as well as Appendix A), the contamination experienced by Ku-Band scatterometers due to the specular reflection of signals from the nadir direction is examined. Here, an analysis of data from a variety of nadir viewing Ku-Band radars is performed to develop an empirical curve for the mean and worst-case specular point returns for different Earth surface types. These curves were used to develop an expression for the minimum antenna sidelobe levels necessary to suppress the undesired nadir echo. It was also shown that, for the high incidence angles at which pencil-beam scatterometers operate, rain contamination can be severe at Ku-Band frequencies. Utilizing data from the TRMM rain radar, it was demonstrated that the dominant rain induced error source for moderate and high wind speeds is the backscattered signal from the rain itself, not attenuation through the rain layer as previously believed. The backscatter from the rain drops is predicted to produce an apparent enhancement of the echo signal strength, a conjecture which has subsequently been verified by analysis of *SeaWinds* data.

8.2 Future Work

The work presented in this dissertation addresses critical aspects of pencil-beam scatterometer design. Nevertheless, several important areas for future research are suggested in order to expand upon this study.

8.2.1 Pencil-Beam Wind Retrieval Algorithms

The primary focus of this dissertation is to develop a methodology for the optimum design of pencil-beam scatterometer *instruments*. The issues associated

with designing geophysical processing *algorithms*, such as those applied to the raw backscatter measurements to obtain estimates of the ocean wind vector, are not addressed in any detail. This is an important area for future research. Algorithms to process fan-beam scatterometer data into wind are quite mature, but the same can not be said for pencil-beam systems. The nature of the wind retrieval is quite different for the two different scatterometer approaches. Whereas a fan-beam scatterometer obtains measurements at fixed azimuth angles but different incidence angles, pencil-beam scatterometers do the opposite – collecting backscatter measurements at constant incidence angles but at variable azimuth angles over the swath. Although the pencil-beam measurement strategy is fundamentally different, the algorithms applied to recent systems (such as *SeaWinds*, for instance) have been simple extensions of those used for fan-beam instruments.

The results of applying fan-beam algorithms to the pencil-beam case have been mixed. Although the generation of data without a "nadir-gap" has been very useful to the science community, some researchers have claimed that the wind retrieval performance is insufficient. The general topic of wind retrieval utilizing a conically-scanning radar thus requires further study. As discussed in Chapter 6, polarimetric measurements have the potential to dramatically improve wind direction accuracy. As part of an overall reevaluation of pencil-beam wind retrieval, polarimetric techniques should be thoroughly investigated, where possible with ground and/or aircraft based measurement experiments.

8.2.2 Rain Contamination

A second major area for future study is how to alleviate the effects of rain contamination. As shown in Chapter 3, the combined effects of backscatter from the rain drops and attenuation through the raining layer can significantly corrupt the measurement of surface backscatter cross-section. These phenomena are particularly severe for the high incidence angles employed by pencil-beam scatterometers, and at the Ku-Band frequency often preferred for the measurement of ocean winds. Because of the existence of rain induced errors in the wind measurements, it is critical that

algorithms be developed to identify raining areas. This may or may not use data sources external to the scatterometer. Also, because the regions where rain occurs – fronts, storms, hurricanes, etc. – are of intense interest to meteorologists, it is also desirable that algorithms be developed to correct for the effects of rain. These algorithms will likely require multi-frequency radiometer measurements. Fortunately, the pencil-beam antenna architecture allows for straightforward incorporation of such capability (see below).

The same sensitivity that allows rain to corrupt scatterometer wind measurements, however, may also allow the scatterometer to function as a *rain measuring* radar. Although current rain radars (such as TRMM) provide high-quality rain profiles, the very narrow swath of these instruments limits their usefulness in global studies. The wide swath and frequent Earth coverage of the scatterometer, along with the rain sensitivity exhibited at Ku-Band frequency, offer the intriguing possibility of adding "rain measurement" to the growing list of scatterometer applications. The issues associated with radar rain retrieval at high incidence angles, as well as the role that range and/or Doppler processing might play in rain detection algorithms require further study.

8.2.3 Passive Channels and Multi-Frequency Scatterometers

The pencil-beam scatterometer technique typically involves the use of a near-circular reflector antenna. Because such antennas are inherently radiometrically stable and broad-band, passive radiometer channels as well as multiple radar frequencies may be accommodated simultaneously. In addition to the detection of rain discussed above, such multi-channel capability has the potential to dramatically expand the list of environmental parameters addressed by spaceborne scatterometers. For example, a Ku-Band channel can be used to detect and characterize snow, whereas an L-Band channel can penetrate the snow layer to determine whether or not the underlying surface is frozen. The planned HYDROS mission, discussed in Chapter 7, uses a combination of active radar and passive radiometer channels to more accurately retrieve soil moisture. Many measurement combinations currently

performed by different instruments may be consolidated into a single pencil-beam instrument in the future.

Appendix A

Characterization of Global Near-Nadir Ku-Band Backscatter

In this Appendix, a model is developed for Ku-Band backscatter in the nadir region (i.e., at near-specular incidence angles). These results are primarily intended for the analysis of nadir contamination as discussed in Chapter 3. This characterization is performed empirically using data from spaceborne radar missions which obtained near-nadir measurements.

A.1 Data From Spaceborne Nadir-Looking Ku-Band Radars

The approach to characterizing σ^o_{nad} is an empirical analysis of data collected by three different sensor systems: the Tropical Rainfall Measurement Mission (TRMM) Precipitation Radar, the Seasat-A Scatterometer System (SASS), and the Topex Altimeter. Taken together, these data sets allow a thorough characterization of near-nadir backscatter over a wide range of surface conditions and seasonal variations. Although primarily an empirical analysis, scattering theory is applied to interpret and inter-relate the results from the different sensors.

A.1.1 TRMM Rain Radar

The TRMM mission was launched in October 1997 in order to study the climatically important phenomena surrounding precipitation in the tropics. Among its suite of sensors is the Precipitation Radar (PR), the first such active rain radar to fly in space [34]. The PR is designed to profile rain by transmitting a pulse in the direction of nadir, and measuring the resultant echo in each of sixty 250 m range gates to determine the rain rate at each altitude in the atmosphere. In addition to

detecting backscatter from hydrometeors, the PR measures the surface backscatter cross-section. Although this feature primarily exists to derive attenuation values for the rain retrieval algorithms, the surface backscatter data by itself forms an unprecedented data base of near-nadir σ^o as a function of incidence angle.

The TRMM spacecraft orbits the Earth at an altitude of 350 km with an inclination angle of 35°. The PR consists of a 2.3 m × 2.3 m phased array antenna with associated electronics operating at 13.8 GHz. The antenna forms an H-polarized beam which is 0.71° in width and which is scanned ±17° from nadir in a plane perpendicular to the motion of the spacecraft. This scanning creates a 215 km measurement swath. TRMM Earth coverage for one day and four day periods is shown in Fig. A.1. In any given 4-day period, the TRMM PR covers virtually all land and ocean areas between ±35° latitude, corresponding to 57% of the Earth's surface. Note, however, that the Earth's polar regions are not covered. In this analysis, we refer to the ±35° latitude region as "tropical", even though this range includes much of the mid-latitude region as well.

In Fig. A.2, typical swath data for the TRMM surface backscatter measurement is shown. In this case, taken from late April 1998, the satellite is passing first over the east coast of Africa (on the left), and then over the Indian ocean (on the right). The center of the swath corresponds to 0° incidence, and the edges to approximately 17° incidence. Note that over land, σ^o is generally low over most incidence angles, but sporadically "spikes up" near nadir. Over ocean, the nature of the backscatter dependence is completely different. Here σ^o is uniformly high, rolling off slowly with incidence angle.

A more quantitative picture is given by sample scatter plots of TRMM data vs. incidence angle for both land and water in Fig. A.3. The TRMM PR samples the surface at discrete incidence angles spaced approximately 0.7° apart. Note the different character of the backscatter data over water as compared to the backscatter over land. The mean backscatter over water is higher than the mean backscatter over land at all incidence angles. Also, the water mean rolls off more gently from the nadir value, whereas the land mean drops more precipitously. The much higher variance of

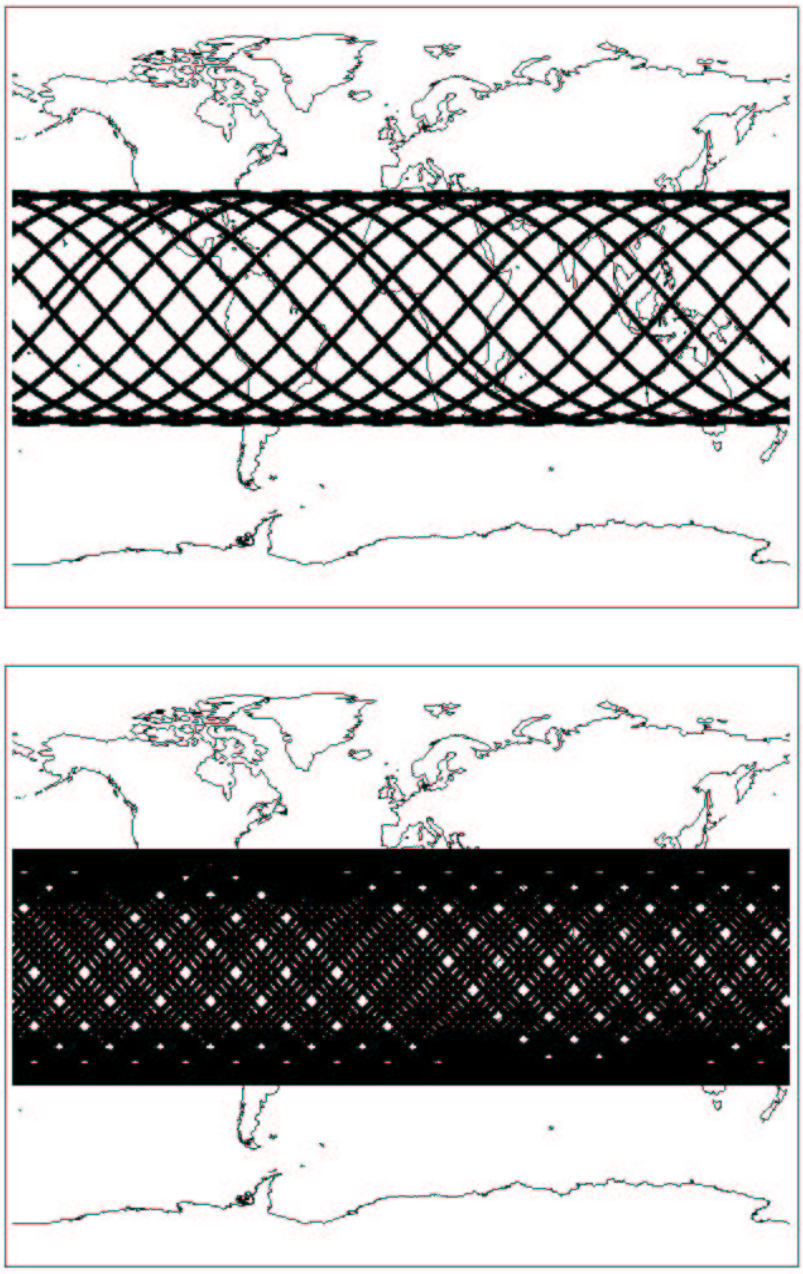

Figure A.1: TRMM PR one day coverage (top) and four day coverage (bottom).

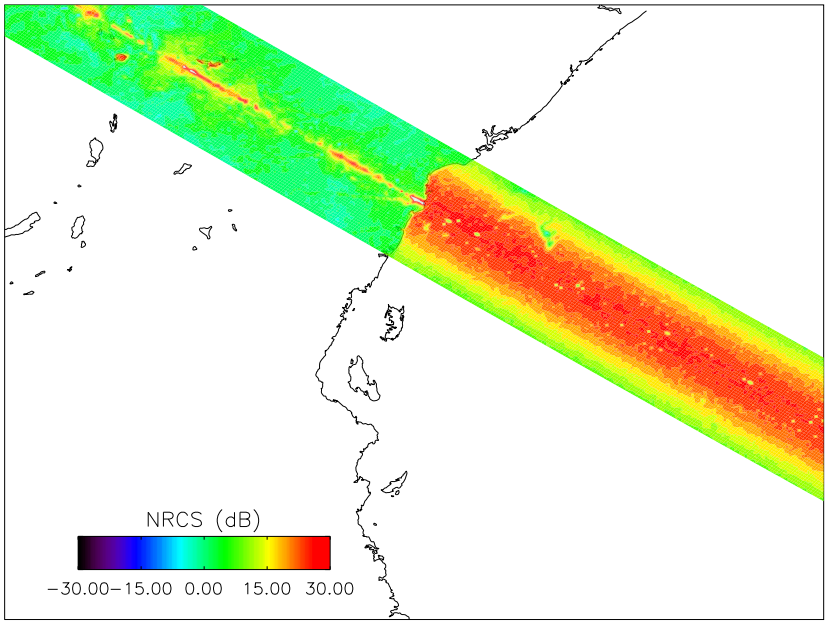

Figure A.2: Example TRMM swath of σ^o data coming off the coast of Africa (left) onto the Indian ocean (right).

the land values, however, has the effect of making the *peak* values at each incidence angle approximately the same for both water and land.

The observed behavior of the mean ocean backscatter is predicted in this incidence angle regime by modeling the sea as an undulating collection of surface facets of varying slopes [23]. On occasion, particularly in inland water-ways near coastlines where swell and wind are damped out, the ocean surface becomes extremely smooth and acts like a specularly reflecting surface. Under these conditions, the backscatter at $< 5°$ incidence increases sharply as the signal is reflected in a mirror-like fashion back to the sensor. Under these same conditions, the signal is reflected away from the sensor at incidence angles greater than 5°, thus sharply lowering the value of σ^o. The behavior over land is consistent with a varying target, corresponding to the different terrains encountered – forests, desserts, cities, mountain slopes, lakes, etc. The area exactly at nadir is often dominated by a strong surface specular return, as can be noted from Fig. A.2.

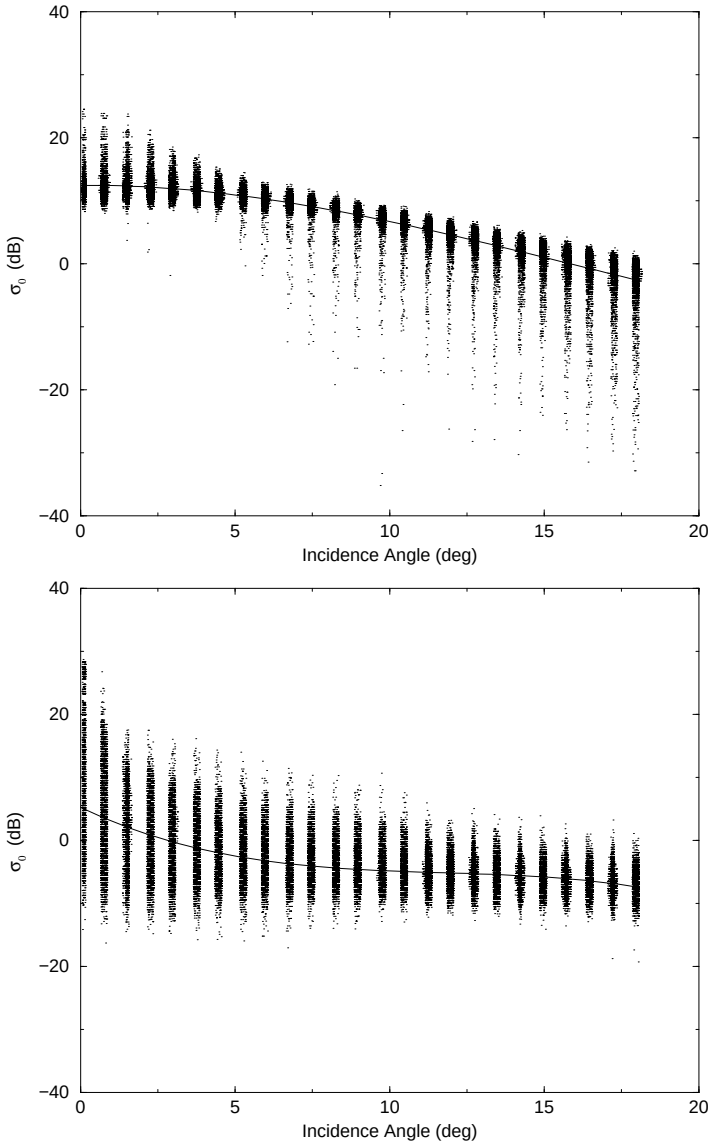

Figure A.3: Scatter plots of TRMM σ^o vs. incidence angle from July, 1998 for ocean (top) and land (bottom). Also shown is a third order polynomial curve fit to the data.

The TRMM data set has the limitation that only the tropical and lower mid-latitudes are covered. This is problematic because new sea ice is known to be a very bright target at nadir. Also, TRMM only utilizes H-polarization, and a scatterometer may use both H- and V-pol. For these reasons, the complementary data sets provide by Seasat and Topex are examined as well.

A.1.2 SASS Near-Nadir Measurements

The Seasat-A scatterometer system (SASS) flew as the first validation flight of a spaceborne, fan-beam wind scatterometer aboard the Seasat mission in 1978. The mission lasted from June 28, 1978 until a satellite failure ended the measurements on October 10, 1978. In addition to the standard Bragg-regime measurements made to determine wind, the SASS also collected measurements of nadir region backscatter near 0°, 4°, and 8° incidence [4]. These measurements were collected at both V- and H-Polarization, with each measurement cell having spatial dimensions of approximately 10 km $\times$ 50 km. The Seasat spacecraft flew in a 790 km altitude orbit with an inclination of 108°, and thus collected measurements up to $\pm 72°$ in latitude. In Fig. A.4, the one day coverage of the SASS near-nadir measurements are shown. Note that the SASS sensor collected data in the polar regions, and thus can be expected to yield information on backscatter from new sea ice in the winter southern oceans and on melting sea ice in the summer northern oceans.

Sample scatter plots of SASS σ^o vs. incidence angle for both ocean and land scenes are displayed in Fig. A.5. Note that the data is limited to incidence angles less than 10°. Note also the general qualitative agreement with the TRMM data over the same range in Fig. A.3.

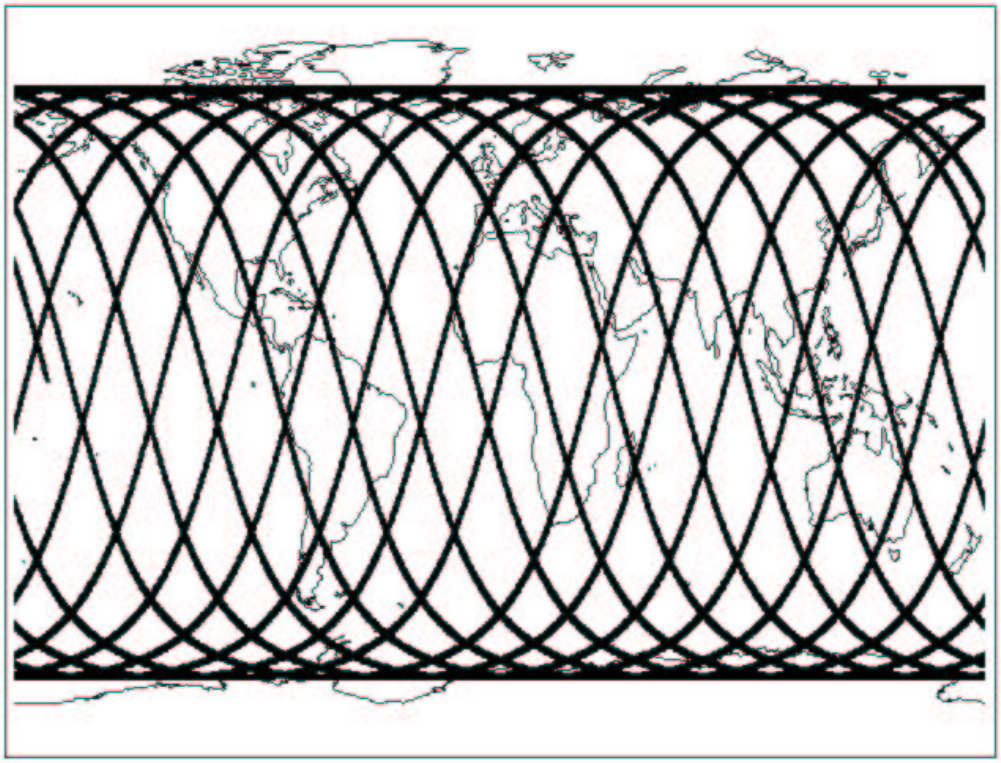

Figure A.4: SASS one-day near-nadir coverage.

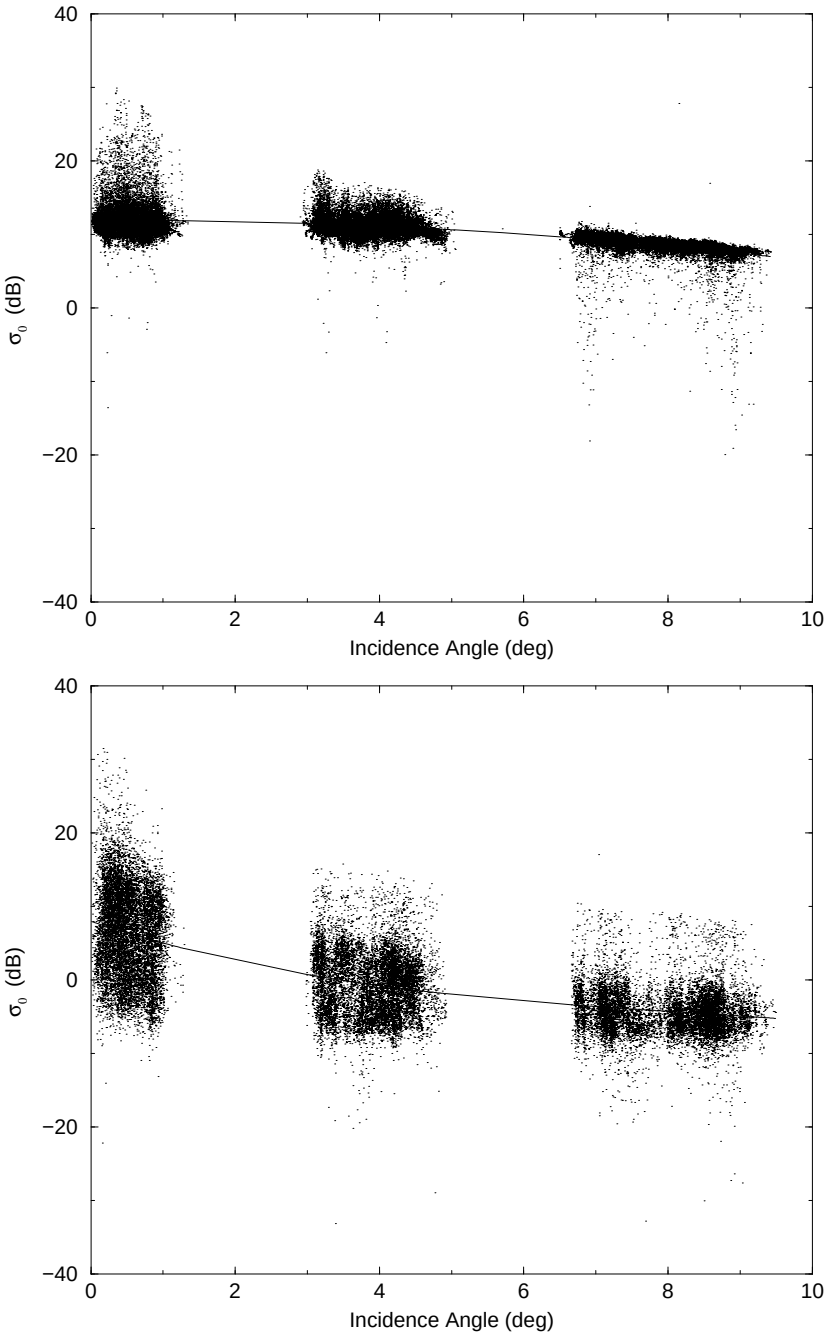

Figure A.5: SASS mean and max σ^o's for land (top) and ocean (bottom).

A.1.3 Topex Altimeter σ^o Data

Although designed for the measurement of sea surface height, spaceborne altimeters also measure surface backscatter cross section. Altimeter measurements, however, are generally insufficient for a complete characterization of near-nadir backscatter, due to the fact that the σ^o measurements are only collected at 0° incidence. In this analysis, data from the Topex altimeter, a successful mission which has been operated continuously for a number of years, is included primarily for a calibration validation of the other instruments. Topex flies in a 1400 km sun-synchronous orbit and has ground track coverage very similar to that shown for SASS in Fig. A.4. A sample time series of ocean σ^o's from the Topex mission is shown in Fig. A.6. Note that the ocean backscatter concentrates about an average value of 12 dB. This mean behavior is occasionally punctuated by sharp σ^o increases or "blooms" when a particularly specular surface is encountered, generally over very calm water conditions.

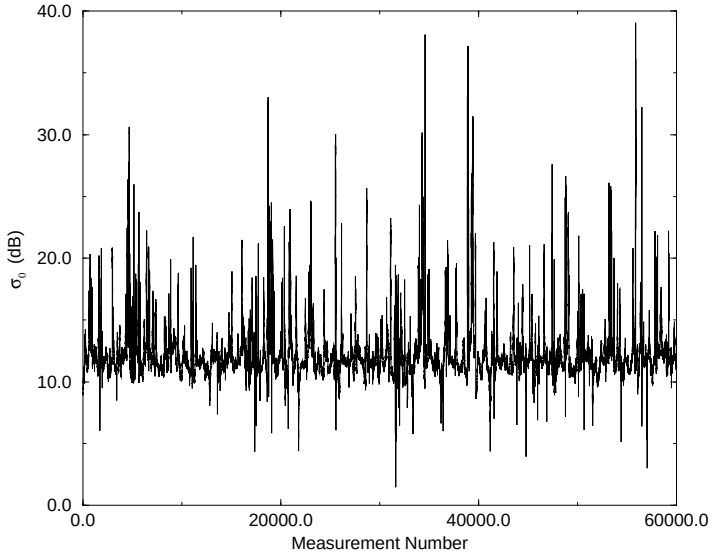

Figure A.6: Topex one orbit time series of ocean σ^o.

Although it is possible to use altimeter data to produce land and ice nadir σ^o's, this typically requires an analysis of the returned waveform and is beyond the scope of this analysis [16]. (The Topex algorithm specification cautions against using the σ^o values reported in the standard data product over land and ice.) Because backscatter from ice regions is such an important factor in determining the "worst-case" nadir return that may be encountered, however, the work of other researchers who have studied the altimeter return from ice extensively is addressed in a later section.

A.2 Near-Nadir Data Intercomparison and Fusion

A.2.1 Calibration Comparison

To gain confidence that data from the various instruments discussed above can be "fused" to form a complete description of near-nadir backscatter over a range of incidence angles, polarizations, and Earth locations, it is first necessary to validate that the instruments are calibrated sufficiently accurately relative to one another. As a calibration "target," the mean ocean backscatter between $\pm 35°$ latitude during the month of July was selected. The ocean was selected because it exhibits lower backscatter variance than land, and the latitude band is where all three sensors overlap. The TRMM data and Topex data used in the calibration comparison were from July, 1998 and the SASS data was from July 1978.

Figure A.7 compares the mean ocean backscatter of the three sensors. The SASS and TRMM data are third order fits to the data as a function of incidence angle, and the one Topex point is the mean value at nadir. Note that the sensors agree to within 1 dB or better. Also note that the V-pol and H-pol curves from SASS are within 0.3 dB of each other. This is an expected result in this incidence angle regime. To assess the sensitivity of seasonal changes, the TRMM data from February, 1999 was examined (not shown). It was found to be less than the July, 1998 curve by about 0.3 dB at all incidence angles. It is not know whether this is a geophysical or instrumental effect, but this level of calibration variation is negligible for our goal of characterizing the nadir contamination for a scatterometer.

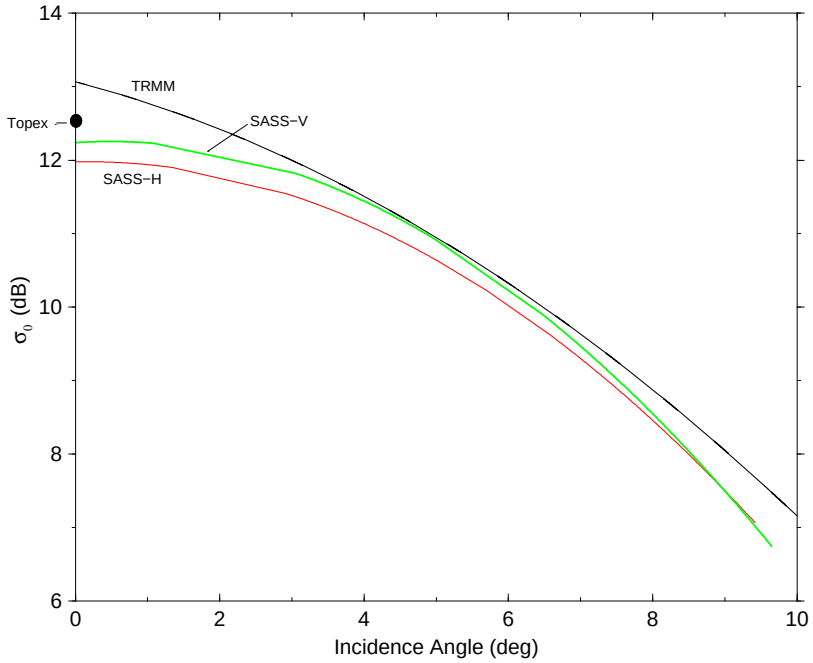

Figure A.7: Comparison of July mean tropical ocean backscatter of TRMM, Topex, and SASS H-pol and V-pol.

A.2.2 Comparison of σ^o Distributions over Different Earth Scenes

Having established that the sensors are sufficiently well calibrated and that the nadir region backscatter is relatively insensitive to polarization, an examination of how the distribution of σ^o varies as a function of surface type and incidence angle is performed. In Fig. A.8, normalized histograms of TRMM σ^o for three incidence angle ranges (0-1, 3-4, and 6-8 degrees) are plotted for the tropical ocean. For comparison, the tropical land backscatter distribution between 0-1 degrees is also plotted. As mentioned earlier, both the TRMM ocean and land distributions exhibit a hard cut-off near 28 dB due to dynamic range issues. Note the much broader distribution of land values, and the narrowing of the ocean distribution centered at 5°. Note also that for the 0-1 degree region, the land backscatter has a greater probability of giving a strong specular return higher than 20 dB.

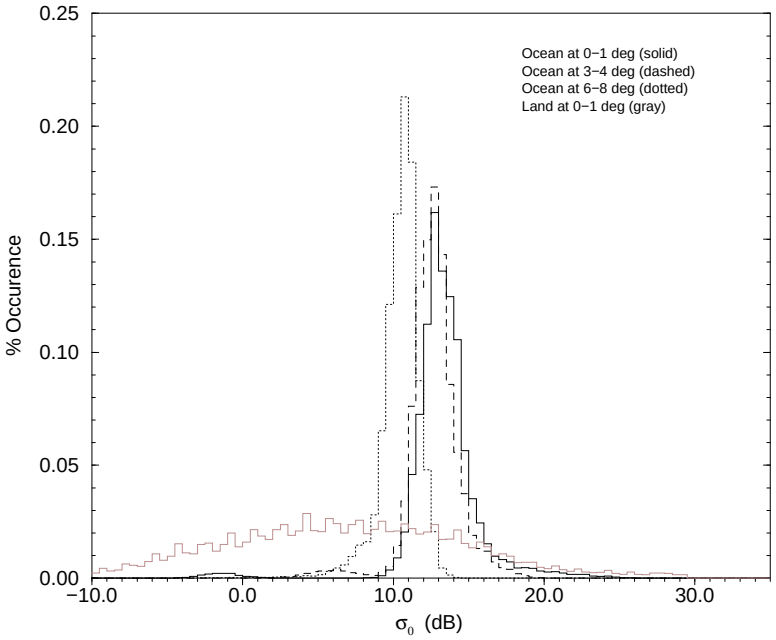

Figure A.8: TRMM ocean 0-1, 3-4, and 6-8 deg incidence and TRMM land 0-1 deg incidence.

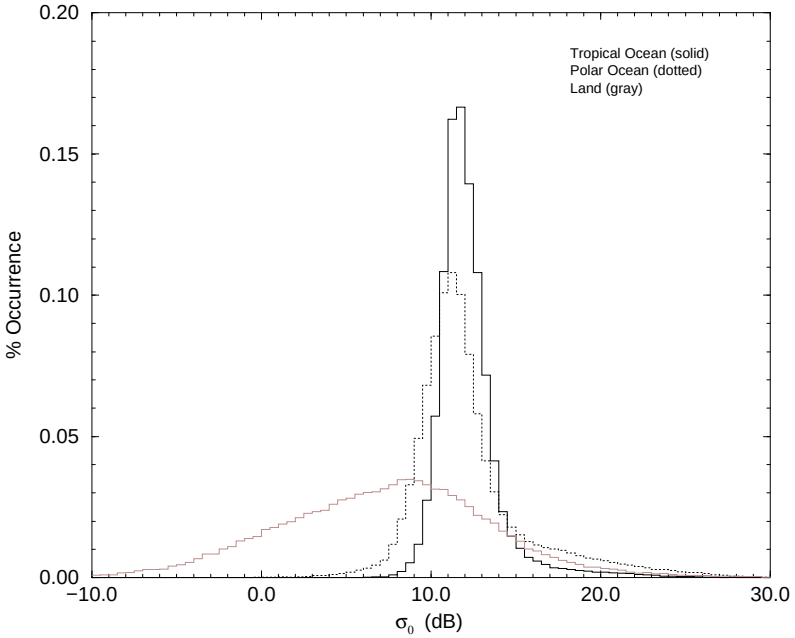

Figure A.9: (a) SASS 0 deg incidence.

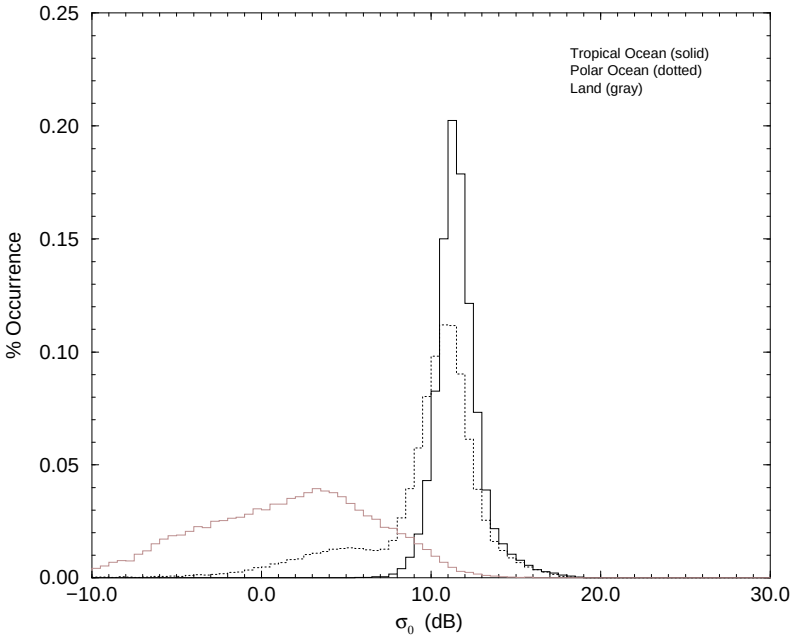

Figure A.9: (b) SASS 3 deg incidence.

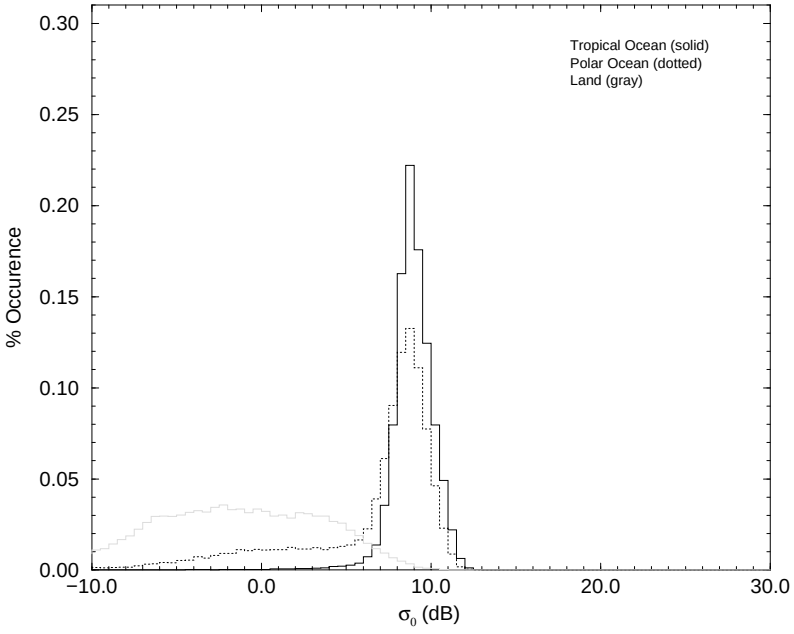

Figure A.9: (c) SASS 6-8 deg incidence.

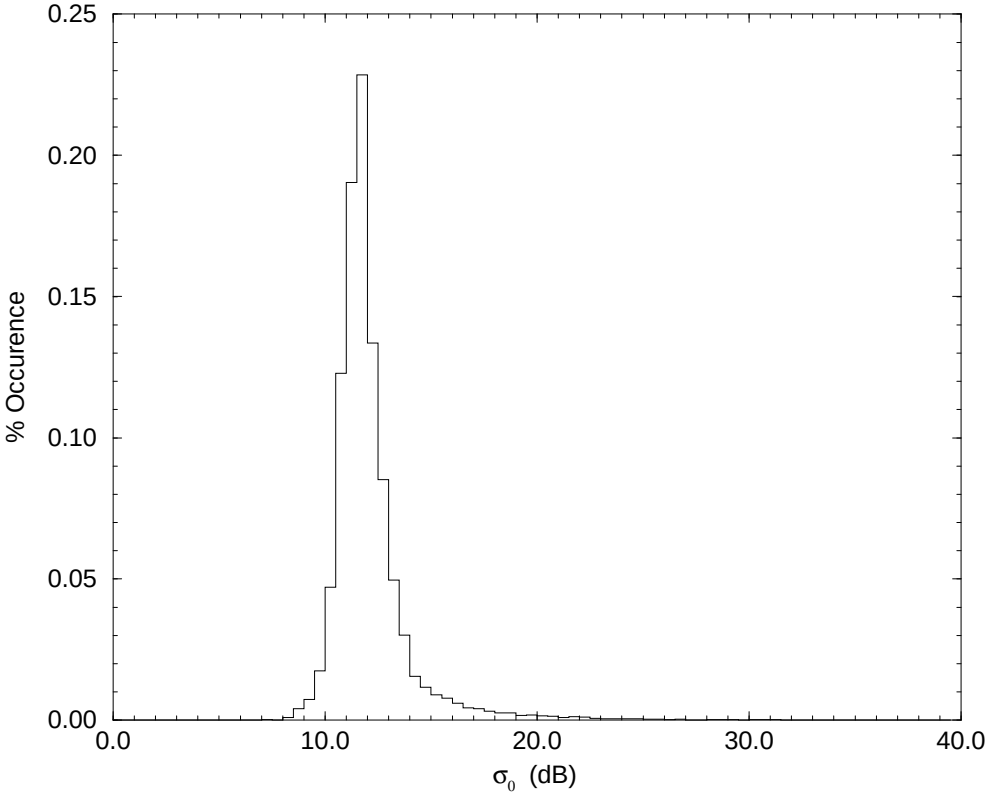

Figure A.10: Topex ocean distribution.

For comparison, Fig. A.9(a)-(c) shows the normalized histograms of SASS data in the same incidence angle ranges of 0-1, 3-4, and 6-8 degrees. Here, each plot contains distributions of the tropical ocean, the extra-tropical ocean (i.e. at latitudes above 35 degrees), and of combined tropical and extra-tropical land. All SASS data shown is from periods in mid- and late-July (namely, orbits 180-210 and orbits 316-400), where H- and V-polarization have been combined.

Of primarily interest in Fig. A.9 is the behavior of the extra-tropical ocean, which is not covered by TRMM. Importantly, we note that the SASS data collected here has not been flagged for sea ice, so the extra-tropical data contains both open ocean and sea ice areas. In July, it is expected that the Antarctic ice sheet is reaching its greatest extent and the Arctic ice sheet is in a late melting stage. In Fig. A.9(a), it is observed that the peak of the extra-tropical ocean distribution is about 1 dB lower than the tropical ocean distribution – likely caused by the higher winds and consequently lower nadir backscatter at high latitudes. The extra-tropical ocean distribution, however, has a pronounced high σ^o "tail" which indicates a much greater probability to produce strong specular returns. This tail is most likely due to the presence of new sea ice in the Antarctic, which forms a very flat specular surface, and melting ice in the Arctic, where enclosed areas of calm water form.

Consistent with the evidence for the presence of ice in Fig. A.9(a), the extented tail in the extra-tropical ocean distribution reverses positions at the slightly off-nadir angles shown in Figs. A.9(b) and A.9(c), and exhibits a higher probability for lower backscatter values. Whereas flat ice surfaces may create a strong specular return near zero incidence, a small angular distance off nadir causes the backscatter to drop considerably. This is a commonly observed characteristic of smooth surfaces where specular scattering dominates [16]. For the liquid ocean, which generally scatters more diffusely because of roughness, the drop-off in backscatter with incidence angle is much more gradual than that of ice. The evidence for the presence of specularly scattering ice in Fig. A.9 emphasizes the importance of including SASS extra-tropical data in the characterization of global backscatter. For completeness, a histogram of

Topex ocean values for July 1998 is plotted in Fig. A.10. Note the general agreement with ice-free nadir ocean backscatter in Fig. A.8 and Fig. A.9(a).

A.2.3 Global Average and Global Peak Backscatter

Taking the TRMM and SASS data sets collectively, a global model of near-nadir backscatter can be constructed. Such a model, expressed in terms of mean and peak backscatter values encountered at each incidence angle, is shown in Fig. A.11. Here the mean curve has been constructed as a fit to both the SASS global and TRMM tropical data, where weighting has been applied to account for the relative frequency of measurements in each data set and for the percentage of the Earth's surface that each data set covers. The peak backscatter is represented by the 99th percentile high backscatter observed at each incidence angle. The peak curve is used to assess the worst-case near-nadir contamination.

It is important to elaborate on the meaning of "peak" backscatter at incidence angles very close to 0° incidence. For a highly specular surface, the effective σ^o varies rapidly with incidence angle and thus becomes a strong function of both the footprint area and range of incidence angles illuminated [16]. For instance, in a study by Ulander and Carlstrom, GEOSAT altimeter ice data was processed so that the footprint diameter was approximately 2 km, thus limiting the measurement to a very narrow range of incidence angles [96]. Ulander and Carlstrom noted that under such conditions, new ice could produce a σ^o approaching 40 dB.

For the present application, however, we need only be concerned about the *integrated* value of σ^o over a somewhat wider range of incidence angles near nadir. As discussed in [16], the theoretical integrated σ^o for a perfect specularly scattering surface is

$$\sigma^o = \frac{|R(0)|^2}{\beta^2} \exp\left[-4k^2\rho^2\right], \tag{A.1}$$

where $|R(0)|$ is the Fresnel reflection coefficient at zero degrees incidence, β is the half-angle of the nadir solid-angle illuminated, k is the wave number of the radar, and ρ is the surface roughness. For a minimum integration step size of 1°, then the minimum value of $\beta = 1°$ applies. If it is further assumed that $|R(0)| = 1$ and $\rho = 0$,

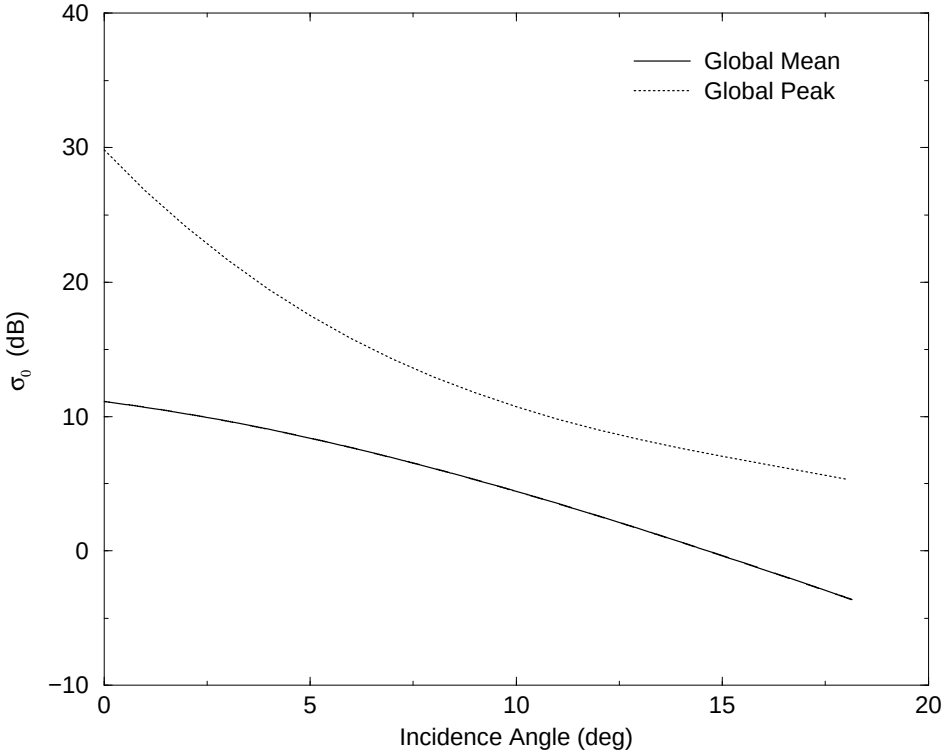

Figure A.11: Global mean and peak (99th percentile) near-nadir backscatter profiles.

creating perfectly specular surface, then $\sigma^o = 35$ dB. At Ku-Band, this value rapidly decreases with any realistic roughness whatsoever. Thus the peak value of 30 dB given in Fig. A.11 is quite reasonable.

Appendix B

K_{pc} Formulation for SeaWinds with Range Discrimination

In this appendix stochastic signal processing theory is applied to derive Eq. (5.28).

B.1 K_{pc} Definition

Let the returned energy for a given slice be E_s, where

$$E_s = E_{s+n} - E_n. \tag{B.1}$$

Here, E_{s+n} is the signal-plus-noise energy measured for the slice, and E_n is an estimate for the noise-only energy associated with the slice. K_{pc} is defined as the normalized standard deviation of E_s, or

$$K_{pc} = \frac{\sqrt{\mathrm{Var}[E_s]}}{\mathcal{E}[E_s]}. \tag{B.2}$$

In general, $\mathrm{Var}[E_s]$ can be written as

$$\mathrm{Var}[E_s] = \mathrm{Var}[E_{s+n}] + \mathrm{Var}[E_n] + 2(\mathcal{E}[E_{s+n}]\mathcal{E}[E_n] - \mathcal{E}[E_{s+n}E_n]). \tag{B.3}$$

An expression for K_{pc} is developed by addressing each term in Eq. (B.3) individually, and then inserting these results into Eq. (B.2).

B.2 Calculating $\mathrm{Var}[E_{s+n}]$

Because

$$\mathrm{Var}[E_{s+n}] = \mathcal{E}[E_{s+n}^2] - \mathcal{E}^2[E_{s+n}], \tag{B.4}$$

expressions for $\mathcal{E}[E_{s+n}]$ and $\mathcal{E}[E_{s+n}^2]$ are needed.

B.2.1 $\mathcal{E}[E_{s+n}]$ Term

The digitally sampled, deramped signal+noise signal incident on the FFT processor is given by

$$x(n) = s(n) + \nu(n), \tag{B.5}$$

where $s(n)$ is the signal component and $\nu(n)$ is the thermal noise component. The detected signal+noise energy at the output of the FFT processing and binning operation is

$$E_{s+n} = \sum_k \left| \sum_{n=0}^{N-1} x(n) e^{-jWkn} \right|^2, \tag{B.6}$$

where the outside summation is over the total periodogram bins used to form the cell and $W = \frac{2\pi}{N}$. Expressing E_{s+n} as

$$E_{s+n} = \sum_k \left[\sum_n x(n) e^{-jWkn} \sum_m x^*(m) e^{jWkm} \right], \tag{B.7}$$

and then taking the expectation,

$$\mathcal{E}[E_{s+n}] = \sum_k \sum_n \sum_m \mathcal{E}[x(n)x^*(m)] e^{jWk(m-n)}. \tag{B.8}$$

Assuming the signal and noise are un-correlated, then

$$\mathcal{E}[E_{s+n}] = \mathcal{E}[E_s] + \mathcal{E}[E_n] \tag{B.9}$$

and

$$\mathcal{E}[x(n)x^*(m)] = \mathcal{E}[s(n)s^*(m)] + \mathcal{E}[\nu(n)\nu^*(m)]. \tag{B.10}$$

The signal and noise terms are now addressed in turn.

From the discussion on the X factor in Chapter 5 the return pulse envelope from each surface scatterer may be assumed rectangular in shape, and thus the dechirped signal component can be written as

$$s(n) = \sqrt{\sigma^o} \sum_i \xi_i c_i \rho_i(n) e^{j(\omega_i n + \psi_i)}. \tag{B.11}$$

Here it is assumed that σ^o is constant over the footprint. The summation is over each ith scattering patch, with ξ_i the Rayleigh random magnitude term for which $\mathcal{E}[\xi_i^2] = 1$, c_i is the total instrument system gain at the patch (including the effects

of antenna gain, range, incremental area, etc.) ω_i is the de-chirped baseband angular frequency corresponding to the patch, and ψ_i is the random phase term. The function $\rho_i(n)$ is defined to be 1 when the sample n corresponds to a time when a backscattered signal from the ith scatterer is present, and 0 otherwise. $\rho_i(n)$ thus takes both the pulse length and range gating effects into account.

The signal term expectation then becomes

$$\mathcal{E}[s(n)s^*(m)] = \sigma^o \sum_i \sum_l \mathcal{E}[\xi_i \xi_l] c_i c_l \rho_i(n) \rho_l(m) \mathcal{E}[e^{j(\psi_i - \psi_l)}] e^{j(\omega_i n - \omega_l m)}. \tag{B.12}$$

Because of the assumed independence of the surface scatterers, $\mathcal{E}[e^{j(\psi_i-\psi_l)}] = 1$ for $i = l$, and $\mathcal{E}[e^{j(\psi_i-\psi_l)}] = 0$ for $i \neq l$. Equation (B.12) becomes

$$\mathcal{E}[s(n)s^*(m)] = \sigma^o \sum_i c_i^2 \rho_i(n) \rho_i(m) e^{j\omega_i(n-m)}. \tag{B.13}$$

The expected value of the signal component is then written as

$$\mathcal{E}[E_s] = \sum_k \sum_n \sum_m \sigma^o \sum_i c_i^2 \rho_i(n) \rho_i(m) e^{j\omega_i(n-m)} e^{jWk(m-n)}. \tag{B.14}$$

Reordering the above terms,

$$\mathcal{E}[E_s] = \sigma_0 \sum_i c_i^2 \sum_k \sum_n \sum_m \rho_i(n) \rho_i(m) e^{j\omega_i(n-m)} e^{jWk(m-n)}. \tag{B.15}$$

Note that

$$\sum_n \sum_m \rho_i(n) \rho_i(m) e^{j\omega_i(n-m)} e^{jWk(m-n)} = \left| \sum_n \rho_i(n) e^{j\omega_i n} e^{-jWkn} \right|^2. \tag{B.16}$$

Assuming that the echo return envelope from a given scatterer is flat, the DFT in Eq. (B.16) is performed to obtain

$$\sum_n \rho_i(n) e^{j\omega_i n} e^{-jWkn} = \beta(i,k), \tag{B.17}$$

where

$$\beta(i,k) = \left(\frac{\exp[j\pi(N_{p,i} + 2n_{s,i})(f_{b,i}T - \frac{k}{N})]}{\exp[j\pi(f_{b,i}T - \frac{k}{N})]} \right) \left(\frac{\sin[\pi N_{p,i}(f_{b,i}T - \frac{k}{N})]}{\sin[\pi(f_{b,i}T - \frac{k}{N})]} \right). \tag{B.18}$$

Here, $f_{b,i}$ is the baseband frequency, T is the sample period, N is the number of FFT samples, $N_{p,i}$ is the number of samples in the return envelope, and $n_{s,i}$ is the

number of the first sample in the return envelope. The factor X from Chapter 5 can be written

$$X = \sum_i c_i^2 \sum_k |\beta(i,k)|^2, \tag{B.19}$$

and consequently

$$\mathcal{E}[E_s] = X\sigma^o. \tag{B.20}$$

As for the thermal noise component of Eq. (B.10),

$$\mathcal{E}[\nu(n)\nu^*(m)] = \mathcal{E}[\nu_R(n)\nu_R(m)] + \mathcal{E}[\nu_I(n)\nu_I(m)] + j\mathcal{E}[\nu_I(n)\nu_R(m)] - j\mathcal{E}[\nu_R(n)\nu_I(m)], \tag{B.21}$$

where ν_R and ν_I are the real and imaginary components of ν. Assuming stationary white Gaussian statistics for the digitized thermal noise sequence, ν_R and ν_I are uncorrelated so the imaginary cross correlation terms go to zero. In addition, when noise is sampled at the Nyquist frequency, the autocorrelation terms are equal but only contribute when $n \neq m$. Consequently,

$$\mathcal{E}[\nu(n)\nu^*(m)] = N_0\delta(n-m)\rho_\nu(n)\rho_\nu(m), \tag{B.22}$$

where δ is the Kronecker delta and $\rho_\nu(n)$ is the time gating function applied to the thermal noise signal. Applying the FFT, magnitude square, and binning operations,

$$\sum_k \sum_n \sum_m N_0\delta(n-m)\rho_\nu(n)\rho_\nu(m)e^{jWk(m-n)} = MN_\nu N_0, \tag{B.23}$$

where M is the total number of bins summed and N_ν is the number of samples in the range gate noise sampling. Ultimately,

$$\mathcal{E}[E_{s+n}] = X\sigma^o + MN_\nu N_0, \tag{B.24}$$

representing the result that the expected signal+noise energy is equal to the sum of the expected signal energy and the expected noise energy.

B.2.2 $\mathcal{E}[E_{s+n}^2]$ Term

The term $\mathcal{E}[E_{s+n}^2]$ is initially written

$$E_{s+n}^2 = \left(\sum_k \left| \sum_n x(n)e^{-jWkn} \right|^2 \right)^2, \tag{B.25}$$

which can be expanded into

$$E_{s+n}^2 = \sum_k \left[\sum_n x(n) e^{-jWkn} \sum_m x^*(m) e^{jWkm} \right] \cdot \sum_h \left[\sum_p x(p) e^{-jWhp} \sum_q x^*(q) e^{jWhq} \right]. \tag{B.26}$$

Re-ordering the terms and taking the expectation,

$$\mathcal{E}[E_{s+n}^2] = \sum_{k,h,n,m,p,q} \mathcal{E}[x(n)x^*(m)x(p)x^*(q)] e^{jWk(m-n)} e^{jWh(q-p)}, \tag{B.27}$$

where the multiple summations have been represented by one summation symbol.

Assuming that $x(n)$ is Gaussian distributed and zero mean, we employ the expansion for the forth order moment of Gaussian random variables to obtain

$$\begin{aligned} \mathcal{E}[x(n)x^*(m)x(p)x^*(q)] &= \mathcal{E}[x(n)x^*(m)]\mathcal{E}[x(p)x^*(q)] \\ &\quad + \mathcal{E}[x(n)x(p)]\mathcal{E}[x^*(m)x^*(q)] \\ &\quad + \mathcal{E}[x(n)x^*(q)]\mathcal{E}[x(p)x^*(m)]. \end{aligned} \tag{B.28}$$

An expression for each of the three terms in Eq. (B.28) is found in turn and then inserted into Eq. (B.27).

Examining the second term in (B.28), the signal and noise are uncorrelated, so

$$\mathcal{E}[x(n)x(p)] = \mathcal{E}[s(n)s(p)] + \mathcal{E}[\nu(n)\nu(p)]. \tag{B.29}$$

From Eq. (B.12),

$$\mathcal{E}[s(n)s(p)] = \sigma^o \sum_i \sum_l \mathcal{E}[\xi_i \xi_l] c_i c_l \rho_i(n) \rho_l(p) \mathcal{E}[e^{j(\psi_i + \psi_l)}] e^{j(\omega_i n + \omega_l m)}. \tag{B.30}$$

Because $\mathcal{E}[e^{j(\psi_i+\psi_l)}] = 0$ for all i and l, Eq. (B.30) is always zero. Further,

$$\begin{aligned} \mathcal{E}[\nu(n)\nu(p)] &= \mathcal{E}[\nu_R(n)\nu_R(p)] - \mathcal{E}[\nu_I(n)\nu_I(p)] + j\mathcal{E}[\nu_I(n)\nu_R(p)] - j\mathcal{E}[\nu_R(n)\nu_I(p)] \\ &= 0, \end{aligned} \tag{B.31}$$

so the second term in Eq. (B.28) is zero. Now, examining the first term in Eq. (B.28), from Eq. (B.13) and (B.22) we have that,

$$\mathcal{E}[x(n)x^*(m)] = \sigma_0 \sum_i c_i^2 \rho_i(n) \rho_i(m) e^{j(\omega_i(n-m))} + N_0 \delta(n-m) \rho_\nu(n) \rho_\nu(m). \tag{B.32}$$

The first term in Eq. (B.28) can then be expanded as

$$\begin{aligned}\mathcal{E}[x(n)x^*(m)]\mathcal{E}[x(p)x^*(q)] \;=\; & \\ & \sigma_0^2 \sum_i c_i^2 \rho_i(n)\rho_i(m) e^{j(\omega_i(n-m))} \sum_l c_l^2 \rho_l(p)\rho_l(q) e^{j(\omega_l(p-q))} \\ & +\sigma_0 \sum_i c_i^2 \rho_i(n)\rho_i(m) e^{j(\omega_i(n-m))} N_0 \delta(p-q)\rho_\nu(p)\rho_\nu(q) \\ & +\sigma_0 \sum_l c_l^2 \rho_l(p)\rho_l(q) e^{j(\omega_l(p-q))} N_0 \delta(n-m)\rho_\nu(n)\rho_\nu(m) \\ & +N_0^2 \delta(n-m)\delta(p-q)\rho_\nu(n)\rho_\nu(m)\rho_\nu(p)\rho_\nu(q). \end{aligned} \tag{B.33}$$

Inserting Eq. (B.33) into Eq. (B.27),

$$\begin{aligned}\sum_{k,h,n,m,p,q} & \mathcal{E}[x(n)x^*(m)]\mathcal{E}[x(p)x^*(q)] e^{jWk(m-n)} e^{jWh(q-p)} \;= \\ & (\sigma^o)^2 \sum_{k,n,m,i} c_i^2 \rho_i(n)\rho_i(m) e^{j(\omega_i(n-m))} e^{jWk(m-n)} \sum_{h,p,q,l} c_l^2 \rho_l(p)\rho_l(q) e^{j(\omega_l(p-q))} e^{jWh(q-p)} \\ + \; & \sigma^o \sum_{k,h,n,m,p,q,i} c_i^2 \rho_i(n)\rho_i(m) e^{j(\omega_i(n-m))} N_0 \delta(p-q)\rho_\nu(p)\rho_\nu(q) e^{jWk(m-n)} e^{jWh(q-p)} \\ + \; & \sigma^o \sum_{k,h,n,m,p,q,l} c_l^2 \rho_l(p)\rho_l(q) e^{j(\omega_l(p-q))} N_0 \delta(n-m)\rho_\nu(n)\rho_\nu(m) e^{jWk(m-n)} e^{jWh(q-p)} \\ + \; & \sum_{k,h,n,m,p,q} N_0^2 \delta(n-m)\delta(p-q)\rho_\nu(n)\rho_\nu(m)\rho_\nu(p)\rho_\nu(q) e^{jWk(m-n)} e^{jWh(q-p)}. \end{aligned} \tag{B.34}$$

Which, performing the summations, becomes

$$\begin{aligned}\sum_{k,h,n,m,p,q} & \mathcal{E}[x(n)x^*(m)]\mathcal{E}[x(p)x^*(q)] e^{jWk(m-n)} e^{jWh(q-p)} \\ & = (X\sigma^o)^2 + 2X\sigma^o M N_\nu N_0 + (M N_\nu N_0)^2 \\ & = \mathcal{E}[E_{s+n}]^2. \end{aligned} \tag{B.35}$$

Addressing the third term in Eq. (B.28),

$$\begin{aligned}\mathcal{E}[x(n)x^*(q)]\mathcal{E}[x(p)x^*(m)] \;=\; & \\ & \sigma^o \sum_i c_i^2 \rho_i(n)\rho_i(q) e^{j(\omega_i(n-q))} \sigma^o \sum_l c_l^2 \rho_l(p)\rho_l(m) e^{j(\omega_l(p-m))} \\ & +\sigma_0 \sum_i c_i^2 \rho_i(n)\rho_i(q) e^{j(\omega_i(n-q))} N_0 \delta(p-m)\rho_\nu(p)\rho_\nu(m) \\ & +\sigma_0 \sum_l c_l^2 \rho_l(p)\rho_l(m) e^{j(\omega_l(p-m))} N_0 \delta(n-q)\rho_\nu(n)\rho_\nu(q) \\ & +N_0^2 \delta(n-q)\delta(p-m)\rho_\nu(n)\rho_\nu(q)\rho_\nu(p)\rho_\nu(m). \end{aligned} \tag{B.36}$$

Inserting Eq. (B.36) into Eq. (B.27),

$$\sum_{k,h,n,m,p,q} \mathcal{E}[x(n)x^*(q)]\mathcal{E}[x(p)x^*(m)]e^{jWk(m-n)}e^{jWh(q-p)} = \tag{B.37}$$

$$(\sigma^o)^2 \sum_{k,n,m,h,p,q,i,l} c_i^2 c_l^2 \rho_i(n)\rho_i(q)\rho_l(p)\rho_l(m)e^{j\omega_i(n-q)}e^{j\omega_l(p-m)}e^{jWk(m-n)}e^{jWh(q-p)}$$

$$+ \quad \sigma^o \sum_{k,n,m,h,p,q,i} c_i^2 \rho_i(n)\rho_i(q)e^{j\omega_i(n-q)}e^{jWk(m-n)}e^{jWh(q-p)}N_0\delta(p-m)\rho_\nu(p)\rho_\nu(m)$$

$$+ \quad \sigma_0 \sum_{k,n,m,h,p,q,l} c_l^2 \rho_l(p)\rho_l(m)e^{j\omega_l(p-m)}e^{jWk(m-n)}e^{jWh(q-p)}N_0\delta(n-q)\rho_\nu(n)\rho_\nu(q)$$

$$+ \quad \sum_{k,h,n,m,p,q} N_0^2\delta(n-q)\delta(p-m)\rho_\nu(n)\rho_\nu(q)\rho_\nu(p)\rho_\nu(m)e^{jWk(m-n)}e^{jWh(q-p)}.$$

B.2.3 Variance of E_{s+n}

The variance of E_{s+n} is given by

$$\mathrm{Var}[E_{s+n}] = \mathcal{E}[E_{s+n}^2] - \mathcal{E}[E_{s+n}]^2. \tag{B.38}$$

Note that the term given by Eq. (B.35) for $\mathcal{E}[E_{s+n}^2]$ cancels with $\mathcal{E}[E_{s+n}]^2$, and the only contribution to the variance is from the term given in Eq. (B.37). Assuming that the echo return is flat, Eq. (B.17) is employed in the evaluation of the summations over n, m, p, and q for the signal terms in Eq. (B.37) to obtain

$$\begin{aligned}\mathrm{Var}[E_{s+n}] &= (\sigma^o)^2 \sum_{k,h,i,l} c_i^2 c_l^2 \beta(i,k)\beta^*(i,h)\beta^*(l,k)\beta(l,h) \\ &\quad + 2\sigma^o N_0 \sum_{k,h,i} c_i^2 \frac{e^{j\pi\frac{(k-h)}{N}(N_\nu+2n_\nu)}\sin(\pi\frac{(k-h)}{N}N_\nu)}{e^{j\pi\frac{(k-h)}{N}}\sin(\pi\frac{(k-h))}{N})}\beta(i,k)\beta^*(i,h) \\ &\quad + N_0^2 \sum_{k,h}\sum_{n=0}^{N_\nu-1}\sum_{m=0}^{N_\nu-1} e^{jW(k-h)(m-n)},\end{aligned} \tag{B.39}$$

where n_ν is the sample corresponding to the beginning of the range gate, and N_ν is the total number of samples during the range gate "open" time.

B.3 Expression for K_{pc}

It is now possible to construct a formula for K_{pc}. If it is assumed that $\mathrm{Var}[E_{s+n}] \gg \mathrm{Var}[E_n]$, a reasonable assumption if the bandwidth of the noise-only measurement is large relative to the signal+noise measurement, and further assumed

that the noise-only estimate and signal+noise estimate can be approximated as independent, from equations Eq. (B.2) and Eq. (B.3),

$$K_{pc}^2 = \frac{\mathrm{Var}[E_{s+n}]}{\mathcal{E}^2[E_s]}. \tag{B.40}$$

Defining the energy signal-to-noise ratio, SNR, as

$$\mathrm{SNR} = \frac{X\sigma_0}{MN_\nu N_0} \tag{B.41}$$

allows us to substitute for N_0 as

$$N_0 = \frac{X\sigma_0}{MN_\nu \mathrm{SNR}}. \tag{B.42}$$

Combining the above,

$$K_{pc}^2 = A + \frac{B}{\mathrm{SNR}} + \frac{C}{\mathrm{SNR}^2}, \tag{B.43}$$

where

$$\begin{aligned}
A &= \frac{1}{X^2}\sum_k\sum_h\sum_i\sum_l c_i^2 c_l^2 \beta(i,k)\beta^*(i,h)\beta^*(l,k)\beta(l,h) \\
B &= \frac{2}{MN_\nu X}\sum_k\sum_h\sum_i c_i^2 \frac{e^{j\pi\frac{(k-h)}{N}(N_\nu+2n_\nu)}\sin(\pi\frac{(k-h)}{N}N_\nu)}{e^{j\pi\frac{(k-h)}{N}}\sin(\pi\frac{(k-h))}{N})}\beta(i,k)\beta^*(i,h) \\
C &= \frac{1}{M^2N_\nu^2}\sum_k\sum_h\sum_{n=0}^{N_\nu-1}\sum_{m=0}^{N_\nu-1} e^{jW(k-h)(m-n)}.
\end{aligned} \tag{B.44}$$

To verify the digital K_{pc} results, the expressions for A, B, and C in Eq. (B.44) were numerically evaluated using values of n_s, N_i, and c_i as generated by the BYU X-Factor computer code [1]. These values are then compared to the approximate values obtained for an ideal band-limited white-noise signal as presented Chapter 4,

$$\begin{aligned}
A &= \frac{1}{B_s T_p} \\
B &= \frac{2}{B_s T_g} \\
C &= \frac{1}{B_n T_g}.
\end{aligned} \tag{B.45}$$

Here, B_s is the slice bandwidth, B_n is the noise channel bandwidth (nominally 1 MHz), T_p is the transmit pulse length (nominally 1.5 ms) and T_g is the range gate length

(2.1 ms). To make the comparison more meaningful, the parameters are computed for a case where they are expected to agree well: a center cell (slice 7, in this case), inner beam, azimuth angle = 90°.

Table B.1: K_{pc} Parameter Comparison: Inner Beam, Cell 7, $\theta_{az} = 90°$.

Parameter	Approximate Value	Computed Value
A	0.080	0.078
B	0.120	0.120
C	0.060	0.058

Examining Table B.1, it is concluded that the values in Eq. (B.45) represent a very good approximation to the exact values given in Eq. (B.44). This is an indication that, for the *SeaWinds* timing, modulation, and processing parameters, the return signal in a slice may be assumed to be bandlimited, stationary random process.

Bibliography

[1] I.S. Ashcraft, D.G. Long, A. Anderson, S. Richards, M.W. Spencer, and B. Jones, "Sigma-0 Retrieval from SeaWinds on QuikSCAT," in Earth Observing Systems IV, W.L. Barnes, ed., *Proceeding of SPIE*, Denver, CO., July 19-20, 1999, vol. 3750, pp. 171-178.

[2] R. Atlas, S.C. Bloom, R.N. Hoffman, E. Brin, J. Ardizzone, J. Terry, D. Bungato, and J.C. Jusem, "Geophysical Validation of NSCAT Winds Using Atmospheric Data and Analyses," *J. of Geophy. Res.*, vol. 104, no. C5, pp. 11,405-11,424, 1999.

[3] E.P.W. Attema, "The Active Microwave Instrument On-Board the ERS-1 Satellite," *Proceedings of the IEEE*, vol. 79, no. 6, pp. 791-799, 1991.

[4] E.M. Bracalante, D.H. Boggs, W.L. Grantham, J.L. Sweet, "The SASS Scattering Coefficient σ^o Algorithm," *IEEE J. of Oceanic Eng.*, vol. OE-5, no. 2, pp. 145-154 1980.

[5] F. Carsey, "Review and Status of Remote Sensing of Sea Ice," *IEEE Journal of Oceanic Engineering*, vol. 14, no. 2, pp. 127-137, 1989.

[6] C.P. Chang, S.C. Lin, C.S. Liou, W.T. Liu, "An Experiment Using NSCAT Winds in the Numerical Prediction of Tropical Mesoscale Rainfall Systems Under the Influence of Terrain," *Geophys. Res. Letters*, vol. 26, no. 3, pp. 311-314, 1999.

[7] D.B. Chelton, E.J. Walsh, J.L. MacArthur, "Pulse Compression and Sea Level Tracking in Satellite Altimetry," *J. of Atmos. and Oceanic Tech.*, vol. 6, 1989, pp. 407-438, 1989.

[8] D. Chen, M.A. Cane, and S.E. Zebiak, "The Impact of NSCAT Winds on Predicting the 1997/1998 El Nino: A Case Study with the Lamont-Doherty Earth Observatory Model," *J. of Geophy. Res.*, vol. 104, no. C5, pp. 11,321-11,327, 1999.

[9] C-Y Chi, D.G. Long, F.K. Li, "Radar Backscatter Measurement Accuracies Using Digital Doppler Processors in Spaceborne Scatterometers," *IEEE Trans. Geosci. Remote Sensing*, vol. GE-24, no. 3, pp. 426-437, 1986.

[10] C-Y Chi and F.K. Li, "A Comparative Study of Several Wind Estimation Algorithms for Spaceborne Scatterometers," *IEEE Trans. Geosci. Remote Sensing*, vol. 26, no. 2, pp. 115-121, 1988.

[11] J.C. Curlander and R.N. McDonough, *Synthetic Aperture Radar: Systems and Signal Processing*, John Wiley and Sons Inc., New York, 1991.

[12] G.W. Davidson and I. Cumming, "Signal Properties of Spaceborne Squint-Mode SAR," *IEEE Trans. on Geosci. Remote Sensing*, vol. 35, no. 3, pp. 611-617, 1997.

[13] D.S. Early and D.G. Long, "Image Reconstruction and Enhanced Resolution Imaging from Irregular Samples," *IEEE Trans. Geosci. Remote Sensing*, vol. 39, no. 2, pp. 291-302, 2001.

[14] D. Early, "A Study of the Scatterometer Image Reconstruction Algorithm and its Applications to Polar Ice Studies," Ph.D. Dissertation, Brigham Young University, Provo, Utah, 1998.

[15] C. Elachi, *Spaceborne Radar Remote Sensing: Applications and Techniques*, IEEE Press, New York, 1987.

[16] F.M. Fetterer, M.R. Drinkwater, K.C. Jezek, S.W. Laxon, R.G. Onstott, L.M. Ulander, "Sea Ice Altimetry," in Microwave Remote Sensing of Sea Ice, F.D. Carsey Ed., AGU Geophysical Monograph 68, Washington D.C., 1992.

[17] R. Fisher, "Standard Deviation of Scatterometer Measurements From Space," *IEEE Trans. Geosci. Electron.*, vol. GE-10, no. 2, pp. 106-113, 1972.

[18] G. Franceschetti and R. Lanari, *Synthetic Aperture Radar Processing*, CRC Press, Boca Raton, FL, 1999.

[19] A. Freeman, W.T.K. Johnson, B. Honeycutt, R. Jordan, S. Hensley, P. Siqueria, and J. Curlander, "The Myth of the Minimum SAR Antenna Area Constraint," *IEEE Trans. Geosci. Remote Sensing*, vol. 38, no. 1, pp. 320-324, 2000.

[20] K.S. Friedman and X. Li, "Monitoring Hurricanes Over the Ocean with Wide-Swath SAR," in *Johns Hopkins APL Technical Digest*, vol. 21, no. 1, pp. 49-57, 2000.

[21] M.H. Freilich, D.G. Long, and M.W. Spencer, "SeaWinds: A Scanning Scatterometer for ADEOS II – Science Overview," *Proceedings of the International Geoscience and Remote Sensing Symposium*, Pasadena, California, August 8-12, 1994, pp. 960-963.

[22] P.L. Frison and E. Mougin, "Monitoring Global Vegetation Dynamics with ERS-1 Wind Scatterometer Data," *Int. J. Remote Sensing*, vol. 17, no. 16, pp. 3201-3218, 1996.

[23] R.E. Glazman and S.H. Pilorz, "Effects of Sea Maturity on Satellite Altimeter Measurements," *J. Geophys. Res.*, vol. 95, no. C3, pp. 2857-2870, 1990.

[24] W.L. Grantham, E.M. Bracalante, W.L. Jones, and J.W. Johnson, "The Seasat-A Satellite Scatterometer," *IEEE J. Oceanic Eng.*, vol. OE-2, pp. 200-206, 1977.

[25] C. Grassotti, S.M. Leidner, J.F. Louis, and R.N. Hoffman, "Development and Application of Visible-Infrared Rain Flag for Scatterometer Data," *Proceeding of the ESA Workshop on Emerging Scatterometer Applications*, Noordwijk, The Netherlands, 5-7 October, 1998, pp. 203-210.

[26] J.N. Huddleston and M.W. Spencer, "SeaWinds: The QuikSCAT Wind Scatterometer," *Proceedings of the IEEE Aerospace Conf.*, Big Sky, MT, March 11-16, 2001.

[27] A.K. Jain, *Fundamentals of Digital Image Processing*, Prentice Hall, Englewood Cliffs, New Jersey, 1989.

[28] J.A. Johannessen, "Emerging Scatterometer Applications: Snow and Ice Session Summary," *Proceeding of the ESA Workshop on Emerging Scatterometer Applications*, Noordwijk, The Netherlands, 5-7 October, 1998, pp. 77-78.

[29] J.A. Kong, ed., *PIER 3 Progress in Electromagnetic Research: Polarimetric Remote Sensing*, Elsevier Science Publishing Co., Inc., New York, 1990.

[30] P. Lecompte, "The ERS Scatterometer Instrument and the On-Ground Processing of its Data," *Proceeding of the ESA Workshop on Emerging Scatterometer Applications*, Noordwijk, The Netherlands, 5-7 October, 1998, pp. 241-260.

[31] C.C. Lin, J. Wilson, F. Impanatiello, and P.S. Park, "A Rotating, Range-Gated, Fanbeam Spaceborne Scatterometer Concept," *Proceedings of the International Geoscience and Remote Sensing Symposium*, Hamburg, Germany, June 28 - July 2, 1999.

[32] J. Kerkmann and D. Klaes, "Perspectives for the Advanced Scatterometer ASCAT on METOP," *Proceeding of the ESA Workshop on Emerging Scatterometer Applications*, Noordwijk, The Netherlands, 5-7 October, 1998, pp. 13-19.

[33] T. Kirimoto and R.K. Moore, "Scanning Wind-Vector Scatterometers with Two Pencil Beams," in *Proceedings of the Conference on Remote Sensing of Oceans and Atmospheres*, NASA Conf. Pub. 2303, pp. 89-97, 1985.

[34] C. Kummerow, W. Barnes, T. Kozu, J. Shiue, and J. Simpson, "The Tropical Rainfall Measuring Mission (TRMM) Sensor Package," *J. of Atmos. and Oceanic Tech.*, vol. 15, no. 3, pp. 809-817, 1998.

[35] S-P. Xie, W.T. Liu, Q. Liu, and M. Nonaka, "Far-Reaching Effects of the Hawaiian Islands on the Pacific Ocean-Atmosphere System," *Science*, vol. 292, no. 5524, pp. 2057-2060, 2001.

[36] J.E. Graf, W-Y Tsai, and W.L. Jones, "Overview of the QuikSCAT Mission – A Quick Deployment of a High Resolution, Wide Swath Scanning Scatterometer for Ocean Wind Measurement," *Southeastcon'98*, April 1998, Orlando, FL.

[37] T.H. Guymer, "A Review of Seasat Scatterometer Data," *Phil. Trans. R. Soc. Lond.*, A. 309, pp. 399-414, 1983.

[38] S. Haykin, *Communication Systems*, 2nd ed., Wiley Publishing, New York, 1983.

[39] J.N. Huddleston and Bryan W. Stiles, "A Multidimensional Histogram Rain-Flagging Technique for SeaWinds on QuikSCAT," *IEEE International Geoscience and Remote Sensing Symposium*, Honolulu, HI, July 24-28, 2000.

[40] J.W. Johnson, L.A. Williams, E.M. Bracalente, F.B. Beck, and W.L. Grantham, "SEASAT-A Satellite Scatterometer Instrument Evaluation," *IEEE J. Oceanic Eng.*, OE-5, no. 2, pp. 138-144, 1980.

[41] P.W. Johnson and D.G. Long, "The Probability Density of Spectral Estimates Based on Modified Periodogram Average," *IEEE Trans. Signal Processing*, vol. 47, no. 5, pp. 1255-1261, 1999.

[42] W.L. Jones, V.J. Cardone, W.J. Pierson, J. Zec, L.P. Rice, A. Cox, and W. B. Sylvester, "NSCAT High Resolution Surface Winds Measurements in Typhoon Violet," *J. Geophys. Res.*, vol. 104, no. C5, pp. 11,247-11259, 1999.

[43] R.L. Jordan, "The Seasat-A Synthetic Aperture Radar System," *IEEE J. of Oceanic Eng.*, vol. OE-5, no. 2, pp. 154-164, 1980.

[44] D.G. Long, "Model-Based Estimation of Wind Fields Over the Ocean from Wind Scatterometer Measurements," Ph.D. dissertation, Univ. of Southern California, Los Angeles, 1984.

[45] D.G. Long, C-Y Chi, and F.K. Li, "The Design of an Onboard Digital Doppler Processor for a Spaceborne Scatterometer," *IEEE Trans. Geosci. Remote Sensing*, vol. 26, no. 6, pp 869-878, 1988.

[46] D. G. Long and J. M. Mendel, "Model-Based Estimation of Wind Fields over the Ocean From Scatterometer Measurements Part I: The Wind Field Model," *IEEE Trans. Geosci. Remote Sensing*, vol. 28. no. 2, pp. 349-360, 1990.

[47] D. G. Long and J. M. Mendel, "Model-Based Estimation of Wind Fields over the Ocean From Scatterometer Measurements Part II: Estimation of the Model Parameters," *IEEE Trans. Geoscience Remote Sensing*, vol. 28. no. 2, pp. 361-373, 1990.

[48] D.G. Long, M.H. Freilich, D.F. Leotta, and D.E. Noon, "A Scanning Scatterometer for the EOS Polar Platform," in *Proc. Int. Geosci. Remote Sensing Symp.*, College Park, MD, May 20-24, 1990, pp. 2447-2450.

[49] D.G. Long, P.J. Hardin, and P.T. Whiting, "Resolution Enhancement of Spaceborne Scatterometer Data," *IEEE Trans. Geosci. Remote Sensing*, vol. 31, no. 3, pp. 700-715, 1993.

[50] D.G. Long and P. Hardin, "Vegetation Studies of the Amazon Basin Using Enhanced Resolution Seasat Scatterometer Data," *IEEE Trans. Geosci. Remote Sensing*, vol. 32, no. 2, pp. 449-460, 1994.

[51] D.G. Long, "Wind Measurement Resolution for a Scanning Pencil-Beam Scatterometer," in *Proc. Int. Geosci. Remote Sensing Symp.*, Pasadena, CA, Aug. 8-12, 1994, pp. 948-952.

[52] D.G. Long and M.R. Drinkwater, "Greenland Ice Sheet Surface Properties Observed by the Seasat-A Scatterometer at Enhanced Resolution," *Journal of Glaciology*, vol. 40, pp. 213-230, 1994.

[53] D.G. Long and M.W. Spencer, "Radar Backscatter Measurement Accuracy for a Spaceborne Pencil-Beam Wind Scatterometer with Transmit Modulation," *IEEE Trans. Geosci. Remote Sensing*, vol. 35, no. 1, pp. 102-114, 1997.

[54] D.G. Long, and D.L. Daum, "Spatial Resolution Enhancement of SSM/I Data," *IEEE Trans. Geosci. Remote Sensing*, vol. 35, no. 2, pp. 407-417, 1998.

[55] D.G. Long and M.R. Drinkwater, "Cryosphere Studies Using NSCAT Data," *IEEE Trans. Geosci. Remote Sensing*, vol. 37, no. 3, pp. 1671-1684, 1999.

[56] M.A. Messeh and S. Quegan, "Global Vegetation Monitoring Using ERS-1 Scatterometer Image Generation and Backscatter Modelling," *Proceeding of the ESA Workshop on Emerging Scatterometer Applications*, Noordwijk, The Netherlands, 5-7 October, 1998, pp. 63-68.

[57] R.E. Milliff, W.G. Large, J. Morzel, G. Danabasoglu, T.M. Chin, "Ocean General Circulation Model Sensitivity to Forcing From Scatterometer Winds," *J. Geophys. Res.*, vol. 104, no. C5, pp. 11,337-11,358, 1999.

[58] R.K. Moore, "Simultaneous Active and Passive Microwave Response of the Earth – The Skylab Radscat Experiment, *Proc. 9th Intl. Symp. on Remote Sensing of the Environment*, Ann Arbor, MI, April 15-19, pp. 189-217.

[59] R.K. Moore and A.K. Fung, "Radar Determination of Winds at Sea," *Proc. of IEEE*, vol. 67, pp. 1504-1521, 1979.

[60] R.K. Moore, J.P. Claassen, Y.H. Lin, "Scanning Spaceborne Synthetic Aperture Radar with Integrated Radiometer," *IEEE Trans. Aero. Elec. Sys.*, vol. AE-17, no. 3, pp. 410-420, 1981.

[61] R.K. Moore, I.J. Birrer, E.M. Bracalente, G.J. Dome, and F.J. Wentz, "Evaluation of Atmospheric Attenuation from SMMR Brightness Temperature for the SEASAT Satellite Scatterometer," *J. Geophys. Research*, vol. 87, no. C5, pp. 3337-3354, 1982.

[62] R.K. Moore, "Effect of Pointing Errors and Range on Performance of Dual-Pencil-Beam Scatterometers," *IEEE Trans. Geosci. Remote Sensing*, vol. 23, no. 6, pp 901-905, 1985.

[63] R.K. Moore, R.G. Kennett, and F.K. Li, "Performance of a Scanning Pencil-Beam Spaceborne Scatterometer for Ocean Wind Measurements," *Proceedings of the International Geoscience and Remote Sensing Symposium*, Edinburgh, Scotland, Aug. 1988, pp. 563-564.

[64] F. Naderi, M.H. Freilich, and D.G. Long, "Spaceborne Radar Measurement of Wind Velocity Over the Ocean–An Overview of the NSCAT Scatterometer System," *Proceedings of the IEEE*, vol. 79, no. 6, pp. 850-866, 1991.

[65] S.V. Nghiem and W-Y. Tsai, "Using a Spaceborne Ku-Band Scatterometer for Global Snow Cover Monitoring," *Proceedings of the International Geoscience and Remote Sensing Symposium*, Hamburg, Germany, Jun 28 - Jul 2, 1998.

[66] S.V. Nghiem, W.T. Liu, and X. Xie, "Flood Detection and Mapping with a Spaceborne Ku-Band Scatterometer," *Proceedings of the International Geoscience and Remote Sensing Symposium*, Hamburg, Germany, Jun 28 - Jul 2, 1998.

[67] C.L. Nikias and A.P. Petropulu, *Higher-Order Spectra Analysis: A Non-Linear Signal Processing Framework*, Prentice-Hall, Englewood Cliffs, New Jersey, 1993.

[68] E.G. Njoku, W.J. Wilson, S.H. Yueh, and Y. Rahmat-Samii, "A Large-Antenna Microwave Radiometer-Scatterometer Concept for Ocean Salinity and Soil Moisture Sensing," in press, *IEEE Trans. Geosci. Remote Sensing.*

[69] J.L. Alvarez Perez, S.J. Marshall, C. Schmullius, M. Habermeyer, K. Gregson, "Resolution Enhancement of ERS Scatterometer Data," *Proceeding of the ESA Workshop on Emerging Scatterometer Applications*, Noordwijk, The Netherlands, 5-7 October, 1998, pp. 57-62.

[70] W.G. Pichel and P. Clemente-Colon, "NOAA CoastWatch SAR Applications and Demonstration," *Johns Hopkins APL Technical Digest*, vol. 21, no. 1, pp. 49-57, 2000.

[71] W.J. Plant, "A Two-Scale Model of Short Wind-Generated Waves and Scatterometry," *J. Geophys. Res.*, vol. 91, no. C9, pp 10,735-10,749, 1986.

[72] Q.P. Remund and D.G. Long, "Sea Ice Extent Mapping Using Ku-Band Scatterometer Data," *J. Geophys. Res.*, vol. 104, no. C5, pp. 11515-11527, 1999.

[73] Q.P. Remund, D.G. Long, and M.R. Drinkwater, "An Iterative Approach to Multisensor Sea Ice Classification," *IEEE Trans. Geosci. Remote Sensing*, vol. 38, no. 4, pp. 1843-1856, 2000.

[74] H.R. Raemer, *Radar System Principles*, CRC Press, Boca Raton, FL, 1997.

[75] W.D. Robinson, C. Kummerow, and W.S. Olson, "A Technique for Enhancing and Matching the Resolution of Microwave Measurements from the SSM/I Instrument," *IEEE Trans. Geosci. Remote Sensing*, vol. 30, no. 3, pp 419-429, 1992.

[76] S.W. Running, J.B. Way, K.C. McDonald, J.S. Kimball, S. Frolking, A.R. Keyser, and R. Zimmerman, "Radar Remote Sensing Proposed for Monitoring Freeze-Thaw Transitions in Boreal Regions," *Eos, Transactions, American Geophysical Union*, vol. 80, no. 19, pp. 213, 220-221, 1999.

[77] R. Sethmann, B.A. Burns, G.C. Heygster, "Spatial Resolution Improvement of SSM/I Data with Image Restoration Techniques," *IEEE Trans. Geosci. Remote Sensing*, vol. 32, no. 6, pp. 1144-1151, 1994.

[78] L.C. Schroeder, D.H. Boggs, G. Dome, I.M. Halberstam, W.L. Jones, W.J. Pierson, and F.J. Wentz, "The Relationship Between Wind Vector and Normalized Radar Cross-Section Used to Derive SEASAT-A Scatterometer Winds," *J. Geophys. Res.*, vol. 87, no. C5, pp. 3318-3336, 1982.

[79] M.W. Spencer and M. Shimada, "Effect of Rain on Ku-Band Scatterometer Wind Measurements," *Proceedings of the International Geoscience and Remote Sensing Symposium*, Helsinki, Finland, June 3-6, 1991, pp. 1285-1287.

[80] M.W. Spencer, W. Tsai, S. Yueh, G. Neumann, "NASA Scatterometer Calibration Philosophy and Approach," *SPIE International Symposium on Aerospace and Remote Sensing*, Orlando, Fl, April, 1993.

[81] M.W. Spencer, C. Wu, and D.G. Long, "Tradeoffs in the Design of a Spaceborne Scanning Pencil Beam Scatterometer: Application to SeaWinds," *IEEE Trans. Geosci. Remote Sensing*, vol. 35, no. 1, pp. 115-126, 1997.

[82] M.W. Spencer, J.E. Graf, "The NASA Scatterometer (NSCAT) Mission," *Backscatter*, vol. 8, no. 4, pp. 18-24, November, 1997.

[83] M.W. Spencer and D.G. Long, "Characterization of Global Near-Nadir Backscatter for Remote Sensing Radar Design," *Proceedings of the International Geoscience and Remote Sensing Symposium*, Hamburg, Germany, June 28 - July 2, 1999.

[84] M.W. Spencer, C. Wu, and D.G. Long, "Improved Resolution Backscatter Measurements with the *SeaWinds* Pencil-Beam Scatterometer," *IEEE Trans. Geosci. Remote Sensing*, vol. 38, no. 1, pp. 89-104, 2000.

[85] M.W. Spencer, W-Y Tsai, and D.G. Long, "High Resolution Scatterometry by Simultaneous Range/Doppler Discrimination," *IEEE International Geoscience and Remote Sensing Symposium*, Honolulu, HI, July 24-28, 2000.

[86] M.W. Spencer, J.N. Huddleston, and B.W. Stiles, "Advanced Design Concepts for a SeaWinds Scatterometer Follow-On Mission," Proceedings of the IEEE Aerospace Conf., Big Sky, MT, March 11-16, 2001.

[87] M.W. Spencer, W. Tsai, and D. G. Long, "High Resolution Measurements with a Spaceborne Pencil-Beam Scatterometer Using Combined Range/Doppler Discrimination Techniques," submitted to *IEEE Trans. Geosci. Remote Sensing*, 2001.

[88] C.C. Schmullius, "Monitoring Siberian Forests and Agriculture with the ERS Wind Scatterometer," *IEEE Trans. Geosci. Remote Sensing*, vol. 35, no. 5, 1997.

[89] B.W. Stiles, B.D. Pollard, and R.S. Dunbar, "Direction Interval Retrieval with Thresholded Nudging – A Method for Improving the Accuracy of QuikSCAT Winds," accepted for publication in *IEEE Trans. Geosci. Remote Sensing*, 2001.

[90] J.R.G. Townshend, C.O. Justice, D. Skole, J-P Malingreau, J. Cihlar, P.M. Teillet, F. Sadowski, and S. Ruttenberg, "The 1-km AVHRR Global Data Set: Needs of the International Geosphere Biosphere Program, *Int. J. Remote Sensing*, vol. 15, no. 17, pp 3417-3441, 1994.

[91] W-Y Tsai, J.N. Huddleston, M.W. Spencer, and R.D. West, "Modeling and Simulation for SeaWinds 1-B System Design and Performance Evaluation," *Proceedings of SPIE: Sensors, Systems, and Next-Generation Satellites*, London, UK, September 1997.

[92] W-Y Tsai, J.E.Graf, C. Winn, J.N. Huddleston, R.S. Dunbar, M.H. Freilich, F.J. Wentz, D.G. Long, W.L. Jones, "Post-Launch Sensor Verification and Calibration of the NASA Scatterometer," *IEEE Trans. Geosci. Remote Sensing*, vol. 37, no. 3, pp. 1517-1542, 1999.

[93] W.Y. Tsai, S.V. Nghiem, J.N. Huddleston, M.W. Spencer, B.W. Stiles, and R.D. West, "Polarimetric Scatterometry: A Promising Technique for Improving Ocean Surface Wind Measurements from Space," *IEEE Trans. Geosci. Remote Sensing*, vol. 38, no. 4, pp. 1903-1921, 2000.

[94] F.T. Ulaby, R.K. Moore, and A.K. Fung, *Microwave Remote Sensing – Active and Passive: Vol. 1*, Addison-Wesley Publishing Company, Reading, MA, 1981.

[95] F.T. Ulaby, R.K. Moore, and A.K. Fung, *Microwave Remote Sensing – Active and Passive: Vol. 2*, Addison-Wesley Publishing Company, Reading, MA, 1981.

[96] L. Ulander and A. Carlstrom, "Radar Backscatter Signatures of Baltic Sea Ice," *Proceedings of the International Geoscience and Remote Sensing Symposium*, Helsinki, Finland, June 3-6, 1991, pp. 1215-1218.

[97] W. Wagner, "A Comparison of ERS Scatterometer Retrieved Soil Moisture Data with Field Observations in the Ukraine," *Proceeding of the ESA Workshop on Emerging Scatterometer Applications*, Noordwijk, The Netherlands, 5-7 October, 1998, pp. 33-38.

[98] J.M. Wallace and P.V. Hobbs, *Atmospheric Science: An Introductory Survey*, Academic Press, Inc., Orlando, FL, 1977.

[99] D.P. Winebrenner, D.G. Long, and B. Holt, "Automatable Observation of Seasonal Transitions on Arctic Sea Ice Using Synthetic Aperture Radar," in C. Tsatsoulis and R. Kwok (eds), *Recent Advances in the Analysis of SAR for Studies in the Polar Oceans*, Springer-Verlager, pp. 129-144, 1998.

[100] V.R. Wismann and K. Boehnke, "Monitoring Snow Properties on Greenland with ERS Scatterometer and SAR," *Proceedings of Third ERS Symposium*, ESA SP-414, vol. 2, pp. 857-86, May 1997.

[101] V. Wisman, "Land Surface Monitoring with Spaceborne Scatterometers" *Proceeding of the ESA Workshop on Emerging Scatterometer Applications*, Noordwijk, The Netherlands, 5-7 October, 1998, pp. 25-32.

[102] C. Wu, J. Graf, M.Freilich, D.G. Long, M. Spencer, W. Tsai, D. Lisman, and C. Winn, "The SeaWinds Scatterometer Instrument," *Proceedings of the International Geoscience and Remote Sensing Symposium*, Pasadena, California, August 8-12, 1994, pp. 1511-1515.

[103] S.H. Yueh, R. Kwok, S-H Lou, and W-Y Tsai, "Sea Ice Identification Using Dual-Polarized Ku-Band Scatterometer Data," *IEEE Trans. Geosci. Remote Sensing*, vol. 35, no. 3, pp. 560-569, 1997.

[104] S.H. Yueh, R. Kwok, S.V. Nghiem, "Polarimetric Scattering and Emission Properties of Targets With Reflection Symmetry," *Radio Science*, vol. 29, No. 6, pp. 1409-1420, 1994.

[105] A.R. Zieger, D.W. Hancock, G.S. Hayne, C.L. Purdy, "NASA Radar Altimeter for the TOPEX/POSEIDON Project," *Proceedings of the IEEE*, vol. 79, no. 6, pp. 810-826, 1991.